Thermoelastic Properties of Materials with Negative Coefficients of Thermal Expansion

by

Carl P. Romao

Submitted in partial fulfilment of the requirements
for the degree of Doctor of Philosophy

at

Dalhousie University
Halifax, Nova Scotia
July 2015

Table of Contents

List of Tables

List of Figures

Abstract

Several families of ceramic materials composed of corner-linked coordination polyhedra are known to display the rare property of negative thermal expansion, *i.e.*, reversible contraction upon heating. However, as shown herein, the ability of these thermomiotic (heat-shrinking) materials to successfully counteract positive thermal expansion depends on their elastic properties. This finding has motivated experimental and computational studies of thermal expansion, elasticity, and their interactions under thermal stress in thermomiotic materials.

Finite element analysis showed that inclusion of compliant or low-thermal-expansion components, or those which undergo pressure-induced phase transitions, can reduce thermal stress due to thermal expansion mismatch. These strategies were applied in the synthesis of composites combining thermomiotic ZrW_2O_8 and $Al_2W_3O_{12}$ and positive-thermal-expansion alumina-toughened zirconia, and in the synthesis of lamellar ZrW_2O_8/polymethylmethacrylate composites. The thermal expansivities of the composites were highly dependent on the stiffnesses of their components.

The chemical flexibility of the $A_2M_3O_{12}$ and $AMgM_3O_{12}$ material families, with thermal expansion ranging from negative to low-positive, was used to investigate relationships between elasticity and thermal expansion. Three series of solid solutions, $In_{2-2x}(HfMg)_xMo_3O_{12}$, $Sc_{2-2x}Al_{2x}W_3O_{12}$, and $Cr_{2-2x}(HfMg)_xW_3O_{12}$, were synthesized and characterized, and significant variations in the thermal expansion and stiffness with composition were observed. In general, materials with larger-magnitude thermal expansion were more compliant. $ZrMgMo_3O_{12}$ was found to have zero thermal expansion, and its structure was used to explain its thermal expansion and that of $A_2M_3O_{12}$ materials. Thermal expansion in this group of materials was related to the ionic forces of the coordination polyhedra, with more distortable polyhedra leading to more negative thermal expansion.

Density functional theory calculations of phonon band structure and experimental heat capacity measurements were performed on the simple thermomiotic material ScF_3, showing the stability of its structure upon cooling to 0.38 K. The elastic tensors and Γ-point phonon frequencies of $Al_2Mo_3O_{12}$, $ZrMgMo_3O_{12}$, and $Sc_2Mo_3O_{12}$ were also calculated. These anisotropic materials showed correlations between axial thermal expansion and stiffness, with thermomiotic axes found to be stiffer. The calculated elastic tensors were then used to model thermal stress due to anisotropic thermal expansion in polycrystals, showing large extremal thermal stresses affected by coupling of thermal expansion and elastic anisotropy.

List of Abbreviations and Symbols Used

A_1, A_2	parameters
ATZ	alumina-toughened zirconia
A_U	universal anisotropy parameter
BE	backscattered electrons
BZ	Brillouin zone
$\mathbf{c}$	stiffness tensor
$\mathbf{c'}$	rotated stiffness tensor
c_{ijkl}, c_{ij}	elements of the stiffness tensor
C_P	molar heat capacity at constant pressure
$C_{P,s}$, $C_{P,p}$	heat capacities of sample and platform
CTE	coefficient of thermal expansion
C_V	molar heat capacity at constant volume
d	spacing between a set of crystallographic planes
DFT	density functional theory
DOS	density of states
e_c	elementary charge
EDS	energy-dispersive spectroscopy
E_{ee}	energy of the Coulombic repulsion of electrons
E_{ii}	energy of the Coulombic repulsion of nuclei
E_{xc}	exchange-correlation energy
F	interatomic force
F_a	attractive force
FEA	finite element analysis
FE	finite element
FEM	finite element method
F_k^2	structure factor
FT	Fourier transform
FWHM	full width at half maximum
G	shear modulus

GGA	generalized-gradient approximation
g_i	degeneracy of the ith mode
G_{ij}	Shear modulus of the plane between axis i and axis j
G_R	Reuss shear modulus
G_V	Voigt shear modulus
h	Planck's constant
I_k	integrated intensity of a Bragg reflection
J_{el}	volume ratio corrected for thermal expansion
J_{th}	volume ratio relative to the reference state
k	Boltzmann's constant
$\mathbf{k}$	wavevector for electronic structure
K	bulk modulus
K_a	bulk modulus of the volume about atom a
k_{e}	Coulomb's constant
$k_{\text{g}}, k_{\text{w}}$	thermal conductances of grease and wires
K_i	bulk modulus of the ith component
K_R	Reuss bulk modulus
K_V	Voigt bulk modulus
ℓ_0	original sample length
LAS	lithium aluminum silicate
LDA	local density approximation
LVDT	linear variable differential transformer
MAS	magic-angle spinning
MEMS	microelectromechanical systems
n	an integer
N	number of atoms
$n_{i,\mathbf{q}}$	phonon occupation number of mode i for wavevector $\mathbf{q}$
NMR	nuclear magnetic resonance
NTE	negative thermal expansion
p	probability
P	pressure

PBE	Perdew–Burke–Ernzerhof
PE	polyethylene
PEG	polyethylene glycol
PIA	pressure-induced amorphization
PIPT	pressure-induced phase transition
PMMA	polymethylmethacrylate
P_{PT}	threshold pressure for a phase transition
PTE	positive thermal expansion
PVA	polyvinyl alcohol
PVP	polyvinylpyrrolidone
$\mathbf{q}$	wavevector for phononic structure
Q	heater power
r	interatomic distance
$\mathbf{r}$	position vector
$\boldsymbol{R}$	second-rank rotation tensor
R_{ij}	elements of the second-rank rotation tensor
r_o	sum of cation and anion radii
R	gas constant
RUM	rigid-unit mode
$\boldsymbol{s}$	compliance tensor
S	entropy
SDBS	sodium dodecylbenzenesulfonate
SE	secondary electrons
SEM	scanning electron microscopy/microscope
s_{ijkl}, s_{ij}	elements of the compliance tensor
t	time
T	temperature
$\boldsymbol{T}$	fourth-rank rotation tensor
TGA	thermogravimetric analysis
T_{onset}	onset temperature of a phase transition
T_p	temperature of the platform

T_s	temperature of the sample
$\hat{T}$	kinetic energy
$\hat{T}_u$	kinetic energy of a non-interacting system
U	potential energy
U_{ext}	external potential
$\hat{U}_{int}$	electron-electron interaction energy
U_w, V_w, W_w	peak width parameters
V	volume
V_a	volume about atom a
V_i	volume of an ideal polyhedron
V_m	molar volume
vol.%	volume percent
V_r	volume of a real polyhedron
VRH	Voigt–Reuss–Hill
VTMS	vinyl trimethoxysilane
$w_{j,k}$	weighting factor
W_{max}	amount of strain energy required to complete a phase transition
W_{min}	amount of strain energy required to begin a phase transition
x	compositional parameter
$\mathbf{x}, \mathbf{y}, \mathbf{z}$	basis vectors
$\mathbf{x'}, \mathbf{y'}, \mathbf{z'}$	rotated basis vectors
XRD	X-ray powder diffraction
Y	Young's modulus
Y_{ii}	Young's modulus along axis i
y_j	peak profile function
YSZ	yttria-stabilized zirconia
Z_-	average anion valence
Z'	real component of the electrical impedance
Z''	imaginary component of the electrical impedance
Z_+	cation valence
ZTA	zirconia-toughened alumina

$\boldsymbol{\alpha}$	thermal expansion tensor
$\boldsymbol{\alpha'}$	rotated thermal expansion tensor
$\alpha_a, \alpha_b, \alpha_c$	thermal expansion along unit cell axes
α_{Bulk}	bulk coefficient of thermal expansion of a composite
α_i	coefficient of thermal expansion of the ith component
α_{ij}	elements of thermal expansion tensor
α_ℓ	(linear) coefficient of thermal expansion along length ℓ
α_V	volumetric coefficient of thermal expansion
β	scale parameter for a Weibull distribution
β_{ii}	Compressibility along axis i
γ	bulk Grüneisen parameter
Γ	centre point of the Brillouin zone
γ_i	Grüneisen parameter of the ith mode
$\gamma_{i,\mathbf{q}}$	Grüneisen parameter of mode i for wavevector $\mathbf{q}$
γ_{ii}	Grüneisen parameter for axis i
γ-MPS	3-(trimethosilyl)propyl methacrylate
ΔH	enthalpy change
$\Delta \ell$	change in sample length
ΔT_{max}	thermal shock resistance
ΔV_{PT}	volume change during a phase transition
$\Delta \alpha_{max}$	maximum difference in thermal expansion between two axes
$\varepsilon_{ij}, \varepsilon_i$	elements of the Cauchy strain tensor
$\boldsymbol{\varepsilon}_{th}$	thermal strain tensor
$\varepsilon_{th,ij}$	elements of thermal strain tensor
ζ	shape parameter for a Weibull distribution
θ	angle between a beam of X-rays and a set of crystallographic planes
θ_D	Debye temperature
ϑ, φ, ψ	random Euler angles
κ_e	electrical conductivity
κ_T	thermal conductivity
λ	wavelength

μ	Poisson ratio
μ_{ij}	Poisson ratio relating an applied strain along axis i to a strain along axis j
v_0	zero-porosity velocity of sound
v_{exp}	measured velocity of sound
v_i	frequency of the ith mode
$v_{i,\mathbf{q}}$	vibrational frequency of mode i for wavevector $\mathbf{q}$
v_l	longitudinal velocity of sound
v_t	transverse velocity of sound
ξ	polyhedral distortion
ρ	density
ρ_0	ground-state density
σ_0	location parameter for a Weibull distribution
$\sigma_1, \sigma_2, \sigma_3$	principal stresses
σ_I	first principal invariant of stress
σ_{ij}, σ_i	elements of the Cauchy stress tensor
σ_{max}	material strength
τ_s, τ_p	relaxation times of sample and platform
Φ	lattice energy
ϕ_i	volume fraction of the ith component
ϕ_p	pore volume fraction
χ^2	goodness-of-fit parameter
Ψ_0	ground-state wavefunction

Acknowledgements

Chapter 1: Introduction[i]

1.1. Introduction to Thermal Expansion

1.1.1. Why are Thermomiotic Materials Interesting?

Most materials change their dimensions when the temperature changes. Usually, the dimensions increase with increasing temperature, and this phenomenon is referred to as positive thermal expansion (PTE). The thermally induced change in dimension of a material in a confined environment can lead to significant stress. If the stress exceeds the strength of the material it will fracture or deform irreversibly, possibly with disastrous consequences.

On the other hand, some materials shrink with increasing temperature, giving rise to negative thermal expansion (NTE). The term 'thermomiotic' (from the Greek, 'thermo' for 'heat' and 'mio' for 'contract') has been introduced to describe such materials.[1] The excitement about thermomiotic materials is that, in principle, they could compensate for positive thermal expansion, presenting materials that would not experience thermal stress failure.

1.1.2. Thermal Expansion

The coefficient of thermal expansion, generally abbreviated as α and also called the CTE, can be defined along a particular length, ℓ, as:[2]

$$\alpha_\ell = \frac{1}{\ell}\left(\frac{\partial \ell}{\partial T}\right)_P, \tag{1.1}$$

where, for example, ℓ, could be one of the principal crystallographic directions (*a, b* or *c,* giving α_a, α_b and α_c, respectively), and T is temperature. The volumetric coefficient of thermal expansion, α_V, is:

$$\alpha_V = \frac{1}{V}\left(\frac{\partial V}{\partial T}\right)_P, \tag{1.2}$$

where V is the volume. Note that both α_ℓ and α_V are intrinsic to a given material at a given temperature, and are independent of the material's size. Both α_V and the directional values of α have units of K^{-1},[ii] but it is important to distinguish the type of CTE. If the material is cubic, $\alpha_V = 3\alpha_a$ but for less symmetric structures, the relationship is not so simple (see Section 1.3.2.1). Indeed, the α values in different directions can have different signs making α_V close to zero.

A typical diagram for an interatomic potential (U as a function of interatomic distance, r; see Figure 1.1) is well-represented by a harmonic potential at low energy (near the bottom of the well), but deviates significantly from harmonicity when there is sufficient thermal energy. The average interatomic distance, $<r>$, depends on the temperature and increases with increasing thermal energy (*i.e.*, with height above the well minimum), as shown in Figure 1.1. This behaviour contrasts with that of the harmonic potential where $<r>$ is independent of temperature, giving $\alpha = 0$ K^{-1}. Therefore, in general terms, the normal positive deviation of the CTE from zero is a measure of the anharmonic interactions in the interatomic potential.[3,4]

[ii] For ease of comparison, CTEs in this work are expressed in units of 10^{-6} K^{-1}. These units are equivalent to the units of MK^{-1} and ppm K^{-1} which are used occasionally in the literature.
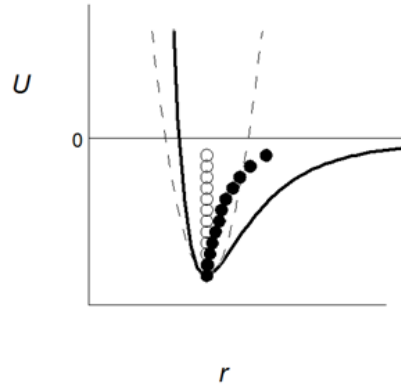
Figure 1.1: Potential energy (U) as a function of interatomic separation (r) for a harmonic system (potential given by - - and average positions at different temperatures, <r>, given by ○) and an anharmonic system (potential given by —— and <r> given by ●). Adapted from Reference 1 with permission.

A few consequences of the potential shown in Figure 1.1 are worth highlighting. One is that as $T \rightarrow 0$ K, the true potential approaches the harmonic potential and $\alpha \rightarrow 0$ K^{-1}. This is true for all materials. Additionally, the relationship between the interatomic force, F, and the interatomic potential, U, is given in general by

$$F = -\left(\frac{\partial U}{\partial r}\right). \tag{1.3}$$

Since stronger interatomic forces lead to steeper potentials, stiffer materials tend to have smaller CTEs.[5] Conversely, if the interatomic potential is weak then the CTE will be larger. Inorganic materials generally have smaller CTEs at a given temperature than organic materials or polymers.[5] For ceramics, α_ℓ typically ranges from approximately 10^{-6} K^{-1} to 10^{-5} K^{-1}, for metals values of the order of 10^{-5} K^{-1} are common, while CTEs of polymers can be larger than 10^{-4} K^{-1}.[1,3,5]

Equation 1.2 can be re-written using a Maxwell relation, as:[6]

$$\alpha_V = K^{-1}\left(\frac{\partial S}{\partial V}\right)_T, \tag{1.4}$$

where S is the entropy and K is the bulk modulus $(= -V (\partial P/\partial V)_T)$. Normally, entropy decreases with compression, but for thermomiotic materials, entropy increases as the volume drops.[6]

The CTE of a material can have far-reaching implications for applications. It is intrinsically tied to the other important thermoelastic properties of a material, such as the bulk and shear moduli. While the CTE quantifies the change of dimension with temperature, the shear modulus quantifies the change of shape following applied shear stress, and the bulk modulus quantifies changes in volume following applied normal, or hydrostatic stress.

1.2. Mechanisms of Negative Thermal Expansion

Several different structural and dynamical NTE mechanisms have been elucidated, although not all of the mechanisms for negative expansion are fully understood for all of the systems where NTE occurs. Herein materials where the mechanism of NTE is vibrational are considered.

1.2.1. Lattice Vibrations

A phonon is a quantized lattice vibration in a crystal. The lattice waves can be along the propagation direction (longitudinal phonons) or across it (transverse phonons). A simple three-atom view of a metal-oxygen-metal (M–O–M) linkage is shown in Figure 1.2. With increasing temperature, the length of the M–O bond increases due to normal (positive) thermal expansion. However, the average M—M distance can decrease due to transverse vibrations as the bridging oxygen in the M–O–M unit vibrates with increasing amplitude.
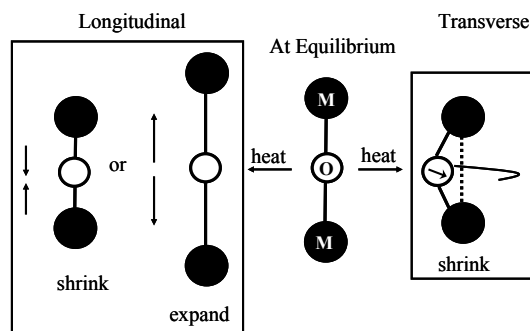
Figure 1.2: Longitudinal vibrations lead to expansion (on average) of the *M*–O–*M* linkage while transverse vibrations could lead to contraction. Adapted from Reference 7 with permission.

In a solid with oxygen-connected rigid polyhedra, the transverse vibration of the *M*–O–*M* unit can result in coupled rocking motion of the polyhedra (Figure 1.2). If the polyhedra rotate in a cooperative manner without much destruction of the polyhedral units, NTE can result from the transverse optic vibration shown schematically in Figure 1.2 as well as from transverse acoustic vibrations.[8] The oxygen atom shown in Figure 1.2 can be replaced by a fluorine atom, giving rise to the metal fluoride group of thermomiotic materials,[1] or by a cyanide ligand which grants the structure additional flexibility.[1] Metal-organic frameworks, where the linking group includes a larger organic molecule, have also been shown in some cases to display NTE.[1]

Librational (*i.e.*, rocking) vibrations in rigid bonds can lead to a decrease in the perceived atomic bond length from diffraction studies relative to true bond length.[9] Figure 1.3 shows a schematic of the effect of libration on a perceived average *M*–O distance. Strong librational modes can accompany transverse vibrations and contraction in the apparent lengths of bonds. The decrease in perceived bond length of Si–O in zeolites as temperature is increased can result in very negative apparent thermal expansion coefficients.[9]
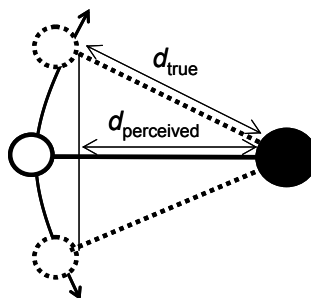
Figure 1.3: Librational vibrations cause the perceived *M*–O distance to decrease as the magnitude of the vibration increases. Styled after Reference 9. Adapted from Reference 1 with permission.

Recall that positive thermal expansion is a result of the anharmonic nature of bonds (Section 1.1.2). Quantification of the anharmonicity in a solid can be achieved with the Grüneisen parameter, γ. The Grüneisen parameter of a vibration can be most rigorously defined, following the approach of Hofmeister and Mao, for a phonon mode *i* in terms of the frequency of that mode v_i as:[10]

$$\gamma_i = -\frac{V_a}{v_i}\frac{\partial v_i}{\partial V_a},\tag{1.5}$$

where V_a is the volume about the vibrating atom(s).[iii] At low temperatures, as a consequence of increased harmonicity, $\gamma_i \rightarrow 0$ as $T \rightarrow 0$ K. Since the mode Grüneisen parameter is proportional to v_i^{-1}, low-energy vibrational modes are generally the largest contributors to thermal expansion.[8]

Equation 1.5 shows that NTE originates from vibrational modes whose frequencies decrease under compression and increase under tension. The connection between this behaviour and vibrational modes of the type shown in Figure 1.2 can be understood by considering their behaviour under tension. Assuming that the *M*–O bonds

---

[iii] Making a distinction between V_a and V (the unit cell volume) is useful in cases where elastic anisotropy or inhomogeneity cause interatomic distances to scale unevenly with pressure.[10]

are stiff, putting the system in tension along the M—M direction will increase the energy

of the transverse vibration.[8] Equivalently, if the M—M distance is fixed an increase in the

amplitude of the transverse vibration due to an increase in temperature will place the

system into tension.[6] For this reason, the vibrational mechanism for NTE described above

has been called the tension effect.[6,8]

In practice, mode Grüneisen parameters are normally determined directly by high-

pressure spectroscopic measurements as:[10]

$$\gamma_i = -\frac{K_a}{v_i}\frac{\partial v_i}{\partial P},$$ (1.6)

where K_a is the bulk modulus of the volume V_a. For practical reasons, K_a is normally

treated as just K, the overall bulk modulus of the material, although this is not strictly true

except in the case of monatomic and diatomic solids, where there is only one nearest-

neighbour distance.[10] For a harmonic solid, v_i is independent of volume so $\gamma_i = 0$ for all

modes. Any deviation from zero in the Grüneisen parameter will therefore be an

indication of the anharmonic interactions in the solid: the larger the magnitude, the larger

the degree of anharmonicity.

The bulk Grüneisen parameter is related to other thermodynamic parameters as a

function of temperature through:[10]

$$\gamma = \frac{K\alpha_V V_\mathrm{m}}{C_V},$$ (1.7)

where V_m is the molar volume and C_V is the constant volume heat capacity. Since C_V, K,

and V_m have positive values, the signs of the Grüneisen parameter and the CTE are the

same (*i.e.*, both negative for NTE). The product of K and α_V is equal to $\left(\frac{\partial P}{\partial T}\right)_V$, so the

Grüneisen parameter is the inverse of the ratio between the energy gained by the material

upon heating ($C_V\ V_\mathrm{m}^{-1}$) and the pressure generated by this energy which acts to expand (or contract) the unit cell.[6]

The bulk Grüneisen parameter is equal to the average of the mode Grüneisen parameters weighted by their contributions to the heat capacity, which is usually quite close to their simple average.[10] The CTE is related to the mode Grüneisen parameters through:

$$\alpha_V = \frac{1}{KV}\sum_{i,\mathbf{q}} h\nu_{i,q}\gamma_{i,\mathbf{q}}\frac{\partial n_{i,\mathbf{q}}}{\partial T}, \tag{1.8}$$

where $\nu_{i,\mathbf{q}}$, $\gamma_{i,\mathbf{q}}$, and $n_{i,\mathbf{q}}$ are the vibrational frequency, Grüneisen parameter and phonon occupation number, respectively, of mode i for wavevector $\mathbf{q}$; Equation 1.8 allows prediction of the CTE from the pressure-dependent phonon dispersion relation, as has been reported, for example, for $Zn(CN)_2$.[11] Equation 1.8 is not strictly valid for solids containing different coordination polyhedra, as the bulk modulus of the volume undergoing vibration should be included in the summation. Such a change corrects the large potential difference ($\leq 25\ \%$) between the Grüneisen parameter as determined by direct measurement of the other variables in Equation 1.7 and the Grüneisen parameter as determined by spectroscopic measurements, $i.e.$, measurements of the mode Grüneisen parameters.[10] Similarly, axial Grüneisen parameters,[12] which include the coupling of the axial CTEs to one another through the elastic stiffness tensor, do not sum to the bulk Grüneisen parameter because the thermal deformation of the material is not always strictly volumetric.[13] However, the solution proposed to this problem by Choy $et\ al.$ in Reference 13 essentially treats all the axial Poisson ratios as zero and the elastic response as isotropic.

In the case of a simple solid with PTE, the quantities K and γ can be qualitatively described as measures of the strength of the chemical bonds in the solid and the anharmonicity of those bonds respectively. Stronger chemical bonds are generally more harmonic; for example the mode Grüneisen parameters of diamond average about 1.25 at room temperature,[14] considerably lower than the typical value of about 2.[15] As α_V decreases with increasing K and decreasing γ, it is easy to state that stronger chemical bonds lead to lower thermal expansion, and indeed this is generally true of PTE materials.[5,16] However, the largest possible variations in the Grüneisen parameters (which reach a maximum value of about 10 in materials held together by dispersive forces)[17,18,19] are considerably smaller than those in the CTE (which can range from 10^{-6} K^{-1} to 10^{-4} K^{-1} for conventional materials).[3] Therefore, around room temperature and above (where C_V is often reasonably close to the Dulong-Petit limit),[3] most of the differences in α_V between materials are determined by differences in K rather than γ (see Equation 1.7).

Stiffness therefore can be expected to play a role in the thermal expansion of thermomiotic materials as well. The bulk and/or Young's moduli of various thermomiotic materials have been reported[20,21,22,23,24,25,26,27,28] and generally have been found to be lower than would be expected from the strengths of their chemical bonds.[16,25] This low stiffness has been ascribed to the same structural factors (*i.e.*, a flexible network structure, void space in the unit cell, and rotation of rigid units) that lead to NTE.[25,29] The values of γ_i belonging to transverse vibrations of bridging atoms are not related to the anharmonicity of a chemical bond, but rather the shallowness of the potential well perpendicular to the *M—M* axis. For example, mode Grüneisen parameters for low-

energy librational modes in the thermomiotic material ScF_3 reach values as low as -300.[30]

As the bulk modulus depends on structural factors as well as the strength of chemical bonds, the relation between K and γ is difficult to predict. However, at temperatures sufficiently high that the heat capacity can be treated as constant, the bulk modulus can be expressed as:[31]

$$K \approx V \frac{\partial^2 \Phi}{\partial V^2} + \frac{kT}{V} \gamma \qquad (1.9)$$

where Φ is the lattice energy, indicating that, for materials with negative Grüneisen parameters, thermal effects can decrease the bulk modulus.[8,31]

1.2.2. Rigid Unit Modes

The rigid-unit mode (RUM) model states that when the temperature of a framework solid increases, linked rigid polyhedra will rock without being distorted and thereby give rise to transverse vibrations perpendicular to the M—M linkage axis.[32,33] Generally, the associated potential is shallow and the vibrations can be excited at low temperatures. M–O–M linkage distortion requires less energy than distortion of the rigid polyhedra, so the framework shrinkage overrides the positive thermal expansion within the polyhedra and gives rise to NTE.

The RUM model was originally developed to describe the behaviour of a large class of materials with the motif of corner-linked coordination polyhedra.[33] The applications of this model include interpretation of the nature of high-temperature phases[33] and linking the magnitude of the transition temperature to the polyhedral stiffness.[34,35,36] The RUM model also has been used to provide insight into the stability

and physical properties of framework silicates.[36,37] In the late 1990s, researchers used the RUM model to explain NTE in β-quartz[38] and the extensive NTE ($\alpha_a = -9 \times 10^{-6}$ K^{-1} from 0.3 to 1050 K)[39] in ZrW_2O_8.[32,40] In certain systems, the polyhedral rotations give rise to small distortions in the polyhedra. These are said to be quasi-RUMs, and occur in the AM_2O_7 family.[41]

A detailed investigation by Tao and Sleight considered the correlation between RUMs and NTE for a series of framework oxides.[42] They used a computer program developed by Hammonds $et\ al.$[43] to determine whether RUMs exist in the dynamical structure of oxides, and found that some oxides show RUMs but NTE is not observed. It also was shown that strong NTE can exist without RUMs. Correlations between RUMs and NTE have also been examined by comparison of the phonon modes which contribute to NTE to those predicted by a RUM model.[8] In many thermomiotic materials, RUMs provide a significant contribution to NTE but other vibrational modes also contribute.[8]

A large family of thermomiotic materials without RUMs is the tungstates and molybdates of the general formula $A_2M_3O_{12}$ where the A and M cations are coordinated by oxygen octahedrally and tetrahedrally, respectively.[44] Members of this family of oxides can exhibit strong, anisotropic NTE over a large temperature range although these compounds do not have RUMs. The NTE in this family can still be understood in terms of the transverse vibrations and tilting of the polyhedra.[44] These vibrational motions can cause significant distortions to the polyhedra,[45,46,47] and the polyhedral distortion of the AO_6 octahedron has been correlated with NTE.[45]

1.3. Applications of Thermomiotic Materials

1.3.1. Current and Potential Applications

Thermomiotic materials have prospective uses in many scientific and engineering fields where thermal expansion must be controlled. The lithium aluminum silicate (LAS) glass ceramic system, in which thermomiotic crystallites are formed in a PTE glass matrix, was the first widely commercialized composite material to achieve near-zero thermal expansion over a wide range of temperatures.[48] These glass ceramics have excellent thermal shock resistance due to their low CTEs (and the small difference in CTE between the two components), and are commonly used as stovetops.[49] LAS glass ceramics are also important optical materials; they can be used to create lenses and mirrors with temperature-independent optical properties.[49]

Commercial LAS glass-ceramics possess very low thermal expansion ($\alpha_\ell \leq 0.15 \times 10^{-6}$ K^{-1}) near room temperature, and can withstand temperatures as high as 1500 K,[50] however their applications are limited at high temperatures due to their partially amorphous nature. The thermal expansion of LAS materials is extremely low in part because the formation of crystallites from the amorphous starting material is carefully controlled by a heating step at about 900 K, but if they are used at temperatures above their heat treatment temperature the crystalline fraction can increase, changing the bulk CTE.[51] These materials begin to exhibit viscoelastic creep (extension under constant load) at temperatures below their glass transition temperature (*e.g.*, 970 K).[50] While it is possible to reduce the creep of these materials by changing the composition and processing conditions, this could also change the thermal expansion behaviour.[50] Near-zero thermal expansion materials including a component such as $Sc_2W_3O_{12}$, which melts

at 1875 K[52] (although its CTE has only been measured up to 1275 K),[53] could potentially offer a large improvement over the usable temperature range of LAS glass-ceramics.

The wide variety of thermomiotic materials discovered since 1996 generally have not yet found commercial applications. However, the large number of recent patents regarding thermomiotic materials testifies to their potential use.[54] Thermomiotic materials have been proposed for use in tires[55] and industrial equipment[56] to improve their ability to withstand thermal cycling. Several porous thermomiotic ceramics exhibit high strength and chemical durability at high temperatures for use in catalytic converters.[57]

Several potential applications for thermomiotic materials in the field of optics have been identified. They can be used as substrates for fibre diffraction gratings, an application that is extremely sensitive to length changes,[58,59,60] and lasers.[61]

In the electronics industry, thermomiotic materials could be used in thermally sealed sockets,[62] or as substrates for high-frequency circuits.[63] They can also be used in packaging to remove thermal stress from CTE mismatch.[64] Thermal actuators combining thermomiotic and PTE components can have enhanced sensitivity to temperature changes,[65,66] which can be used to improve the efficiency of microelectromechanical systems (MEMS).[66]

Thermal excursions of dental fillings during their curing[67] or the consumption of hot and cold beverages[68] can cause damage due to mismatched CTEs, which can be reduced by inclusion of a thermomiotic component in the filling material.[69]

1.3.2. Criteria for Applications

The potential applications of any thermomiotic material are dictated by its physical and chemical properties. Two major goals to thermomiotic materials research

are finding materials with large negative CTEs, and finding materials with near-zero

CTEs which can be tuned to zero by atomic substitution[53,70,71,72,73,74,75,76,77,78] or

introduction of guest species.[79,80,81] The first approach allows the material to be used as a

component in composite materials and structures in relatively small quantities. The

second approach can, in theory, yield a material which experiences neither thermal

expansion nor thermal stress.

Negative thermal expansion is fundamentally a thermoelastic phenomenon, and

the usefulness of thermomiotic materials is due to their unique thermoelastic properties.

However, these thermoelastic properties are often also what prevent thermomiotic

materials from attaining more widespread application. Materials that are used for their

electronic, optical, magnetic, thermal, chemical, or other physical properties which have

poor mechanical properties can often have these deficiencies corrected for by

reinforcement with stronger or stiffer materials. For example, optical materials can be

strengthened by transparent nanofibres.[82] However, thermomiotic materials that are being

used to counteract PTE cannot easily be reinforced with the addition of additional PTE

material, as that would lead to a situation where there is more PTE to counteract,

requiring additional thermomiotic material.

1.3.2.1.   Properties of the CTE Tensor

The thermal expansion of an anisotropic material is completely described by the

second-rank tensor $\boldsymbol{\alpha}$, where:

$$\boldsymbol{\alpha} = \begin{bmatrix} \alpha_{11} & \alpha_{12} & \alpha_{13} \\ \alpha_{12} & \alpha_{22} & \alpha_{23} \\ \alpha_{13} & \alpha_{23} & \alpha_{33} \end{bmatrix}. \qquad (1.10)$$

This tensor is related to the thermal strain tensor, ε_{th}, as:

$$\varepsilon_{\text{th},ij} = \alpha_{ij}\Delta T. \tag{1.11}$$

Because ε_{th} is symmetric, so is $\boldsymbol{\alpha}$.[83] For a single crystal, if the three principal axes of $\boldsymbol{\alpha}$ coincide with the basis vectors of the unit cell, the off-diagonal elements of $\boldsymbol{\alpha}$ vanish and each diagonal element α_{ii} corresponds to α_{ℓ} along a crystallographic axis. Symmetry restricts the number of independent α_{ii}; cubic, tetragonal and orthorhombic lattice systems have one, two and three different values α_{ii} of respectively. Non-orthotropic lattice systems always have non-zero off-diagonal components of $\boldsymbol{\alpha}$ in an orthogonal basis.[84] The off-diagonal elements α_{ij} lead to shear strains during thermal expansion. Only in orthotropic lattice systems can α_V be expressed as

$$\alpha_V = \alpha_a + \alpha_b + \alpha_c, \tag{1.12}$$

where α_a, α_b, and α_c are the CTEs along the three unit cell axes.

Thermal stress results from intimate contact between materials with different CTEs.[16,85,86] The amount of thermal stress, which increases with the difference between the CTEs of the components,[16] reduces the material's wear resistance with respect to thermal cycling, and can cause undesirable pressure-induced phase transitions. The damage caused by thermal stress can be mitigated by reducing the grain size. The strain energy per particle scales with the particle volume, and the energy released by a fracture along a grain boundary scales with its surface area;[16] therefore the strength of the material is increased by using smaller particles.

Even single-component polycrystalline bodies experience intrinsic thermal stress at grain boundaries if their thermal expansion is anisotropic.[16] These stresses can be sufficiently large to cause failure. For this reason, the anisotropy of $\boldsymbol{\alpha}$ is an important determinant of the thermomechanical properties of a polycrystalline material. These

considerations can be more important at lower temperatures, as α tends to become more anisotropic as the temperature decreases.[16] The $A_2M_3O_{12}$ family of thermomiotic materials especially tends to display anisotropic thermal expansion.[45] The thermal stress caused by anisotropic thermal expansion and CTE mismatch together can be very large; for example it is used to crush quartzite rocks by heating them.[16]

1.3.2.2.   Chemical and Thermodynamic Criteria

The thermal stability of thermomiotic materials is of utmost importance as it determines their useful operational temperature range. The metal oxide thermomiotic materials (*e.g.* ZrW_2O_8) have an advantage in this area, as they can be stable (or long-term metastable) at temperatures of over 1000 K.[87] Metal cyanide thermomiotic materials (*e.g.* $Zn(CN)_2$) also can be stable at over 1000 K in inert atmosphere[88] but decompose at lower temperatures in air.[89] Many metal oxide thermomiotic materials are known to be metastable at ambient conditions;[90] they can begin to decompose into their component oxides above room temperature.[87] This metastability can complicate preparation of phase-pure materials.

Temperature-induced solid-solid phase transitions can increase[87] or decrease[91,92] the CTE of a thermomiotic material. These phase transitions can change the lattice system of the unit cell,[91] cause structural disorder,[87] or remove a superstructure.[93] If the volume of the unit cell changes during the phase transition the material can be damaged.[94] The temperature at which a phase transition occurs can be modified by the introduction of impurities.[95]

Some thermomiotic materials have been found to undergo pressure-induced phase transitions and/or amorphization at relatively low pressures.[96,97,98] These transitions lower

the volume of the unit cell and usually increase the CTE. A general relationship between thermomiotic behaviour and propensity to pressure induced amorphization due to steric hindrance has been proposed.[99] Thermal stress in PTE/NTE composites has been suspected to be sufficient to cause pressure-induced phase transitions.[85,86] Increased temperature usually increases the pressure required to cause these phase transitions, and can reverse them.[99,100]

The chemical composition of a thermomiotic material is another important parameter with a large impact on its potential uses. Members of the class of metal oxide thermomiotic materials almost always include either tungsten or molybdenum in their composition; a metal oxide with a +6 oxidation state seems to be required to form the crystal structures that display thermomiotic behaviour. This creates difficulties, as WO_3 has a high embodied energy (200 MJ kg^{-1}),[101] and relatively little tungsten is produced worldwide (72,000 t in 2011).[102] Molybdenum, on the other hand, is a more promising material as larger quantities (250,000 t in 2011) are produced,[102] largely as a by-product of copper mining. However, molybdates are generally more likely to be hygroscopic than tungstates; for example $ZrMo_2O_8$ is hygroscopic while ZrW_2O_8 is not.[103] Vanadium is a special case, as it is included in the thermomiotic material ZrV_2O_7, the structure of which is closely related to that of ZrW_2O_8; however ZrV_2O_7 only displays NTE above 375 K.[104] While vanadium is produced in relatively low amounts worldwide (60,000 t in 2011),[102] V_2O_5, which is used as a catalyst, is cheaply available and global mineral resources of vanadium total over 63 million tons.[102] However, other NTE materials containing vanadium have yet to be discovered as they have for tungsten and molybdenum. Another

potential replacement for molybdates and tungstates is sulphates, which can form

materials with structures related to that of $Sc_2W_3O_{12}$, *e.g.* $Y_2S_3O_{12}$ and $Yb_2S_3O_{12}$.[105]

A class of thermomiotic materials which does not include tungsten or

molybdenum is the sodium super-ionic conductors which are based on $NaZr_2(PO_4)_3$;

substitutions of the metal ions can lead to thermal expansion properties that differ

greatly,[106] allowing for tailoring of the CTE. This class of NTE materials has been known

longer than any other, but has not found widespread use due to its members' anisotropic

thermal expansion.

Other metals which can be found as oxides in the +6 or higher oxidation state

include chromium, manganese, osmium, rhenium, and ruthenium, however these oxides

tend to be volatile, reactive, health hazards and/or prohibitively expensive.[88] The metal

cyanides, another family of thermomiotic materials (*e.g.* $Zn(CN)_2$, $Cd(CN)_2$), generally

pose severe health hazards.[88]

1.3.2.3. Mechanical Criteria

As discussed above, metal-oxide thermomiotic materials tend to have lower bulk

moduli than those of comparable ceramics. This low stiffness has a deleterious effect on

the utility of these materials in combination with PTE materials. There are several

theoretical models for the bulk CTE of a mixture of materials; generally they include an

average of the component CTEs weighted by their bulk moduli (see Chapter 4).[16] Stiffer

components have a greater impact on the bulk CTE of the mixture because they are able

to deform the other components more than they are themselves deformed during

expansion and contraction. Consequently, larger quantities of thermomiotic material are

required to compensate for PTE of metals and ceramics than would be expected from the

rule of mixtures (weighting of properties by composition). The problem can be avoided

somewhat by using a thermomiotic material in conjunction with a compliant material

such as a polymer,[107] but large amounts of thermomiotic material are still required due to

the polymer's characteristically large PTE, to the point where it can become impractical

to disperse that much thermomiotic material in the polymer.[108]

NTE is inherently a structural phenomenon as is illustrated by the creation of

macroscopic objects which possess NTE in two[109,110,111,112] or three[113] dimensions,

despite being made entirely of PTE materials. These constructs are composed of

components of variable CTEs and stiffnesses arranged in a geometry that leads to NTE.

These geometries generally involve expansion that causes the structure to bend into

empty space, reducing the volume.[109,110,111,113] The principles used in the development of

these macrostructures could inform the design of micro- or nanostructures that enhance

NTE, or even the development of new thermomiotic chemistries. For example, a 3D

thermomiotic macrostructure composed of rods of differing CTEs could potentially be

replicated chemically by replacing rods of different materials with organic linkages of

different bond harmonicity.[113]

Studies of 2D thermomiotic macrostructures *via* topology optimization showed

that structures optimized to have the highest possible bulk modulus for a given CTE had

lower bulk moduli for more negative CTEs.[114] These results were consistent with

mathematically derived bounds for the CTEs and bulk moduli of the composite materials,

given certain constraints (Figure 1.4).[114] The thermomiotic macrostructures are in some

ways analogous to thermomiotic materials. A thermomiotic material, for example

$Y_2Mo_3O_{12}$, is often structurally composed of two subunits (Y–O and Mo–O bonds), of
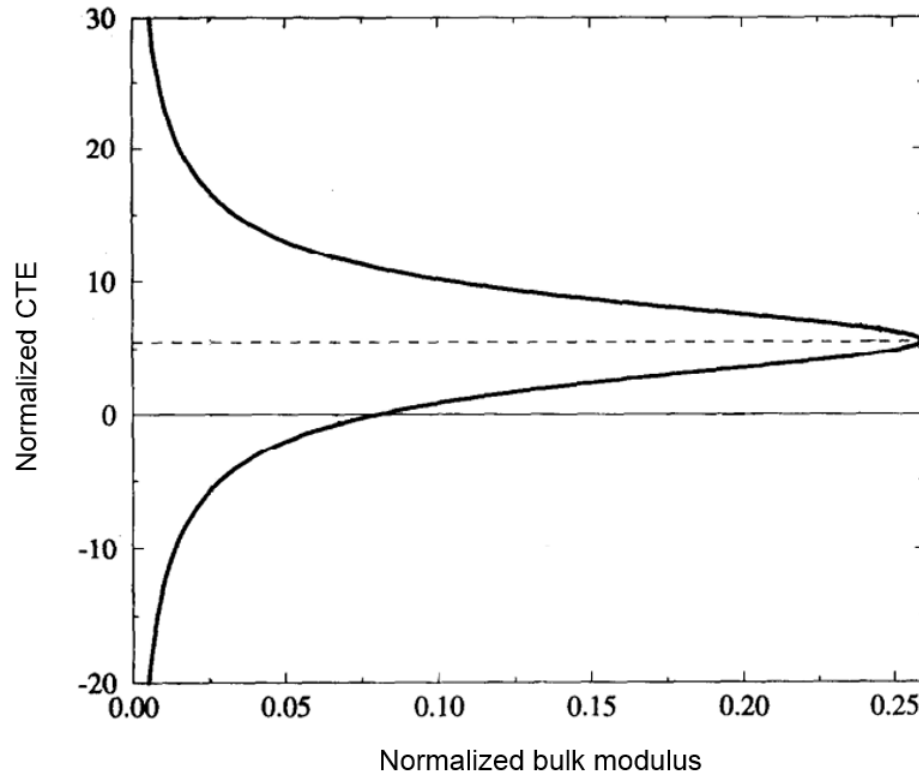
Figure 1.4: Theoretical bounds of CTEs and bulk moduli for 2D composites consisting of two isotropic phases and a void phase (given certain values of the CTEs, elastic constants, and volume fractions of the components) expressed in terms of the CTEs and bulk moduli of the components. Adapted from Reference 114 with permission.

differing stiffnesses,[iv] CTEs, and void space. In both cases the presence of void space is important to allow room for the structure to shrink into upon heating. Obviously there are many dissimilarities as well, most notably that the mechanism of NTE in the 2D macrostructures is static displacement while in thermomiotic materials it is dynamic displacement, but the confirmation of these bulk modulus—CTE relations for macroscopic structures provides reason to question whether similar relations exist for atomic structures. If similar relations do exist for NTE materials in general, the creation

---

[iv] For an example of an experimental correlation between the varying stiffnesses of coordination polyhedra in a series of NTE materials with changes in the CTE, consult Reference 45.

20

of materials with more negative CTEs might not necessarily result in materials that are more useful at counteracting PTE.

The elastic properties can also be related to the CTE as a measure of a material's thermal shock resistance (maximum sudden temperature change without failure, ΔT_{max}). One scenario for which ΔT_{max} can be calculated exactly is for a thin homogenous isotropic plate which undergoes strength-controlled fracture under conditions of poor heat transfer, then:[115]

$$\Delta T_{max} = A_1 \frac{\sigma_{max} \kappa_T}{Y |\alpha_V|}, \qquad (1.13)$$

where A_1 is a parameter dependent on the geometry and heat flow rate, κ_T is the thermal conductivity, σ_{max} is the material strength, and Y is the Young's modulus. The ΔT_{max} value is useful to evaluate how a material will perform under thermoelastic stress.[116] From Equation 1.13 it can be easily seen that if the CTE of a homogenous, isotropic material approaches zero, the ability of that material to withstand thermal shock will be increased.

For simple solids, the pressure derivative of the bulk modulus can be calculated as follows: [117]

$$\left(\frac{\partial K}{\partial P} \right)_T = \frac{5}{3} + 2 \frac{\Sigma_{i,\mathbf{q}} v_{i,\mathbf{q}}^2 \gamma_{i,\mathbf{q}}}{\Sigma_{i,\mathbf{q}} v_{i,\mathbf{q}}^2}, \qquad (1.14)$$

implying that materials with negative Grüneisen parameters, and therefore NTE are likely to have negative values of $\left(\frac{\partial K}{\partial P} \right)_T$. Thermomiotic materials will become more compliant under pressure, not stiffer as is the case with PTE materials, exacerbating their low stiffness. Negative values of $\left(\frac{\partial K}{\partial P} \right)_T$ have been reported for thermomiotic zeolites,[118]

Zn(CN)$_2$,[29] Cd(CN)$_2$,[24] as well from a general model of thermomiotic solids as an infinite chain of linked metal atoms.[8,31] If a thermomiotic material with a large negative value of $\left(\frac{\partial K}{\partial P}\right)_T$ is used to counteract PTE, the resulting thermal stress would cause it to soften, potentially reducing its ability to counteract PTE. However, the thermomiotic material will also experience less stress at higher pressures,[16] and, since $\left(\frac{\partial \alpha}{\partial P}\right)_T$ is generally negative,[8] the thermal expansion of the material will become more negative. Since $\left(\frac{\partial K}{\partial P}\right)_T$ and $\left(\frac{\partial \alpha}{\partial P}\right)_T$ have not been extensively reported for thermomiotic materials, it remains to be seen whether these pressure derivatives are large enough to have significant effects following thermal stress.

Like thermal expansion, the elastic properties of a material can be anisotropic. The elastic stiffness tensor, c, is a fourth-rank tensor defined so that:[119]

$$\sigma_{ij} = c_{ijkl}\varepsilon_{kl} \tag{1.15}$$

where σ_{ij} and ε_{kl} are elements of the second-rank Cauchy stress and strain tensors respectively. The elastic compliance tensor, s, is defined so that[119]

$$\varepsilon_{ij} = s_{ijkl}\sigma_{kl}; \tag{1.16}$$

s is the inverse of the stiffness tensor. The symmetry of the stress and strain tensors under statics allows the use of Voigt notation ($\sigma_{11} = \sigma_1$, $\sigma_{22} = \sigma_2$, $\sigma_{33} = \sigma_3$, $\sigma_{23} = \sigma_4$, $\sigma_{13} = \sigma_5$, $\sigma_{12} = \sigma_6$), which represents c and s as 6 × 6 matrices with elements c_{ij} and s_{ij}. Unlike α, c and s have more than one unique element even in the case of cubic symmetry, and generally have off-diagonal elements due to the Poisson effect, which couples strain along one axis with strain along another axis.[119] Various axial elastic moduli can be determined for a single crystal from c and s.[119]

1.4. Use of Non-Hookean Materials with Thermomiotic Materials

Combining thermomiotic materials with non-Hookean materials can circumvent the connection between bulk modulus and thermal expansion. Non-Hookean materials are those which undergo some form of deformation outside of the linear (Hookean) relationship between stress and strain. Examples of non-Hookean behaviour include plastic deformation, viscoelastic creep and relaxation, and pressure-induced phase transitions (PIPTs). What these processes have in common is the conversion of strain energy into another form of energy, either potential or thermal. Another example is the group of nonlinear elastic materials such as rubber, which can reversibly undergo large deformations but lack a linear stress-strain relationship. The non-Hookean materials offer the potential to shelter stress-sensitive thermomiotic materials from thermal stress which could cause otherwise undesirable PIPTs or pressure-induced amorphization (PIA). Non-Hookean properties could also decrease the effective bulk modulus of a material (*e.g.* by exhibiting ductility) at large strain, leading to a smaller effective thermal expansivity. It is important to note that because thermomiotic materials have often been found to be pressure sensitive,[99] they can be considered to have some non-Hookean behaviour themselves.

An example of a ceramic system for which the mechanical properties are improved by a non-Hookean property is that of yttria-stabilized zirconia (YSZ). YSZ is a solid solution of Y_2O_3 (usually 3–6 mol %) in ZrO_2, which exists normally in a monoclinic phase at room temperature.[120] Upon heating above about 1250 K, the ZrO_2 will enter the tetragonal phase and will remain in this metastable phase upon cooling due to the Y-doping. Tetragonal ZrO_2 has a smaller molar volume than the monoclinic phase,

and when it is placed under tension it undergoes a tetragonal-monoclinic phase transition that increases the volume of the unit cell.[121] When this transition occurs due to the stress field surrounding a crack, the resulting volume expansion halts crack propagation by creating compression in opposition to the tensile stress near the crack tip;[121] this process can greatly increase the toughness of materials containing YSZ. A common use of YSZ is in combination with Al_2O_3, forming zirconia-toughened alumina (ZTA), if YSZ is the minor phase, or alumina-toughened zirconia (ATZ),[v] if alumina is the minor phase. ZTA is more than four times as tough as pure Al_2O_3.[121] YSZ (or a similar material) could be used in conjunction with a thermomiotic material to produce a near-zero thermal expansion material with increased toughness; in fact such composites have been prepared as a mixture of YSZ and ZrW_2O_8.[122]

Soft materials such as polymers often exhibit nonlinear elastic behaviour such as plasticity. Biocomposites such as nacre[123] and limpet teeth[124] exhibit high strength due to their combination of mineral and biological components in a nanostructured fashion.

1.5. Zirconium Tungstate

Cubic zirconium tungstate (ZrW_2O_8) exhibits isotropic negative thermal expansion over a wide temperature range from 0.5 to 1050 K,[87] and is therefore an attractive candidate for inclusion in near-zero thermal expansion composites that could be used at various temperatures. It is the most well-studied thermomiotic material, and for that reason it is convenient to study it as a benchmark material, as is done in some of the

---

[v] The addition of Al_2O_3 to YSZ increases its stiffness and hardness but decreases its toughness.[121] In light of this information, the name "alumina-toughened zirconia" must be considered a misnomer; perhaps "alumina-stiffened zirconia" would be more apt. However, "alumina-toughened zirconia" has been used herein in order to ensure consistency with the literature.

present work, and therefore its properties and some of the literature concerning ZrW_2O_8-containing composite materials are discussed in this section. There exist two cubic thermomiotic phases, α-ZrW_2O_8 and β-ZrW_2O_8, from 0.5 to 430 K and 430 to 1050 K, respectively.[87] Although both phases are metastable with respect to ZrO_2 and WO_3 below 1378 K,[125] in practical terms, ZrW_2O_8 can be considered to be stable below 1050 K. However, because ZrW_2O_8 decomposes into its constituent oxides between 1378 K and 1050 K, quenching is required following high-temperature synthesis of phase-pure ZrW_2O_8 or materials containing ZrW_2O_8.[87] Quenching can be expected to cause thermal shock and introduce thermal stress, especially because of the low thermal conductivity of ZrW_2O_8[126] (see Equation 1.13).

The CTEs of the two cubic phases are -9×10^{-6} K^{-1} for α-ZrW_2O_8 and -5×10^{-6} K^{-1} for β-ZrW_2O_8.[87,127] Both cubic phases undergo a pressure-induced phase transition, beginning at a pressure of approximately 100 MPa, to an orthorhombic phase, denoted as γ-ZrW_2O_8.[96] The orthorhombic phase has a lower magnitude CTE ($\alpha_\ell = -1 \times 10^{-6}$ K^{-1}) than either of the cubic phases.[96] The structures of the cubic and orthorhombic phases are compared in Figure 1.5. Formation of γ-ZrW_2O_8 could increase the CTE of composites containing cubic ZrW_2O_8 during thermal cycling. A phase transition from γ-ZrW_2O_8 to α-ZrW_2O_8 occurs upon heating to 400 K under atmospheric pressure.[96] Various morphologies of ZrW_2O_8 micro- and nanoparticles have been reported in the literature that could potentially be incorporated into composite materials.[128,129,130]

The excellent thermal stability of cubic ZrW_2O_8 predisposes it to applications in refractory near-zero thermal expansion ceramics. ZrW_2O_8 remains in a thermomiotic cubic phase up to 1050 K and melts incongruently at 1530 K.[87] The stable phase below
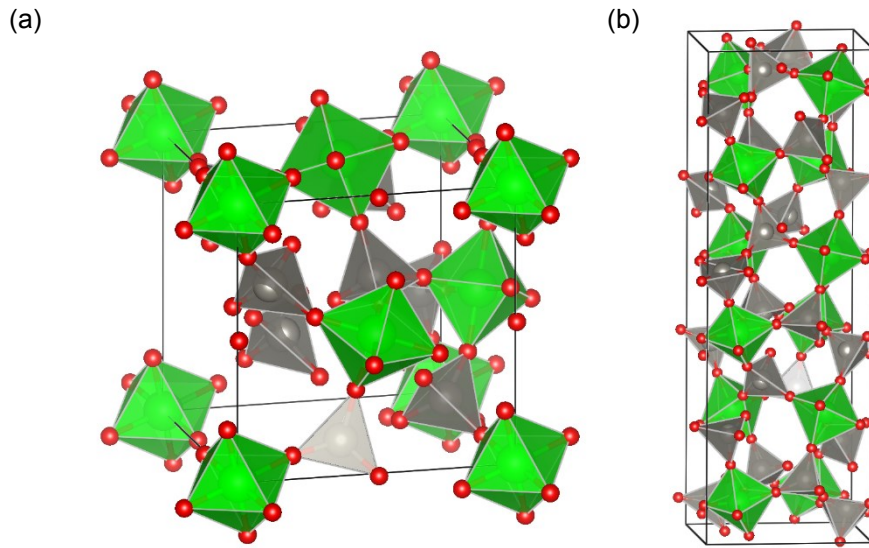
Figure 1.5: The crystal structures of (a) cubic ($P2_13$) α-ZrW_2O_8[87] and (b) orthorhombic ($P2_12_12_1$) γ-ZrW_2O_8,[96] with ZrO_6 octahedra shown in green, WO_4 tetrahedra shown in grey, and oxygen atoms shown in red.

the melting point is the cubic phase. Furthermore, under high-temperature conditions undesirable γ-ZrW_2O_8 would be removed from the composite during heating ensuring that γ-ZrW_2O_8 would not build up in the composite after many temperature cycles. Cracks in a brittle ceramic material also can be removed by annealing at sufficiently high temperatures due to increased ductility, improving the number of heating cycles that the material can withstand before thermal stress causes material failure.

Several preparation methods of composite ceramics with near-zero CTEs composed of ZrO_2 as the matrix material and ZrW_2O_8 as the filler material have been reported in the literature.[131,132] This composite system is especially of interest because ZrW_2O_8 can be formed *in situ* during sintering of the ceramic *via* reaction of ZrO_2 and WO_3, streamlining processing. Modification of the sintering conditions and the introduction of small amounts of a sintering aid have been reported to produce composites with varying microstructures that differ in their pore fraction and pore

morphology.[122] Changes in the microstructure of the composite resulted in bulk materials with a range of Young's moduli but quantitatively similar CTEs. Several finite element analyses of ZrW_2O_8-containing composites predict sufficiently high compressive stress to create some γ-ZrW_2O_8 in the filler particles upon cooling.[85,86,133]

Polymeric composites using ZrW_2O_8 as a filler also present an interesting potential application.[107,134,135,136,137] Polymers typically have large positive CTEs, which are undesirable in some applications, *e.g.* where they will be subject to thermal cycling or where dimensional stability is important. The large isotropic negative CTE of ZrW_2O_8 offers the possibility of significant reduction of thermal expansion at low filler loadings. Additionally, a variety of nano- and microparticulate morphologies of ZrW_2O_8 have been reported,[128,129,130,136] offering the potential of tailoring the properties of a composite by changing the microstructure.[136] However, efficient dispersion of the filler in the matrix and effective grafting of the filler to the matrix pose significant challenges.[136,137]

1.6. $A_2M_3O_{12}$ and AMgM_3O_{12} Materials

Several different crystal structures exist for compounds with the $A_2M_3O_{12}$ formula. However, only the phases where A is a small rare earth (Ho^{3+} to Lu^{3+}, ionic radius 0.90 Å to 0.87 Å)[138] or other trivalent metal (In^{3+} to Al^{3+}, ionic radius 0.80 Å to 0.54 Å)[138] assume framework structures in the orthorhombic *Pbcn* or in the monoclinic *P*2$_1$/*c* space groups (Figure 1.6). The connectivity in both framework structures is the same: AO$_6$ octahedra connect through vertices to six MO$_4$ tetrahedra which share all their vertices with adjacent AO$_6$ octahedra. These materials have a high degree of chemical flexibility, being able to form a wide range of solid solutions.[53] This chemical flexibility
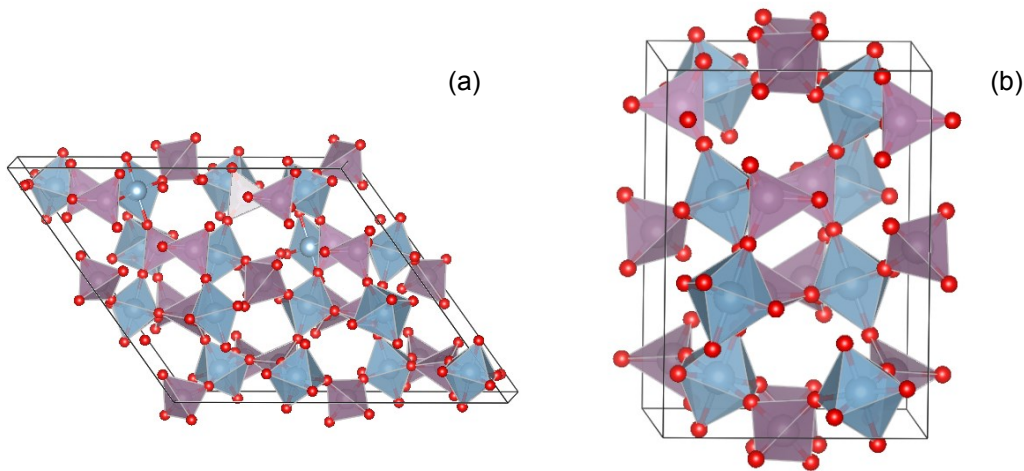
Figure 1.6: The (a) monoclinic $P2_1/c$ (low-temperature)[139] and (b) orthorhombic *Pbcn* (high-temperature)[140] phases of $Al_2Mo_3O_{12}$, with AlO_6 octahedra shown in blue, MoO_4 tetrahedra shown in purple, and oxygen atoms shown in red.

could be related to their open-framework structures, which have low energy barriers to rotation of polyhedra.[141]

The orthorhombic and monoclinic structures descend from the denser garnet structure, which has three different fully occupied cation environments: octahedral, tetrahedral, and 8-fold coordinate. The orthorhombic and monoclinic $A_2M_3O_{12}$ framework structures are similar. Whereas garnet has full occupation of the 8-fold sites, they are totally empty in the framework structures, creating microchannels. This can be a hindrance ($Y_2Mo_3O_{12}$,[142,143,144] $Y_2W_3O_{12}$,[145] and rare-earth phases[146] are highly hydroscopic due to water in the microchannels) or advantageous (fast ionic conduction through the insertion of small cations such as Li^+ inside the framework structure).[147,148]

The $A_2M_3O_{12}$ materials which adopt the orthorhombic structure generally transform to a monoclinic phase at lower temperatures, although in some cases such as $Sc_2W_3O_{12}$, $Y_2W_3O_{12}$, and $Y_2Mo_3O_{12}$ this phase transformation is apparently frustrated even at the lowest temperatures examined.[45,149,150] However, the monoclinic phases are

denser than the orthorhombic, and the former demonstrate only positive thermal expansion. The orthorhombic-to-monoclinic phase transformation is displacive with a very small enthalpy of transition, 2 kJ mol^{-1} or less.[151] Higher-temperature phase transitions are seen for Fe-, Cr-, and Al-based tungstates and molybdates in comparison to compounds with trivalent cations with lower electronegativity. Generally the $A_2Mo_3O_{12}$ orthorhombic phases transform to their monoclinic counterparts at temperatures higher than for $A_2W_3O_{12}$.[149,150,152,153]

Another peculiarity of $A_2M_3O_{12}$ phases is the lack of complete rigidity of their polyhedra. The distortion of a coordination polyhedron can be calculated following the Makovicky and Balić-Žunić approach, where the polyhedral distortion (ξ) is defined as:[154]

$$\xi = (V_i - V_r)/V_i \qquad (1.17)$$

with V_r and V_i being the volumes of a real polyhedron and an ideal polyhedron with the same circumscribed sphere radius, respectively. While ZrO_6 octahedra in ZrW_2O_8 are known to be highly distorted ($\xi \approx 20$ %), this distortion is independent of temperature (0.3 K to 1050 K).[45] The polyhedra in $A_2M_3O_{12}$ materials are also distorted, but at a much lower level ($\xi < 1$ %) and this distortion increases with increasing temperature.[45] A correlation has been established between the degree of distortion of AO_6 and the coefficient of thermal expansion, suggesting that less rigid octahedra lead to more negative CTEs within the $A_2M_3O_{12}$ family.[45] Liang *et al.*[143] used Raman spectroscopy to show that in $A_2M_3O_{12}$ high-energy optical phonon modes, due to distortion of MO_4, together with the low-energy transverse thermal vibrations as commonly observed for the AM_2O_8 crystal family, are responsible for NTE. The contribution of optic modes

involving polyhedral distortion to NTE has been investigated computationally and found to be significant in $Y_2Mo_3O_{12}$[46] and $Y_2W_3O_{12}$.[8,47] Ideal rigid-unit modes, involving only changes in A–O–M bond angles, are geometrically impossible in the $Sc_2W_3O_{12}$ structure because they cannot be constructed from undistorted polyhedra, so the involvement of polyhedral distortion is unsurprising.[42]

In an attempt to synthesize $A_2M_3O_{12}$ compounds with a controllable coefficient of thermal expansion, Suzuki and Omote[155] substituted the A^{3+} cation with Hf^{4+} and Mg^{2+} in a 1:1 ratio. Instead of $HfMgW_3O_{12}$ in an orthorhombic $Pbcn$ structure, they obtained an orthorhombic phase identified as $Pnma$ or $Pna2_1$ at room temperature. However, Gindhart et al. reported a monoclinic $P2_1/a$ structure for $HfMgW_3O_{12}$ at room temperature, showing a transition to an orthorhombic $Pnma$ or $Pna2_1$ space group between 400 and 473 K.[91] The orthorhombic phase demonstrates NTE. The reversibility of this phase transition suggests that the connectivity in $Pnma$ or $Pna2_1$ would be similar to the one established for the $Pbcn$ space group. Other phases, such as $HfMgMo_3O_{12}$[156] and $ZrMgW_3O_{12}$[157] adopt an orthorhombic phase at ambient and higher temperatures. The full crystal structure of $ZrMgMo_3O_{12}$, a member of this class of ceramics, has been resolved as reported here in Chapter 5.

In a further demonstration of the chemical flexibility of the $A_2M_3O_{12}$ family, Cheng et al. have recently reported the synthesis of a series of $Y_{2-x}(LiMg)_xMo_3O_{12}$ materials.[148] In these materials, Y^{3+} was replaced by Li^+ and Mg^{2+} in amounts up to $x = 0.9$ while remaining in a $Pbcn$ phase.[148] NTE was reported for the materials with $x = 0.1$ and $x = 0.3$, indicating that the framework structure was retained even after substitution

of two smaller cations for one rare earth cation.[148] The substituted materials showed

reduced hygroscopicity, a finding attributed to coarsening of the microstructure.[148]

1.7. Central Questions of the Thesis and Research Goals

The central questions which guided the research presented herein include: what is

the relation between elastic properties and thermal expansion in thermomiotic materials,

and how are those properties related to structural factors? In the case of materials with

anisotropic NTE, is there a relation between the CTE and stiffness along each

crystallographic axis? How can one compensate for deficiencies in the mechanical

properties of thermomiotic materials? How do elastic properties and thermal expansion

interact in composites and polycrystals where thermal stress is present?

The research reported herein has been conducted under the hypothesis that the

mechanical properties of thermomiotic materials are an important component of their

overall thermoelastic behaviour, and that the mechanical properties show significant

variations which are related to thermal expansion. Specifically, it was hypothesized that

there is a negative correlation between the magnitude of the CTE and the stiffness for

thermomiotic materials, and where the CTE tensor is anisotropic the elastic tensor can be

expected to show similar anisotropy. Furthermore, it was hypothesized that elastic

anisotropy and CTE anisotropy can couple to influence the bulk properties of

thermomiotic materials.

To answer the questions posed above, a combination of experimental and

computational approaches has been applied. Experiments included synthesis and

characterization of novel materials and those for which the reported properties, especially

elastic properties, were inadequately known. In general, the goal of the experiments

performed was to expand the domain of what is known about the thermoelastic properties of thermomiotic materials, especially their elastic properties and behaviour under thermal stress. Computations were used primarily to determine properties such as thermal stress distributions, elastic tensors, and phonon energies, all of which are difficult to determine experimentally in full.

Initial computational research concerning thermal stress in composite materials containing thermomiotic components was carried out in order to quantify the magnitudes of thermal stress in these materials, and to explore how thermal stress is related to microstructure and composition and how thermal stress can affect thermal expansion in stress-sensitive materials. Subsequently, ceramic and ceramic-polymer composites containing ZrW_2O_8 were synthesized and characterized in order to examine how the microstructure and the thermoelastic properties of the components interact with the bulk thermal expansion. This initial research established the importance of further investigation of the interplay between thermal expansion and elastic properties in thermomiotic materials.

Identification of correlations between structure and properties is very difficult in the absence of crystal structures including atomic positions, so the crystal structure of $ZrMgMo_3O_{12}$ was solved using NMR crystallography and its properties characterized with the goal of obtaining insights into materials from the AMgM_3O$_{12}$ family. A number of materials from the $A_2M_3O_{12}$ and AMgM_3O$_{12}$ families and their solid solutions were synthesized as monophasic polycrystals and their CTEs and elastic moduli were measured in an effort to find correlations between the two properties. Computational and experimental studies of ScF_3 and related materials were used to connect thermal

properties to thermal expansion, lattice flexibility, and other phononic properties. The elastic tensors of $A_2Mo_3O_{12}$ materials and $ZrMgMo_3O_{12}$ were calculated, allowing relation of axial thermal expansion and anisotropic elastic properties through axial Grüneisen parameters. Finally, the calculated elastic tensors were used to understand thermal stress in polycrystalline $Al_2Mo_3O_{12}$ and $Y_2Mo_3O_{12}$, giving a complete picture of their thermoelasticity.

Chapter 2: Techniques and Methods

2.1. Synthesis of Ceramics *via* Solid-state Reaction[vi]

In 1958 S. W. Bradstreet described the synthesis of ceramics as a process in which "minerals of inconstant composition and doubtful purity are exposed to immeasurable heat long enough to carry unknown reactions partially to completion, forming the heterogeneous non-stoichiometric materials known as ceramics."[158] In the subsequent decades scientific knowledge of the physical processes which occur in ceramics at high temperatures has increased considerably, as has the quality of the raw materials used for ceramics research, but synthesis of ceramics often still involves mixing precursor materials and then heating them at temperatures and for times sufficient to achieve the desired effect. This solid-state reaction method, or ceramic method, is a well-known processing route used to obtain thermodynamically stable phases at high temperatures through solid-state diffusion. In this section, the general solid-state reaction methods used to prepare ceramic composite materials (Chapter 4) and monophasic $A_2M_3O_{12}$ and AMgM_3O_{12} materials and solid solutions thereof (Chapters 5 and 6) are described. Additional details, including the sources of reagents and their purity, are provided in the relevant Experimental Procedures sections.

To obtain, for example, ZrW_2O_8 from binary oxides, it is necessary to mix ZrO_2 and WO_3. Mixing these oxides in a ball mill, for times as long as 24 h, can ensure a

---

[vi] Portions of this section were adapted with permission from Romao, C. P.; Miller, K. J.; Whitman, C. A.; White, M. A.; Marinkovic, B. A. Negative Thermal Expansion (Thermomiotic) Materials. In *Comprehensive Inorganic Chemistry II*; Reedijk, J.; Poeppelmeier, K., Ed.; Elsevier: Oxford, UK, 2013; Vol. 4, p 128–151. The author's contributions to this manuscript involved preparation of an outline, writing the sections regarding macroscopic NTE, applications, Raman spectroscopy, computational methods, metal cyanide materials, microstructure, and composite materials, and editing the whole manuscript.

homogeneous distribution and a high contact area.[159] Ball milling also causes mechanical

activation of the precursor powder, *e.g.* due to high stresses and temperatures at the

impact zone, generating defects. Ball milling increases the surface area of the precursor

powders by breaking initial crystallites, especially those with starting sizes higher than

100 nm.[160,161] The increasing concentration of defects during ball milling accelerates self-

diffusion and therefore also solid-state reactions. Therefore, a mechanically activated

powder has a higher coefficient of self-diffusion in comparison to the non-activated one.

However, when a new phase, in this case ZrW_2O_8, starts to nucleate and grow at the

contacts between ZrO_2 and WO_3 particles, the rate of reaction starts to be controlled by

the coefficients of diffusion of Zr^{4+} or W^{6+} in ZrW_2O_8. Since the overall kinetics are slow,

solid-state synthesis is rather time consuming.

The first step in the preparation of ceramics *via* the solid-state reaction method

used here was weighing the desired amounts of reagents in 4–5 g batches into stainless

steel 50 mL grinding jars. When compounds or solid solutions were synthesized from

WO_3 or MoO_3, a small amount of extra WO_3 ($\approx$ 15 mg) or MoO_3 ($\approx$ 50 mg) beyond the

stoichiometric amount was added to counterbalance loss of those materials due to

volatility during sintering. The reagents were then milled in a high-energy ball mill

(SPEX 8000M) to ensure good mixing and reduce the mean particle size. The composite

materials described in section 4.1 were milled using stainless steel grinding media (5

beads per batch, 1.25 cm diameter), for 1–1.5 h, while the monophasic polycrystalline

materials described in Chapter 6 were milled for 12 h using stabilized zirconia grinding

media (6 beads per batch, 1 cm diameter). Weighing of beads before and after milling

and EDS analysis (to check for the presence of iron) showed that the milling process did not introduce significant amounts of impurities.

The ensuing ball-milled powder was then pressed into pellets using a 5 mm die (for dilatometric samples) or a 15 mm die (for samples for ultrasonic measurement of the velocity of sound) and a Carver Laboratory Press, model C, with a force of 10^4 N. The pellets had heights ranging from 1–4 mm. Subsequently, the pellets underwent reactive sintering. Fused quartz sintering vessels were used to avoid the reaction of WO_3 or MoO_3 with Al_2O_3 sintering vessels. Sintering was performed in a tube furnace in air by Andy George (Department of Physics and Atmospheric Science, Dalhousie University), typically using a 10 K min^{-1} heating ramp. Natural cooling was used except for materials containing ZrW_2O_8, which were air-quenched to avoid decomposition.

2.2. X-ray Diffraction

X-ray powder diffraction (XRD) is an extremely versatile tool for analysis of polycrystalline materials. X-ray diffraction functions on the principle that a collimated monochromatic beam of X-rays will be diffracted by the electrons in a crystal lattice, creating an interference pattern. The condition for constructive interference is given by the Bragg equation:[162]

$$2d \sin \theta = n\lambda, \qquad\qquad (2.1)$$

where d is the spacing between a set of crystallographic planes, θ is the angle between the incoming X-rays and the crystallographic planes, n is an integer, and λ is the wavelength of the X-rays (Figure 2.1). If the crystal is sufficiently large, X-rays will only leave the crystal at angles where θ fulfills the Bragg condition. These outgoing X-rays form a diffraction pattern which is related to the crystal structure in reciprocal space.
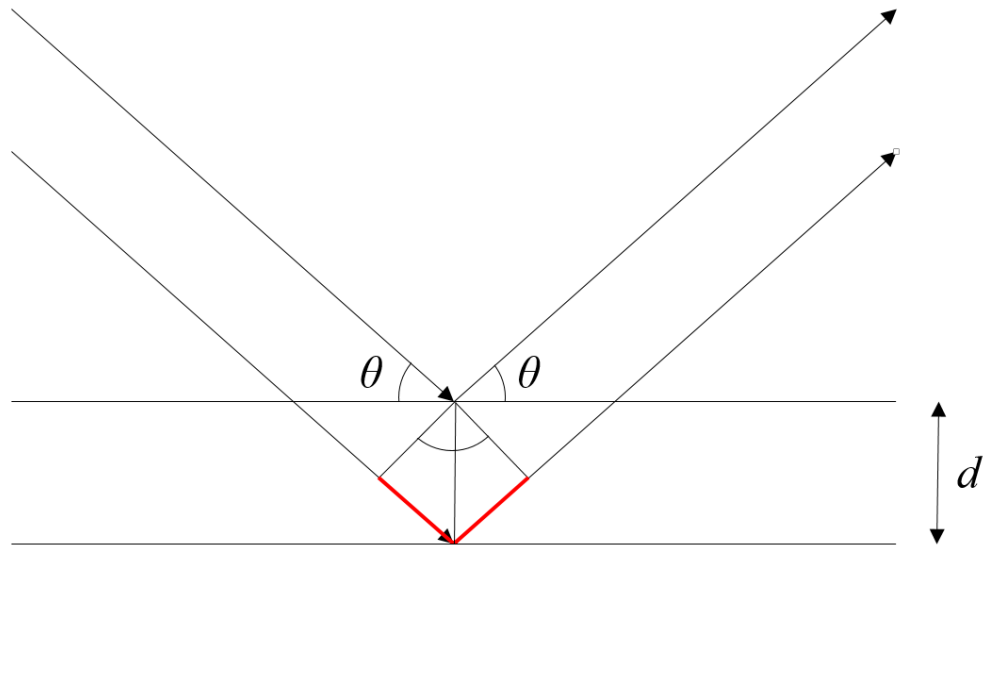
Figure 2.1: A geometric depiction of Bragg diffraction. Two rays are reflected at an angle θ by planes of atoms separated by a distance d. The difference in distance traveled between the two rays, shown as red line segments, is equal to $2d \sin \theta$; for constructive interference to occur this distance must equal an integer multiple of the wavelength λ.

When X-ray diffraction is performed on a polycrystalline sample, however, the random orientation of the crystallites will produce a diffraction pattern that is essentially a projection of the 3D reciprocal lattice into 1D, complicating structure determination. Nevertheless, powder diffraction is a very valuable tool because the resulting diffractogram has a very strong relationship with the details of the material's structure, both in terms of the positions of the peaks (*vide supra*) and their intensities, which are related to the positions of the atoms in the material by a structure factor and to the identities of the atoms by an atomic scattering factor. When the identity of the material in question is known or can be guessed, XRD is invaluable at providing confirmation.

A number of factors can impact the XRD experiment in a way that broadens the typically very sharp lineshapes of the diffraction pattern. For crystals of finite size, the destructive interference is not total for values of θ for which the Bragg condition fails to hold, and therefore the intensity of the diffracted X-rays is somewhat dispersed in space.[162] The broadening due to particle size is inversely proportional to the particle diameter and the cosine of θ.[162] If the crystallites are subject to some inhomogeneous strain, perhaps due to residual thermal stress, there will be a corresponding distribution of lattice constants in the sample, a consequent variation in the spacing, d, and therefore variation in the values of θ which satisfy the Bragg condition.[162] If impurities are present in the sample, they can cause microstresses in the material and corresponding broadening.[162] There is also some broadening due to the instrumental setup.[162]

2.2.1. Collection of X-ray Diffractograms

XRD analysis of ceramic samples was performed at Dalhousie University. Some of the diffractograms were acquired in the laboratory of Dr. Mark Obrovac, Department of Chemistry, using a Rigaku Ultima IV diffractometer, with a Cu Kα X-ray source, a linear detector, and a Si (510) zero-background sample holder. Data were collected in 0.05° 2θ increments with 2 s time elapsed per increment. Other diffractograms were acquired by Andy George, Department of Physics and Atmospheric Science, using a Siemens D-500 powder diffractometer with a Cu Kα X-ray source, a point detector, and a diffracted beam monochromator. Powders were prepared by breaking the pellets with a hammer (when necessary), followed by grinding with an agate mortar and pestle. As a precaution, some samples containing ZrW_2O_8 (see Chapter 4) were heated to about 140 °C prior to analysis in order to remove any γ-ZrW_2O_8 formed during quenching or

grinding, although this had no noticeable effect on the diffractograms. All diffractograms were acquired at room temperature.

2.2.2. Refinement of X-ray Diffractograms

Following collection of X-ray diffractograms, refinement was carried out in order to extract useful data. In most cases, the goal of the refinement was to verify that synthesized materials were phase-pure and to determine their space group and lattice constants; this was achieved with the use of Le Bail refinement.[163] Le Bail refinement is a type of whole powder pattern decomposition, *i.e.*, it decomposes the pattern into the contributions of each Bragg reflection, but does not attempt to fit the intensities and therefore determine the structure.[163] This method is useful for analysis of $A_2M_3O_{12}$ materials, whose complex structures preclude structure determination from powders using a laboratory X-ray source (see Table 5.2 in Chapter 5). The Le Bail method takes advantage of the following approximation for the observed integrated intensity of a Bragg reflection (I_k) by summation over the peak profiles (y_j) that can contribute to the observed intensity:

$$I_k = \sum_j w_{j,k} F_k^2 y_j(\text{obs})/y_j(\text{calc}), \tag{2.2}$$

where $w_{j,k}$ is a weighting factor and F_k^2 is the calculated structure factor.[163,164] The Le Bail refinement begins by setting all the F_k^2 to some arbitrary value, then reinjecting the I_k values as F_k^2 each time the parameters to be determined are refined. In this manner the refinement can proceed without calculation of the structure factor, and therefore the positions or even the identities of the atoms, being required.

Le Bail refinement was carried out in Rietica[165] using a Newton-Raphson algorithm.[166] Pseudo-Voigt peak profile functions (convolutions of Gaussian and

Lorentzian profiles)[167] were used. The most important refined parameters were the unit cell basis vectors, the parameters U_w, V_w, and W_w, which determine the full width at half maximum (FWHM) of a peak at θ as

$$(\text{FWHM})^2 = U_w \tan^2 \theta + V_w \tan \theta + W_w, \qquad (2.3)$$

the mixing parameter for the Gaussian and Lorentzian components of the profiles, and the background correction parameters, which were refined as the coefficients of a fifth-order polynomial. Other parameters refined were a correction to the zero point of 2θ, a correction for finite sample height, and a peak asymmetry parameter.[164]

The quality of the refinements was assessed primarily using the goodness-of-fit parameter (χ^2). This parameter can be defined as the ratio between the weighted profile residual factor (the sum of squares of the relative residuals weighted by the inverse of the uncertainty) and the expected residual factor (an estimate of the minimum possible weighted profile residual factor based on the number of degrees of freedom of the refinement).[168] Typically the values of χ^2 obtained following refinement were < 2.

In several cases refinement of X-ray diffractograms was performed to obtain an estimate of the composition of a mixed-phase material. In these cases, Rietveld refinement was performed using structural information obtained from the literature or the PDF-2 database.[169] Refinement of the composition and the peak-shape parameters was then performed with Rietica or automatically following phase identification in Match![170] without refinement of the structure being necessary. Match! is a commercial phase identification software package which compares peak positions and intensities from experimental powder patterns to those in a database, in this case PDF-2.

2.3. Thermal Analysis

2.3.1. Dilatometry[vii]

Dilatometry is a useful technique for the determination of CTE in bulk specimens; it can also be used to determine phase transition temperatures and vacancy information (concentration and formation enthalpy). In this technique, the linear change of sample length is recorded as a function of temperature, generally by a push-rod. The recorded pattern is plotted as $\Delta\ell/\ell_0$ (thermal strain) versus temperature, where $\Delta\ell$ and ℓ_0 are the change and the original sample length, respectively.

The main of a push-rod dilatometer are the linear variable differential transformer (LVDT), push-rod, furnace, and a thermometer (Figure 2.2). The push-rod is connected to the ferromagnetic core of the LVDT, and pushes against the sample so that changes in length are recorded by the LVDT as a voltage due to the movement of the ferromagnetic core. The rod and its surrounding tube are made from a low thermal expansion material with a high melting temperature, *e.g.* fused silica or alumina.

Sample preparation is important for accurate dilatometry, and it is important that the samples be well consolidated and have flat and parallel ends. Dilatometry can be carried out with lab-built instruments or commercial instruments. Current push-rod dilatometers can have $\Delta\ell/\ell_0$ accuracy better than $\pm$ 1 %.[171,172] Note that this does not necessarily convert to a fixed % uncertainty in CTE; CTEs closer to zero have the largest

---

[vii] Portions of this section were adapted with permission from Romao, C. P.; Miller, K. J.; Whitman, C. A.; White, M. A.; Marinkovic, B. A. Negative Thermal Expansion (Thermomiotic) Materials. In *Comprehensive Inorganic Chemistry II*; Reedijk, J.; Poeppelmeier, K., Ed.; Elsevier: Oxford, UK, 2013; Vol. 4, p 128–151. The author's contributions to this manuscript involved preparation of an outline, writing the sections regarding macroscopic NTE, applications, Raman spectroscopy, computational methods, metal cyanide materials, microstructure, and composite materials, and editing the whole manuscript.
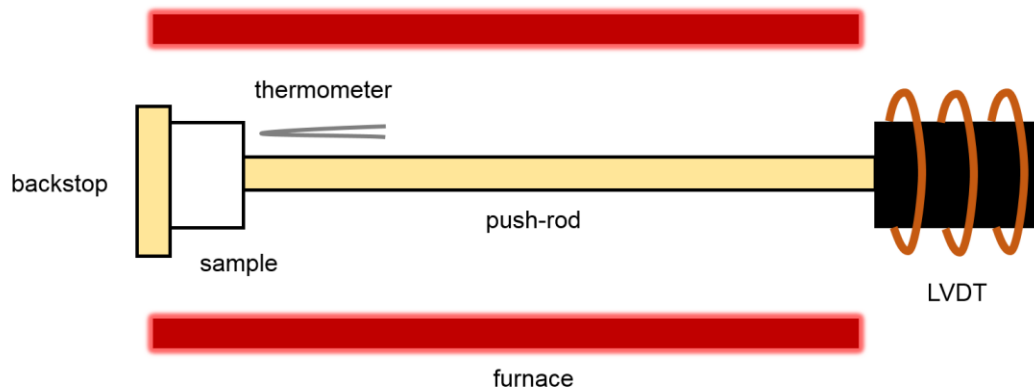
Figure 2.2: A schematic view of the principal components of a push-rod dilatometer. The LVDT measures changes in length of the sample, push-rod, and backstop as a function of temperature. The expansion of the push-rod and backstop is subtracted based on a calibration standard.

relative uncertainty. The uncertainty of a measurement of a material whose CTE is close to zero can be estimated by performing multiple measurements on the same material, see Chapter 5 and Reference 76.

Dilatometry was used to measure the CTEs of the prepared ceramics. Two dilatometers were used; both were alumina push-rod dilatometers, model DIL 402C, made by NETZSCH. The dilatometric experiments were performed at PUC-Rio in the laboratory of Dr. Bojan Marinkovic (results of Section 4.1, and Figure 5.5 and Figure 5.6), and in the High-temperature Thermal Analysis Laboratory of Dr. Steve Corbin, Department of Civil and Resource Engineering and Dr. Paul Bishop, Department of Process Engineering and Applied Science, at Dalhousie University (all other results). When possible, the samples were polished using a SiC abrasive (320 grit) and a polishing jig prior to analysis in order to ensure that the ends were flat and parallel, however most of the $A_2M_3O_{12}$ samples (Chapter 6) were too fragile to withstand polishing on the jig and were gently polished by hand using 320 grit SiC abrasive instead. The dilatometer used

was calibrated with amorphous SiO_2 (at Dalhousie) or polycrystalline Al_2O_3 standards (at PUC-Rio) with lengths as close as possible to that of the samples (1–4 mm).

In most cases, it was not possible to measure several dilatometric heating and cooling curves of a given material due to time constraints. Therefore, an estimated uncertainty of 0.5×10^{-6} K^{-1} was assumed for these cases. Following consideration of cases where several dilatometric experiments were performed (see Chapter 4, Chapter 5, and Reference 76), this value was determined to be a conservative estimate of the uncertainty of a single measurement.

2.3.2. Thermogravimetric Analysis

Thermogravimetric analysis (TGA) is conceptually a simple technique; a sample is heated while resting on a balance and changes in mass are measured as a function of temperature and time.[171] This method can be used to examine many properties of materials; it was used in the current work to determine the compositions of organic/inorganic composites (Section 4.2.3), and hygroscopicity and decomposition temperatures of molybdate materials (Sections 5.3.1 and 6.2). The first two determinations involve processes which directly have volatile products, while the second produces MoO_3. Upon heating above 700 °C, MoO_3 rapidly sublimes,[173] as shown in Figure 2.3.

TGA was performed in the laboratory of Dr. Mark Obrovac using a NETZSCH TG 209 F3 instrument. All measurements were performed under flowing Ar (to protect the instrument at elevated temperature) using fused quartz sample pans, which are unreactive with MoO_3 and WO_3. Typical sample masses were ≈ 20 mg; the internal microbalance of the instrument was used to weigh the samples prior to measurement.
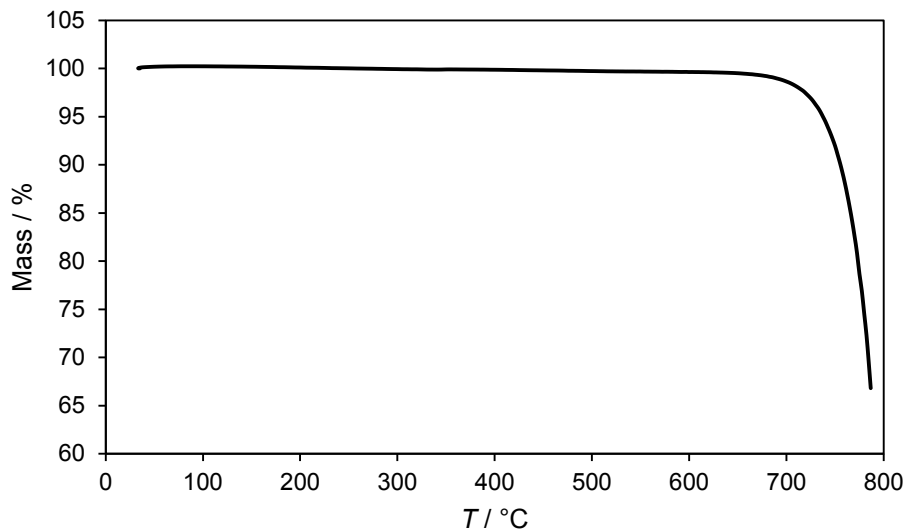
Figure 2.3: TGA thermogram of MoO_3 (Sigma-Aldrich, 99.5 %), showing sublimation upon heating. A 20 K min^{-1} heating rate was used from room temperature to 500 °C followed by a 10 K min^{-1} heating rate to 800 °C.

2.3.3. Relaxation Calorimetry

Relaxation calorimetry is a method used to measure the heat capacity at constant pressure (C_P) of materials. It is capable of providing measurements of good accuracy (1 % for 5 K < T < 300 K and 5 % for 0.7 K < T < 5 K)[174] on small samples (as small as 1 mg).[171] The method of measurement of a relaxation calorimeter begins by affixing the sample to a heating platform with a thermally conductive grease.[171] The assembly is heated or cooled to the measurement temperature, and then a pulse of heat is applied while the temperature of the platform is measured.[171] The sample and platform, which is weakly thermally coupled to a heat sink, increase in temperature while the pulse is applied and then cool after it is turned off.[171] During cooling, the temperature of the platform (T_p) can be modeled as a relaxation process as:

$$T_p(t) = T_0 + A_1 e^{-t/\tau_s} + A_2 e^{-t/\tau_p} \qquad (2.4)$$

44

where t is the time since the end of the pulse, τ_s and τ_p are relaxation times related to the

transfer of heat from the sample to the platform and from the platform to the heat sink,

respectively, T_0 is the temperature of the heat sink, and A_1 and A_2 are constants.[171] Since

the temperature of the platform is known as a function of time, a fit to the data

(performed by the instrumental software) can be used to extract the values of τ_s and τ_p.[175]

These are, in turn, related to the heat capacities of the sample ($C_{P,s}$) and the platform

($C_{P,p}$) as:

$$\tau_s = C_{P,s}/k_g \qquad (2.5)$$

and

$$\tau_p = C_{P,p}/k_w, \qquad (2.6)$$

where k_g is the thermal conductance of the grease and k_w is the thermal conductance of

the wires coupling the platform to the heat sink.[171] Then, the heat equations of the system,

$$C_{P,s}\frac{dT_s}{dt} = k_g(T_s(t) - T_p(t)) \qquad (2.7)$$

and

$$C_{P,p}\frac{dT_p}{dt} = k_g\left(T_s(t) - T_p(t)\right) - k_w\left(T_p(t) - T_0\right) + Q(t) \qquad (2.8)$$

are solved to find the temperature of the sample as a function of time ($T_s(t)$) and $C_{P,s}$

knowing the heater power $Q(t)$, and $C_{P,p}$ (measured in a separate experiment).[171] The

assembly is then heated or cooled to a different temperature and the process is repeated.

A commercial relaxation calorimeter (Physical Property Measurement System

model 6000 from Quantum Design) was used to determine the heat capacities of ScF_3 and

related materials (see Chapter 7). Sintered pelletized samples ($\approx$ 1 mm thick) were broken

into small shards ($< 3 \times 3$ mm) prior to measurement. Heat capacities were measured

from 2 K to 300 K using a ^{4}He cryostat and Apiezon® N grease, from 275 K to 390 K using a ^{4}He cryostat and Apiezon® H grease, and from 0.35 K to 10 K using a ^{3}He cryostat and Apiezon® N grease. Each reported data point met two reliability criteria: $\geq$ 90 % thermal coupling constant between sample and platform (defined as $k_g/(k_g + k_w)$) and $\geq$ 40 % sample contribution to the total heat capacity (defined as $C_{P,s}/(C_{P,s} + C_{P,p})$).

2.4. Scanning Electron Microscopy

In order to observe the microstructure of the prepared ceramic materials, several were examined using scanning electron microscopy (SEM). SEM provides a much higher spatial resolution than optical microscopy due to the fact that electrons, which have rest mass, have a much smaller wavelength than light at the same energy.[176] The scanning electron microscope produces a beam of high-energy electrons which are scanned over the sample in a raster pattern. These electrons interact with the sample in several ways. Some electrons eject other electrons from the sample; when the ejected secondary electrons are detected they provide topographical information.[176] Some electrons are elastically scattered by the sample and return back in the direction of the beam; the number of these backscattered electrons depends on the mass of the scattering atom.[176] This dependence gives the resulting micrographs contrast between different materials within the sample. X-rays are also produced by the electron beam's interaction with the sample.[176] The energy of these X-rays is characteristic of the element producing them; analysis of the X-ray energies by energy-dispersive X-ray spectroscopy (EDS) can allow quantitative determination of the composition of an area of the sample.[176]

Imaging was performed on fracture surfaces. Prior to imaging, samples were mounted on metal stubs using carbon tape and sputter coated with a 50/50 Au/Pd alloy to

a thickness of 15–30 nm using an Ar plasma sputtering system. SEM imaging was primarily performed at the Scientific Imaging Suite in the Department of Biology at Dalhousie University using a Zeiss 1455 VP scanning electron microscope equipped with a backscattered electron (BE) detector and a secondary electron (SE) detector.[viii] Some additional SEM imaging and EDS analysis was performed with the assistance of Patricia Scallion, Dalhousie SEM–FIB Facility, using a Hitachi S-4700 FEG scanning electron microscope equipped with a SE detector and an Oxford Inca Energy Dispersive X-ray analysis system. The SEM used is indicated in the results shown.

2.5. Ultrasonic Measurement of the Velocity of Sound

Ultrasonic measurements of the velocity of sound were performed in order to measure the elastic properties of bulk polycrystalline thermomiotic materials (see Chapter 6). These measurements provided the longitudinal (v_l) and transverse (v_t) velocities of sound, which were converted to bulk (K) and shear (G) moduli as:[177]

$$G = \rho v_t{}^2, \tag{2.9}$$

and

$$K = \rho v_l{}^2 - \frac{4G}{3}, \tag{2.10}$$

where ρ is the density. The bulk and shear moduli were analysed because these are more fundamental than, for example, the Young's moduli and Poisson ratios, as the bulk and shear moduli correspond to the material's resistance to changes in volume and in shape, respectively.

[viii] A secondary electron detector detects primarily, although not solely, secondary electrons.

The polycrystalline samples measured could not be processed to completely remove porosity. Therefore, a correction for porosity was adopted assuming:[177]

$$v_{\text{exp}} = v_0(1 - \phi_{\text{p}}), \qquad (2.11)$$

where v_{exp} is the measured velocity of sound, v_0 is the corrected, zero-porosity velocity of sound, and ϕ_{p} is the pore fraction. This correction assumes spherical crystallites, and has been shown experimentally introduce only a small uncertainty (< 10 %) for pore fractions $\lesssim 25$ %.[177]

Prior to ultrasonic measurement, sintered cylindrical polycrystalline samples (see Section 2.1) were weighed and their dimensions (thickness and diameter) were measured three times each using calipers in order to determine their density. At least three samples of each material were measured. In some cases, the edges of the pellet were uneven, usually due to damage to the green form prior to sintering. In these cases the uneven portion was removed *via* polishing, and the areas of the top and bottom surfaces were determined photographically. The pellet was placed on a colour-contrasting background and photographed at a 90° angle alongside a reference object (Canadian \$2 coin a.k.a. "toonie," diameter 28 mm). The reference object was subsequently used to convert the area of the surface in pixels into the area of the surface in mm^2 using GIMP.[178] This method gave results consistent with the caliper density.

The pore fraction of the material was determined by comparison of the measured density of the samples to the theoretical density as determined by XRD (see Section 2.2). The theoretical density could alternatively have been determined by pycnometry, which can directly measure the volume of a powdered sample. Attempts were made to use He pycnometry (AccuPyc II 1340) to measure the densities of the synthesized materials,

however the results were inconsistent. Many of the measurements showed decreases in density when repeated cycling was performed (see Figure 2.4). In discussion with other users of the instrument, it was determined that this is a common behaviour and that performing only one cycle is common practice when time constraints preclude performing possibly hundreds of cycles required for a high-accuracy result. However, with only one replicate measurement, the method would not be expected to provide an accuracy advantage over XRD, so theoretical densities from XRD were used to determine the pore fractions of the samples.
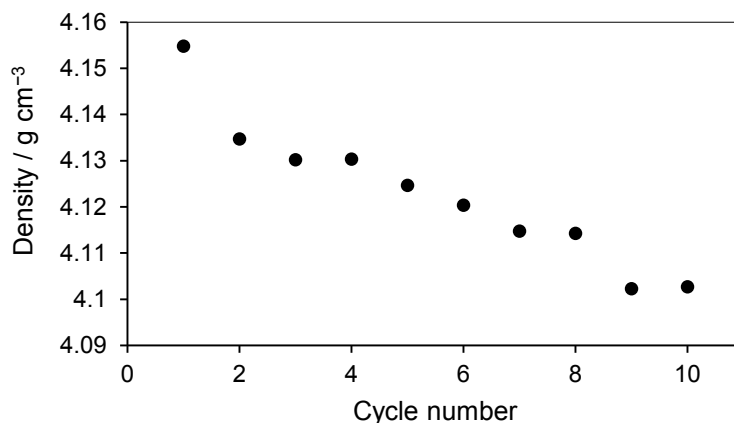
Figure 2.4: Density of $HfMgMo_3O_{12}$ powder as measured by He pycnometry. The measured apparent density decreased steadily with repeated cycling. The XRD-derived density was 3.818 g cm^{-3}, which is consistent with the literature value of 3.803 g cm^{-3}.[153]

Measurements of the velocity of sound were performed using a Panametrics 25-DL Ultrasonic Thickness Gauge in the laboratory of Dr. Josef Zwanziger. The longitudinal velocity of sound was measured with a M202 transducer (10 MHz), using glycerol (Aldrich, 99.5 %) as a coupling fluid. Glycerol was chosen because, in order to avoid introduction of macro- and microcracks into the samples, it was not desirable in all cases to finely polish the surfaces of the samples due to their fragility; glycerol is

recommended by Panametrics for use with rough surfaces.[179] Additionally, the high

viscosity of glycerol greatly slows infiltration of the couplant into microcracked

materials. The transverse velocity of sound was measured with a V156 transducer (5

MHz), using Panametrics shear coupling fluid. Three measurements of each velocity

were made per sample.

The principle of operation of the ultrasonic thickness gauge is simple: the

transducer, using a piezoelectric element, outputs a pulse of sound into the material to be

measured and then detects an echo returned from the far edge. Since the thickness of the

material was measured beforehand, the velocity can then be determined from the transit

time of the sound through the material. The transverse and longitudinal transducers used

two slightly different modes of operation. The transverse transducer had its piezoelectric

element located in direct contact with the coupling fluid, so the transit time was measured

from the initial sound pulse to the echo.[179] The longitudinal transducer incorporated a

delay element through which the sound pulse traveled prior to arriving at the sample. At

the interface between the delay element and the sample, an echo occurred. The transit

time through the sample was then determined as the delay between this frontwall echo

and the backwall echo.[179]

Two ways of treating the uncertainty of the measurements were compared. In the

first, the standard error of the mean (95 % confidence level) resulting from averaging

multiple measurements on each sample was propagated through to give an uncertainty on

the final elastic constants. In the second, the standard error of the mean resulting from

averaging the values from the different samples was determined directly. The second

method produced considerably larger uncertainties, and therefore it was concluded that

the major contributor to the uncertainty was sample-to-sample variation. This variation could have arisen from factors such as inaccuracies in the measurement of density and microcracking due to thermal stress anisotropy (see Chapter 9). Therefore, the uncertainties reported from ultrasonic measurements were calculated using the second method and reported at the 95 % confidence level.

The methodology used to characterize the elastic properties of bulk polycrystalline samples of $A_2M_3O_{12}$ materials was validated by comparison of the measured bulk moduli of $Al_2W_3O_{12}$ (45 ± 4 GPa) and $Sc_2W_3O_{12}$ (36 ± 6) GPa (see Chapter 6 for additional details) to literature values (48 GPa[26] and 31 GPa,[27] respectively) obtained by variable-pressure XRD. The values agree within the margin of error, validating the experimental approach.

2.6. Raman Spectroscopy

Due to the importance of vibrational dynamics in thermomiotic materials, Raman spectroscopy is an important tool in their characterization. In solids, Raman spectroscopy uses the interactions of photons with optic phonons to probe the vibrational energy levels of the Γ (centre) point of the Brillouin zone. When light is scattered by a material, most of the photons interact elastically with the material (*e.g.*, by Rayleigh or Mie scattering), however inelastic interactions are also possible. The change in energy of the photon is referred to as the Stokes shift if it results from a phonon being created in the lattice or the anti-Stokes shift if a phonon is absorbed. In Raman spectroscopy, a monochromatic beam of light is scattered by a sample, and the scattered photons are collected, often excluding the elastically scattered photons with a filter. The energies of the photons are determined either dispersively or by Fourier transform of an interferometer signal (FT-Raman). Then,

the energies of the Stokes and/or anti-Stokes shifts are known and the Raman vibrational spectrum is given from the energies of these shifts.

Raman spectroscopy is a particularly convenient technique because spectra can be collected quickly and without preparation or modification of the sample. The selection rules for Raman spectroscopy require the vibrational mode to change the polarizability of the material in order to be Raman-active; this excludes, for example, contributions from the components of air including H_2O and CO_2. However, the intensity of a peak in the Raman spectrum is therefore related to the derivatives of the polarizability and it is difficult to interpret intensities or changes in intensities by reference to the phonon density of states (DOS). Instead, analysis of Raman spectra is usually limited to the peak positions and changes thereof.

In this work, Raman spectra were collected using Nicolet NXR 9650 FT-Raman spectrometer with a 1064 nm excitation laser, with spectral resolution of 1 cm^{-1}. Samples were either mounted directly in a holder as sintered pellets or placed in glass tubes in powdered form. Fortunately, due to the absence of atoms at symmetric positions in the $A_2M_3O_{12}$[180,181] and AMgM_3O_{12} (see Section 5.3.5) families, all of their vibrational modes are Raman-active. However, the infrared excitation laser light used is often absorbed by strongly coloured samples, which prevented a comprehensive study of the Raman spectra of the materials described in Chapter 6.

2.7. The Finite Element Method

The finite element method (FEM) is a computational tool used to solve physical problems in continuum mechanics over complex geometries by discretization of the geometry into a mesh of elements. Finite element analysis (FEA) can be used in

conjunction with experimental or computational methods to connect physical properties of materials to potential applications. Mathematically, FEM finds a numerical solution to a series of differential equations, relating some dependent variable(s) to independent variable(s), applied over a domain (the geometry), contingent on appropriate boundary conditions.[182]

The first step in solving a problem through FEA is determination of an appropriate model geometry. FEM software is able to handle very complex geometries, however simplifying the problem can result in significant computational time savings. In the case of modeling a micromechanical system such as a ceramic, appropriate assumptions about the system to be modeled must be used. The model geometry is then divided into a mesh of elements. The mesh defines many of the qualities of the model, such as the accuracy of the numerical solution, its spatial resolution, and the computational complexity of the model. In any case where quantitative results are desired from a model, a mesh convergence study must be performed. The mesh convergence study solves some aspect of the model with varying mesh sizes, ensuring that the results are invariant in the mesh size chosen.

Each element in the mesh is assigned a shape function which interpolates the dependent variables over its space. This yields a series of matrix equations, one per element. These local matrix equations are associated with one another, forming the global matrix equation.[182] The global equation is modified to account for the boundary conditions, and then solved by matrix inversion.[182] The dependent variables solved for (*e.g.*, displacement) can then be used to determine other variables of interest (*e.g.*, stress).

All of the finite element analysis reported herein was completed using the commercial software package COMSOL Multiphysics, v. 4,[183] using the Structural Mechanics and Heat Transfer modules.

2.8. Density Functional Theory

Density functional theory (DFT) can be used as a powerful and efficient method to calculate the electronic structures and other related properties of materials. The foundation of DFT is the Hohenberg-Kohn theorems, which state that for a system of interacting particles (*e.g.*, electrons) in an external potential, $U_{ext}(\mathbf{r})$, this potential is uniquely related within the addition of a constant to the ground-state particle density function $\rho_0(\mathbf{r})$.[184] Furthermore, a total energy functional $E[\rho(\mathbf{r})]$ can be defined which yields the energy of a given $\rho(\mathbf{r})$ for any $U_{ext}(\mathbf{r})$.[184] The function that minimizes $E[\rho(\mathbf{r})]$ is the ground state density, $\rho_0(\mathbf{r})$. In combination, the theorems show that it is possible to determine $\rho_0(\mathbf{r})$, $U_{ext}(\mathbf{r})$, and the ground-state wavefunction $\Psi_0(\mathbf{r})$ by self-consistent minimization of the energy.[184] Specifically, for a system of electrons and stationary nuclei, $E[\rho(\mathbf{r})]$ can be expressed as:

$$E[\rho(\mathbf{r})] = \hat{T}[\rho(\mathbf{r})] + \hat{U}_{int}[\rho(\mathbf{r})] + \int U_{ext}(\mathbf{r})\,n(\mathbf{r})d\mathbf{r} + E_{ii}, \qquad (2.12)$$

where $\hat{T}$ is the kinetic energy of the electrons, $\hat{U}_{int}$ is the electron-electron interaction energy, and E_{ii} is the energy of the Coulombic interactions between the nuclei.[184]

On their own, the Hohenberg-Kohn theorems do not make determination of the ground state of a many-particle system tractable because the many-body interactions of the particles are simply included in $\hat{U}_{int}$. This determination can be accomplished by use of the Kohn-Sham *ansatz*, in which a system of non-interacting particles with the same ground-state density function as the interacting system is presupposed.[184] The energy of

this non-interacting system differs from that of the real system, by definition, by the exchange-correlation energy ($E_{xc}[\rho(\mathbf{r})]$) plus the energy of the Coulombic repulsion of the electrons ($E_{ee}[\rho(\mathbf{r})]$).[184] This definition allows replacement of Equation 2.12 with:

$$E[\rho(\mathbf{r})] = \hat{T}_{u}[\rho(\mathbf{r})] + \int U_{ext}(\mathbf{r})n(\mathbf{r})d\mathbf{r} + E_{ii} + E_{ee}[\rho(\mathbf{r})] + E_{xc}[\rho(\mathbf{r})], \quad (2.13)$$

where $\hat{T}_{u}$ is the kinetic energy term for the non-interacting system.[184] Dynamic multi-body interactions are confined to $E_{xc}[\rho(\mathbf{r})]$.[184]

While no general mathematical expression for $E_{xc}[\rho(\mathbf{r})]$ is known, many approximations have been developed.[184] The simplest approximation, which is often used in solids because of its generality, reasonable accuracy, and low computational cost, is the local density approximation (LDA), which equates E_{xc} for a point of a given density to E_{xc} of a uniform electron gas with the same density.[184] The generalized-gradient approximations (GGA) also consider the gradient of the density at each point.[184] Calculations using LDA tend to overestimate the binding energies of electrons, leading to underestimation of cell volumes and overestimation of elastic constants, whereas for GGA the reverse is true.[184,185]

DFT calculations were carried out using the ABINIT code in order to determine the phonon DOS and related properties of ScF_3 (Chapter 7) and the elastic tensors and Γ-point phonon energy of $A_2M_3O_{12}$ and $AMgM_3O_{12}$ materials (Chapter 8).[186] The results in Chapter 8 were obtained using computational resources provided by Compute Canada, specifically the ACENET[187] and WestGrid[188] consortia, taking advantage of the massive parallelization functionality of ABINIT.[189] ABINIT is designed to study periodic systems such as crystalline solids, and so it composes wavefunctions as linear combinations of a plane wave basis set and performs calculations in reciprocal space.[190,191] This basis set is

defined by a cut-off energy, which was determined for each material studied by a convergence study. The criterion used was the internal pressure reaching convergence within 1 %. In order to determine the electronic structure of the whole Brillouin zone, calculations must sample the phase space of the plane waves, as determined by the wavevector **k**. Therefore, the electronic structure is calculated for a series of **k**-points in a shifted Monkhorst-Pack grid in reciprocal space.[192] The spacing between points in this grid was determined by another convergence study.

In order to reduce the computational expense required, core electrons were modeled using pseudopotentials rather than being directly included in the calculations. Pseudopotentials essentially treat some of the closed-shell electrons as being uninvolved in chemical bonds; this treatment is reasonable when the object of the study is to determine properties related to bonding and vibrational dynamics, as here, so long as the number of electrons excluded from the pseudopotential is sufficiently large. The pseudopotentials can be tested by, for example, comparing lattice parameters or bulk moduli to experimental values.

Calculation of the phononic and elastic properties of a material began by importing the structure into an ABINIT input file using the cif2cell program,[193,194] which proved effective except in the case of $ZrMgMo_3O_{12}$, which was imported incorrectly, presumably due to its different space group ($Pna2_1$), and was therefore input manually. The convergence studies described above were performed to determine appropriate values of the plane wave energy cut-off and the **k**-point grid spacing. Then, the structure was optimized to remove internal stresses and ensure that subsequent calculations consider a structure at a minimum of the potential energy surface. This allowed

calculations of properties using response functions, which involve the derivatives of the energy with respect to some perturbation. The perturbations required are those with respect to atomic displacement,[195,196] electric fields,[195,196] and homogenous strains.[197] The derivative databases recording the responses to these perturbations were then combined to yield phonon energies and elastic tensors. The frequencies were corrected for errors due to finite sampling on the effective charges by imposition of the acoustic sum rule (*i.e.*, the energies of the acoustic bands at $\mathbf{q} = 0$ are required to be zero).[196] In the case of ScF$_3$, integration of the phonon energies over the Brillouin zone was performed to obtain thermal properties.[198]

Chapter 3: Finite Element Analysis of Composite Materials Containing a Thermomiotic Component

The following finite element results are presented as attempts to understand some of the mechanical dynamics inherent to thermomiotic materials, including their propensity to experience thermal stress while counteracting PTE and to undergo pressure-induced phase transitions as a result of that thermal stress.

3.1. Thermal Stress in a ZrB$_2$/SiC Composite Material

In order to validate the finite element methodology used in this chapter, a finite element analysis of thermal stress in a well-characterized composite system, reported in the literature, has been performed. This system consists of SiC microparticles (30 vol.%) embedded in a ZrB$_2$ matrix (70 vol.%), densified by hot pressing.[199] The CTE of the matrix, ZrB$_2$, ($\alpha_\ell = 5.2 \times 10^{-6} \, \mathrm{K}^{-1}$)[199] is higher than that of the filler, SiC, ($\alpha_\ell = 3.3 \times 10^{-6} \, \mathrm{K}^{-1}$),[199] so during cooling the SiC filler experiences compressive stress while the matrix experiences tensile stress, as occurs in the composite materials discussed in the remainder of Chapter 3. The compressive thermal stress in the SiC particles following processing has been experimentally determined as 810 MPa by measurement of the Raman shifts.[199] Thermal stress evolution had been measured during cooling from 2075 K to room temperature using neutron diffraction, and the stress relaxation point had been determined to be approximately 1675 K (*i.e.*, thermal stress begins to accumulate below this temperature).[199]

These literature experimental results were used to design a simple finite element model, using the techniques used to model NTE/PTE composites in the remainder of Chapter 3. The model consisted of four spherical SiC particles embedded in a cube of

ZrB$_2$ that modeled the matrix. The radius of the filler particles was chosen to replicate the 30 vol.% loading in the experimental composite.[199] Roller boundary conditions (allowing displacement in the direction parallel to the boundary but not in the perpendicular direction) were applied on three faces of the model, while the other three sides were left unconstrained. A temperature drop of 1400 K was modeled by setting the boundaries of the model at a fixed temperature 1400 K below the initial temperature of the material. The actual choice of initial and final temperatures is not relevant to the results since the material properties input to the model were assumed to be temperature invariant.

The thermal stress distribution thus calculated was evaluated in terms of the first principal invariant of stress (σ_I); this quantity is defined as the trace of the Cauchy stress tensor:[200]

$$\sigma_I = \sigma_1 + \sigma_2 + \sigma_3, \tag{3.1}$$

where σ_1, σ_2, and σ_3 are, for example the three principal stresses (as its name implies, σ_I is independent of the choice of basis vectors). The first principal invariant of stress is related to the pressure as:[200]

$$P = -\sigma_I/3. \tag{3.2}$$

The thermal stress distribution is shown in Figure 3.1. The finite element model predicts an average compressive thermal stress of 2 GPa in the SiC filler particles following cooling by 1400 K. This stress level is considerably higher than the experimental observation, by greater than a factor of two. Of course, tensile stresses in a real material on the order of 2 GPa would be expected to cause microcracks, releasing stress. Modeling this process using FEA could be possible with the use of an empirical damage model which would, however, require a considerably larger basis of experimental data.
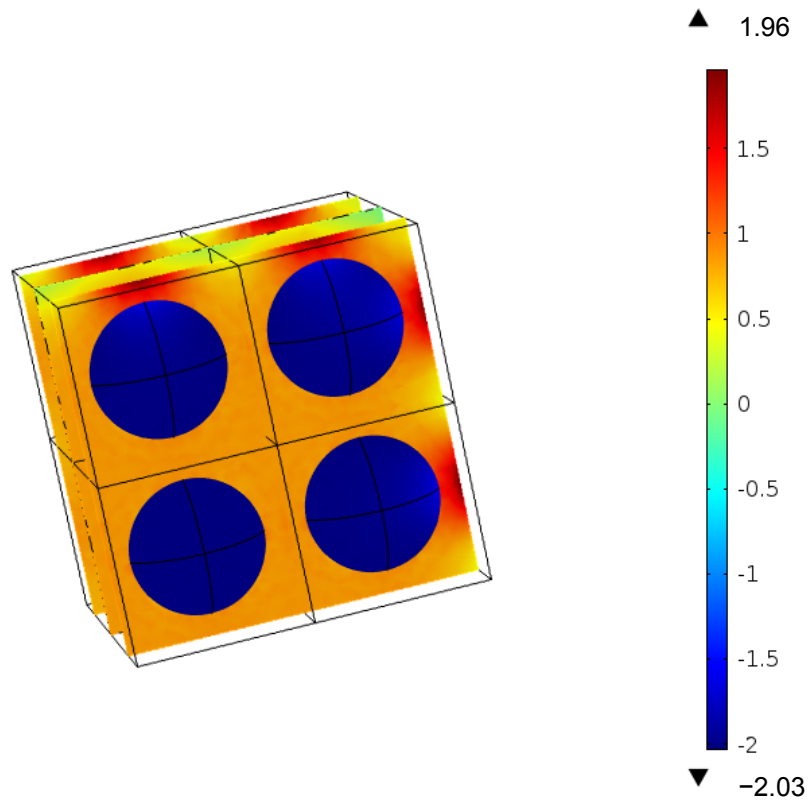
Figure 3.1: Distribution of the first principal invariant of stress in GPa in a modelled composite of SiC (filler) in ZrB_2 (matrix) following a temperature drop of 1400 K.

The main purpose of this model is that it assesses the accuracy of the finite element methodology as qualitative: it is capable of predicting thermal stresses with the correct order of magnitude but the results should not be treated as quantitatively accurate predictions of the thermal stress levels in composite materials. Although FEA is capable of producing analytically correct determinations of stress for models where the geometry and material properties can be modeled exactly,[182] the exact geometry of a polycrystal cannot easily be determined or modeled and the material properties of grain boundaries and interfaces are not generally known. Therefore, this qualitative level of accuracy is not unexpected.

3.2. Effects of Porosity on Thermal Stress

A series of finite element models was created in order to examine the effect of porosity on a ZrW_2O_8 filler/ZrO_2 matrix composite. The inspiration for the models was a work by Sun *et al.* (Reference 122) describing such composite materials with a variety of pore sizes and morphologies, including highly densified systems where the residual porosity is mainly located at the matrix/filler interface. The FE models were intended to determine how pore size and morphology affect the thermal stress distribution in such composites, especially the compressive thermal stress that the ZrW_2O_8 filler experiences upon cooling. Compressive stress above about 300 MPa causes a PIPT to the orthorhombic γ-phase which has a much less negative CTE than the cubic α- and β-phases (see Section 1.5).[96]

The 2D models used were composed of eight or nine ZrW_2O_8 particles arranged in a square or hexagonal packing arrangement in order to measure the interactions of a central particle with its nearest neighbours. Pores were modeled by elliptical voids in the matrix material, with the ellipses being concentric with the circular filler particles. The pore volume and the length of the matrix-filler interface were varied by varying the major and minor axes of the ellipses, respectively. The orientation of the pores relative to their neighbours was varied between parallel and perpendicular. Quench cooling was modeled by fixing the temperature of the outer perimeter of the matrix at a temperature 350 K lower than that of the filler material. The material properties used in the model corresponded to room temperature. These conditions were similar to those used in Reference 85, a finite element analysis of thermal stress in ZrW_2O_8/ZrO_2 composites without porosity.

A typical thermal stress distribution is shown in Figure 3.2: there was large compressive stress in the filler particles, especially near the thin crack-like areas where pore, matrix, and filler all meet. The compressive stress was greater than the 300 MPa threshold for the PIPT in all cases. Thermal stress was found to depend strongly upon the length of the matrix-filler interface, with longer interfaces leading to increased stress. The other factors (packing, pore volume, pore orientation) had smaller effects on the magnitude of the stress, with square packing, parallel pores, and smaller pore volume all leading to increased stress.
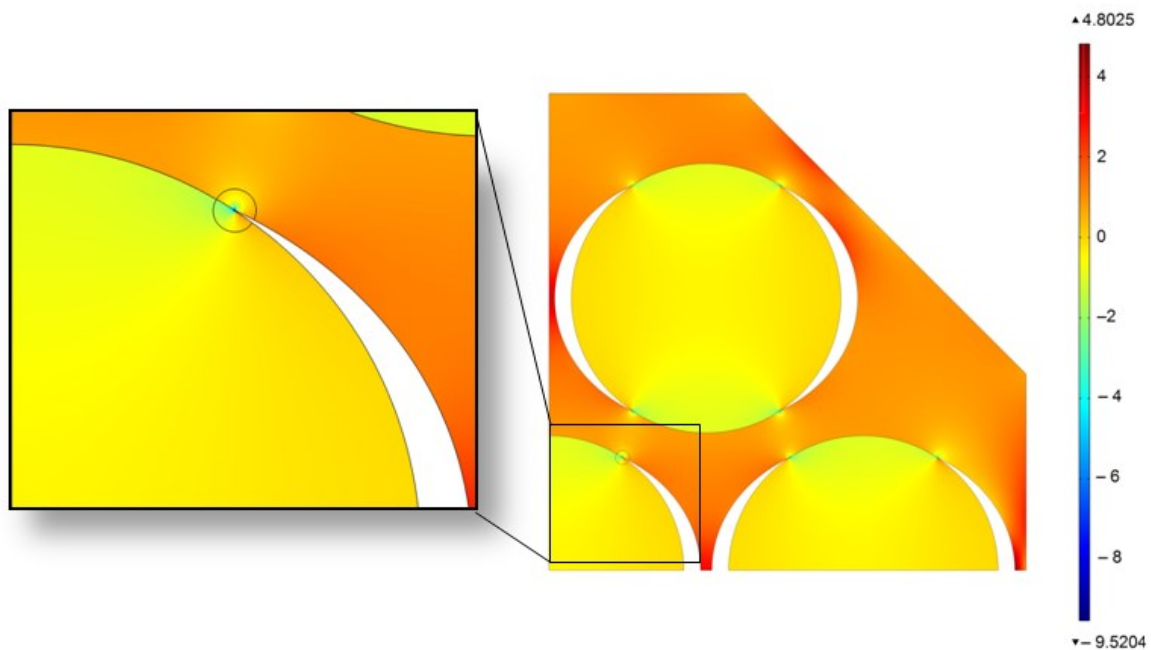
Figure 3.2: The distribution of the first principal invariant of stress in GPa in a representative 2D model of ZrW_2O_8 particles in a porous ZrO_2 matrix, following cooling by 350 K. Anisotropy in the stress distribution in the filler particles was caused by the pores.

The models suggest that ZrW_2O_8 could be protected from thermal stress by decreasing the amount of contact between matrix and filler, and literature micrographs suggested that this is possible while still having a relatively small overall pore volume.[122]

This would be advantageous because the small pore volume would lead to a higher stiffness of the bulk material.[16] Unfortunately, it proved impossible to determine the overall coefficient of thermal expansion of the modeled material. The pores at the boundary of the material shrank in an unconstrained manner, and the total volume change of the material was largely determined by this factor. Consequently, the effect of changing the length of the matrix-filler interface on the thermal expansion of the bulk material could not be determined. As the pore fraction increases, a decreased effect of the ZrW_2O_8 filler on the thermal expansion of the matrix can be expected. Therefore, in practice a balance must be struck by control of the porosity between reduction of the bulk CTE and protection of the components from thermal stress.

In order to test what would happen in a situation where some of the pores closed upon cooling, a model including contact forces was prepared. This contact model had extremely small pores which closed completely upon cooling by 350 K. The surfaces of the matrix and filler materials were designated as contact pairs (curved surfaces which are not allowed to interpenetrate), and a contact force resulted from their interaction. The contact force was determined by an empirical penalty stiffness factor, simulating the surfaces' resistance to penetration.

The stress distribution resulting from the contact model can be seen in Figure 3.3. Its features include greatly homogenized stress distributions throughout both matrix and filler, although the orientation of the pores still has some effect on the final distribution. The average stress in the filler particles increased, but the maximum stress decreased; this makes the PIPT more likely to occur but crack initiation less likely to occur. The area closest to the original matrix-filler interface in the filler particle experienced slightly
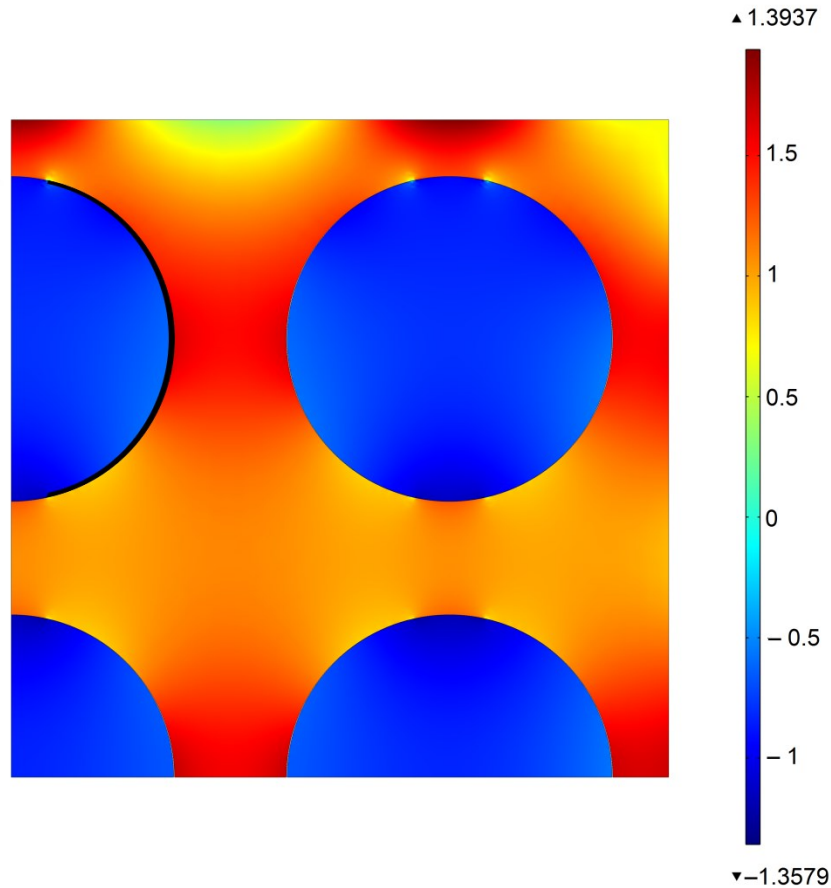
Figure 3.3: First principal invariant of stress distribution in GPa after complete pore closure in a contact model of a ZrW_2O_8 filler/ZrO_2 matrix composite with small pores after cooling by 350 K. The closed pores lie along the right and left surfaces of the filler particles (shown in black on the upper-left particle); the contact surfaces are bound at both ends by the stress minima at the former pore-matrix-filler intersections.

higher stress than the remainder of the particle. This higher stress is attributable to the

small amount of space the filler particle has to freely expand prior to contact. Notably,

the local stress maxima (where pore, matrix, and filler meet) in the case with open pores

become local stress minima when the pores close. This relaxation could significantly

increase the material's fracture resistance by changing the location of high stress areas.

In order to determine how the thermal stress contributes to the pressure-induced formation of γ-ZrW$_2$O$_8$ it was necessary to determine how much strain energy is required to complete the phase transition. This calculation was performed following the method of Abeyaratne et al..[201] First, based on the compressive stress required to begin the β to γ phase transition, it was assumed that the tensile stress required to cause a γ-ZrW$_2$O$_8$ to β-ZrW$_2$O$_8$ phase transition is equal to 300 MPa. This quantity would probably be impossible to determine experimentally as ZrW$_2$O$_8$ would be expected to fail under tension before a phase transition could be observed at such a high stress, but assuming the phase transition is reversible in this regard is reasonable. Secondly, it was assumed that the temperature is sufficiently close to 430 K that the two phases are near thermal equilibrium. Thirdly, the strain energy function was assumed to be piecewise quadratic and therefore the stress-strain relationship remained piecewise linear. Then:[201]

$$W_{min} = P_{PT}^2 (2K)^{-1},$$ (3.3)

where W_{min} is the amount of strain energy required to begin the phase transition, P_{PT} is the hydrostatic pressure at which the phase transition begins and K is the bulk modulus of the material (58 GPa), and:[201]

$$W_{max} = \frac{P_{PT}}{2}\left(\frac{\Delta V_{PT}}{2} - \frac{P_{PT}}{K}\right),$$ (3.4)

where W_{max} is the amount of strain energy required to complete the phase transition after W_{min} is reached, and ΔV_{PT} is the relative difference in volume between the two phases. The molar volume of γ-ZrW$_2$O$_8$ is 94.8% of that of β-ZrW$_2$O$_8$,[96] so the phase transition results in a 5.2% decrease in volume. The resulting value of W_{max} (147 J mol^{-1}) was used

to find the amount of γ-ZrW_2O_8 formed as a function of temperature drop for each geometry (Figure 3.4).

Figure 3.4 shows that the compressive stress in the filler particles crosses the 300 MPa threshold required to begin the PIPT following relatively small temperature drops ($\approx$ 100 K), however this does not necessarily translate into immediate full conversion to the γ-phase, as considerably larger temperature changes are required to push the phase transition to completion. This result shows the importance of considering strain energy when determining the thermomechanical properties of these composites, in contrast with previous research[85,86] that had assumed that γ-ZrW_2O_8 was formed as soon as the threshold stress was exceeded. It is not exactly clear as to what properties a particle which is in an intermediate state between the β- and γ-phases might have, but the percentages shown in Figure 3.4 could be thought of as statistical trends for a large assembly of particles in different geometrical configurations clustered around an average or representative geometry.
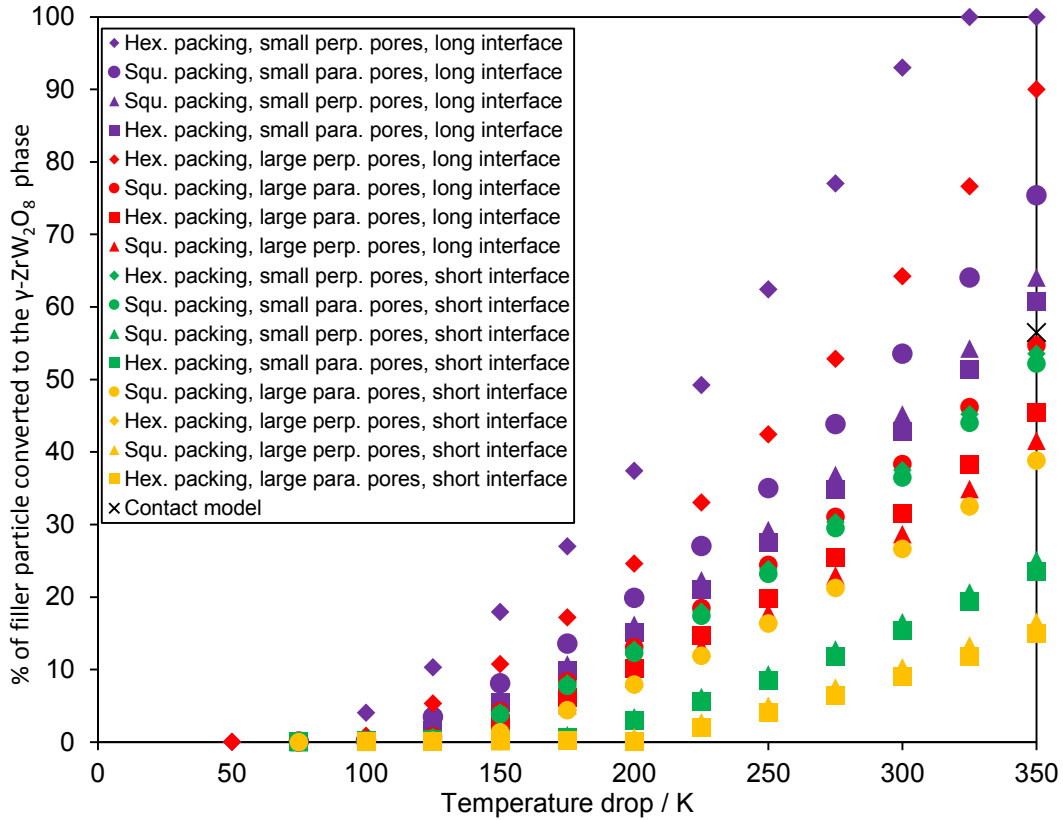
Figure 3.4: Progress of the pressure-induced phase transition for models of ZrW_2O_8 filler particles in a porous ZrO_2 matrix with various geometries as a function of change in temperature. The legend gives the packing (hexagonal or square). Perpendicular pores around a filler particle are oriented 90° to the pores of neighbouring filler particles, whereas parallel pores are oriented in the same direction as neighbouring pores.

3.3. Hyperelastic Material Model for a Pressure-induced Phase Transition

Cubic ZrW_2O_8, as it progresses through a PIPT to γ-ZrW_2O_8, can be described mechanically as a hyperelastic material, that is, one for which the elastic behaviour can be described by a strain energy density function, where each strain state has a corresponding energy density.[201] This approach follows that used by Abeyaratne *et al.* to model austenitic-martensitic transitions.[201] The stress-strain relationship follows the assumptions laid out in the previous section, leading to the strain energy function shown in Figure 3.5. The strain energy density function was piecewise quadratic; there are two

energy minima corresponding to the normal and pressure-induced polymorphs, respectively. By comparison, the strain energy density function for a linear elastic material would also be quadratic, with a single energy minimum at a volume ratio of unity. The total volume ratio (J_{th}) was corrected for thermal expansion to the elastic volume ratio (J_{el}) prior to its use in the strain energy density function as follows:[200]

$$J_{el} = J_{th}(1 + \alpha_V \Delta T)^{-1}. \tag{3.5}$$

The strain energy density function shown in Figure 3.5 only considers changes in volume ratio and therefore hydrostatic stresses. In order to model this function in COMSOL, the "Nearly Incompressible Hyperelastic Material" physics model was used. This physics model simply divides the strain energy density into a volumetric and an isochoric, or shear, portion. However, modeling the isochoric portion of the strain energy density function proved problematic. The most reasonable choice of an isochoric strain energy density function would be from the St. Venant-Kirchoff hyperelastic material model, which is simply an extension of a linear elastic (Hookean) material model for large strains.[202] However, the calculations failed to reach convergence while using this material model. This problem could possibly be solved by increasing the mesh density, but convergence was not reached even at the limits of the computational resources available in the lab. Instead, the neo-Hookean model was used for the isochoric strain energy density. This model matches the Hookean case for small strains, but becomes less stiff for large strains.[202]

Several additional assumptions are implicit in this model. The α→β thermal phase transition was not included. The crystallographic orientation of the ZrW_2O_8 crystallites was not considered. The model used assumes that the α→γ PIPT occurs in the same
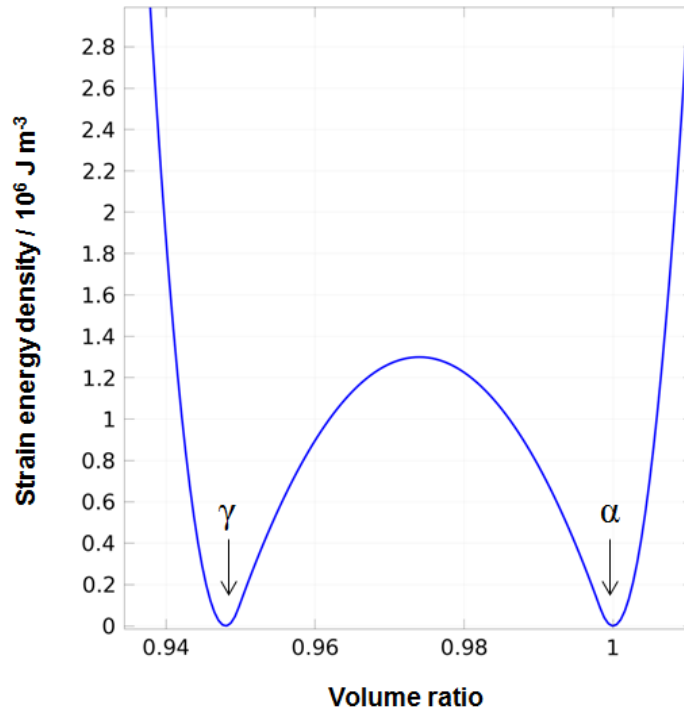
Figure 3.5: The hyperelastic strain energy density function for ZrW_2O_8. The volume ratio is corrected for thermal expansion, and is given relative to the strain-free (α-phase) state. The two energy minima corresponding to the two thermodynamically stable phases are marked.

manner regardless of the orientation of the applied strain, when in actuality the shape of

the crystallites should change during the phase transition, due to the breaking of

symmetry inherent in the cubic to orthorhombic transition. However, the structural

changes involved in the α→γ PIPT are relatively small, and although the molar volume

decreases considerably, the orthorhombic unit cell is close in its proportions to three

cubic unit cells stacked on each other (for α-ZrW_2O_8 a = 9.1575 Å; for γ-ZrW_2O_8 a =

9.067 Å, b = 27.035 Å, c = 8.921 Å).[96] Additionally, the thermal stress applied in the

model geometry used was fairly uniform spatially.

   The model geometry used to implement the hyperelastic material model was a 3D

model composed of cubic-packed spherical ZrW_2O_8 particles in a ZrO_2 matrix. Nine

ZrW$_2$O$_8$ particles were included, to simulate the interactions of the central particle with its nearest neighbours. A variable temperature drop was simulated by fixing the boundaries of the model at a temperature lower than the initial temperature. The material properties used in the model corresponded to those at room temperature. The magnitude of the simulated temperature drop varied from 50 K to 1750 K. A temperature drop of 1750 K would be larger than a drop from the upper limit of the thermal stability range of ZrW$_2$O$_8$ to absolute zero, and therefore is unlikely to actually occur, but such a large stress could also be caused by some combination of thermal stress and an external load.

Figure 3.6(a) shows the progress of the PIPT for various temperature drops. The progress was approximately linear with respect to the change in temperature especially at smaller temperature drops. This was in contrast to the quadratic trend seen in Figure 3.4, when the PIPT was not modeled exactly. The reason for this difference can be determined from Figure 3.5: the strain energy function was composed of two quadratic functions, one with a positive second derivative and one with a negative second derivative. This combination leads to an approximately linear progress overall.

Figure 3.6(b) shows the evolution of the thermal stress in the filler particle. The thermal stress begins to decrease in magnitude after the PIPT begins, as the phase transition made compression more energetically favourable. This continues until the thermal stress actually reaches zero and begins to enter tension. The thermal stress in the matrix material was also zero at this point. The tension continues to increase because the threshold thermal stress has been crossed, but the collapse of the structure into the orthorhombic form is restrained by the surrounding matrix material. Following the completion of the PIPT, the tensile stress quickly decreases, passing through zero again,
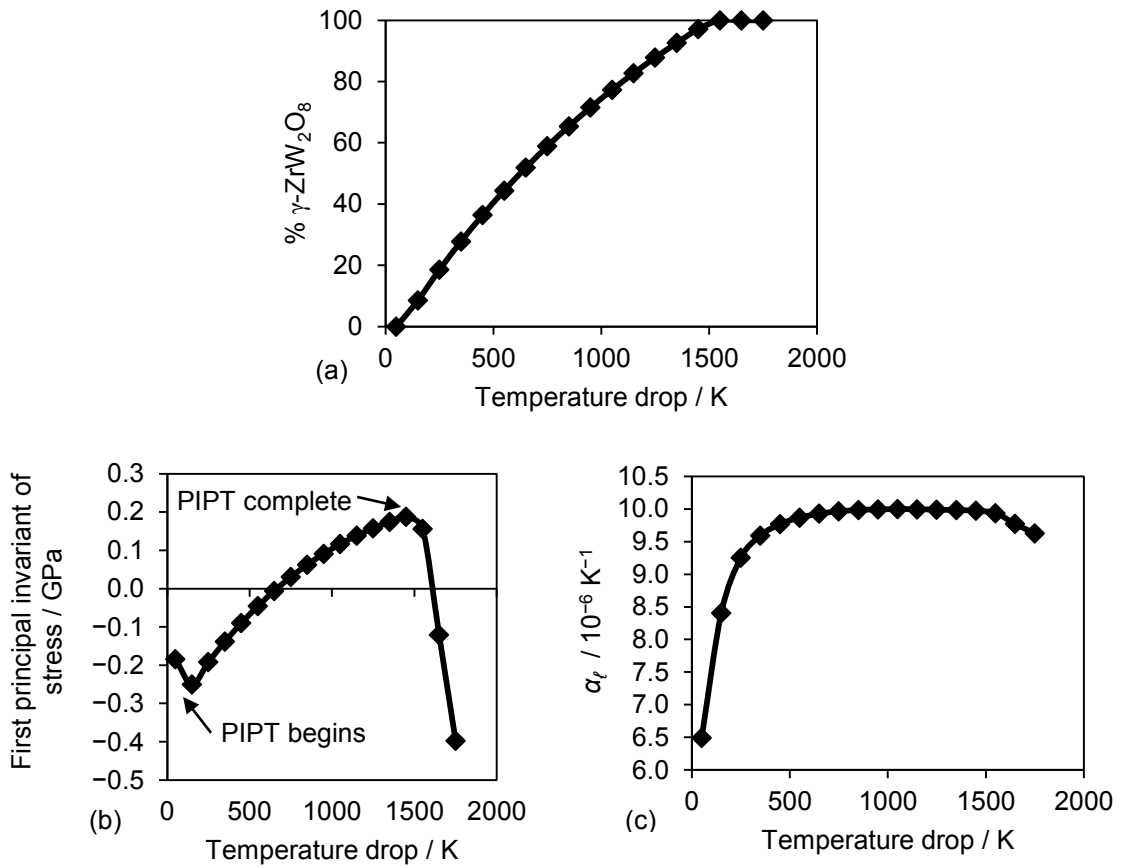
Figure 3.6: (a) Progress of the α→γ PIPT in ZrW_2O_8 (expressed in terms of the amount of γ-ZrW_2O_8 formed), (b) thermal stress in the central ZrW_2O_8 filler particle, and (c) effective coefficient of thermal expansion in the modeled composite (which consisted of hyperelastically modeled ZrW_2O_8 filler in a ZrO_2 matrix) following various temperature drops.

before becoming strongly compressive.

Figure 3.6(c) shows the effective CTE of the modeled ZrW_2O_8/ZrO_2 composite material after various temperature drops. Clearly, the ability of the ZrW_2O_8 filler to act to suppress the PTE of the matrix material decreased precipitously as the PIPT progresses, until the CTE of the bulk material was practically equal to that of the matrix material alone ($\alpha_\ell = 10 \times 10^{-6}$ K^{-1}). Therefore the PIPT can be seen to compensate for the mechanical weakness of ZrW_2O_8 in one way, by reducing the thermal stress it experiences, while simultaneously making its bulk modulus effectively zero. However, if

71

the microstructural environments of the filler particles were sufficiently heterogeneous that a minority of the ZrW_2O_8 passed through the phase transition, the effect could be beneficial, as the overall thermal stress of the material would decrease. The ZrW_2O_8 that underwent the PIPT would be absorbing strain energy to make the bulk material stronger. Of course, the desirability of this effect depends strongly on the application; if the material can be cycled above the temperature required to reverse the PIPT (393 K),[96] the PIPT will not permanently change the CTE of the material.

3.4.   Inclusion of a Phase of Intermediate Thermal Expansion

The inclusion of $Al_2W_3O_{12}$ in ZrW_2O_8/ZrO_2 composites can be accomplished by addition of a small amount of Al_2O_3 to the starting material.[122] $Al_2W_3O_{12}$ melts at a lower temperature than ZrW_2O_8, and if it is a liquid at the temperature used to sinter the composite it can fill many of the pores, resulting in a much denser bulk material.[122] $Al_2W_3O_{12}$ is also a low thermal expansion material ($\alpha_\ell = 2.1 \times 10^{-6}$ K^{-1})[203] so if it is included in an NTE/PTE composite its thermal expansion would be between that of the other two components. In order to find the effect that a component of intermediate CTE would have on the thermal stress distribution, a simple finite element model was created. The 2D model was composed of a matrix of square particles, each randomly assigned as NTE, PTE, or zero thermal expansion, with the CTE of the thermomiotic material of equal magnitude but opposite sign of the PTE material. The mechanical properties of the three types of material were all identical. Several random configurations of the particles were observed.

Figure 3.7 shows the stress distribution in two representative models, one with a thermomiotic phase and a PTE phase and one with an additional zero thermal expansion
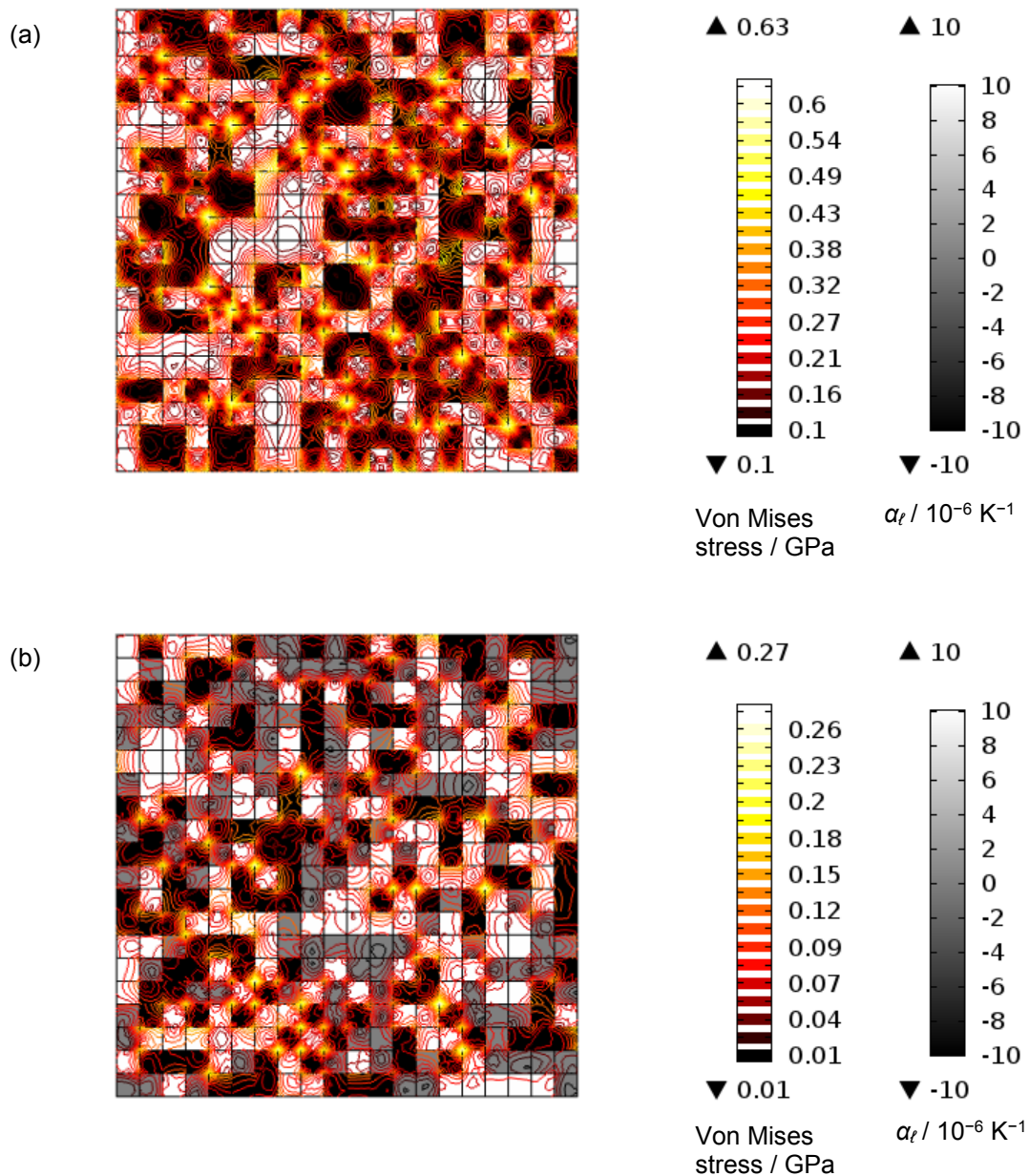
Figure 3.7: Thermal stress distribution following cooling by 350 K in (a) a model with two components, one NTE and one PTE and (b) a model with three components, one NTE, one PTE, and one with zero thermal expansion.

phase. The thermal stress was lower, on average, when the intermediate component is added (Figure 3.7(b)) than when it was not present (Figure 3.7(a)). The near-zero thermal expansion material experienced notably lower thermal stress because of its lack of expansivity, but it also lowered the thermal stress in the other components. The thermal

stress maxima were located at vertices where two thermomiotic particles are each adjacent to two PTE particles. The addition of the near-zero thermal expansion material made these high-stress areas less likely to occur. In general, the stress at an interface between two materials can be seen to be proportional to the difference in thermal expansivity across the interface. Introduction of a material of intermediate thermal expansion created more interfaces, but the interfaces were, on average, of lower stress.

These models are too crude to lead to any quantitative conclusions, but they do validate the concept that inclusion of a material such as $Al_2W_3O_{12}$ with a low-magnitude CTE would reduce the thermal stress in a composite.

3.5. Thermal Stress in an $Al_2Mo_3O_{12}$/Polyethylene Composite[ix]

In this section, FEA of thermal stress in a series of composite materials consisting of $Al_2Mo_3O_{12}$ nanopowder in a polyethylene (PE) matrix is described, with the goal of determining whether it is likely that thermal stresses in these materials would be sufficient to cause ductility in the matrix or fracture of the filler. These materials were synthesized and characterized primarily in the laboratory of Dr. Bojan Marinkovic at PUC-Rio, as described in Reference 204. The experimental results showed a 46 % reduction in thermal expansivity following a modest filler loading of 1.1 vol.%.[204] This large reduction was attributed to good matrix-filler bonding resulting from use of vinyl

---

[ix] This section was adapted with permission from: Soares, A. R.; Ponton, P. I.; Mancic, L.; d'Almeida, J. R. M.; Romao, C. P.; White, M. A.; Marinkovic, B. A. *J. Mater. Sci.* **2014**, *49*, 7870–7882. The author's contributions to this paper included measurement of the bulk elastic properties of $Al_2Mo_3O_{12}$ and finite element analysis of thermal stress in the $Al_2Mo_3O_{12}$/polyethylene composites, and writing the relevant sections of the manuscript.

trimethoxysilane (VTMS) to surface-modify the filler particles prior to their inclusion in the matrix.[204]

Prior to the FEA, the mechanical properties of $Al_2Mo_3O_{12}$ were determined because they had not previously been reported in the literature. Bulk $Al_2Mo_3O_{12}$ pellets were prepared in order to measure their mechanical properties using ultrasonic transduction. The synthesis was performed using a solid-state reaction method, using Al_2O_3 (Sigma-Aldrich, 99.7 %) and MoO_3 (Sigma-Aldrich, 99.5 %) as precursors. The synthetic procedure described in Section 2.1 was used. An X-ray diffractogram (Rigaku Ultima IV diffractometer) of the monophasic product is presented in Appendix A, Figure A1.[x] The three resulting pellets had an average height of 4.78 mm and a density fraction 73 % of theoretical.

Following correction for porosity (see Section 2.3.2), the longitudinal velocity of sound of monoclinic $Al_2Mo_3O_{12}$ was determined (see Appendix B for uncorrected values), following the procedure described in Section 2.5, as 3.29 ± 0.16 m ms^{-1} and the transverse velocity of sound was determined as 2.29 ± 0.22 m ms^{-1}. These values correspond to a bulk modulus of 13.5 ± 1.3 GPa and a shear modulus of 18.2 ± 0.7 GPa. Interestingly, the values indicate that monoclinic $Al_2Mo_3O_{12}$ has a near-zero Poisson ratio, specifically 0.036 ± 0.088. The bulk modulus measured by ultrasonic measurement was consistent with that determined using the Turner model to analyse the thermal expansion of the composites.[204]

---

[x] For ease of comparison, all X-ray diffractograms in this thesis are presented in Appendix A.

FEA was used to assess the thermal stress that could be expected in VTMS-grafted-$Al_2Mo_3O_{12}$/PE composites upon cooling. The model geometry chosen was that of nine spherical filler particles of monoclinic $Al_2Mo_3O_{12}$ embedded at random positions in a cube of PE, where the volume fraction of filler was varied to match the experimental compositions. A mesh of tetrahedral elements was generated in COMSOL and the mesh size used was shown by a mesh convergence study to produce results convergent to within 1 %.

The VTMS grafting was assumed, based on the experimental results described in Reference 204, to produce perfect interfaces between matrix and filler. Both $Al_2Mo_3O_{12}$ and PE were treated as linear elastic materials. Assumption of perfect interfaces and linear elasticity leads to the calculated stress being a conservative estimate; the stress in the actual composite could be reduced by imperfect interfaces or ductility. Therefore, the results of the finite element analysis should be treated as qualitatively accurate. Due to the low volume fractions of filler used, the size, shape, and distribution of the particles did not substantially influence the results and these parameters were not varied as part of this study. The boundary conditions used were a temperature drop of 100 K on all sides of the material and roller boundaries on three perpendicular sides.

FEA was used to calculate the thermal stresses experienced in the composites following a 100 K temperature drop, using room-temperature material properties. Cooling of the modeled composites induced compressive thermal stresses in the VTMS-grafted-$Al_2Mo_3O_{12}$ and tensile thermal stresses in the PE matrix due to their mismatched CTEs. The compressive stress in the filler particles reached a maximum of 22 MPa, and was invariant with the filler loading. The maximum tensile and shear stresses in the PE

matrix are shown in Figure 3.8. The maximum tensile stress increased approximately linearly with filler loading, while the maximum shear stress increased nonlinearly.
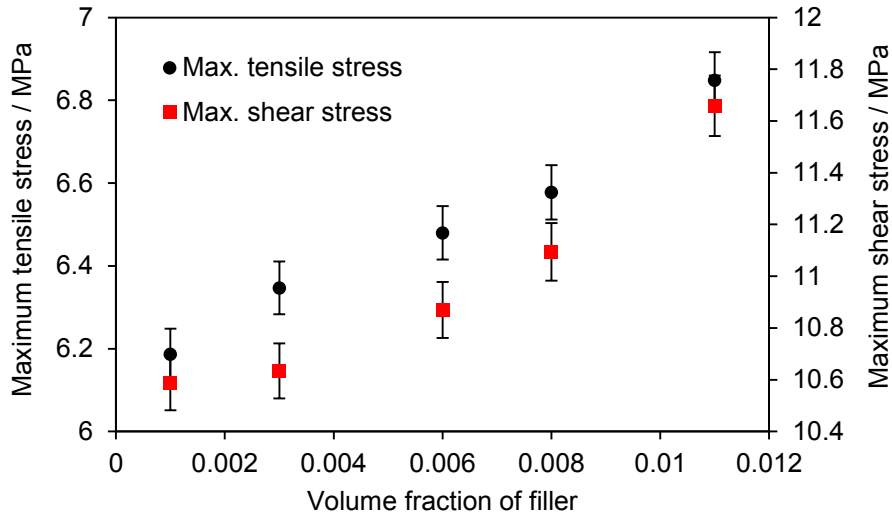
Figure 3.8: Maximum tensile and shear stresses in the PE matrix as a function of the filler ($Al_2Mo_3O_{12}$) content of the modeled $Al_2Mo_3O_{12}$/PE composites following a temperature drop of 100 K. Uncertainty based on finite mesh size effects of 1 % is shown. Adapted from Reference 204 with permission.

The CTE of the composite on addition of filler was calculated to decrease only slightly, but more than would be predicted by the rule of mixtures (Figure 3.9). The discrepancy between the finite element models and the experimental result is possibly due to the finite size of the model, which prevents accurate modelling of the constraint of the thermal expansion of the matrix due to the filler since the bulk of the matrix material is unconstrained.

The thermal stresses calculated by the finite element method for VTMS-grafted-$Al_2Mo_3O_{12}$/PE composites following cooling by 100 K were below the yield strength of the PE matrix[204] as well as the level that would be expected to affect the $Al_2Mo_3O_{12}$ filler.[205] Therefore, the composites would be expected to be mechanically stable following thermal shock of 100 K or less, due to the absence of plastic deformation of the
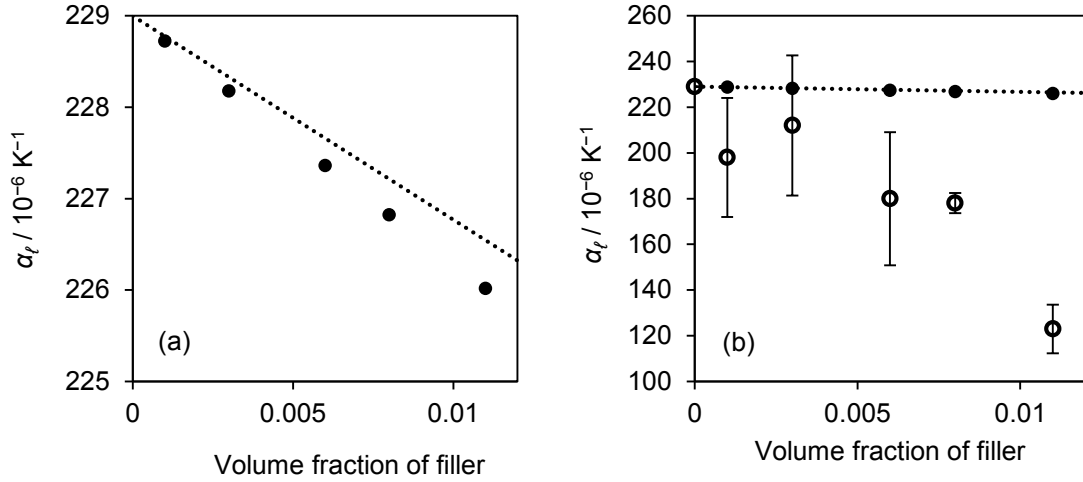
Figure 3.9: (a) The CTE of a modeled $Al_2Mo_3O_{12}$/PE composite is shown as ($\bullet$) as a function of the filler ($Al_2Mo_3O_{12}$) content. The CTE predicted by the rule of mixtures is shown as a dotted line. In (b), experimental results ($\circ$) and uncertainties[204] are shown alongside the information from (a), on a different scale. The CTE of PE was measured as $\alpha_\ell = 229 \times 10^{-6}$ K^{-1} in Reference 204, and the CTE of $Al_2Mo_3O_{12}$ was taken as $\alpha_\ell = 9.5 \times 10^{-6}$ K^{-1}.[205]

matrix or fracture of the $Al_2Mo_3O_{12}$ filler. However, addition of $Al_2Mo_3O_{12}$ in amounts

considerably above 1.1 vol.% might increase the thermal stress in the matrix above the

yield strength of the PE due to the nonlinear increase in the thermal shear stress in the

matrix. Although there is considerable CTE mismatch between PE and $Al_2Mo_3O_{12}$, the

low stiffness of the matrix reduces the magnitude of the thermal stresses considerably, in

addition to allowing reduction of the CTE by addition of only a small amount of filler.

3.6. Conclusions

The finite element analyses presented in this chapter have demonstrated that while

thermal stress in thermomiotic/PTE composites inherently presents a major obstacle to

their use, it can be mitigated in several ways. Microstructural modification, use of non-

Hookean materials, incorporation of phases of intermediate thermal expansion and the

use of compliant materials are all viable strategies to reduce thermal stress in composites.

The experimental realization of these methods is presented in Chapter 4.

Chapter 4: Synthesis and Characterization of Composite Materials Containing a Thermomiotic Component

4.1. Reduction of the Thermal Expansivity of Alumina-toughened Zirconia by Incorporation of Zirconium Tungstate and Aluminum Tungstate[xi]

4.1.1. Background

The considerable interest in including thermomiotic materials (also known as negative thermal expansion materials) in composites is due to their ability to counteract positive thermal expansion and thereby create novel near-zero thermal expansion materials.[1,9,136] Thermomiotic materials have been included in composites in conjunction with polymers,[107, 136,137] metals,[206,207,208,209] and ceramics.[100,122,131,132,210,211,212,213] Ceramic-thermomiotic composite materials are especially appealing because of their high-temperature stability, exceeding conventional near-zero thermal expansion materials such as LAS glass ceramics and Invar (see Section 1.3).

The majority of reports of composites containing thermomiotic materials include ZrW_2O_8,[1] although composites including molybdate,[214] lithium aluminum silicate,[215] and nitride[216] thermomiotic materials also have been reported. ZrW_2O_8 has large isotropic negative thermal expansion over a large temperature range (0.3 to 1050 K),[127] qualities that make it a good candidate for use in composites. However, there are challenges to producing useful ZrW_2O_8-containing composites. As discussed in Chapter 3, due to the large mismatch between the thermomiotic and positive thermal expansion components

---

there is significant thermal stress present following sintering.[85,86,133] ZrW_2O_8 is much less stiff than conventional ceramics,[217] which reduces the stiffness of composites it is included in at high loading.[131] Densification of ZrW_2O_8-containing ceramics is complicated by the fact that ZrW_2O_8 melts at 1255 °C.[87,125] The addition of a small amount of $Al_2W_3O_{12}$, a low thermal expansion material[203,218,219,220,221] which melts[222] below the melting point of ZrW_2O_8,[125] has been shown to aid densification considerably,[131] and would be expected to reduce thermal stresses (see Section 3.4).

The aim of this study was to synthesize novel ceramic materials in which ZrW_2O_8 and $Al_2W_3O_{12}$ are formed by an *in situ* reaction of WO_3 with ATZ (see Section 1.4 for a description of the properties of ATZ) in order to reduce the CTE of ATZ. Previous research concerning similar composites has shown the potential to form ZrW_2O_8/ZrO_2 composites by an *in situ* reaction of WO_3 with ZrO_2[122] as well as the use of YSZ in combination with ZrW_2O_8,[131] but *in situ* synthesis of ZrW_2O_8 and $Al_2W_3O_{12}$ using YSZ as the ZrO_2 precursor together with WO_3 has not previously been reported.

4.1.2. Experimental Procedures

$ZrW_2O_8/Al_2W_3O_{12}/ATZ$ composites were prepared by *in situ* formation of ZrW_2O_8 and $Al_2W_3O_{12}$ by the solid-state reaction method. The reagents used were YSZ (Aldrich, ZrO_2 with 5.3 mol % Y_2O_3, 99.5 % pure on trace metals basis excluding 2 % HfO_2), monoclinic ZrO_2 (Aldrich, 99 %), Al_2O_3 (Sigma-Aldrich, 99.7 % trace metals basis), WO_3 (Fluka, 99.9 %), ZrW_2O_8 (Alfa Aesar, 99.7 % metals basis excluding < 0.3 % Hf) and TiO_2 (Aldrich, anatase, 99 %). TiO_2 was used in a small proportion ($\approx$ 1 %) as a sintering aid because the composites must be sintered below the usual sintering

temperatures of ATZ ($\approx$ 1500 °C).[223] Both TiO_2 and Y_2O_3 can be incorporated into ZrW_2O_8 as a solid solution in small quantities, with Ti^{4+} and Y^{3+} replacing Zr^{4+}.[224,225]

In these experiments, ZrW_2O_8 and $Al_2W_3O_{12}$ were made *in situ* via the reaction of WO_3 (limiting reagent) and YSZ (or monoclinic ZrO_2) and Al_2O_3, where the latter were in excess. In the synthesis conditions it is reasonable to assume, for the purpose of formulating initial compositions of reagents, that ZrW_2O_8 and $Al_2W_3O_{12}$ were formed in the starting mole ratio of YSZ (or monoclinic ZrO_2) and Al_2O_3. Because of the need for 2 (or 3) moles of WO_3 to produce 1 mole of ZrW_2O_8 (or $Al_2W_3O_{12}$), a relatively small proportion of ZrO_2 and Al_2O_3 actually react to form ZrW_2O_8 and $Al_2W_3O_{12}$. However, because of the large increase in molar volume between ZrO_2 and ZrW_2O_8, and Al_2O_3 and $Al_2W_3O_{12}$, respectively, the resulting composite has a large volume fraction of the thermomiotic ZrW_2O_8 and $Al_2W_3O_{12}$ phases.

A range of starting compositions was explored (Table 4.1), aimed to make near-zero thermal expansion composites, as calculated by the rule of mixtures. It was assumed that the WO_3 would react with Al_2O_3 and YSZ in proportion to their molar ratio, with WO_3 as the fully consumed limiting reagent. The initial compositions for reaction were *ca*. 35 mass % YSZ (or monoclinic ZrO_2), 15 mass % Al_2O_3, and 50 mass % WO_3.

Preparation of composite samples followed the procedure described in Section 2.1 in 4–5 g batches. The precursor powders were ball-milled for 1 to 1.5 h using stainless steel grinding media, to ensure good mixing and reduce the mean particle size. The ensuing ball-milled powder was then pressed into pellets using a 5 mm die. The pellets had an average height of about 3 mm.

Table 4.1: Starting experimental compositions, by mole percent.

Sample	ZrO_2 (yttria-stabilized) / mol %	Al_2O_3 / mol %	TiO_2 / mol %	WO_3 / mol %	ZrW_2O_8 / mol %	ZrO_2 (unstabilized) / mol %	Sintering time / h	Rule of mixtures predicted CTE / 10^{-6} K^{-1}
1	0	11.49	0.69	32.67	0	55.15	15	−1.2
2	61.32	9.20	0.30	29.18	0	0	15	−0.95
3	0	16.65	0.49	14.52	10.12	58.22	15	−0.92
4	59.52	18.34	0.27	12.46	9.41	0	15	0.03
5	44.91	23.37	0.20	31.52	0	0	15	−0.13
6	49.50	19.34	0.20	30.96	0	0	15	−0.48
7	49.50	19.34	0.20	30.96	0	0	21	−0.48
8	44.91	23.37	0.20	31.52	0	0	21	−0.13
9	12.40	60.03	0.34	15.9	11.34	0	15	0.17
10	12.40	60.03	0.34	15.9	11.34	0	6	0.17
11	14.05	67.37	0.60	0	17.98	0	6	−1.1

The pellets were subjected to heat treatment to cause the formation of ZrW_2O_8 and $Al_2W_3O_{12}$ and sintering. The pellets were placed in an unsealed fused silica sintering vessel and heated in a tube furnace in air. Heating at a rate of 10 K min^{-1} from room temperature to 600 °C was followed by heating as quickly as possible (about 30 K min^{-1} to start but slower at higher temperatures) to 1200 °C. Heating rapidly serves several purposes. One reason is to have formation of $Al_2W_3O_{12}$ and ZrW_2O_8 in proportion to the starting ZrO_2 and Al_2O_3, since $Al_2W_3O_{12}$ begins to form at temperatures above 900 °C,[218] lower than the temperature of formation of ZrW_2O_8 (1105 °C).[87] Furthermore, although the melting temperature of $Al_2W_3O_{12}$ is *ca.* 1250 °C, melting can occur at lower temperatures in the presence of ZrO_2 and WO_3,[131] and therefore the presence of too much $Al_2W_3O_{12}$ could cause the pellet to lose its structural integrity. Rapid heating also minimizes loss of WO_3, as it begins to sublime above 800 °C.[173] After rapid heating to 1200 °C, the sample was held at that temperature for 6 to 21 h (see Table 4.1 for sintering

times) and then quenched in air. Quenching is necessary to prevent the decomposition of ZrW_2O_8 into its component oxides.[127]

The microstructures of the prepared composite materials were examined using SEM, as described in Section 2.4. SEM imaging was performed with a Zeiss 1455 VP microscope using a BE detector at an accelerating voltage of 20 kV and a working distance of 9 mm. EDS analysis was also performed, by Patricia Scallion.

^{27}Al magic-angle-spinning nuclear magnetic resonance (MAS-NMR) measurements were performed on a Bruker Avance NMR spectrometer with a 16.5 T magnet (182.47 MHz ^{27}Al Larmor frequency) by Dr. Ulrike Werner-Zwanziger. Additional experimental details are available in Reference 226.

X-ray diffractograms, from 10° to 70° in 2θ at 0.05° increments, were collected by Andy George using a Siemens D-500 powder diffractometer, as described in Section 2.2.

Dilatometry was used to measure the CTEs of the prepared composites, as described in Section 2.3.1. Dilatometric experiments were carried out by heating the samples from 25 to 700 °C at a rate of 5 K min^{-1}, followed by cooling from 700 °C to 40 °C at a rate of approximately 2 K min^{-1}.

TGA measurements (see Section 2.3.2) performed from room temperature to 1000 °C at a ramp rate of 30 K min^{-1}.

4.1.3. Results and Discussion

4.1.3.1. Microstructural Characterization

The microstructure of the composites was characterized by SEM (Figures 4.1–4.3). The typical microstructure consisted largely of highly densified regions, where the
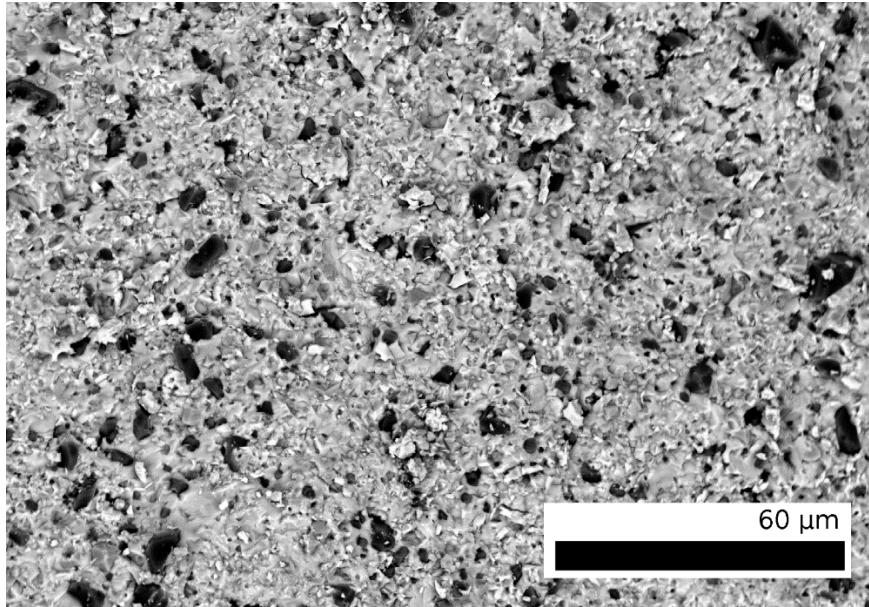
Figure 4.1: A SEM micrograph of Sample 5, a $ZrW_2O_3/Al_2W_3O_{12}/ATZ$ composite (see Table 4.1 and Table 4.2 for composition). Some regions of higher porosity were found throughout the composites, in contrast to the densified regions where molten $Al_2W_3O_{12}$ had been present. See Figure 4.2 for a higher magnification micrograph of the same sample.
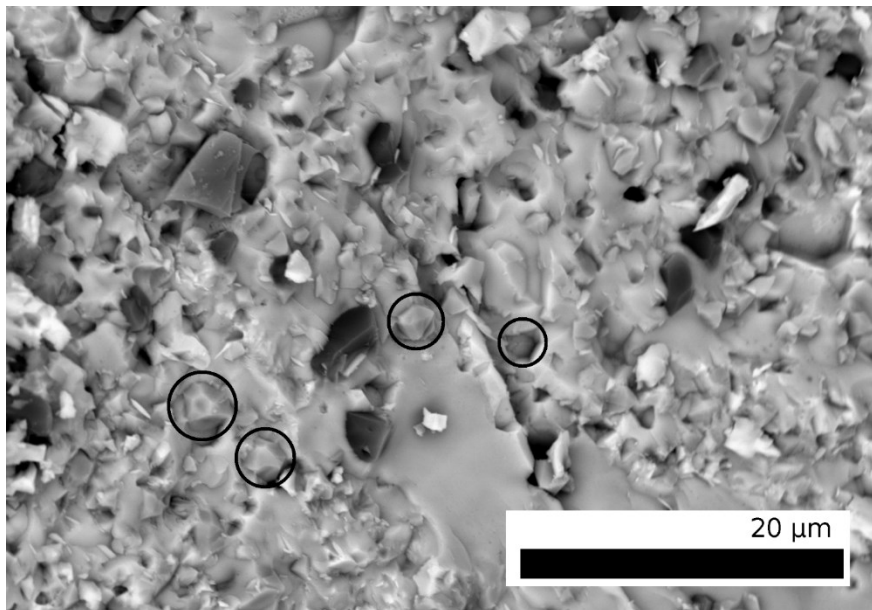
Figure 4.2: A SEM micrograph of the same sample as Figure 4.1 (a $ZrW_2O_3/Al_2W_3O_{12}/ATZ$ composite, see Table 4.1 and Table 4.2 for composition) on a different scale and region. The largest, dark crystallites are Al_2O_3, as verified by EDS. The slightly smaller crystallites of intermediate darkness are likely monoclinic ZrO_2 (several examples are marked with circles). The matrix is composed of much smaller crystallites which likely are a mixture of $Al_2W_3O_{12}$ and ZrW_2O_8.
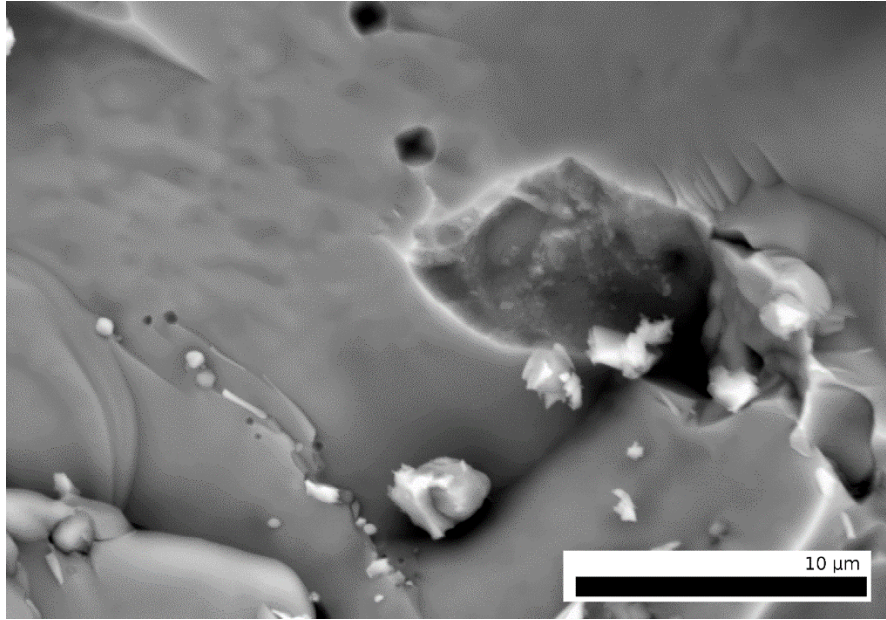
Figure 4.3: A SEM micrograph of Sample 1, a $ZrW_2O_3/Al_2W_3O_{12}/Al_2O_3$/monoclinic ZrO_2 composite (see Table 4.1 and Table 4.2 for composition). There is little visible microstructure.

influence of (formerly) liquid $Al_2W_3O_{12}$ could be clearly seen (Figure 4.1). The μm-sized

crystallites embedded in a mostly homogenous matrix were confirmed as Al_2O_3 by EDS.

Other sub-μm crystallites also could be found in the matrix but their size

prevented their definite identification by EDS. XRD results (*vide infra*) suggest that these

crystallites were likely monoclinic ZrO_2. These crystallites were embedded in a matrix

likely consisting of nanometric crystallites of $Al_2W_3O_{12}$ and ZrW_2O_8, although the two

components cannot be distinguished from each other in Figure 4.2. Regions of higher

porosity were also present. Formation of liquid $Al_2W_3O_{12}$ appeared to have been less

pronounced in these areas. Materials made with monoclinic ZrO_2 showed significantly

different microstructures than those made with YSZ (Figure 4.3), specifically much

greater homogeneity and reduced porosity due to their different compositions (*vide infra*).

4.1.3.2.   Compositional Analysis

Solid state ^{27}Al NMR was used to characterize the aluminum environments quantitatively. Two peaks were resolved at maximum positions around 15 ppm and −8 ppm. Their relative intensities were integrated between 35 to 3 ppm (15 ppm peak) and between 3 to −22 ppm (−8 ppm peak). Figure 4.4 shows examples of typical spectra of the composites (a-c) in comparison to the spectra of $Al_2W_3O_{12}$ (d) and Al_2O_3 (e). An earlier literature report[227] places the ^{27}Al MAS NMR isotropic shift resonance of a single crystal of $Al_2W_3O_{12}$ at −4 ppm in a 14.1T magnetic field. This difference in shifts is probably mostly due to the second-order quadrupole shift of the central transition at two different fields.

It is worth noting that overall the formation of $Al_2W_3O_{12}$ type environments, as measured by NMR, was highest for the two samples that included unstabilized zirconia, with 38 % ± 10 % (Sample 1) and 24 % ± 10 % (Sample 3) of alumina converted to the $Al_2W_3O_{12}$ type environments. A similarly high number (29 % ± 10 %) was only found for Sample 2. All other samples contained less than 20 % ± 10 % $Al_2W_3O_{12}$ type environments, some as low as 4 %. The material with the lowest $Al_2W_3O_{12}$ content (Sample 11) did not have any WO_3 in its initial composition; the WO_3 that formed $Al_2W_3O_{12}$ came from the decomposition of ZrW_2O_8 during heating. The addition of more Al_2O_3 to the starting material resulted in a lower $Al_2W_3O_{12}/Al_2O_3$ ratio, as the amount of $Al_2W_3O_{12}$ formed was relatively constant regardless of initial composition, at about 0.5 g per 4 g batch of starting material. The major exception was where monoclinic ZrO_2 was used instead of YSZ as the starting material (Samples 1 and 3), which had about 50 % more $Al_2W_3O_{12}$ form than the average, resulting in the non-granular microstructure seen
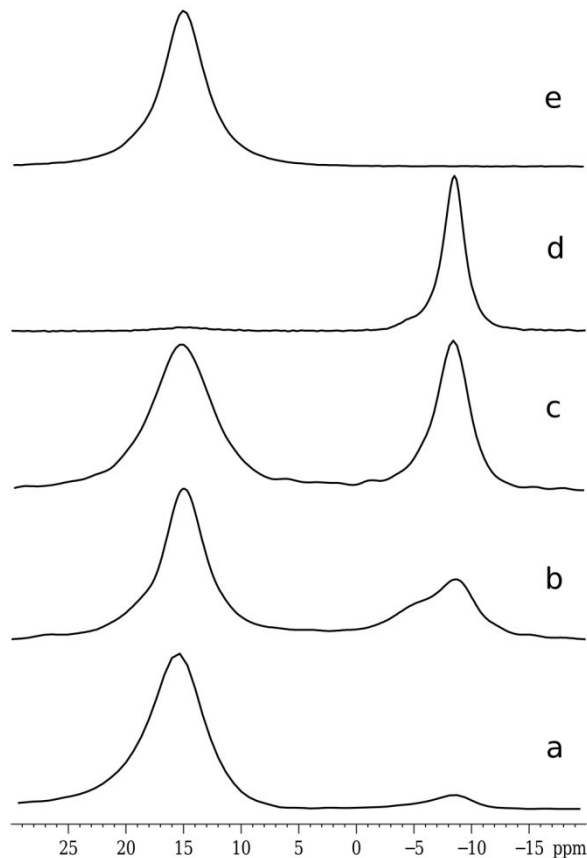
Figure 4.4: Comparison of ^{27}Al MAS NMR spectra from $ZrW_2O_3/Al_2W_3O_{12}/Al_2O_3/ZrO_2$ composites: (a) Sample 10, (b) Sample 2, and (c) Sample 1; and from (d) $Al_2W_3O_{12}$ and (e) Al_2O_3. See Table 4.1 and Table 4.2 for compositions.

in Figure 4.3.

The nearly constant amount of $Al_2W_3O_{12}$ formed is consistent with the SEM results, which showed large crystallites of Al_2O_3 still present in the composites. Because the crystallites of Al_2O_3 had a smaller surface area to volume ratio than ZrO_2, they would be expected to react more slowly with the surrounding WO_3. This effect is compounded by the fact that materials in the $A_2M_3O_{12}$ family generally are formed more slowly than ZrW_2O_8.[127,151]

The X-ray diffractogram for a representative composite (Sample 7) is presented in Appendix A, Figure A2. Due to the large number of phases and small crystallite sizes for

$Al_2W_3O_{12}$ and ZrW_2O_8, only qualitative Rietveld fits could be obtained. ^{27}Al MAS NMR, which does not require crystallinity, gives more accurate $Al_2W_3O_{12}/Al_2O_3$ ratios than XRD. However, the XRD results do qualitatively demonstrate the presence of $Al_2W_3O_{12}$ and ZrW_2O_8 with submicron particle sizes. Little tetragonal (*i.e.*, phase stabilized) ZrO_2 was found to be present compared to monoclinic ZrO_2. This finding was common to all of the synthesized ceramics, even when the diffraction experiment was performed on a pellet that had not been crushed, indicating that the low amount of tetragonal ZrO_2 was not due to a pressure-induced phase transition during crushing. It is likely that the tetragonal ZrO_2 precursor was converted to monoclinic ZrO_2 during ball milling, but the ZrO_2-Y_2O_3 phase diagram indicates that heating to 1200 °C should be more than sufficient to reconvert it to the tetragonal phase.[120] However, the thermal stress caused by quench cooling could be sufficient to transform most of the tetragonal ZrO_2 into the monoclinic form. In this case, the material would still be strengthened by the YSZ, because the transition would have closed many microcracks which would otherwise have persisted.

The X-ray diffractograms showed a small amount of cubic WO_3 (< 1 mass%) present in the composites, probably from slight decomposition of ZrW_2O_8 upon cooling.[127,228]

To check whether a significant amount of WO_3 is volatilized upon heating, a pelletized sample (98.0568 mg) of the green powder used to make Samples 6 and 7 was tested using TGA from room temperature to 1000 °C using the same temperature ramp conditions as used during sintering. A < 2 % mass loss occurred between room temperature and 700 °C, probably due to loss of water and/or CO_2, followed by a < 1 %

mass loss between 700 °C and 1000 °C, presumably due to volatilization of WO_3 (Figure 4.5). From this experiment, as well as similar results in the literature[100,173,212] it was concluded that the mass loss during heating does not significantly affect the final composition of the composites.
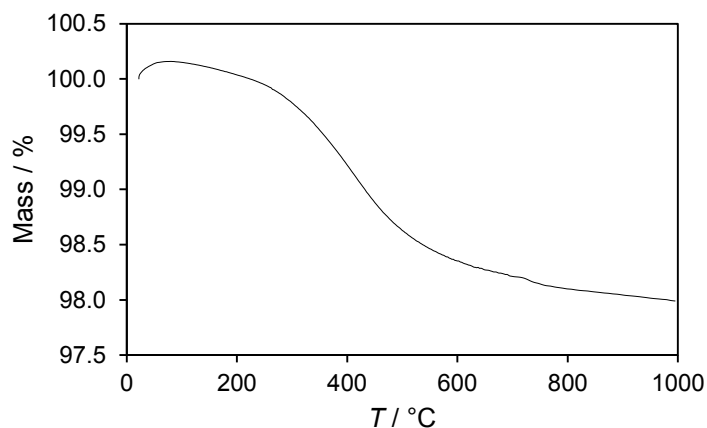
Figure 4.5: TGA thermogram of a pelletized sample of $YSZ/Al_2O_3/WO_3$ green powder subjected to the temperature ramp conditions used to synthesize $ZrW_2O_3/Al_2W_3O_{12}/ATZ$ composites (Samples 6 and 7, see Table 4.1 and Table 4.2 for compositions).

4.1.3.3. Thermal Expansion

CTEs of the composites were determined by dilatometry. An example set of dilatometric curves is shown in Figure 4.6. Generally no special features were found in the dilatometric curves. The CTEs of the prepared composites, as measured between 40 and 700 °C, were within the range $\alpha_\ell = (5.1 \pm 0.5) \times 10^{-6}$ K^{-1} and $(6.9 \pm 0.5) \times 10^{-6}$ K^{-1}, averaging $\alpha_\ell = 6.2 \times 10^{-6}$ K^{-1}. While this is not the desired near-zero thermal expansion, the results represent up to 50 % decrease in CTE relative to ATZ, with its $\alpha_\ell = 10 \times 10^{-6}$ K^{-1}.[229] Attempts to prepare composites with lower CTEs by inclusion of more WO_3 resulted invariably in the melting point of the green body falling below the temperature required to form ZrW_2O_8 (1105 °C).
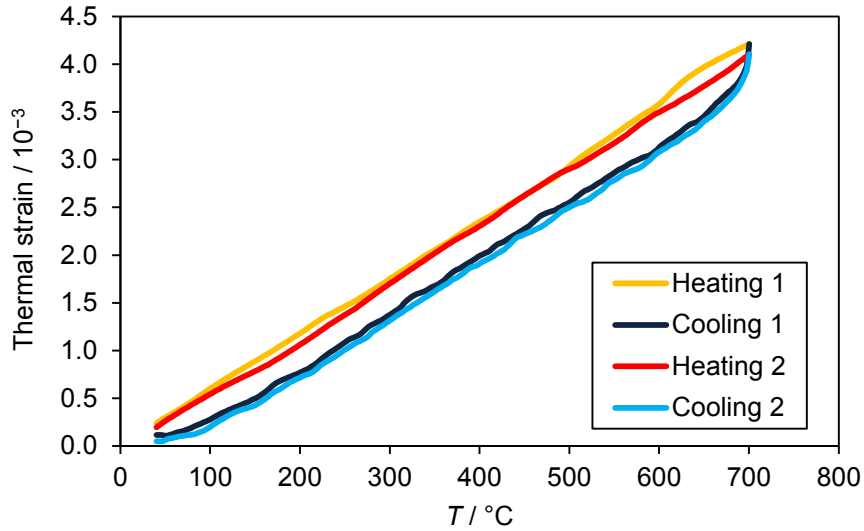
Figure 4.6: A series of dilatometric curves of a ZrW$_2$O$_8$/Al$_2$W$_3$O$_{12}$/ATZ composite (Sample 8, see Table 4.1 and Table 4.2 for composition). The graph plots the thermal strain, which is the change in length per initial length, as a function temperature. "Heating 1" or "Cooling 1" refer to whether the thermal expansion was measured as the temperature increased or decreased and the cycle number. The CTE of this sample (average value from two cooling curves) was $\alpha_\ell = (6.6 \pm 0.5) \times 10^{-6}$ K^{-1}. Some hysteresis due to microcrack formation and healing is visible.

Interestingly, no change in the CTE at 155 °C corresponding to the α→β transition of ZrW$_2$O$_8$[87] was detected. The change in volume associated with this phase transition was considered to be one of the major obstacles to the use of ZrW$_2$O$_8$ in composites.[87] The negligible influence of the phase transition could be due to substitutional defects (*e.g.* Y$_{Zr}$' or Ti$_{Zr}$^{x}) in the ZrW$_2$O$_8$, which could both decrease the temperature at which the phase transition occurs and reduce the change in CTE and molar volume between the α- and β-phases.[225]

When two composites of identical compositions but different sintering times are compared, the ones sintered longer were more dense and had slightly higher CTEs. The longer sintering time could lead to reduction of some of the residual porosity and subsequently increase mechanical contact between phases. The lowest CTE material ($\alpha_\ell = 5.1 \times 10^{-6}$ K^{-1}) had been made with monoclinic ZrO$_2$, not YSZ (Sample 1).

91

Quantification of the amount of $Al_2W_3O_{12}$ allowed the remainder of the

compositions of the composites to be determined (excluding pore volume), based on the

assumption that all of the WO_3 was transformed into $Al_2W_3O_{12}$ or ZrW_2O_8. With

knowledge of the compositions, the measured CTEs could be compared against

mathematical models of thermal expansion. The rule of mixtures, the simplest

mathematical model, can be expressed as:[16]

$$\alpha_{\text{Bulk}} = \sum_i \alpha_i \phi_i, \tag{4.1}$$

where α_{Bulk} is the CTE of the bulk material and α_i and ϕ_i are the CTE and volume

fraction, respectively, of the ith component. The Turner model is an extension of the rule

of mixtures, including the effect of variations in the bulk modulus:[16]

$$\alpha_{\text{Bulk}} = \frac{\sum_i K_i \alpha_i \phi_i}{\sum_i K_i \phi_i}, \tag{4.2}$$

where K_i is the bulk modulus of the ith component. There exist more complicated

expressions for the thermal expansivity of a composite, but they are generally formulated

for two-component composites and do not generalize easily to those with additional

components.[16]

The experimentally measured CTEs from dilatometry are compared against the

model CTEs in Figure 4.7 and Table 4.2. The predicted CTEs were calculated presuming

that all of the ZrO_2 was in the monoclinic phase, in accordance with the XRD results. The

reagent compositions and the final compositions are given in Table 4.1 and Table 4.2,

respectively. The bulk modulus of ZrW_2O_8 was taken as 13 GPa,[xii,131] and its CTE (in the

---

[xii] Polycrystalline ZrW_2O_8 has been shown to be considerably more compliant than would be expected from the bulk modulus ($K \approx 70$ GPa) as measured from variable pressure diffraction.[131] Here a value based on experiments on bulk ZrW_2O_8 with a very small amount of $Al_2W_3O_{12}$ added to aid densification was used.[131]
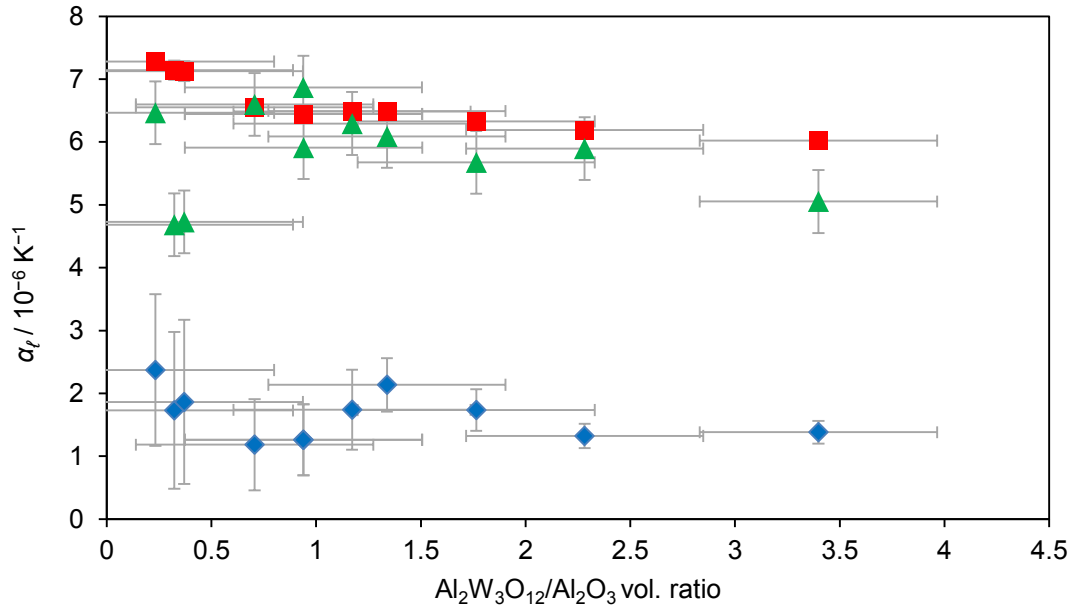
Figure 4.7: The dilatometrically measured CTEs (▲) of various $ZrW_2O_8/Al_2W_3O_{12}/Al_2O_3/ZrO_2$ composites are compared against the predicted CTEs from the rule of mixtures (♦) and the Turner model (■) (see Equations (4.1) and (4.2)). See Table 4.1 and Table 4.2 for exact compositions and CTEs.

Table 4.2: Molar ratios of $Al_2W_3O_{12}$ to Al_2O_3 as determined by ^{27}Al NMR, deduced sample compositions by volume percent, and coefficients of thermal expansion as measured experimentally and as calculated by the rule of mixtures and the Turner model for $ZrW_2O_8/Al_2W_3O_{12}/Al_2O_3/ZrO_2$ composites.

Sample	Mol. ratio $Al_2W_3O_{12}$/ Al_2O_3	Vol. % $Al_2W_3O_{12}$	Vol. % Al_2O_3	Vol. % ZrW_2O_8	Vol. % ZrO_2	Measured CTE / 10^{-6} K^{-1}	Rule of mixtures CTE / 10^{-6} K^{-1}	Turner model CTE / 10^{-6} K^{-1}
1	0.6±0.1	23±2	7±0.4	38±2.5	33±0.5	5.1±0.5	1.4±0.2	6.02±0.02
2	0.4±0.1	14±3	6±0.4	42±2.7	38±0.6	5.9±0.5	1.3±0.2	6.19±0.02
3	0.31±0.1	18±4	10±0.7	37±4.7	35±1.0	5.7±0.5	1.7±0.3	6.33±0.04
4	0.24±0.1	16±6	12±0.9	35±6.0	37±1.3	6.1±0.5	2.1±0.4	6.49±0.05
5	0.21±0.1	21±8	18±1.4	37±8.9	25±1.9	6.3±0.5	1.7±0.6	6.48±0.08
6	0.17±0.1	14±7	15±1.2	43±7.9	27±1.7	5.9±0.5	1.3±0.6	6.45±0.07
7	0.17±0.1	14±7	15±1.2	43±8.0	27±1.7	6.9±0.5	1.3±0.6	6.45±0.07
8	0.12±0.1	13±10	19±1.5	45±10.2	23±2.1	6.6±0.5	1.2±0.7	6.55±0.09
9	0.07±0.1	15±17	40±2.5	40±18.3	5±3.6	4.7±0.5	1.9±1.3	7.13±0.16
10	0.06±0.1	13±16	40±2.4	42±17.5	5±3.4	4.7±0.5	1.7±1.2	7.14±0.15
11	0.04±0.1	10±16	42±2.3	38±16.8	9±3.4	6.5±0.5	2.4±1.2	7.28±0.13

β phase) as -5×10^{-6} K^{-1};[127] the bulk modulus of $Al_2W_3O_{12}$ was determined to be 46 GPa (see Chapter 6), and its CTE was taken as 2×10^{-6} K^{-1};[220,221] the bulk modulus of Al_2O_3 was taken as 254 GPa[230] and its CTE was taken as 8×10^{-6} K^{-1};[231] and the bulk modulus of monoclinic ZrO_2 was taken as 187 GPa,[232] and its CTE was taken as 7×10^{-6} K^{-1}.[233] The rule of mixtures gave inaccurate predictions of the CTEs of the products. (However, the realized compositions gave rule-of-mixtures CTEs that were close to zero, validating the synthetic methodology.) The Turner model effectively predicted the CTEs of the composites, demonstrating the strong influence of the bulk modulus of the thermomiotic materials on the effective CTEs.

Earlier reports of ZrW_2O_8/ZrO_2 composites[100,131] showed a negative deviation of experimental CTEs from the rule of mixtures, as observed here. The composites in Reference 100 differed from the ones synthesized in this work by the absence of Al_2O_3 and $Al_2W_3O_{12}$. The composites reported in Reference 131 contained ZrW_2O_8, YSZ, a small amount of $Al_2W_3O_{12}$, and no Al_2O_3. In both cases the morphologies consisted of large particles of ZrW_2O_2 embedded in a matrix of much smaller ZrO_2 crystallites.

Two materials with a high ZrW_2O_8/ZrO_2 volume ratio (Samples 9 and 10, see Table 4.2) had experimental CTEs lying between the Turner and rule of mixtures values. These materials were made with pre-synthesized ZrW_2O_8 and no starting WO_3, and subsequently contained little $Al_2W_3O_{12}$. The addition of larger amounts of $Al_2W_3O_{12}$ in the other cases, as well as the presence of the stiff Al_2O_3, reduced the influence of the thermomiotic components on the overall thermal expansivity.

The present results show that using thermomiotic materials to effectively counteract positive thermal expansion would be very difficult when the thermomiotic

component is much stiffer than that of the positive thermal expansion component. Composites combining a thermomiotic component with more compliant materials such as polymers (Section 4.2) or metals might provide greater reduction in CTE magnitude.

4.1.4. Conclusions

In this study, mixtures of ATZ and WO_3 were used to prepare composites containing ZrW_2O_8, $Al_2W_3O_{12}$, and ATZ by *in situ* solid-state reactions. Composites with ATZ as the precursor were shown to form less $Al_2W_3O_{12}$ than those synthesised using a mixture of Al_2O_3 and monoclinic ZrO_2. The addition of ZrW_2O_8 and $Al_2W_3O_{12}$ to ATZ lowered the CTE of the composites by up to 50%, but much less than predicted by the rule of mixtures. The Turner model successfully predicted the thermal expansivity of the composites, showing the impact of the low stiffnesses of thermomiotic materials on their inability to counteract positive thermal expansion.

4.2.   A Lamellar ZrW_2O_8/Polymethylmethacrylate Composite

4.2.1. Background

Bio-composite materials such as nacre, which have unique directional thermal and mechanical properties due to their layered composite structures, suggest an interesting potential avenue to tailor the properties of ceramic materials.[123,234] Lamellar ceramic structures similar to that of nacre can be created by a freeze casting process, where the swift directional growth of ice crystals produces the structure.[235,236,237,238] The ice is removed by freeze drying, and then following sintering the ceramic can be functionalized and finally impregnated with a polymer.[235,238] A former post-doctoral fellow in Dr. Mary Anne White's lab, Dr. Ran Chen, developed an experimental setup for the preparation of

such lamellar ceramic-polymer composite materials.[238] As combining thermomiotic

materials effectively with polymers presents many challenges,[107,134,135] this method could

produce a low-expansion material with increased toughness[239] and possibly other novel

properties, such as highly anisotropic thermal and ionic conductivity.

The goal of this investigation was to demonstrate as a proof of concept that a

lamellar thermomiotic ceramic could be produced *via* freeze-casting and subsequently

impregnated with a polymer. ZrW_2O_8 was chosen as the thermomiotic ceramic

component for this study because of its isotropic NTE and its commercial availability,

while polymethylmethacrylate (PMMA) was chosen as the polymeric component because

of its relative ease of synthesis. The synthesis of lamellar ZrW_2O_8 was performed with

the assistance of Anderson de Farias Periera, an undergraduate research assistant in Dr.

Mary Anne White's lab in the summer of 2013. Anderson prepared the ZrW_2O_8-water

slurries and performed the subsequent freeze-casting and freeze-drying steps under the

author's supervision.

4.2.2. Synthesis

In order to produce lamellar ZrW_2O_8 *via* freeze-casting, a suspension of ZrW_2O_8

powder in water was required. Due to the high density of ZrW_2O_8 (5.09 g cm^{-3}),[87] this

was accomplished with some difficulty. To facilitate the suspension, the ZrW_2O_8

feedstock (Alfa Aesar, 99.7% [metals basis excluding Hf], Hf < 0.3 %) was ball-milled

for 12 h (see Section 2.1) to reduce the particle size, followed by sifting with a 100 mesh

sieve. The size distribution of the resulting particles was assessed qualitatively using

SEM (Hitachi S-4700 FEG microscope, SE detector, 20 kV accelerating voltage, 11.6

mm working distance, see Section 2.4). This analysis revealed particle sizes on the order

of 1 μm and smaller (Figure 4.8).
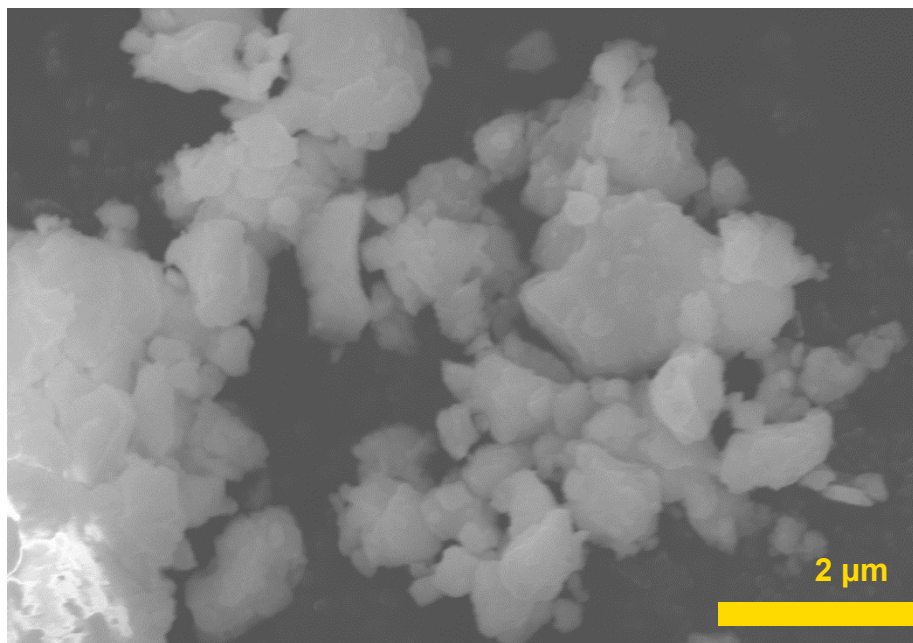
Figure 4.8: Representative SEM image of ZrW_2O_8 powder following 12 h of ball-milling to reduce the particle size.

Suspensions of ZrW_2O_8 in water were prepared with several test dispersants:

PMMA (Aldrich, 100 mesh, 99 %), polyvinyl alcohol (PVA, 100 mesh, Aldrich, 99 %),

sodium dodecylbenzenesulfonate (SDBS, Aldrich, technical grade), polyvinylpyrrolidone

(PVP-10, Sigma), polyethylene glycol (PEG-400, BDH), polyoxyethylene (20) sorbitan

monooleate (Tween 80, Anachemia) and sorbitan monooleate (Span 80, Fluka). The

suspensions were prepared in 1–2 g batches in 5 mL glass vials. First, the pH of the

(deionized) water was adjusted by addition of dilute acetic acid or KOH solution

followed by pH measurement with litmus paper. A range of pH from 3 to 10 was tested

as a means of adjusting the zeta potential (a measure of the charge surrounding a particle

in solution).[240] Subsequently, 1 vol.% PVA was added to the solution (the PVA acted as a

binder for the green ceramic form, allowing it to retain its shape following freeze-drying),

97

followed by heating with stirring on a hot plate set at 95 °C until the PVA was solubilized. The solution was then cooled to 40 °C and the dispersant (1–5 vol. %) was added, followed by the ZrW_2O_8 (17 vol. %) while maintaining stirring. The sample was then degassed under vacuum for 10 min, then ultrasonicated for 5 min to break up agglomerates. The solutions were allowed to sit undisturbed for at least one week and the stability of the dispersion was assessed visually based on the presence and/or amount of sedimentation.

Thirty-nine different solutions were prepared by Anderson de Farias Periera and evaluated for their ability to form a colloidal suspension of ZrW_2O_8. SDBS (at 5 vol. % and solution pH 3) was the first surfactant found to give an acceptable dispersion, so initial freeze-casting experiments were carried out using it. The freeze-casting process began with the production of the suspension using the procedure described above. The suspension was then poured into a circular polycarbonate mould (diameter ≈ 1 cm, height ≈ 3 cm) on a copper base that was placed on a Peltier cooling plate held at −24 °C. A vacuum flask was placed over the apparatus to reproducibly control the temperature of the system. Once freezing was completed, the sample was removed from the mould using a rubber-tipped plunger and freeze-dried for 24 h at −50 °C and 1 kPa (Edwards Modulyo Freeze Dryer System). Sintering of these samples proved problematic, however. Although bulk ZrW_2O_8 is metastable at temperatures up to 775 °C,[87] sintering the freeze-cast samples at 700 °C or 650 °C resulted in visible decomposition into the component oxides. This decomposition could be related to the small size of the ZrW_2O_8 particles, or some chemical interaction with SDBS or its decomposition products. However, no such effect was reported when ZrW_2O_8 nanoparticles were prepared using a hydrothermal

method using SDBS as a surfactant.[129] Holding the material at 500 °C for up to 72 hours did not cause decomposition but also failed to sinter the material.

An alternative sintering method was employed to combat the problem of decomposition: insertion of the freeze-cast ZrW_2O_8 into a furnace held at 1200 °C for 150 s followed immediately by water-quenching. The goal of this method was to heat the material above the lower limit of phase stability of ZrW_2O_8 (1100 °C) for long enough to reverse decomposition from heating, but not so long that the lamellar microstructure was destroyed. Water-quenching helped prevent additional decomposition during cooling. At this time, it had been determined that Span 80 (1 vol.%, solution pH 3) was also able to produce a suspension of ZrW_2O_8 in water, and a freeze-cast sample made using Span 80 was also subjected to the new sintering conditions. While samples made with SDBS did not retain their lamellar microstructure following sintering at 1200 °C for 150 s, the sample made with Span 80 did. The results presented below pertain to the sample made using Span 80.

A portion of the sample prepared using Span 80 as the surfactant was used for SEM and XRD characterization (see Section 4.2.3). The remainder was treated with 3-(trimethosilyl)propyl methacrylate (γ-MPS, Alfa Aesar, 97 %) prior to polymer infiltration. The γ-MPS treatment was performed by submersing the sintered lamellar ZrW_2O_8 in a solution of 5 % γ-MPS in methanol at 80 °C for 2 h and then at room temperature overnight. Following rinsing with deionized water, the sample was left to air-dry. Subsequently, polymer infiltration with MMA was performed using the procedure described in Reference 238. Methyl methacrylate (Aldrich, 99 %), sodium lauryl sulfate (Fluka, 99 %), and potassium persulfate (Aldrich, 99.95 %) were used as reagents.

4.2.3. Characterization

X-ray diffraction was used to determine the phase purity of the freeze-cast ZrW$_2$O$_8$ following sintering (Rigaku Ultima IV diffractometer, see Section 2.2). Using Match! to analyse the diffraction data using the PDF-2 database,[169] the composition of the material was estimated to be 86 vol.% ZrW$_2$O$_8$, 11 vol.% ZrO$_2$ and 3 vol.% WO$_3$ (see Appendix A, Figure A3). Clearly, the sintering path used still allowed a significant amount of decomposition to occur, however the material still exhibited considerable negative thermal expansion (*vide infra*).

The microstructure of the freeze-cast ZrW$_2$O$_8$ was characterized by SEM (Figure 4.9) using a Hitachi S-4700 FEG microscope, 5 kV accelerating voltage, 13.2 mm working distance, SE detector (see Section 2.4). The freeze-casting process was successful at producing a lamellar microstructure, with lamellae *ca.* 30 μm thick separated by *ca.* 50 μm of void space. These lamellae were considerably thicker than those reported for Al$_2$O$_3$ in Reference 238, however there were several differences between the experiments: the present experiment used a cooling plate which could only reach a higher minimum temperature (−24 °C *vs.* −40 °C) and the Al$_2$O$_3$ particle sizes used (40–400 nm) were smaller. Both factors would be expected to lead to thinner Al$_2$O$_3$ lamellae. Many bridges between the lamellae are present in the ZrW$_2$O$_8$ material.

Following infiltration with PMMA, the sample was examined again *via* SEM (see Section 2.4) using a Zeiss 1455 VP microscope equipped with a SE detector using a 20 kV accelerating voltage and a 28 mm working distance (Figure 4.10). The polymer infiltration and grafting was determined to have been successful, as PMMA filled the spaces between the ZrW$_2$O$_8$ lamellae. The PMMA morphology consisted of spheroidal
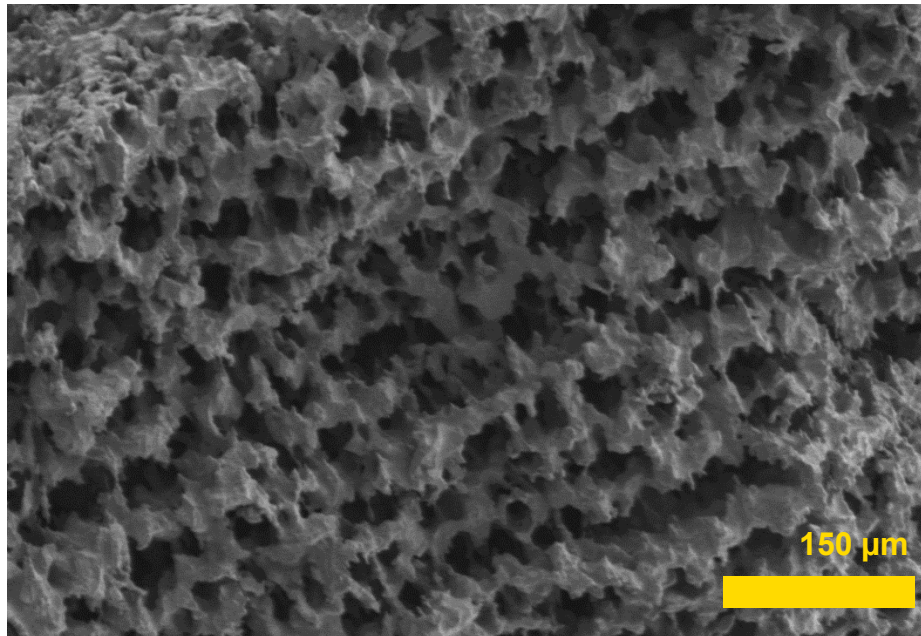
Figure 4.9: SEM image of freeze-cast ZrW$_2$O$_8$, showing the ordered lamellar structure with bridges throughout the material.
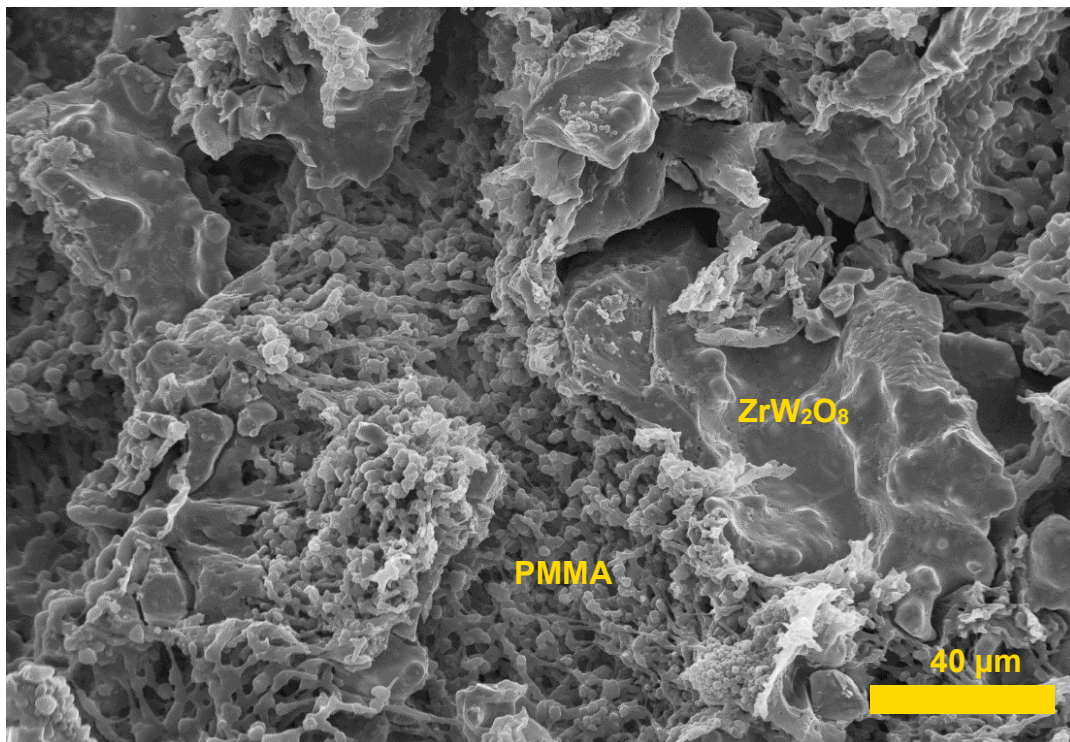
Figure 4.10: SEM image of the ZrW$_2$O$_8$/PMMA composite, showing polymer infiltration between two ZrW$_2$O$_8$ lamellae.

submicron-diameter particles with considerable porosity between them. This morphology is likely a result of the method used to synthesize the PMMA (stirring methylmethacrylate in water with a surfactant); a similar morphology was reported in Reference 238. The inclusion of porosity in the PMMA would effectively make it more compliant, reducing thermal stress; however this would also reduce its ability to increase the toughness of the bulk composite.

The thermal expansion of the composite in a direction roughly perpendicular to the lamellae was measured dilatometrically (see Section 2.3.1). A 1.765 mm long portion of the sample was used. In order to avoid any melting of the PMMA, three thermal cycles were carried out from 25 °C to 125 °C using a heating rate of 5 K min^{-1} and a cooling rate of 2 K min^{-1} (Figure 4.11). A large, irreversible negative strain (-1.2 %) was observed during the first heating cycle, however the following cycles were repeatable. The linear CTE, as measured from three cooling cycles, was $\alpha_\ell = (-7.6 \pm 0.5) \times 10^{-6}$ K^{-1}. This is relatively close to the CTE of pure ZrW_2O_8 in this temperature range ($\alpha_\ell = -9 \times 10^{-6}$ K^{-1}),[127] indicating that the PMMA had only a small effect on the bulk CTE of the composite, and that impregnation of lamellar thermomiotic ceramics with a polymer can result in a bulk polymer-ceramic composite with negative thermal expansion. The sample did not have sufficient cross-sectional area in the direction parallel to the lamellae to permit measurement in that direction.

TGA was performed on a 14.9318 mg portion of the sample used for dilatometry in order to determine the PMMA loading (Figure 4.12). The material was heated from 25 °C to 350 °C at a rate of 5 K min^{-1} and then held isothermally at 350 °C for 30 min to ensure complete decomposition of the PMMA.[241] A 9.5 % mass loss was observed upon

(a)

T / °C

(b)

T / °C
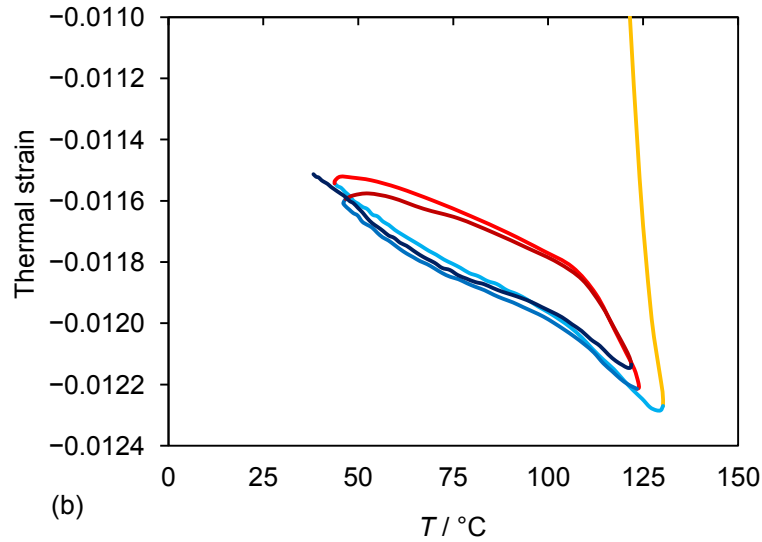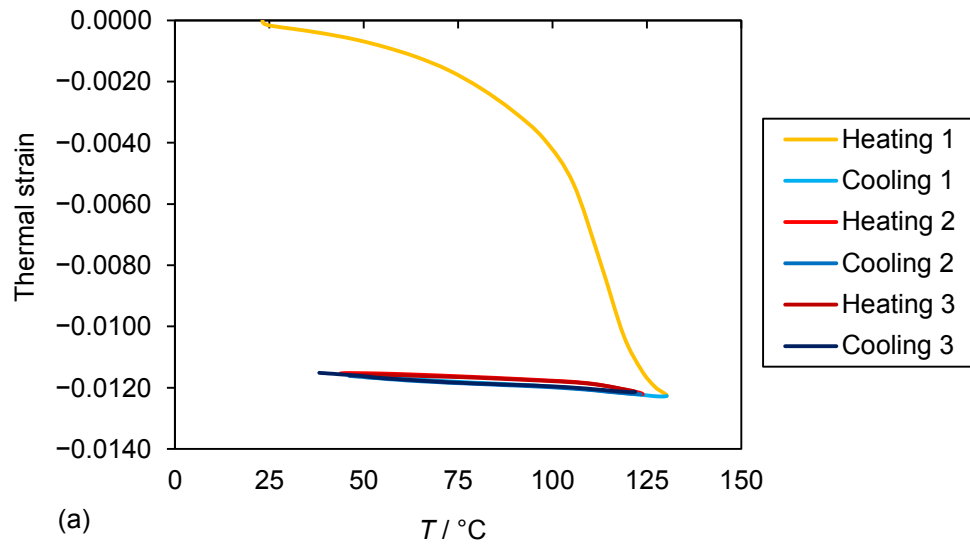
Figure 4.11: Dilatometric heating and cooling curves of the lamellar ZrW_2O_8/PMMA composite. Heating 1, Cooling 1, *etc*. refers to whether the measurement was performed while increasing or decreasing the temperature and the cycle number. A large, irreversible negative thermal strain occurred during the first heating, but subsequently the dilatometric curves were repeatable. (a) Shows overall results, (b) shows a close-up of results after the first heating.
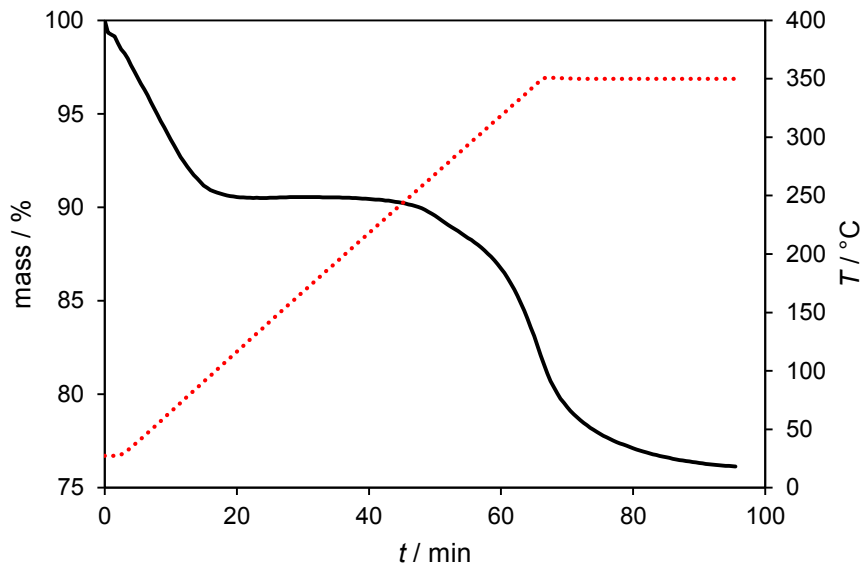
Figure 4.12: TGA thermogram of the ZrW_2O_8/PMMA composite, with mass % shown as (—) and temperature shown as (● ● ●), both as functions of time.

heating between 25 °C and 100 °C, corresponding to the large negative strain seen in this temperature region on the first heating from dilatometry. Given the temperature at which it occurs, the thermal event can be attributed to removal of water from the PMMA and corresponding shrinkage, as PMMA is known to take up water from the atmosphere.[242] Mass loss from 150–250 °C has been reported in bulk PMMA,[241] and was attributed to desorption of solvent. Due to the high surface area of the PMMA in the composite (Figure 4.10), there is the potential for considerable adsorption of water from the atmosphere.

An additional mass loss of 14.4 % from decomposition of PMMA was observed upon heating above 200 °C. This result corresponds to a composition for the composite of 55 vol.% ceramic and 45 vol.% PMMA, following the removal of water.[87,243] Knowledge of the composition of the material allows its thermal expansion to be compared with that predicted by several models. The rule of mixtures (Equation 4.1) predicts a CTE of $\alpha_\ell =$ 34.3 × 10^{-6} K^{-1}, while the Turner model (Equation 4.2) predicts a CTE of $\alpha_\ell = 2.4 \times 10^{-6}$

104

K^{-1},[xiii,] showing the large impact of the different bulk moduli of the components.[244,245] However, the Turner model still did not predict the experimental bulk CTE ($\alpha_\ell = -7.6 \times 10^{-6}$ K^{-1}) accurately. Unlike the materials discussed in Section 4.1 for which the thermal expansion was close to that predicted by the Turner model, the ZrW_2O_8/PMMA composites have an ordered microstructure. Layered composites can display interesting and unusual thermal expansion properties when they are composed of materials of very different stiffnesses and CTEs.[246,247] The CTE of a layered ZrW_2O_8/PMMA composite with the experimental layer dimensions and volume ratios can be predicted using the equations of Lim for stacked laminates.[247] The predicted CTE in the direction perpendicular to the layers is $\alpha_\ell = -25 \times 10^{-6}$ K^{-1}, a much more negative value than the observed $\alpha_\ell = -7.6 \times 10^{-6}$ K^{-1}. However, the observed microstructure differs from a pure layered microstructure because of the presence of many bridges between the lamellae, which would have some effect on the CTE of the bulk composite. The effects of the bridges on the bulk CTE can be approximated by considering the PMMA as cylindrical inclusions in a ZrW_2O_8 matrix. The thermal expansion of such a material can be calculated using the Klemens model for composites with cylindrical inclusions;[248] the result for a 55 vol. % ZrW_2O_8/45 vol. % PMMA composite is $\alpha_\ell = -0.5 \times 10^{-6}$ K^{-1}. Therefore, the observed CTE can be explained by the microstructure being intermediate between alternating layers of ZrW_2O_{12} and PMMA, and cylindrical PMMA inclusions in a ZrW_2O_8 matrix.

[xiii] Material properties used for these calculations: ZrW_2O_8, $\alpha_\ell = -9 \times 10^{-6}$ K^{-1},[127] $K = 75$ GPa,[25] $G = 34$ GPa;[25] PMMA, $\alpha_\ell = 75 \times 10^{-6}$ K^{-1},[242] $K = 12$ GPa,[243] $G = 2$ GPa;[243] ZrO_2, $\alpha_\ell = 7 \times 10^{-6}$ K^{-1},[232] $K = 187$ GPa;[233] WO_3, $\alpha_\ell = 10 \times 10^{-6}$ K^{-1},[244] $K = 45$ GPa.[245] The Lim and Klemens models only accommodate two-component composites so the effect of the ZrO_2 and WO_3 was neglected.

4.2.4. Conclusions

Lamellar ZrW_2O_8, and subsequently a lamellar ZrW_2O_8/PMMA composite, were successfully synthesized. Polymer impregnation of a surface-modified lamellar substrate proved to be an effective way to combine a thermomiotic material and a polymer in a composite. The composite as a whole proved to be thermomiotic, with a large negative CTE in the direction perpendicular to the lamellae. The freeze-casting method used is highly flexible, implying that the thermal expansion and other properties of the composite could be tailorable by modification of the microstructure of the ZrW_2O_8.

Chapter 5: Structure Determination and Properties of the Zero Thermal Expansion Material $ZrMgMo_3O_{12}$[xiv]

5.1. Background

There are two primary ways to use thermomiotic materials to synthesize novel zero thermal expansion materials; the first is to use them in combination with positive thermal expansion materials, *e.g.* in a composite,[122,134,209] as discussed in Chapters 3 and 4. The second is to tailor their structural features chemically in order to produce a material with an intrinsic zero coefficient of thermal expansion.[53,71,72,73,74,75,76,77,78,79,249] The second route avoids potential problems involving thermal expansion mismatch and can, in theory, lead to zero-thermal-expansion materials that would experience no thermal stress. In this chapter it is shown that $ZrMgMo_3O_{12}$ exhibits zero thermal expansion over a wide temperature range, and this exceptional property is related to its structure, as determined by NMR crystallography.

$ZrMgMo_3O_{12}$ belongs to a group of materials that have the general formula AMgM_3O_{12}, where A is a tetravalent cation such as Zr^{4+} or Hf^{4+} and M is Mo^{6+} or W^{6+} (see Section 1.6). These materials typically have low-magnitude CTEs at room temperature.[156,250,251] They are also of interest because of the high ionic conductivity

---

[xiv] This chapter was adapted with permission from Romao, C. P.; Perras, F. A.; Werner-Zwanziger, U.; Lussier, J. A.; Miller, K. J.; Calahoo, C. M.; Zwanziger, J. W.; Bieringer, M.; Marinkovic, B. A.; Bryce, D. L.; White, M. A. *Chem. Mater.* **2015**, *27*, 2633–26476. Copyright 2015 American Chemical Society. The author's contributions to this manuscript included identification of $ZrMgMo_3O_{12}$ as a suitable material for NMR crystallography, synthesis of $ZrMgMo_3O_{12}$, ^{17}O-enriched MoO_3, and ^{17}O-enriched $ZrMgMo_3O_{12}$, dilatometric measurement of the CTE, TGA measurement of the decomposition temperature, DSC measurement of the phase transition temperature, collection of the Raman spectrum, measurement of ionic conductivity, measurement of the bulk elastic constants, analysis of the structure of $ZrMgMo_3O_{12}$ and $A_2M_3O_{12}$ materials from the literature in terms of various quantitative structural parameters and determination of correlations between structure and properties, and writing the relevant sections of the manuscript.

reported for $HfMgW_3O_{12}$.[252,253] AMgM_3O_{12} materials display low-magnitude thermal expansion in an orthorhombic space group, which had previously been determined through indexing analysis to be either $Pna2_1$ or $Pnma$.[91,156] However, no atomic-level crystal structures of AMgM_3O_{12} materials have previously been determined. The absence of structural information has precluded understanding of the mechanisms of thermal expansion in these materials, especially regarding the origins of low-magnitude thermal expansion.

AMgM_3O_{12} materials are related to the $A_2M_3O_{12}$ family of thermomiotic materials, where A is a trivalent cation and M is Mo^{6+} or W^{6+} (see Section 1.6). $A_2M_3O_{12}$ materials display negative or low-positive thermal expansion in the $Sc_2W_3O_{12}$ structure ($Pbcn$ space group),[149] consisting of corner-linked AO_6 octahedra and MO_4 tetrahedra. The unit cell of the $Sc_2W_3O_{12}$ structure contains 68 atoms; this large unit cell, and the great difficulty of producing single crystals from volatile MoO_3 and WO_3 precursors,[1] obfuscates structure determination in $A_2M_3O_{12}$ and AMgM_3O_{12} materials.

Thermal expansivity in $A_2M_3O_{12}$ materials has been shown to correlate negatively with the inherent distortion of the AO_6 polyhedron[45,153] defined as the difference between the volume of the real polyhedron and an ideal polyhedron with the same circumscribed sphere radius.[154] For $A_2M_3O_{12}$ materials for which atomic positions at various temperatures have been reported, the inherent distortion correlates with the derivative of distortion with temperature, and it has been suggested that non-rigidity of coordination polyhedra enhances NTE in the $A_2M_3O_{12}$ structure.[45,46]

Much effort has been expended in recent years towards the goal of solving, or refining, crystallographic structures with the use of solid-state NMR data, sometimes in

combination with theoretical modeling and powder diffraction. This approach has come to be known as NMR crystallography.[254,255] Information concerning the connectivity in zeolites[256,257] and aluminophosphates[258,259,260] has also been used to solve the crystal structure of framework systems *ab initio*. $ZrMgMo_3O_{12}$ is an ideal candidate for such a crystal structure refinement approach as the electric field gradient tensors for all of the nuclei (^{17}O, ^{25}Mg, ^{91}Zr and ^{95}Mo) can be determined experimentally *via* solid-state NMR. NMR spectroscopy has been shown to be particularly useful in helping to elucidate the mechanism responsible for NTE in other materials.[261,262,263,264] Furthermore, as is shown below, $ZrMgMo_3O_{12}$ exhibits zero thermal expansion over a wide temperature range, and the NMR crystallography approach is able to provide a structure that is sufficiently accurate to delineate the origins of the remarkable CTE.

NMR spectroscopy of $ZrMgMo_3O_{12}$ was performed by Frédéric Perras and Dr. David Bryce at the University of Ottawa and by Dr. Ulrike Werner-Zwanziger, Department of Chemistry, at Dalhousie University on samples of $ZrMgMo_3O_{12}$ prepared by the author and Dr. Kimberly Miller. Subsequent refinement of the structure of $ZrMgMo_3O_{12}$ by NMR, XRD and DFT was performed by Frédéric Perras and Dr. David Bryce. Characterization of the intrinsic CTE of $ZrMgMo_3O_{12}$ was performed using variable-temperature XRD at the University of Manitoba by Joey Lussier and Dr. Mario Bieringer. Experimental details for measurements not performed by the author are available in Reference 265.

5.2. Experimental Procedures

5.2.1. Synthesis of $ZrMgMo_3O_{12}$ and ^{17}O-enriched $ZrMgMo_3O_{12}$

$ZrMgMo_3O_{12}$ was synthesized by a solid-state reaction method following the

procedure described in Section 2.1. ZrO_2 (Aldrich, 99 %), $Mg_5(CO_3)_4(OH)_2 \cdot 5H_2O$ (Alfa Aesar, 98 %), and MoO_3 (Sigma-Aldrich, 99.5 %) were used as reagents. Reactive sintering of the pellets for 12 h at 700 °C in air formed $ZrMgMo_3O_{12}$, as confirmed by XRD ($\gtrsim$ 99 % pure) (Siemens D-500 powder diffractometer, pattern collected by Andy George, see Appendix A, Figure A4 for diffractogram). Samples were synthesized using this method for all the reported experiments, except for the ^{17}O NMR studies.

^{17}O-enriched MoO_3 was synthesized by hydrolysis of $MoCl_5$ as a precursor to ^{17}O-enriched $ZrMgMo_3O_{12}$. In a dry N_2 atmosphere in a glove box, 1.7375 g $MoCl_5$ (Alfa Aesar, 99.6 %) was sealed with a magnetic stir bar in a dry round-bottom flask. The flask was then placed in an ice bath on a magnetic stir plate. Using a syringe, 5 mL of CCl_4 was added to dissolve the $MoCl_5$, followed by 0.4958 g of enriched H_2O (Aldrich, 40 to 45 atom % ^{17}O). The reaction was allowed to proceed for 24 h, yielding a green-black solid. The flask was then opened and placed in a sand bath held at 150 °C to evaporate the CCl_4; 1.269 g of solid product was subsequently recovered. This solid was presumed to be a mixture of molybdenum oxides, hydroxides, and chlorides,[266] but was not characterizable from diffraction patterns in the PDF-2 database.[169] To determine the yield of $Mo^{17}O_x$ from the reaction of $MoCl_5$ with $H_2{}^{17}O$, a small portion of the product was held at 500 °C for 3 h in an inert atmosphere to remove the hydroxides and chlorides from the solid, giving a black solid which was identified from XRD by Match! phase analysis software as approximately 67 % MoO_2 and 33 % Mo_4O_{11}.[169] The remaining hydrolysis product was subsequently heated to a temperature of 500 °C for 2 h in air, producing a pale blue-green solid that was confirmed by XRD to be MoO_3. During heating a considerable amount of MoO_x was volatilized, resulting in a yield of 57 % for

this step. The volatility of MoO_3 at 600 °C has been reported to be low (0.1 % h^{-1})[173] in dry atmosphere, but it is enhanced in the presence of water vapour.[173] The ^{17}O-enriched MoO_3 was then mixed with stoichiometric amounts of ZrO_2 (Aldrich, 99 %) and $C_4H_2Mg_5O_{14} \cdot 5H_2O$ (Alfa Aesar, 98 %) and ball-milled for 6 h in a planetary ball mill with polyurethane grinding jars and stabilized zirconia grinding media. Following milling, the precursor powder was pressed into a pellet and calcined in air at 471 °C for 6 h to remove water, CO_2, and any polyurethane, followed by reactive sintering in air at 690 °C for 12 h. The monophasic nature of the resulting $ZrMgMo_3O_{12}$ was confirmed by XRD ($\gtrsim$ 99 % purity) (Siemens D-500 powder diffractometer, collected by Andy George, see Appendix A, Figure A5). The ^{17}O-enriched $ZrMgMo_3O_{12}$ was used only for the ^{17}O NMR experiments.

5.2.2. Characterization

The bulk CTE of $ZrMgMo_3O_{12}$ was measured *via* dilatometry (see Section 2.3.1). The measurements were performed from room temperature to 700 °C at a heating rate of 10 K min^{-1}, and at a natural cooling rate of approximately 5 K min^{-1}.

DSC was used to delineate any phase transitions in $ZrMgMo_3O_{12}$ with a 20.43 mg sample in an aluminum pan using a TA Instruments Q200 series DSC equipped with a liquid N_2 cooling head. Michel Johnson, Dalhousie University, assisted with the measurements. The temperature range studied was −175 °C to 35 °C with a temperature ramp rate of 5 K min^{-1}. The instrument was calibrated using a 5.12 mg sample of indium in an aluminum pan. Measurements were performed under He purge gas.

TGA was performed on a 21.74 mg sample of $ZrMgMo_3O_{12}$ to determine whether the material had taken up water from the atmosphere, and to determine its decomposition

temperature. The sample was heated at a rate of 20 K min^{-1} from room temperature to 500 °C and at a rate of 10 K min^{-1} from 500 °C to 900 °C (see Section 2.3.2).

The Raman spectrum of $ZrMgMo_3O_{12}$, with a spectral resolution of 1 cm^{-1}, was collected at room temperature (see Section 2.6).

The mechanical properties of $ZrMgMo_3O_{12}$ were determined by measurement of the transverse and longitudinal velocities of sound at room temperature (see Section 2.5).

The electrical impedance of $ZrMgMo_3O_{12}$ was determined using a Solartron SI 1260 Impedance/Gain Phase analyser to assess ionic conductivity. AC impedance of a sintered pellet (12.67 mm diameter, 1.75 mm height) was measured using Pyroduct 597-A electrodes over a temperature range from 340 °C to 520 °C in air. The experimental setup used to perform the AC impedance measurements at elevated temperatures was developed by Courtney Calahoo, Dalhousie University. The AC impedance was measured while decreasing the frequency from 3 MHz to 100 Hz, with an amplitude of three different values, 50 mV, 75 mV and 100 mV, to check that the response was linear. The instrumental setup was validated by measuring the ionic conductivity (κ_e) of $Sc_2W_3O_{12}$ in comparison with a literature value from Reference 267 (Figure 5.1). At this point a number of discrepancies in the literature were discovered. The conductivity reported for $Sc_2W_3O_{12}$ in Reference 267 is consistent with that reported in Reference 268, but not with that in an earlier paper, Reference 269, despite these papers sharing many of the same authors. The discrepancy is obscured by a switch from displaying the data as $\log_{10}(\kappa_e T)$ to $\log_{10}(\kappa_e)$. Additionally, while the data shown in Figure 5.1 matches the data in References 267 and 268, the activation energy calculated from Figure 5.1 (90 kJ mol^{-1}) does not match the reported value (44 kJ mol^{-1}). This is most likely due to an error in
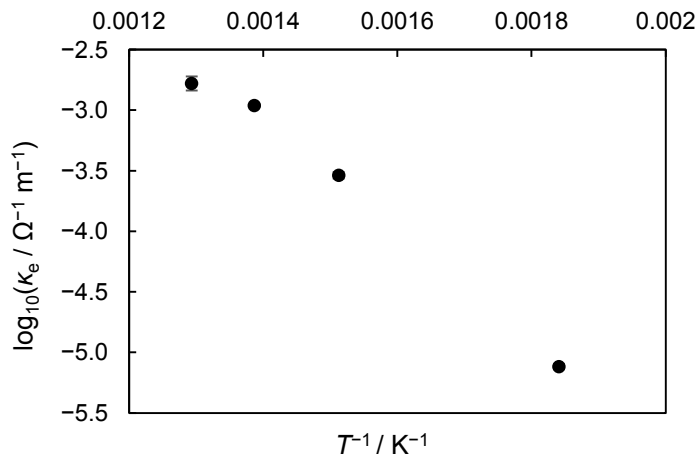
Figure 5.1: Ionic conductivity (κ_e) of $Sc_2W_3O_{12}$ (plotted on a logarithmic scale), reported here to validate the measurement apparatus (*cf.* Reference 267).

calculating the activation energy, specifically using the slope of a plot of $\log_{10}(\kappa_e T)$ *vs.* T^{-1} rather than $\ln(\kappa_e T)$ *vs.* T^{-1}. Correcting for this apparent error would lead to a literature value for the activation energy of 101 kJ mol^{-1}. Attempts to measure the conductivity of $HfMgW_3O_{12}$ for comparison with Reference 252 resulted in sample decomposition as a result of application of the AC voltage.

5.3. Results and Discussion

5.3.1. Phase Stability

DSC of $ZrMgMo_3O_{12}$ showed a solid-solid phase transition at $-126\ ^\circ C$ upon heating and an enthalpy change, ΔH, of 195 J mol^{-1} (Figure 5.2). Based on the phase transition in $HfMgMo_3O_{12}$ at $-98\ ^\circ C$,[270] and solid-solid transitions in many $A_2M_3O_{12}$ materials (see Section 1.6), $ZrMgMo_3O_{12}$ is likely in a monoclinic $P2_1/a$ phase (with positive thermal expansion; *vide infra*) below $-126\ ^\circ C$. To determine the upper temperature limit of phase stability, TGA was performed (Figure 5.3), showing decomposition beginning at *ca.* 750 $^\circ C$. This information indicates a broad temperature range of stability for the orthorhombic phase of $ZrMgMo_3O_{12}$ ($-126\ ^\circ C$ to 700 $^\circ C$).

113
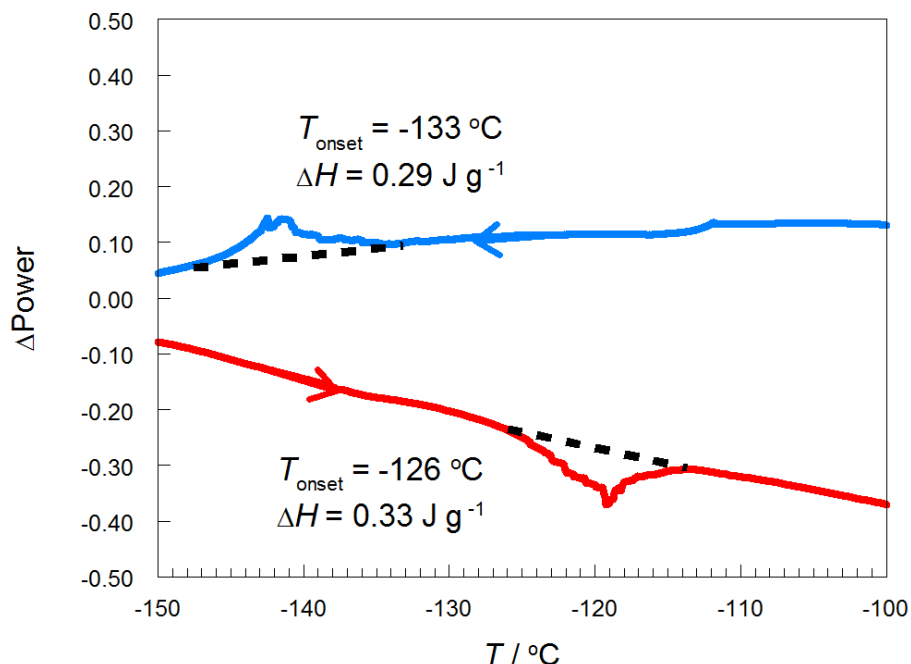
Figure 5.2: DSC thermogram of $ZrMgMo_3O_{12}$ (exotherm up) with cooling/heating direction, onset temperatures, peak temperatures, and transition enthalpy changes (ΔH) shown. The DSC curves did not show any additional thermal events in the temperature range −160 to 30 °C.
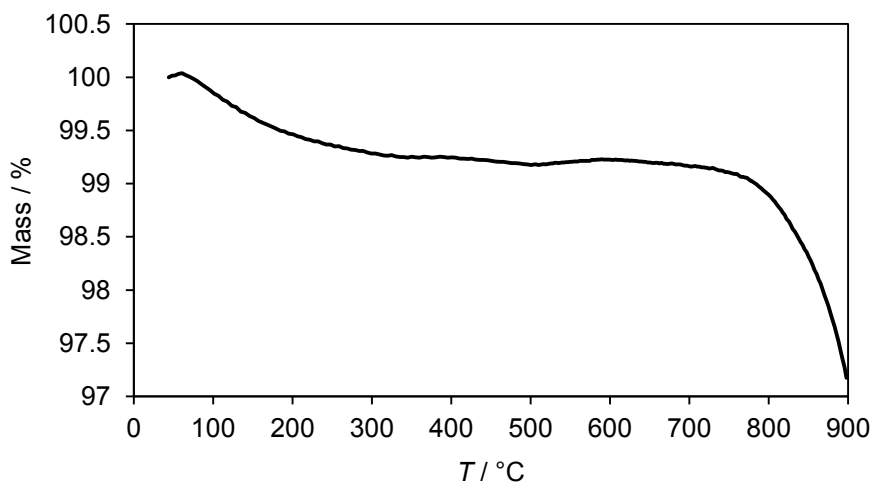
Figure 5.3: TGA thermogram of $ZrMgMo_3O_{12}$. Mass loss due to water from the atmosphere is very low, < 1 %, showing that it is not very hygroscopic. Decomposition into constituent oxides (followed immediately by sublimation of MoO_3, which is reflected in the thermogram) begins at approximately 750 °C.

5.3.2. Thermal Expansion

Dilatometric curves for $ZrMgMo_3O_{12}$ on cooling are shown in Figures 5.4, 5.5, and 5.6. Often, the first heating curve is less representative of the CTE than the cooling
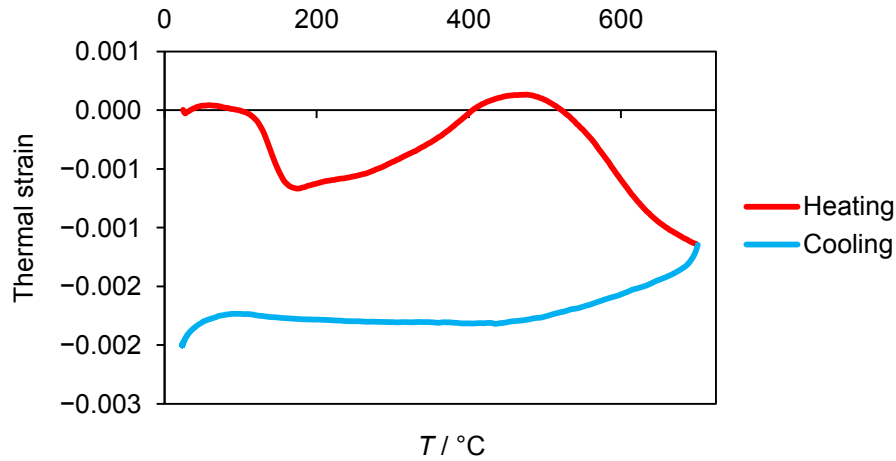
Figure 5.4: A dilatometric heating and cooling curve of a ZrMgMo$_3$O$_{12}$ sample, showing the change in length with respect to the original length as a function of temperature. "Heating" and "Cooling" refer to whether the sample temperature was being increased or decreased during the measurement. The CTE as determined *via* linear regression on cooling from 23 °C to 500 °C is $\alpha_\ell = 0.41 \times 10^{-6}\,\text{K}^{-1}$. This dilatometric curve was acquired at Dalhousie University. Adapted from Reference 265 with permission.
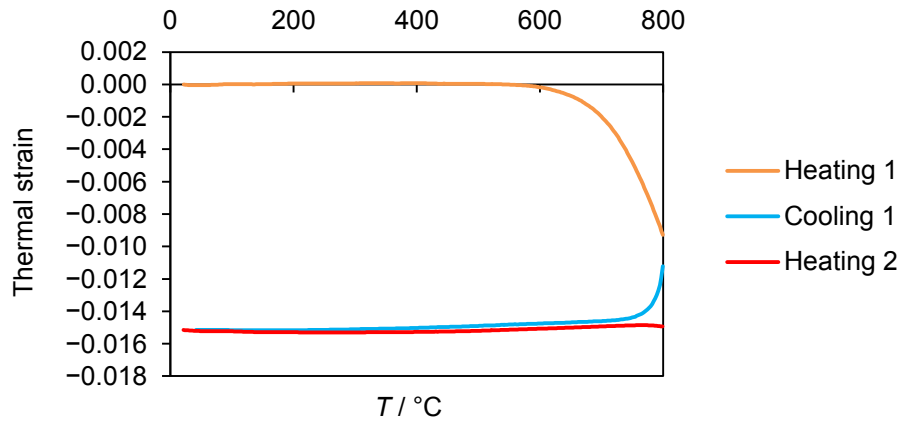
Figure 5.5: A dilatometric heating and cooling curve of another ZrMgMo$_3$O$_{12}$ sample, showing the change in length with respect to the original length as a function of temperature. In this case, data from the second cooling run were lost due to a power failure. The CTE was determined *via* linear regression from the first heating curve from 30 °C to 600 °C as $\alpha_\ell = -0.01 \times 10^{-6}\,\text{K}^{-1}$, from the first cooling curve from 30 °C to 700 °C as $\alpha_\ell = 0.9 \times 10^{-6}\,\text{K}^{-1}$ and from the second heating curve from 30 °C to 700 °C as $\alpha_\ell = 0.4 \times 10^{-6}\,\text{K}^{-1}$. This dilatometric curve was acquired at PUC-Rio by Dr. Bojan Marinkovic.
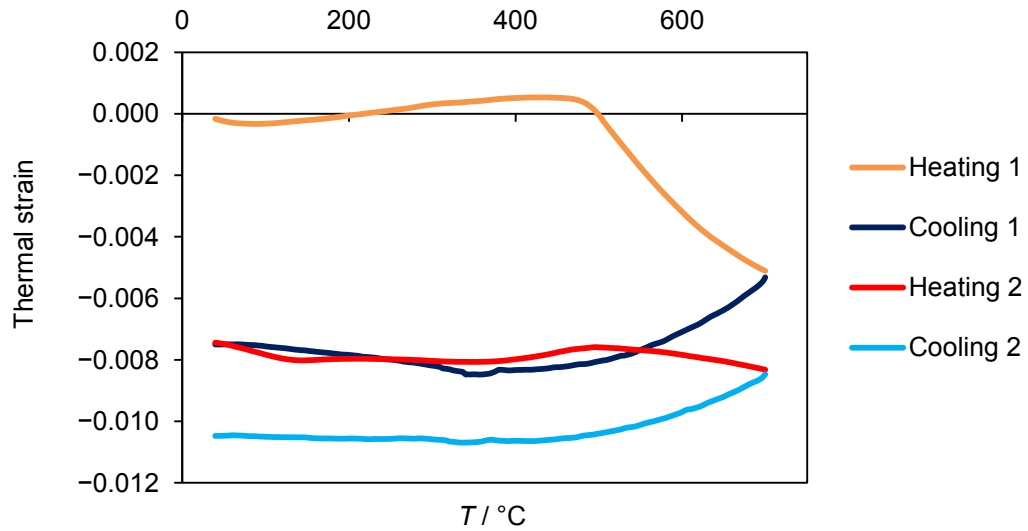
Figure 5.6: A dilatometric heating and cooling curve of a third $ZrMgMo_3O_{12}$ sample, made in a separate synthesis, showing the change in length with respect to the original length as a function of temperature. The measurement was considerably affected by microcrack healing and formation during the first heating. The CTE was determined *via* linear regression from the first cooling curve from 30 °C to 500 °C as $\alpha_\ell = -2 \times 10^{-6}$ K^{-1}, from the second heating curve as $\alpha_\ell = -1 \times 10^{-6}$ K^{-1} and from the second cooling curve from 30 °C to 400 °C as $\alpha_\ell = -0.5 \times 10^{-6}$ K^{-1}. This dilatometric curve was acquired at PUC-Rio by the author and Dr. Kimberly Miller.

curve or subsequent heating curves, as the first heating curve is influenced the most by microcrack healing in the sample and desorption of surface water on the alumina pushrod. These effects are especially prominent here because of the low intrinsic thermal expansivity of $ZrMgMo_3O_{12}$. The bulk CTE of polycrystalline $ZrMgMo_3O_{12}$ is remarkably small, with an average value of $\alpha_\ell = (-0.3 \pm 0.1)^{xv} \times 10^{-6}$ K^{-1} from 23 °C to 500 °C, based on seven runs on three samples. From 500 °C to 700 °C the bulk CTE is dominated by extrinsic, microstructural effects (microcrack healing upon heating and microcrack formation on cooling).

---

xv Uncertainty reported at the 95% confidence level.

The intrinsic CTE of $ZrMgMo_3O_{12}$, as determined from variable-temperature XRD (see Reference 265 for details), is very close to zero between 25 °C and 450 °C during heating ($\alpha_\ell = (0.17 \pm 0.02)^{xvi} \times 10^{-6}$ K^{-1}) and cooling ($\alpha_\ell = (0.15 \pm 0.03) \times 10^{-6}$ K^{-1}). By comparison, the CTEs of traditional oxide ceramics are typically 1.5 to 2 orders of magnitude larger than that of $ZrMgMo_3O_{12}$ in this temperature range.[271,272] The magnitude of the CTE of $ZrMgMo_3O_{12}$ is lower across this temperature range than that of many commonly used zero thermal expansion materials such as fused quartz and Invar; it is also lower than that of several zero thermal expansion materials which have recently been reported in the literature.[53,70,73,74,75,76,77,273] Above 450 °C the linear thermal expansion coefficient increases by almost an order of magnitude with values of $\alpha_\ell = (0.9 \pm 0.3) \times 10^{-6}$ K^{-1} and $\alpha_\ell = (1.0 \pm 0.3) \times 10^{-6}$ K^{-1} during heating and cooling, respectively.[265] The CTE in this temperature range is still quite low by comparison to conventional materials, however.[271,272] The CTE for $ZrMgMo_3O_{12}$ reported herein is considerably closer to zero than was reported by Song et al.,[251] and the results here are corroborated by the CTE as measured by variable-temperature X-ray diffraction over a much larger set of temperature points,[265] and by dilatometric (Figure 5.6) and variable-temperature X-ray diffraction results on a second sample of $ZrMgMo_3O_{12}$ made in a separate synthesis.[265]

Axial CTEs, measured upon heating, are $\alpha_a = (-2.5 \pm 0.2) \times 10^{-6}$ K^{-1}, $\alpha_b = (-4.7 \pm 0.2) \times 10^{-6}$ K^{-1}, and $\alpha_c = (7.6 \pm 0.2) \times 10^{-6}$ K^{-1} from 25°C to 450°C.[265] From 450 °C to 650 °C the axial CTEs are $\alpha_a = (-0.5 \pm 0.2) \times 10^{-6}$ K^{-1}, $\alpha_b = (-2.5 \pm 0.2) \times 10^{-6}$ K^{-1}, and

---

[xvi] Uncertainties reported at the 95% confidence level.

$\alpha_c = (5.8 \pm 0.2) \times 10^{-6}$ K^{-1}.[265] Because the CTE of ZrMgMo$_3$O$_{12}$ is anisotropic, bulk samples could experience thermal stress and microcracking upon heating and cooling (see Chapter 9). However, thermal cycling results (Figures 5.5 and 5.6.) indicate reduced microcracking effects after the first heating. An important measure of an orthotropic material's propensity for thermal stress is the CTE anisotropy, quantified as $\Delta\alpha_{max}$ (the maximum difference between two axial CTEs). For ZrMgMo$_3$O$_{12}$ between 25 °C and 450 °C, $\Delta\alpha_{max} = 12 \times 10^{-6}$ K^{-1}, a value slightly higher than reported for orthorhombic In(HfMg)$_{0.5}$Mo$_3$O$_{12}$, In$_2$Mo$_3$O$_{12}$, and HfMgMo$_3$O$_{12}$;[76] $\Delta\alpha_{max}$ for ZrMgMo$_3$O$_{12}$ decreases to 8.3×10^{-6} K^{-1} over the temperature range 450 °C to 650 °C.

The intrinsic (X-ray derived) thermal expansion coefficients[265] agree qualitatively with the dilatometry results. Both data sets show only very small volume changes from room temperature up to approximately 450 °C and larger expansion at higher temperatures. Notably the dilatometric data indicate a very small negative expansion coefficient up to 450 °C, whereas the intrinsic expansion coefficient is also small but positive. The difference suggests that microstructural effects influence the bulk CTE.

5.3.3. Mechanical Properties

Mechanical properties of thermomiotic and near-zero CTE materials are very important in determining their suitability for potential applications, whether they are to be used in bulk form or incorporated in a composite, because they influence the thermal stresses experienced and the degree to which positive thermal expansion can be counteracted (see Chapters 3 and 4). The transverse and longitudinal velocities of sound of ZrMgMo$_3$O$_{12}$, corrected to zero porosity (see Appendix B for uncorrected data), were determined here as $v_t = 2624 \pm 63$ m s^{-1} and $v_l = 4314 \pm 58$ m s^{-1} (uncertainties based on

three samples), which correspond to a bulk modulus of 31 ± 3 GPa and a shear modulus of 22 ± 1 GPa, both quite low in comparison to conventional oxide ceramics. Low stiffness is common to many thermomiotic materials (see Section 1.3.2.3).

5.3.4. Structure Determination

The above findings of zero thermal expansion in $ZrMgMo_3O_{12}$ can only be fully understood with detailed knowledge of its structure. However, it was not possible to grow single crystals of $ZrMgMo_3O_{12}$. Furthermore, although the powder diffraction approach can, in principle, resolve unknown crystal structures *ab initio*, powder diffraction experiments using synchrotron x-ray[156] and neutron[157] sources were unable to delineate the crystal structures, or even the space groups, of the related phases $HfMgMo_3O_{12}$ and $HfMgW_3O_{12}$. Therefore, an alternate structure-determination approach, NMR crystallography, was taken. The NMR-refined crystal structure obtained from this method is similar in quality to what can be obtained using single-crystal X-ray diffraction.[265] The NMR-refined structure is shown in Figure 5.7, and the fractional coordinates for the atoms are given in Table 5.1. The space group was determined to be *Pna*2_1, a subgroup of *Pbcn*. The connectivity of the coordination polyhedra in this structure is analogous to that in the structure of $Sc_2W_3O_{12}$[277] and features ordering of the Mg and Zr cations, suggesting that $ZrMgMo_3O_{12}$ could have high ionic conductivity similar to that of $HfMgW_3O_{12}$.[252]
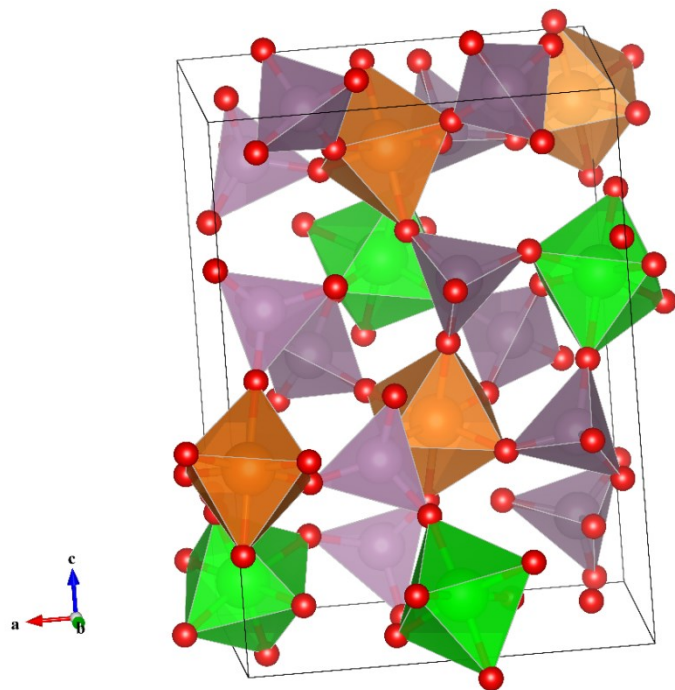
Figure 5.7: The NMR-refined structure of ZrMgMo$_3$O$_{12}$. O atoms are shown in red, MgO$_6$ coordination polyhedra in orange, ZrO$_6$ in green, and MoO$_4$ in purple. An alternative view, showing the alignment of Mg^{2+} along [110] is shown in Figure 5.11. Adapted from Reference 265 with permission.

Table 5.1: Fractional coordinates for the atoms in the NMR-refined structure of ZrMgMo$_3$O$_{12}$, at room temperature.

Atom	x	y	z	Multiplicity and Wyckoff letter
Zr1	0.0361	0.4975	0.6156	4a
Mg1	0.4628	0.5000	0.3732	4a
Mo1	0.7485	0.2766	0.4844	4a
Mo2	0.1303	0.6607	0.3510	4a
Mo3	0.6105	0.3623	0.1410	4a
O1	0.1065	0.8418	0.3548	4a
O2	0.8772	0.3912	0.5407	4a
O3	0.0227	0.5846	0.2526	4a
O4	0.3243	0.3357	0.3961	4a
O5	0.0870	0.5858	0.4722	4a
O6	0.3052	0.6306	0.3248	4a
O7	0.4953	0.4392	0.2260	4a
O8	0.5756	0.4293	0.0207	4a
O9	0.1691	0.3277	0.5829	4a
O10	0.6206	0.3740	0.4238	4a
O11	0.2116	0.5984	0.6752	4a
O12	-0.0857	0.6742	0.6410	4a

5.3.5. Phonon Modes

As an additional step in validating the structure, and in consideration of the importance of dynamics[1,45,274,275] in framework materials, the Γ-point optic phonon frequencies were calculated using CASTEP by Frédéric Perras (see Appendix C). The calculated Γ-point optic phonon frequencies of $ZrMgMo_3O_{12}$, compared to those previously reported for $Y_2Mo_3O_{12}$, show an increased number of modes below 50 cm^{-1} but otherwise a general increase in mode energies.[274]

All of the $ZrMgMo_3O_{12}$ modes are Raman-active, and therefore the calculated modes can be compared to experiment (Figure 5.8). Approximate assignments of vibrational modes are based on studies of $Y_2Mo_3O_{12}$ and $Al_2W_3O_{12}$.[180,181] Of special interest are the modes below about 200 cm^{-1}, which include the librational and translational optic modes that have been related to polyhedral rotations and NTE (see Section 1.2.1). The low-energy modes in $ZrMgMo_3O_{12}$ have similar relative intensities to what was observed for $Al_2W_3O_{12}$,[181] but have much higher relative intensities than for $Y_2Mo_3O_{12}$.[181] The similarity of the Raman spectra of $ZrMgMo_3O_{12}$ and $A_2M_3O_{12}$ materials suggests similar dynamics and potentially a similar mechanism of thermal expansion reduction. The calculated Raman-active modes replicate the observed librational, translational, and bending mode energies well, but predict a smaller spread of stretching-mode energies than observed.
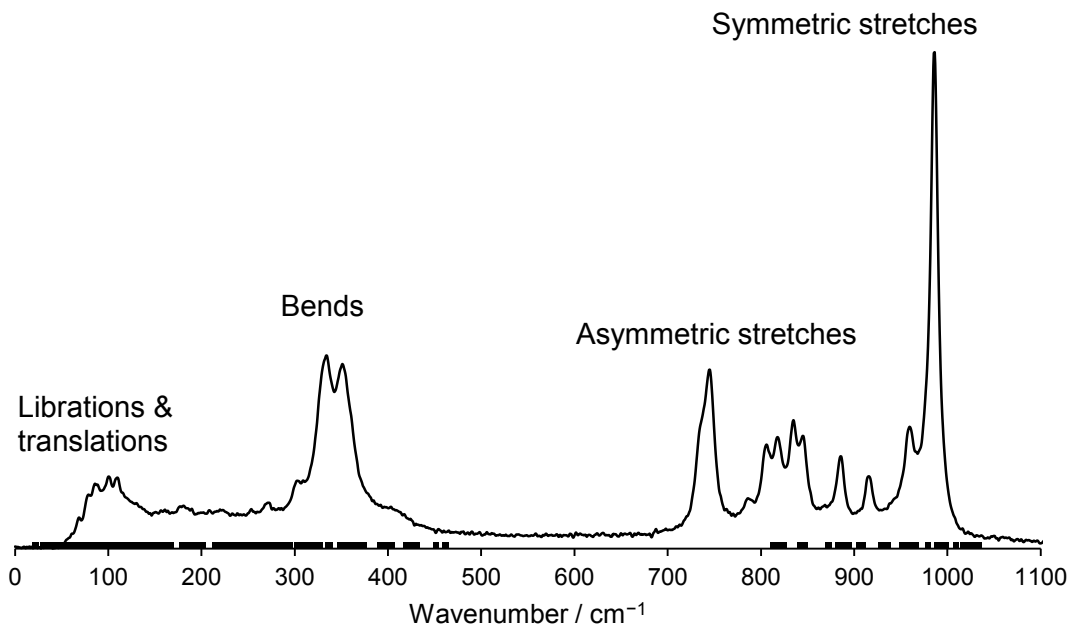
Figure 5.8: The experimentally-determined Raman spectrum of $ZrMgMo_3O_{12}$. Calculated Γ-point optic phonon frequencies are shown as (▪). Adapted from Reference 265 with permission.

5.3.6. Conductivity

$ZrMgMo_3O_{12}$ shows significant conductivity, 4.1×10^{-4} Ω^{-1} m^{-1} at 520 °C (see Figures 5.9 and 5.10); this level of conductivity in an insulating solid indicates a considerable ionic conductivity, as was previously reported in the structurally related material $HfMgW_3O_{12}$,[252] although several orders of magnitude less than fast ionic conductors.[276] The Nyquist plots (Figure 5.9) indicate only one time constant, consistent with a single species as the major contributor to the conductivity. Ionic conductivity is not surprising given the crystal structure; if the Mg^{2+} ions are mobile the structure can be viewed as a network of ZrO_6 and MoO_4 polyhedra with Mg^{2+} in cavities that are connected along several directions (Figure 5.11). The conductivity of $ZrMgMo_3O_{12}$ is significantly lower than was reported for $HfMgW_3O_{12}$;[252] it falls within the range of
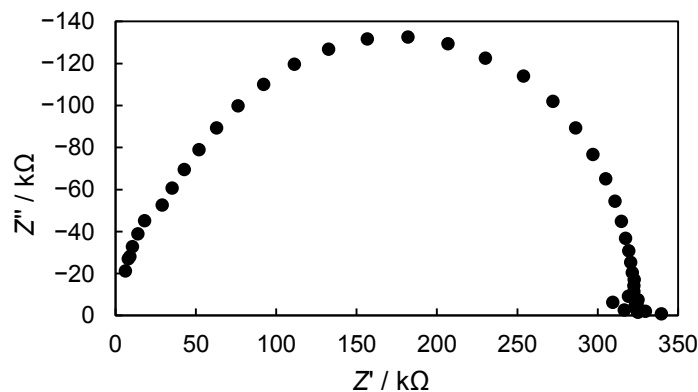
Figure 5.9: Nyquist plot of the real (Z') and imaginary (Z'') components of the impedance of $ZrMgMo_3O_{12}$, measured at 400 °C.
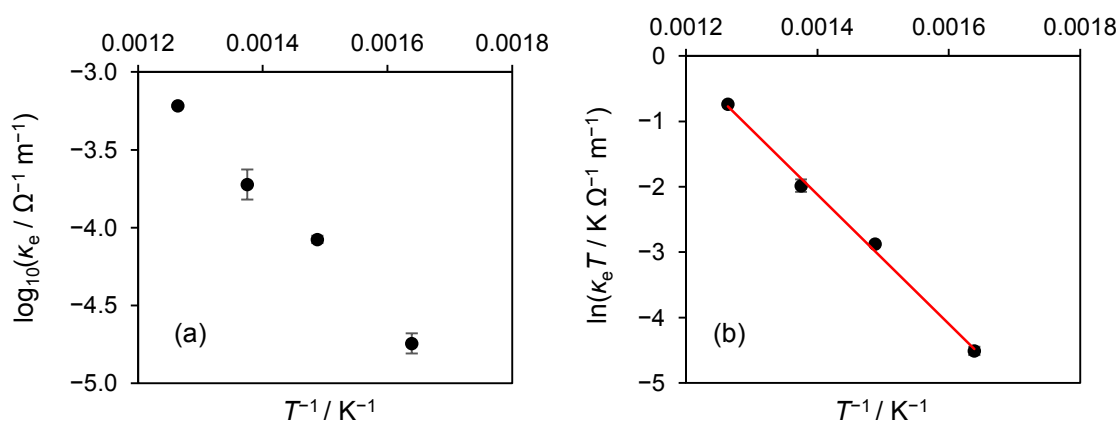
Figure 5.10: Ionic conductivity, κ_e, of $ZrMgMo_3O_{12}$ (a) plotted on a logarithmic scale and (b) as $\ln(\kappa_e T)$. The correlation coefficient relating $\ln(\kappa_e)$ to T^{-1} is smaller than that relating $\ln(\kappa_e T)$ to T^{-1} (0.9959 vs. 0.9965), supporting the assertion that conductivity in $ZrMgMo_3O_{12}$ is ionic. The derivative of $\ln(\kappa_e T)$ with respect to T^{-1} is equal to the activation energy (82 kJ mol^{-1}) divided by the gas constant, R.[252]

conductivities of A^{3+} ions in $A_2M_3O_{12}$ materials such as $Al_2W_3O_{12}$ and $Sc_2Mo_3O_{12}$.[267] The activation energy for ionic conductivity in $ZrMgMo_3O_{12}$ was determined to be 82 kJ mol^{-1} (Figure 5.10) which is close to that of $HfMgW_3O_{12}$ (80.6 kJ mol^{-1})[252] and the fast ion conductor $LiAlSiO_4$ (81 kJ mol^{-1}).[276]
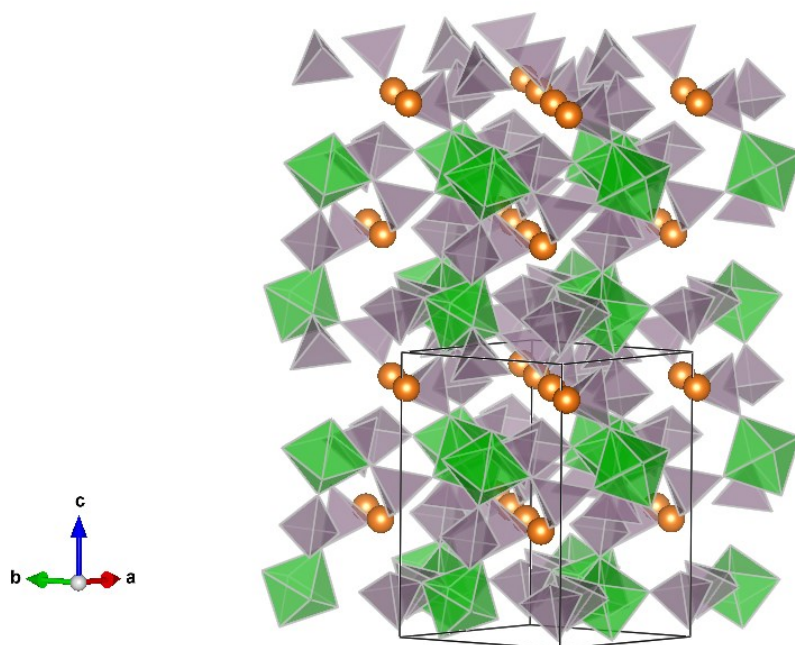
Figure 5.11: The NMR-refined structure of $ZrMgMo_3O_{12}$, with a view emphasizing the positions of the Mg^{2+} cations (orange spheres), with MoO_4 tetrahedra shown in purple and ZrO_6 octahedra shown in green.

5.3.7. Correlation of Structure and Properties

The orthorhombic $Pna2_1$ structure of $ZrMgMo_3O_{12}$ (Figure 5.7) is related to the $Pbcn$ $Sc_2W_3O_{12}$ structure with the Zr^{4+} and Mg^{2+} ions associated with the Sc^{3+} sites. In this section, structure and bonding features of all orthorhombic $A_2M_3O_{12}$ structures of sufficient quality from the literature are compared to $ZrMgMo_3O_{12}$. Sources of structural data and CTEs are given in Table 5.2.

The reduction in symmetry from $Pbcn$ (space group number 60) to $Pna2_1$ (space group number 33) leads to the addition of one crystallographically distinct Mo site and six O sites, as well as the splitting of the A site into a Zr site and a Mg site. This in turn allows a greater variation in the distribution of M-O-A angles compared to the $Pbcn$ orthorhombic phases of $A_2M_3O_{12}$ materials (Figure 5.12). The M-O-A bond angle distribution of $ZrMgMo_3O_{12}$ is the broadest yet reported for this family of materials. Not

Table 5.2: Intrinsic CTEs and structures from the literature of materials in the orthorhombic *Pbcn* $Sc_2W_3O_{12}$ structure and $ZrMgMo_3O_{12}$.

Material	α_ℓ / 10^{-6} K^{-1}	Range of measurement of α_ℓ / °C	Structure determination method	References
$Al_2Mo_3O_{12}$	2.4	250 to 650	Neutron powder diffraction	140, 159
$Al_2W_3O_{12}$	2.1	50 to 550	Neutron powder diffraction	203, 220
$Fe_2Mo_3O_{12}$	1.8	550 to 750	Neutron powder diffraction	140, 159
$Cr_2Mo_3O_{12}$	0.7	400 to 750	Synchrotron XRD	159
$ZrMgMo_3O_{12}$	**0.16**	**25 to 450**	**NMR crystallography**	**Current work**
$In_2Mo_3O_{12}$	−1.9	370 to 760	Synchrotron XRD	153
$Sc_2Mo_3O_{12}$	−2.1	−93 to 27	Single-crystal XRD	150, 277
$Sc_2W_3O_{12}$	−2.2	−263 to 176	Single-crystal XRD	149, 277
$Lu_2Mo_3O_{12}$	−6.0	25 to 700	Synchrotron XRD	146, 278
$Y_2W_3O_{12}$	−7.0	20 to 800	Neutron powder diffraction	220
$Er_2Mo_3O_{12}$	−7.6	25 to 700	Synchrotron XRD	146, 278
$Y_2Mo_3O_{12}$	−9.0	−263 to 176	Synchrotron XRD	45

all of the materials in this family follow the same trend regarding average *M*-O-*A* bond angle, but they can be separated into three groups of materials with similar properties (Figure 5.12). The average *M*-O-*A* angles of the molybdate $A_2M_3O_{12}$ materials and $ZrMgMo_3O_{12}$ are remarkably consistent; all fall within 1.5° of 156.6°. By contrast, the $A_2W_3O_{12}$ materials trend towards increasing average *M*-O-*A* angle with increasingly negative thermal expansion. The $A_2Mo_3O_{12}$ materials that are orthorhombic at room temperature (Figure 5.12(a)) show decreasing *M*-O-*A* angle spread with increasing NTE, while those that are monoclinic at room temperature (Figure 5.12(b)) show relatively consistent angles with changing CTE. The high *M*-O-*A* angle range for $ZrMgMo_3O_{12}$ correlates with both its low orthorhombic-monoclinic phase transition temperature and its zero thermal expansion.

Inherent distortions (*i.e.*, distortions at the lowest temperature where data are available, see Equation 1.17) of AO_6 polyhedra in $ZrMgMo_3O_{12}$ and $A_2M_3O_{12}$ materials, as calculated by IVTON,[279] are shown in Figure 5.13. The negative correlation of the

125
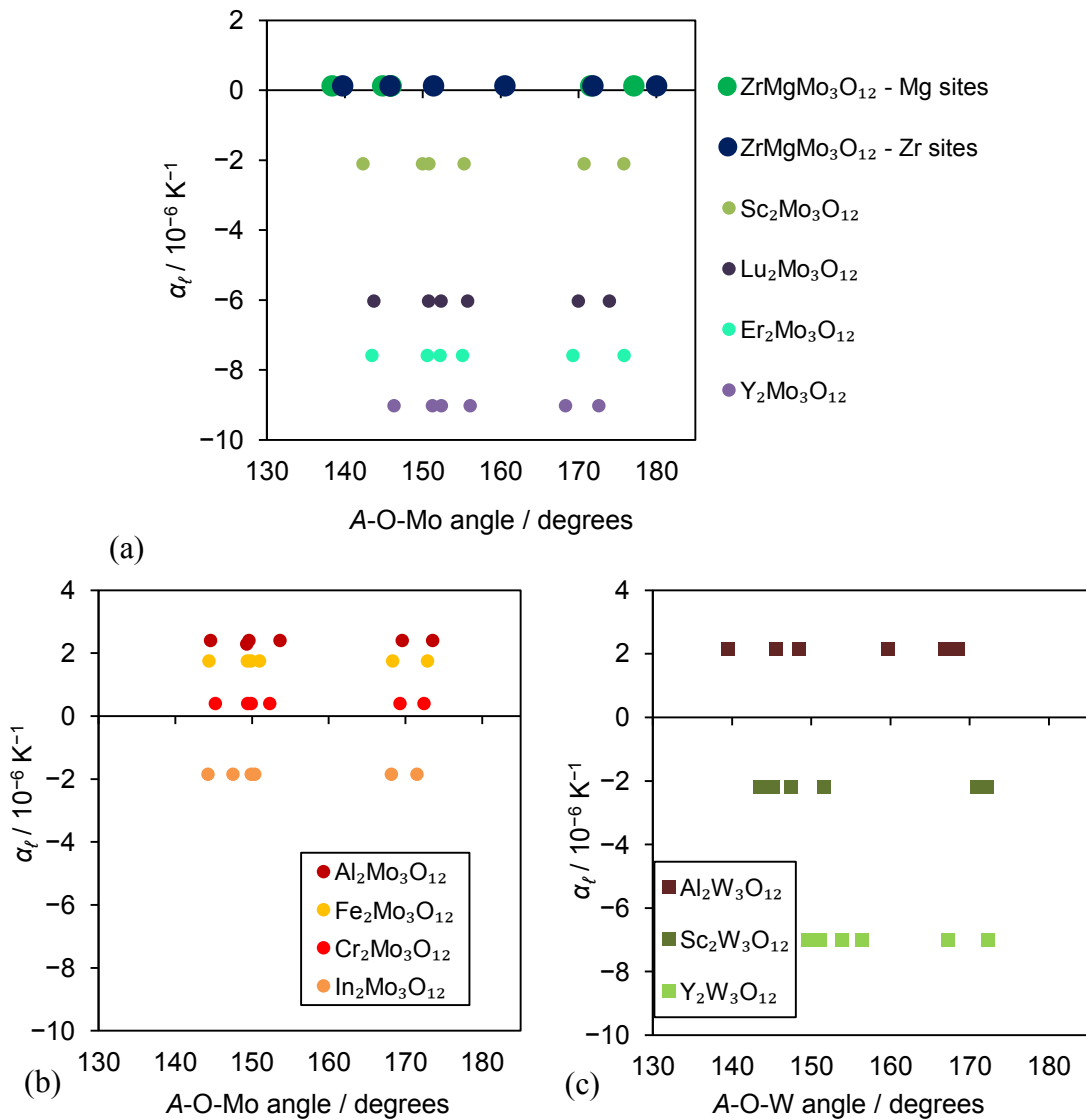
Figure 5.12: Correlation of CTE in the orthorhombic phase of $A_2Mo_3O_{12}$ materials with M-O-A/Mg bond angles for (a) $A_2Mo_3O_{12}$ materials which exist in an orthorhombic phase at room temperature, (b) $A_2Mo_3O_{12}$ materials which undergo a phase transition into their orthorhombic phase above room temperature, and (c) $A_2W_3O_{12}$ materials (all of which are stable in an orthorhombic phase at room temperature). Information for $A_2M_3O_{12}$ materials was taken from the literature; see Table 5.2 for references. Adapted from Reference 265 with permission.

CTE with polyhedral distortion is clearly visible for the $A_2Mo_3O_{12}$ materials, while the

average distortion value for ZrO_6 and MgO_6 polyhedra is higher than would be expected

from its CTE, as the average distortion value is close to that of $Sc_2Mo_3O_{12}$. The MgO_6

octahedron has an inherent distortion close to what would be expected from the CTE.
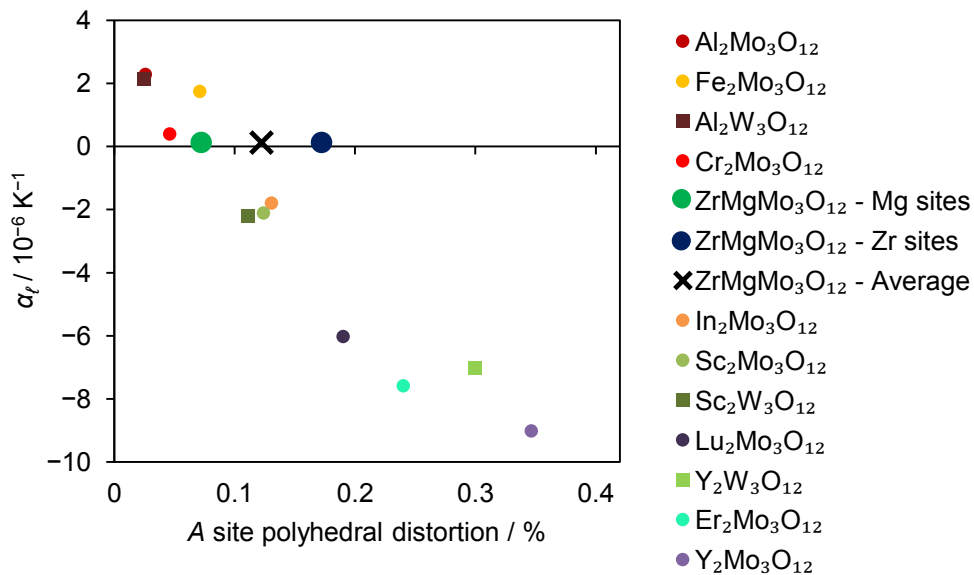
Figure 5.13: Coefficients of thermal expansion as a function of inherent polyhedral (AO_6) distortion in $ZrMgMo_3O_{12}$ (large symbols) and $A_2M_3O_{12}$ materials. Structural information regarding $A_2M_3O_{12}$ materials was taken from the literature; see Table 5.2 for references. Adapted from Reference 265 with permission.

AO_6 distortion in $ZrMgMo_3O_{12}$ is largely related to variance of the O-A-O angles within the octahedra, as is common in $A_2M_3O_{12}$ materials (Figure 5.14). To determine the causes of zero thermal expansion in $ZrMgMo_3O_{12}$ one must consider both the origins of the polyhedral distortion in $ZrMgMo_3O_{12}$ and how much the polyhedra would be expected to distort with increasing temperature.

Polyhedral distortion in $A_2M_3O_{12}$ materials is generally correlated with the Shannon ionic radius[138] of the A cation, as shown in Figure 5.15, with larger cations permitting and/or causing larger polyhedral distortions. However, Zr^{4+} and Mg^{2+} have nearly identical radii yet very different levels of polyhedral distortion, with Mg^{2+} close to the trend for $A_2M_3O_{12}$ materials. A very large inherent distortion (19.8 %) in ZrO_6 octahedra was found in ZrW_2O_8,[45] but this distortion is essentially static and the NTE mechanism in ZrW_2O_8 does not involve distortion of the rigid polyhedra. It is therefore
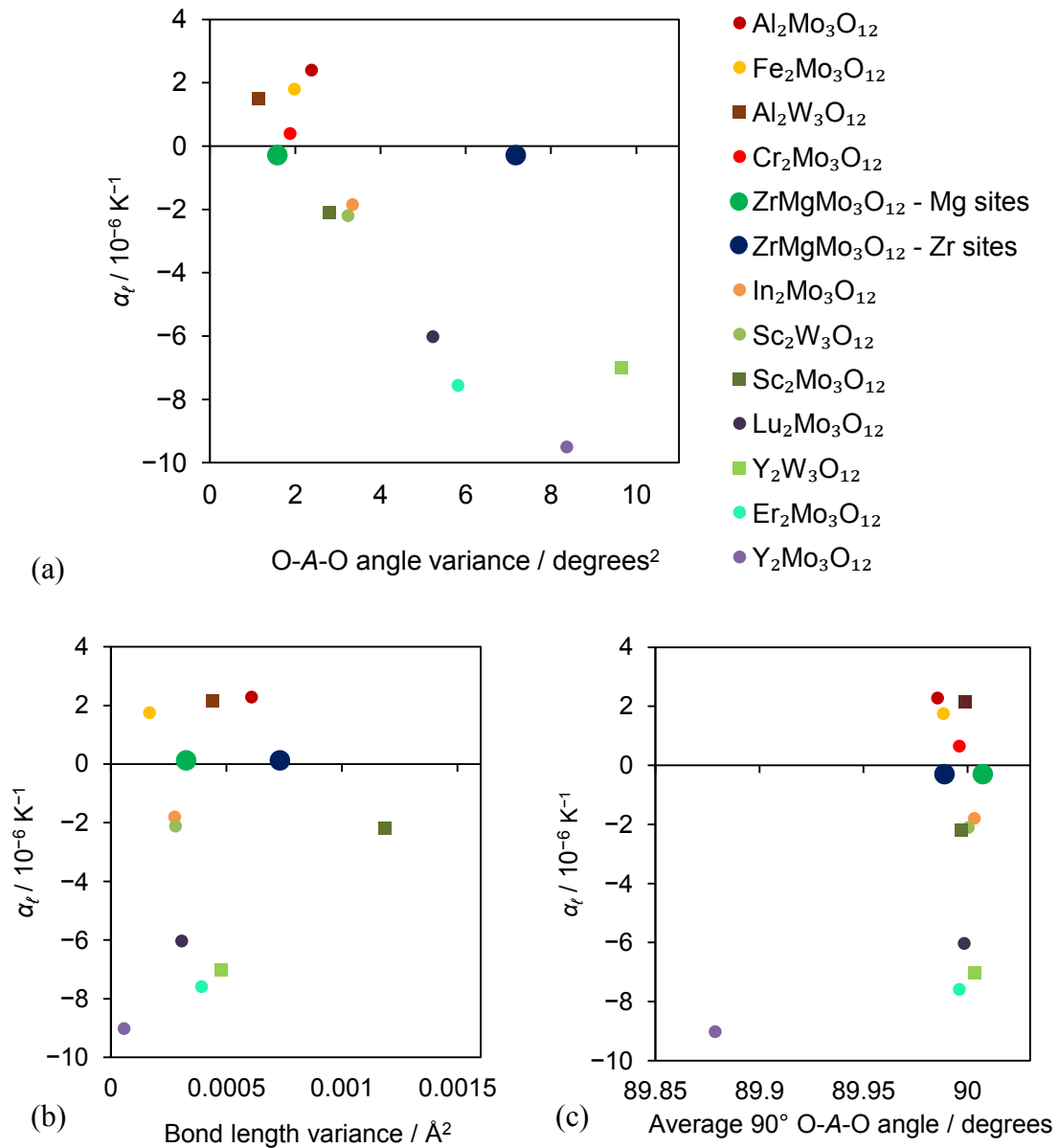
Figure 5.14: Coefficients of thermal expansion of $ZrMgMo_3O_{12}$ (large symbols) and $A_2M_3O_{12}$ materials compared to three causes of polyhedral distortion: (a) O-*A*-O angle variance, (b) bond length variance, and (c) the average 90° O-*A*-O angle. The O-*A*-O angle variance is the dominant contributor to the polyhedral distortion (Figure 5.13) except in the case of $Y_2Mo_3O_{12}$. Structural information regarding $A_2M_3O_{12}$ materials was taken from the literature; see Table 5.2 for references.
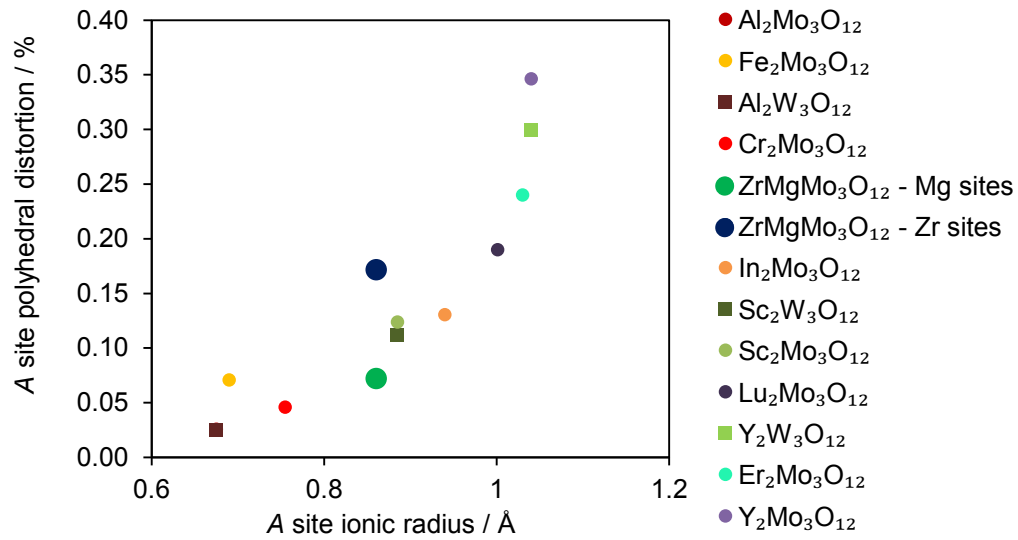
Figure 5.15: Inherent polyhedral distortion (AO_6) in ZrMgMo$_3$O$_{12}$ and $A_2M_3O_{12}$ materials as a function of the Shannon ionic radii of the A site cations[138] (inherent polyhedral distortions of AlO$_6$ in Al$_2$Mo$_3$O$_{12}$ and Al$_2$W$_3$O$_{12}$ are nearly identical and these two points overlap). Structural information regarding $A_2M_3O_{12}$ materials was taken from the literature; see Table 5.2 for references. Adapted from Reference 265 with permission.

plausible that the distortion of the ZrO$_6$ octahedra in ZrMgMo$_3$O$_{12}$ is also static. The inherent polyhedral distortion for $A_2M_3O_{12}$ materials increases nonlinearly with increasing ionic radius. This nonlinearity could be related to the instability of the orthorhombic Sc$_2$W$_3$O$_{12}$ structure above a critical A cationic radius; $A_2W_3O_{12}$ materials with A greater in size than Ho^{3+} (104.1 pm) and A_2Mo$_3$O$_{12}$ materials with A greater in size than Y^{3+} (104 pm) crystallize in a variety of structures different from that of Sc$_2$W$_3$O$_{12}$.[146,280]

The ease of distortion of the AO_6 polyhedra could be rationalized, more fundamentally, in terms of the magnitude of the attractive forces (F_a) between the $A^{2+/3+/4+}$ cation and the O^{2-} anion. To estimate this attractive force, and the consequent ease of distortion of the ZrO$_6$, MgO$_6$ and other octahedra, the ionic attractive force can be used.[281] This is expressed as $-k_eZ_+Z_-e_c^2/r_o^2$ where k_e is Coulomb's constant, Z_+ is the valence of the cation, Z_- is the average valence of the anions, e_c is the elementary charge

129

and r_o is the sum of the cation and anion radii.[138] This method relates the ability of the polyhedra to distort directly to the force of the ionic attraction between the cation and anion. Polyhedral stiffness can impact thermal expansion directly through its interaction with the mode Grüneisen parameters (see Equation 1.8 and associated discussion). Instead of using standard valences, these attractive forces were calculated using the bond valence method[282] within IVTON.[279] Inherent polyhedral distortion is expressed as a function of the ionic attractive force in Figure 5.16, showing that the inherent distortions of the ZrO_6 and MgO_6 polyhedra are highly different from AO_6 polyhedra for $A_2M_3O_{12}$ materials. However, estimating their average effect, together they could act like a conventional A site.
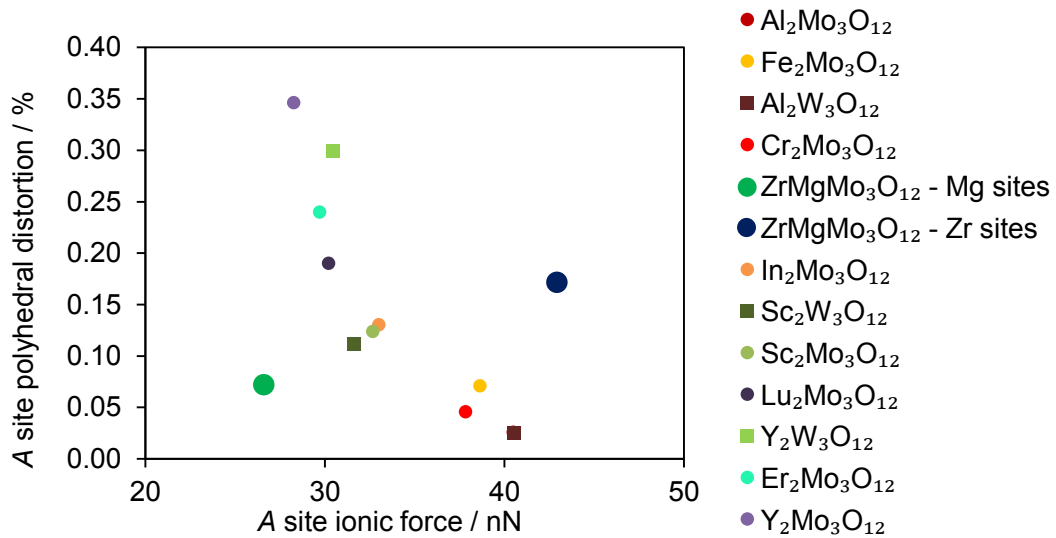
Figure 5.16: Inherent polyhedral distortion (AO_6) in $ZrMgMo_3O_{12}$ (large symbols) and $A_2M_3O_{12}$ materials as a function of their A site ionic force. Structural information regarding $A_2M_3O_{12}$ materials was taken from the literature; see Table 5.2 for references.

Coefficients of thermal expansion of $A_2M_3O_{12}$ materials and $ZrMgMo_3O_{12}$ are shown as a function of their A site ionic force in Figure 5.17. Instead of using the sum of Shannon ionic radii to calculate the interatomic distance and thereby the cationic force, average crystallographic A-O bond distances could have been used. This choice gives a

130
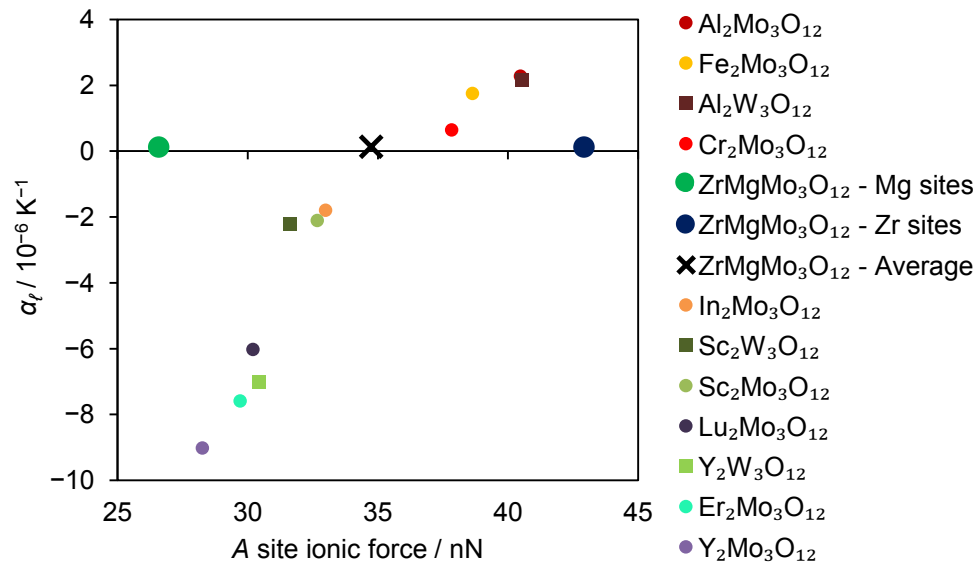
Figure 5.17: Coefficients of thermal expansion of $ZrMgMo_3O_{12}$ (large symbols) and $A_2M_3O_{12}$ materials as a function of their A site ionic force. Structural information regarding $A_2M_3O_{12}$ materials was taken from the literature; see Table 5.2 for references. Adapted from Reference 265 with permission.

weaker correlation to the CTEs of the compounds (Figure 5.18), especially at the extremes of thermal expansion of the data set. This difference could be due to the underestimation of bond lengths in thermomiotic materials as measured by diffraction, due to the librational motion of the oxygen atoms, which, when time-averaged over the course of a diffraction experiment, reduces the apparent bond lengths.[6] The general trend is increased CTE with increased ionic force. A clear difference is visible upon comparison of Figure 5.17 to Figure 5.15: $ZrMgMo_3O_{12}$, $Fe_2Mo_3O_{12}$, and $Er_2Mo_3O_{12}$ fit the A site ionic force trends better, suggesting that the ionic force offers a good estimate of the distortability of the AO_6 polyhedron for $A_2M_3O_{12}$ materials and $ZrMgMo_3O_{12}$, and that the zero thermal expansion behaviour of $ZrMgMo_3O_{12}$ is due to a mixed effect from the more rigid ZrO_6 octahedra and the more distortable MgO_6 octahedra.
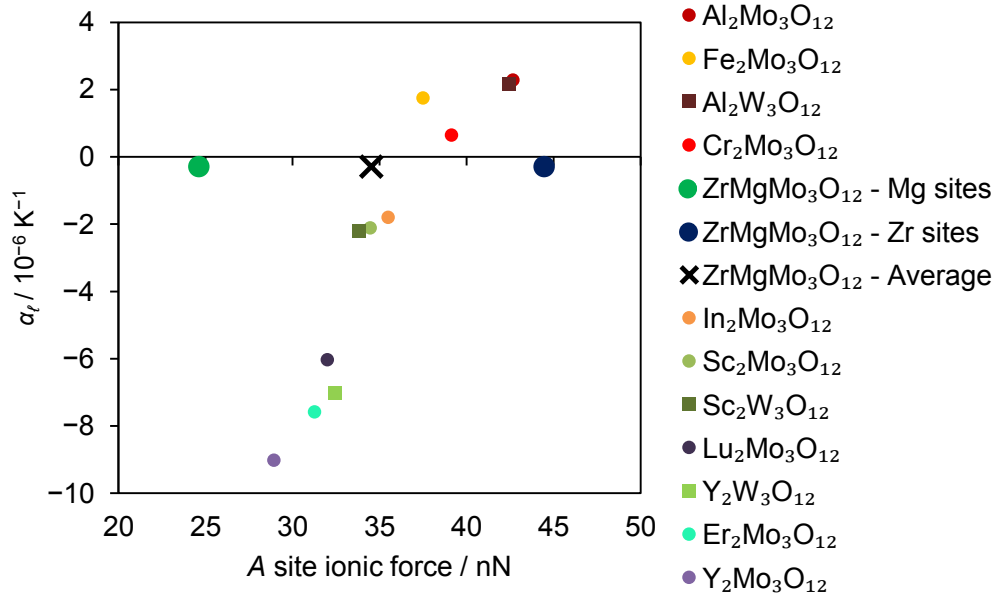
Figure 5.18: Coefficients of thermal expansion of $ZrMgMo_3O_{12}$ (large symbols) and $A_2M_3O_{12}$ materials as a function of their A site ionic force, calculated as a function of the A-O bond length rather than the sum of ionic radii. Structural information regarding $A_2M_3O_{12}$ materials was taken from the literature; see Table 5.2 for references.

This assertion regarding the polyhedral rigidity of $ZrMgMo_3O_{12}$ is supported by examination of the other physical properties discussed above, including the presence of low-frequency optic modes in the Raman spectrum and the calculated vibrational spectrum, and the measured bulk modulus. Specifically, the bulk modulus of orthorhombic $ZrMgMo_3O_{12}$ (31 ± 3 GPa) is less than that of orthorhombic $Al_2W_3O_{12}$ (48 GPa),[26] similar to that of orthorhombic $Sc_2Mo_3O_{12}$ (32 ± 2 GPa)[26] and $Sc_2W_3O_{12}$ (31 ± 3 GPa),[27] and greater than that of orthorhombic $Y_2W_3O_{12}$ (27 GPa)[28] and $Y_2Mo_3O_{12}$ (21 ± 3 GPa) (see Chapter 8) indicating that the overall rigidity of $ZrMgMo_3O_{12}$ is close to what would be expected given its CTE.

The absence of significant hygroscopicity in $ZrMgMo_3O_{12}$ can also be explained through knowledge of its structure. The atomic packing fractions (with the volume of each atom defined to be equal to that of a sphere whose radius is equal to half the nearest-

neighbour distance) of $ZrMgMo_3O_{12}$ and $A_2M_3O_{12}$ materials are shown in Figure 5.19;

the packing fraction of $ZrMgMo_3O_{12}$ (0.17) is larger than for $A_2M_3O_{12}$ materials that are

known to incorporate water into their crystal structures[45,146,28] and is close to those of the

non-hygroscopic $A_2M_3O_{12}$ materials $Sc_2Mo_3O_{12}$ and $In_2Mo_3O_{12}$.
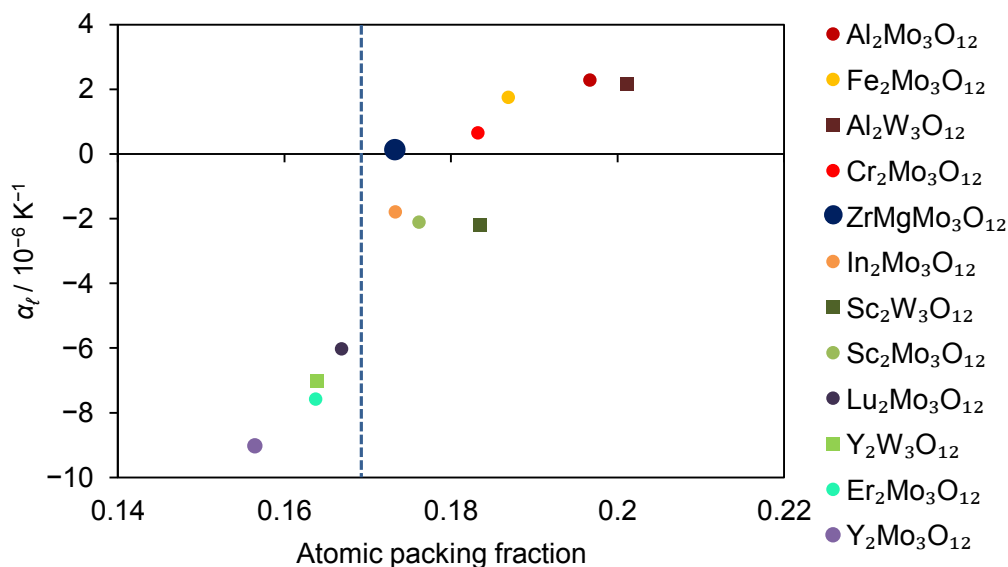
Figure 5.19: Atomic packing fractions of $ZrMgMo_3O_{12}$ (large symbol) and $A_2M_3O_{12}$
materials shown in comparison to their coefficients of thermal expansion. The dotted blue
line separates materials with significant hygroscopicity due to incorporation of crystal
waters (to the left of the line) from those without this property. Structural information
regarding $A_2M_3O_{12}$ materials was taken from the literature; see Table 5.2 for references.

5.4. Conclusions

It has been demonstrated that $ZrMgMo_3O_{12}$ is a zero thermal expansion material.

It is thermally stable in its orthorhombic phase from -125 °C to 700 °C. Unlike some

members of the $A_2M_3O_{12}$ family, it is not hygroscopic.

The bulk average value of the linear thermal expansion coefficient, as determined

from dilatometry, is $\alpha_\ell = (-0.3 \pm 0.1) \times 10^{-6}\,K^{-1}$ from 23 °C to 500 °C. The average linear

intrinsic CTE, as determined by X-ray diffraction, also is very close to zero: $\alpha_\ell = (0.16 \pm$

$0.02) \times 10^{-6}\,K^{-1}$ from 25 °C to 450 °C and $\alpha_\ell = (0.9 \pm 0.3) \times 10^{-6}\,K^{-1}$ from 450 to 700

°C. The small differences between intrinsic and extrinsic thermal expansion at lower temperatures are probably due to microstructure, and especially behaviour of microcracks. Nevertheless, the average linear CTE is exceptionally small over a wide temperature range. However, the CTE is anisotropic, with the maximum difference between two axial CTEs for $ZrMgMo_3O_{12}$ between 25 °C and 450 °C, $\Delta\alpha_{max}$, being 12.3 $\times 10^{-6}$ K^{-1}.

The structure of $ZrMgMo_3O_{12}$, intractable by X-ray powder diffraction and not feasible by single crystal X-ray diffraction, was determined by NMR crystallography, making use of NMR activity of all the nuclei, ^{91}Zr, ^{25}Mg, ^{95}Mo, and ^{17}O. In order to obtain the ^{17}O NMR, a synthesis method for ^{17}O-enriched MoO_3 was developed. The space group of the orthorhombic phase of $ZrMgMo_3O_{12}$ is $Pna2_1$ and its structure is related to the structure of $Sc_2W_3O_{12}$, with ordering of Mg^{2+} and Zr^{4+} cations. The structure suggests the possibility of ionic conductivity, which was confirmed experimentally. The solution of the structure of $ZrMgMo_3O_{12}$ should aid in the structure determination of other $AMgM_3O_{12}$ materials with interesting thermal expansion properties.

The calculated and experimental Raman spectra both indicate a high density of low-frequency modes associated with librations of quasi-rigid units that could play a role in negative thermal expansion in this framework structure. Velocity of sound measurements revealed low bulk and shear moduli relative to conventional oxide ceramics, again supporting flexibility of the linked polyhedra.

Compared with the orthorhombic phases of $A_2M_3O_{12}$ materials, $ZrMgMo_3O_{12}$ shows the broadest distribution of M-O-A angles yet reported. While the average inherent

distortion of $A\mathrm{O}_6$ polyhedra in $\mathrm{ZrMgMo_3O_{12}}$ is similar to that of materials with negative, rather than near-zero CTEs, distortion of the MgO_6 octahedra alone is a better predictor of the average CTE. The distortion in ZrO_6 is likely static in nature. The average A-site ionic force in both $\mathrm{ZrMgMo_3O_{12}}$ and in a wide range of $A_2M_3\mathrm{O}_{12}$ materials is a useful predictor of the CTE. Therefore, it was possible to use the crystal structure to understand the properties of $\mathrm{ZrMgMo_3O_{12}}$, providing further experimental validation of the structure.

Chapter 6: Mechanical Properties and Thermal Expansion of $A_2M_3O_{12}$ and AMgM_3O_{12} Materials and Their Solid Solutions

6.1.   Background

The mechanical properties of thermomiotic materials are an essential component of their overall thermoelastic behaviour, as they influence their suitability for applications (Section 1.3.2.3), propensity to thermal stress (Chapter 3), and the thermal expansivity of their composites (Chapter 4). Additionally, reduction of stiffness can be expected to lead to larger-magnitude CTEs (Chapter 1). However, mechanical properties have not previously been extensively reported in the literature. Aside from ZrW_2O_8,[25] reporting of the elastic constants of thermomiotic materials has generally been limited to bulk moduli obtained from variable-pressure XRD.[26,27,28,283] Although variable-pressure XRD can give important information regarding pressure-induced phase transitions and other structural changes, it provides only the bulk modulus and directional compressibilities. Therefore, information is only obtained about the material's response to changes in volume, not changes in shape (*i.e.,* shear deformation).

The $A_2M_3O_{12}$ and AMgM_3O_{12} families of materials offer a large amount of diversity both in terms of their chemistry and thermal expansion properties (see Section 1.6). It is possible to synthesize solid solutions from this family whose CTEs range from positive to negative.[53,284] In this chapter, the synthesis of several series of solid solutions is reported, as is the characterization of their CTEs (*via* dilatometry) and bulk and shear moduli (*via* ultrasonic measurement of the velocity of sound) with the goal of examining correlations between thermal expansivity and elastic properties.

Three series of solid solutions were studied: $In_{2-2x}(HfMg)_xMo_3O_{12}$, $Sc_{2-2x}Al_{2x}W_3O_{12}$, and $Cr_{2-2x}(HfMg)_xW_3O_{12}$ ($0 \leq x \leq 1$).

Intrinsic thermal expansion of the $In_{2-2x}(HfMg)_xMo_3O_{12}$ series has previously been characterized for $x = 0$, 0.25, 0.5, and 1;[76,153,156,284] the thermal expansivity closely follows the rule of mixtures between thermomiotic $In_2Mo_3O_{12}$[153] and low-positive thermal expansion in $HfMgMo_3O_{12}$,[156] with near-zero thermal expansion reported for $In(HfMg)_{0.5}Mo_3O_{12}$.[76] $HfMgMo_3O_{12}$ exists in an orthorhombic phase (presumed to be $Pna2_1$, see Chapter 5) at room temperature; however materials of the general formula $In_{2-2x}(HfMg)_xMo_3O_{12}$ with $x \leq 0.5$ are known to exist in monoclinic $P2_1/a$ phases at room temperature.[76,153,156,284] The $x = 0.75$ member of the series has not been previously reported and was synthesized and characterized herein.

Thermal expansion in the $Sc_{2-2x}Al_{2x}W_3O_{12}$ series, which also varies between positive ($Al_2W_3O_{12}$)[220] and negative ($Sc_2W_3O_{12}$)[149] thermal expansion, has been previously studied *via* dilatometry[53,285,286] and variable-temperature XRD.[149,220,285] All members of the series ($0 \leq x \leq 1$) are stable at room temperature in an orthorhombic *Pbcn* phase.

The third series, $Cr_{2-2x}(HfMg)_xW_3O_{12}$, has not previously been reported. $HfMgW_3O_{12}$ has been reported to be thermomiotic, although reports conflict concerning whether it is stable in a monoclinic or orthorhombic phase at room temperature.[91,155] Only one report of the properties of $Cr_2W_3O_{12}$ has been published,[287] and the thermal expansion properties reported (intrinsic axial, intrinsic volumetric, and bulk) are highly inconsistent with each other.

6.2. Experimental Procedures

Samples were synthesized using methods described in Section 2.1. The reagents used were Al_2O_3 (Sigma Aldrich, 98.7 %), HfO_2 (Aldrich, 98 %), In_2O_3 (Fluka, 99.9 %), $Mg_5(CO_3)_4(OH)_2 \cdot 5H_2O$ (Alfa Aesar, 98 %), MoO_3 (Sigma-Aldrich, 99.5 %), Sc_2O_3 (Alfa Aesar, 99 %), and WO_3 (Fluka, 99.9 % and Alfa Aesar, 99.8 %). Molybdate $A_2M_3O_{12}$ materials decompose upon heating at temperatures lower than their melting point, which complicates sintering by placing a low limit on the sintering temperature. Temperatures reported in the literature as producing the desired monophasic material are not always sufficiently high to produce an adequately densified material.

Sintering temperatures for molybdate materials were optimized using decomposition temperatures determined *via* TGA for $In_2Mo_3O_{12}$ and $HfMgMo_3O_{12}$ (see Section 2.3.2). $HfMgMo_3O_{12}$ (34.1099 mg sample) was subjected to a 30 K min^{-1} ramp to 600 °C followed by a 10 K min^{-1} ramp to 900 °C and $In_2Mo_3O_{12}$ (39.5531 mg sample) was subjected to a 30 K min^{-1} ramp to 750 °C followed by a 10 K min^{-1} ramp to 990 °C. TGA thermograms of these materials are shown in Figure 6.1. Tungstate materials melt upon heating without decomposition, so sintering temperatures were determined by consultation of literature values.[52,91,222] The absence of decomposition allowed the materials to be sintered closer to their melting points and less sintering time was required.

The experimental sintering temperatures and times used are summarized in Table 6.1. In order to adequately densify $In_2Mo_3O_{12}$ and $HfMgMo_3O_{12}$, sintering very close to the decomposition temperature was required. The sintering temperatures required resulted in a small amount of decomposition (*vide infra*). Sintering Cr_2O_3 and WO_3 at 800 °C did not result in formation of $Cr_2W_3O_{12}$ as was described in Reference 287, so it was
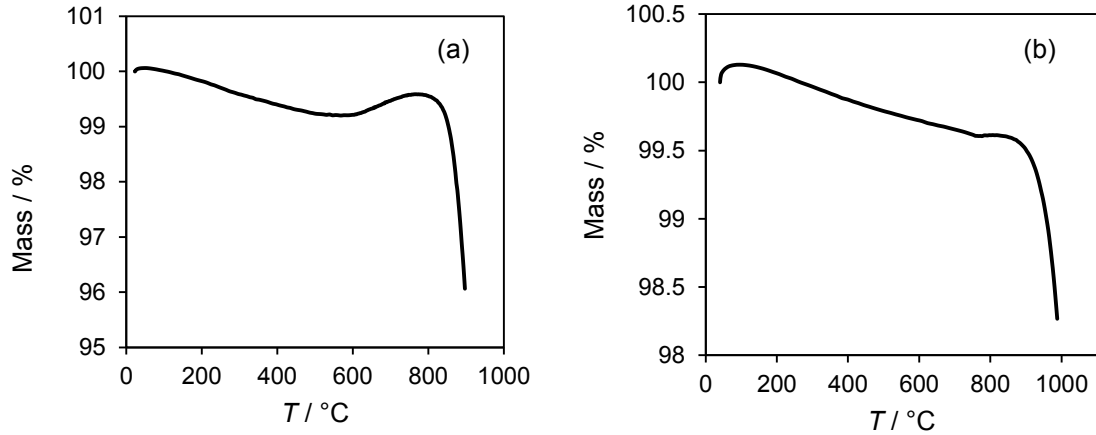
Figure 6.1: TGA thermograms of (a) $HfMgMo_3O_{12}$ and (b) $In_2Mo_3O_{12}$, showing decomposition into constituent oxides and subsequent sublimation of MoO_3 upon heating.

Table 6.1: Sintering temperatures and times for $A_2M_3O_{12}$ and $AMgM_3O_{12}$ materials and their solid solutions.

Material	Sintering temperature / °C	Sintering time / h
$In_2Mo_3O_{12}$	905	24
$In_{1.5}(HfMg)_{0.25}Mo_3O_{12}$	730	24
$In(HfMg)_{0.5}Mo_3O_{12}$	730	24
$In_{0.5}(HfMg)_{0.75}Mo_3O_{12}$	775	24
$HfMgMo_3O_{12}$	775	24
$Cr_2W_3O_{12}$	1000	12
$Cr_{1.5}(HfMg)_{0.25}W_3O_{12}$	1100	12
$Cr(HfMg)_{0.5}W_3O_{12}$	1100	12
$Cr_{0.5}(HfMg)_{0.75}W_3O_{12}$	1100	12
$HfMgW_3O_{12}$	1100	12
$Al_2W_3O_{12}$	1000	12
$Al_{1.5}Sc_{0.5}W_3O_{12}$	1000	12
$AlScW_3O_{12}$	1000	12
$Al_{0.5}Sc_{1.5}W_3O_{12}$	1000	12
$Sc_2W_3O_{12}$	1100	12

performed at a higher temperature.

XRD was used to check the phase purity of the samples and determine their lattice constants following the procedures used in Section 2.2. The bulk CTEs of the $Al_{2-2x}Sc_{2x}W_3O_{12}$ and $Cr_{2-2x}(HfMg)_xW_3O_{12}$ series and $In_{0.5}(HfMg)Mo_3O_{12}$ were determined dilatometrically (see Section 2.3.1). The CTEs of the remainder of the

139

$In_{2-2x}(HfMg)_xMo_3O_{12}$ series have been well-characterized previously.[76,153,156,284]

Unfortunately, for some of the materials collection of dilatometric data was limited to a

maximum temperature of 500 °C because of a problem with a seal in the instrument,

which introduced artefacts into data acquired above that temperature. The transverse and

longitudinal velocities of sound of all the materials were measured ultrasonically (see

Section 2.5).

6.3. Results and Discussion

6.3.1. $In_{2-2x}(HfMg)_xMo_3O_{12}$

6.3.1.1. Lattice Constants

X-ray diffractograms of $In_{2-2x}(HfMg)_xMo_3O_{12}$ materials were refined using the Le

Bail method in the *Pna*2$_1$ setting for $x = 1$ and in the *P*2$_1$/*a* setting otherwise (see

Appendix A, Figures A6–A10 for diffractograms). The refined lattice constants,

presented in Table 6.2 and Figure 6.2, were consistent with those previously reported in

the literature.[76,153,156,284] $In_{0.5}(HfMg)_{0.75}Mo_3O_{12}$, which has not been previously reported

in the literature, shows a reversal in the relative lengths of the *a*- and *c*-axes with respect

to the other monoclinic members of the series. This reversal is also seen in the

$Cr_{2-2x}(HfMg)_xW_3O_{12}$ series between $x = 0.75$ and $x = 0.5$ (*vide infra*), and could be

related to a change in the space group of the high-temperature orthorhombic phase from

*Pna*2$_1$ to *Pnca*, as $In(HfMg)Mo_3O_{12}$ has been reported[284] to transition to a *Pnca* phase at

163 °C while $HfMgMo_3O_{12}$ adopts *Pna*2$_1$ at room temperature.

The *P*2$_1$/*a* phases of $HfMgMo_3O_{12}$[156] and $HfMgW_3O_{12}$[91] were both reported to

have the *c*-axis longer than the *a*-axis, however due to the experimental conditions used

Table 6.2: Lattice constants of $In_{2-x}(HfMg)_xMo_3O_{12}$ materials ($Pna2_1$ setting for $x = 1$ and $P2_1/a$ otherwise), goodness-of-fit values, and mean densities, expressed as % of the theoretical density, for sintered pellets. Literature results, where available, are shown in italics for comparison.

Material	a / Å	b / Å	c / Å	β / °	χ^2	Mean density / % theoretical
$In_2Mo_3O_{12}$	16.2503(4)	9.5786(3)	18.9053(5)	125.320(2)	0.514	74.9
Reference 153	*16.272*	*9.592*	*18.921*	*125.2*		
$In_{1.5}(HfMg)_{0.25}Mo_3O_{12}$	16.2097(4)	9.5433(3)	18.884(1)	125.368(2)	0.633	73.3
Reference 284	*16.223*	*9.5614*	*18.879*	*125.35*		
$In(HfMg)_{0.5}Mo_3O_{12}$	16.128(1)	9.5193(6)	18.791(1)	125.31(1)	0.873	68.0
Reference 76	*16.2147*	*9.5582*	*18.8797*	*125.396*		
$In_{0.5}(HfMg)_{0.75}Mo_3O_{12}$	18.8095(2)	9.5109(1)	16.1016(2)	125.296(1)	0.869	85.6
$HfMgMo_3O_{12}$	9.556(5)	9.4406(5)	13.1651(7)	90	1.086	83.2
Reference 156[xvii]	*9.57067*	*13.15713*	*9.48283*	*90*		
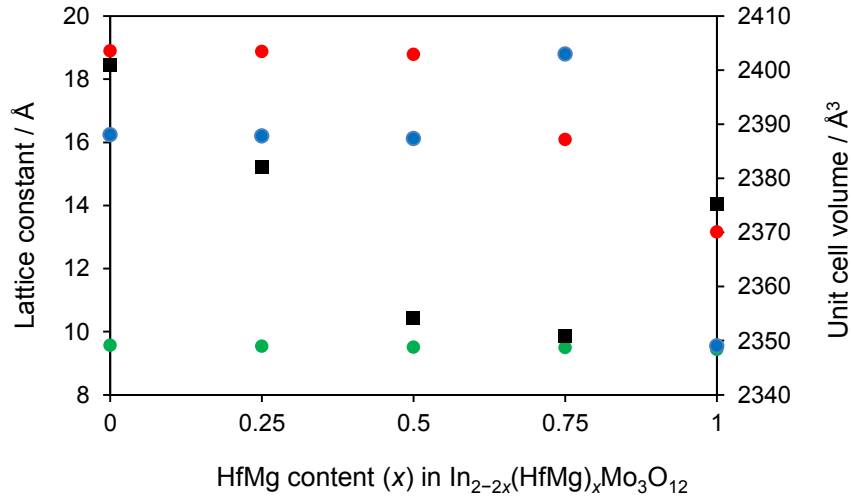
Figure 6.2: Lattice constants of the a- (•), b- (•), and c- (•) axes and unit cell volumes (■) of $In_{2-x}(HfMg)_xMo_3O_{12}$ materials ($Pna2_1$ setting for $x = 1$ and $P2_1/a$ otherwise). The unit cell volume of orthorhombic $HfMgMo_3O_{12}$ has been multiplied by two in order that the number of formula units per unit cell is consistent with that of the monoclinic materials. Error bars corresponding to estimated standard deviations are smaller than the symbols.

[xvii] In Reference 156, the Le Bail refinement was carried out in the *Pnma* space group.

in these literature reports there is some potential for error, as described below. Due to the large number of peaks in the diffractogram and the use of the Le Bail method, there is only one significant difference between the two axis settings. As shown in Figure 6.3, a peak due to the (6 0 −3) reflection appears at approximately 28.1° in 2θ. In the case of $HfMgMo_3O_{12}$ this peak would not have been observable because of a peak from the sample holder in that region in the literature diffraction pattern,[156] while in the case of $HfMgW_3O_{12}$ it would have been obscured by a peak from an internal standard[91] (it is seen in the present investigation of $HfMgW_3O_{12}$, see Section 6.3.3.1). It is also possible that this peak could be due to the presence of a small HfO_2 impurity, however no other extra peaks related to decomposition products are visible in the diffraction pattern.
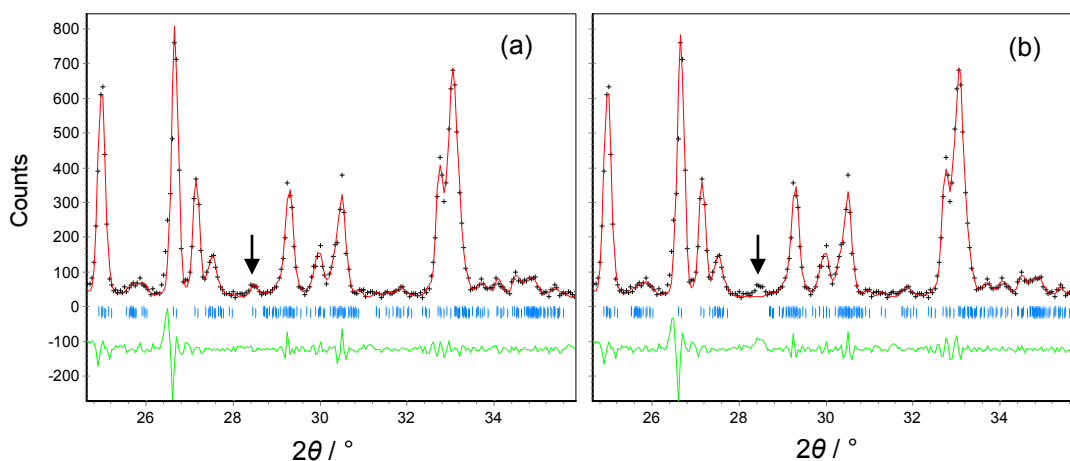
Figure 6.3: A portion of the present X-ray diffractogram of $In_{0.5}(HfMg)_{0.75}Mo_3O_{12}$ refined in $P2_1/a$ with (a) $a \approx 18.8$ Å and $c \approx 16.1$ Å and (b) with $a \approx 16.1$ Å and $c \approx 18.8$ Å. Experimental data are shown as black crosses, the Le Bail fit to the data as a red line, the peak positions as blue ticks, and the residual as a green line. The position of the major peak which differs between the two choices of axis lengths is shown with an arrow; the first choice is consistent with the data.

As discussed above, the sintering conditions necessary to produce reasonably densified samples caused a small amount of decomposition in $In_2Mo_3O_{12}$ and $HfMgMo_3O_{12}$. Therefore, MoO_3[288] and In_2O_3[289] or HfO_2[290] were included in the refinements for those materials. Because the patterns were refined using the Le Bail

method, the amounts of decomposition products could not be determined directly, however the absence of mass loss at *ca.* 700 °C in the TGA thermograms (Figure 6.1) indicates that very little MoO_3 is present (*cf.* Figure 2.3) and that decomposition was limited to a few percent at most. Since the thermal expansion and velocity of sound are, to first approximation, bulk-average properties, this is not expected to significantly affect the results.

6.3.1.2. Thermal Expansion

The CTE of $In_{0.5}(HfMg)_{0.75}Mo_3O_{12}$ was determined dilatometrically between room temperature and 700 °C using a ramp rate of 5 K min^{-1} upon heating and cooling. The results are shown in Figure 6.4. The CTE, as determined *via* linear regression on cooling from 125 °C to 700 °C, is $\alpha_\ell = -1.4 \times 10^{-6}$ K^{-1}. As is usual for $A_2M_3O_{12}$ and AMgMo$_3$O$_{12}$ materials, $In_{0.5}(HfMg)_{0.75}Mo_3O_{12}$ undergoes a phase transition at *ca.* 50 °C into a (presumably) orthorhombic phase with increased volume and decreased thermal expansion. The CTE of $In_{0.5}(HfMg)_{0.75}Mo_3O_{12}$ (125 °C to 700 °C) is considerably more negative than would be expected from the rule of mixtures. This is especially surprising as other members of this series of solid solutions had been shown to follow the rule of mixtures quite closely.[284] The deviation from the predicted CTE can be seen clearly in Figure 6.5.

Because materials with anisotropic thermal expansion can show large microstructural effects on the bulk CTE due to microcrack healing and formation,[205] the microstructure of $In_{0.5}(HfMg)_{0.75}Mo_3O_{12}$ was examined using SEM (Hitachi S-4700 FEG, SE detector, 5 kV accelerating voltage, 15.3 mm working distance, see Section 2.4). The microstructure was found to be very similar to that of $In(HfMg)_{0.5}Mo_3O_{12}$[156] and
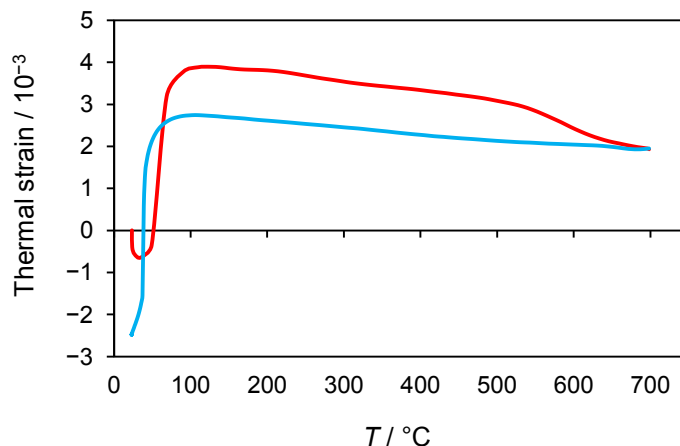
Figure 6.4: A dilatometric heating (red line) and cooling (blue line) curve of In$_{0.5}$(HfMg)$_{0.75}$Mo$_3$O$_{12}$, showing the change in length with respect to the original length (thermal strain) as a function of temperature. The heating curve is shown in red and the cooling curve is shown in blue. The onset of a phase transition, observed as a large change in volume, can be seen at *ca.* 50 °C.
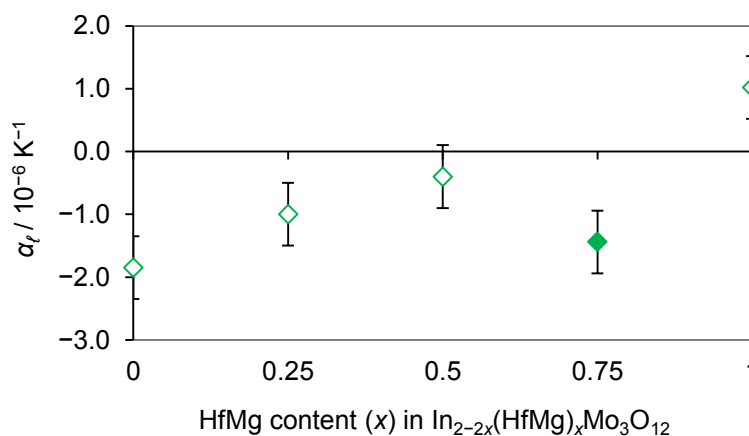
Figure 6.5: The CTE of In$_{0.5}$(HfMg)$_{0.75}$Mo$_3$O$_{12}$ from 125 °C to 700 °C (filled symbol) is compared to literature values of the CTEs of In$_2$Mo$_3$O$_{12}$ (370 °C to 760 °C),[76] In$_{1.5}$(HfMg)$_{0.25}$Mo$_3$O$_{12}$ (300 °C to 700°C),[284] In(HfMg)$_{0.5}$Mo$_3$O$_{12}$ (225 °C to 650°C),[156] and HfMgMo$_3$O$_{12}$ (25 °C to 740°C)[153] (open symbols). An estimated uncertainty is also shown.

HfMgMo$_3$O$_{12}$;[153] significant amounts of microcracking or other microstructural

anomalies were not found (Figure 6.6).[xviii] Therefore, the intrinsic CTE of

---

[xviii] Although the micrograph was acquired from a fracture surface, if a sufficiently large amount of microcracking had occurred to cause a significant deviation from the intrinsic CTE it would be expected that some microcracks would be visible.[205]
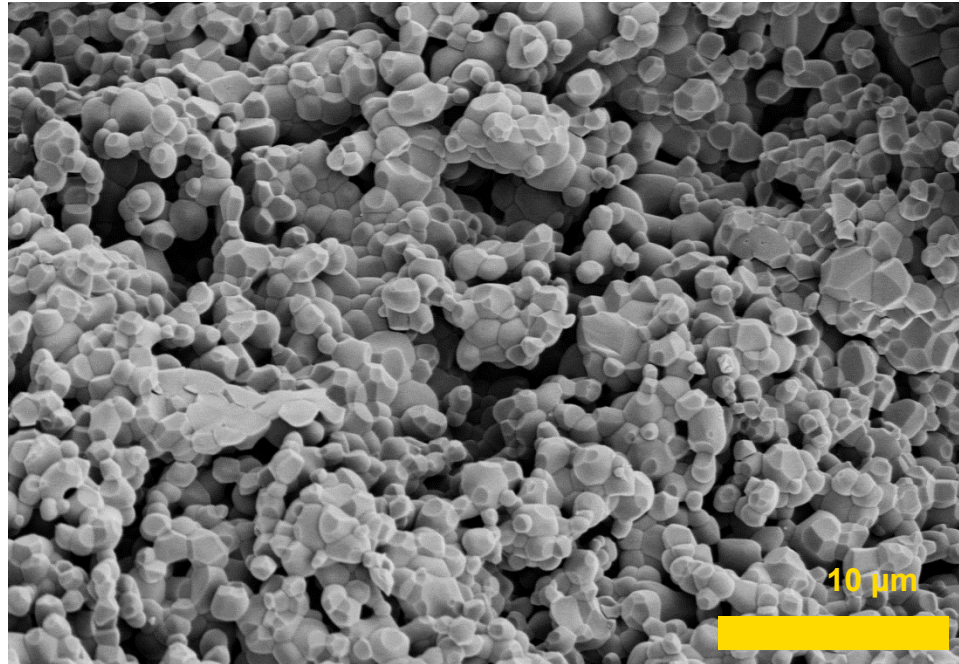
Figure 6.6: A SEM micrograph of polycrystalline $In_{0.5}(HfMg)_{0.75}Mo_3O_{12}$.

$In_{0.5}(HfMg)_{0.75}Mo_3O_{12}$ is likely the same as the bulk CTE within the margin of error shown in Figure 6.5. The discontinuity in thermal expansion in $In_{2-2x}(HfMg)_xMo_3O_{12}$ at $0.5 < x < 0.75$ could potentially be related to a compositional boundary between solid solutions which adopt $Pna2_1$ and those that adopt $Pbcn$, *i.e.* a boundary between materials with disordered Hf^{4+} and Mg^{2+} cations and those with ordered Hf^{4+} and Mg^{2+}. This hypothesis could be tested using variable-temperature XRD to determine whether the space group of the orthorhombic phase is $Pbcn$ or $Pna2_1$.

6.3.1.3.   Mechanical Properties

The longitudinal and transverse velocities of sound, corrected for porosity (see Appendix B for uncorrected velocities), of $In_{2-2x}(HfMg)_xMo_3O_{12}$ materials are shown in Figure 6.7(a). By comparison to Figure 6.5, a clear relationship between the velocities of sound and the CTE can be seen. The velocities of sound follow the same trend with
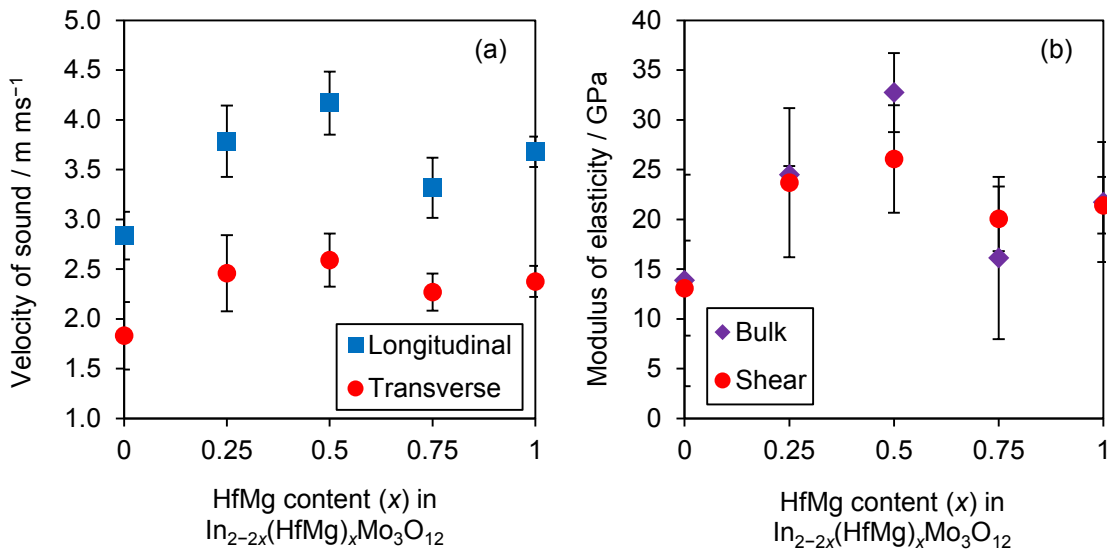
Figure 6.7: (a) Longitudinal and transverse velocities of sound and (b) bulk and shear moduli of $In_{2-2x}(HfMg)_xMo_3O_{12}$. All measurements were performed at room temperature, on the monoclinic phases for $x \leq 0.75$ and on the orthorhombic phase for $x = 1$. The bulk and shear data points overlap for $x = 0$, 0.25, and 1.

composition as the CTEs, with an anomaly at $x = 0.75$. However, it should be noted that the densities of the materials for $x \leq 0.5$ fell below the level of 75 % of theoretical for which the correction for porosity is expected to be reliable (see Section 2.5). Therefore, the corrected velocities likely underestimate the actual fully densified velocity somewhat.

The bulk and shear moduli of $In_{2-2x}(HfMg)_xMo_3O_{12}$ materials are shown in Figure 6.7(b). As is the case for the velocities of sound, the elastic moduli follow the same trend as the CTE. All members of the series have unusually low stiffness for oxide ceramics, with the stiffness of the most thermomiotic members, $In_2Mo_3O_{12}$ and $In_{0.5}(HfMg)_{0.75}Mo_3O_{12}$, being exceptionally low. The material with the smallest-magnitude CTE, $In(HfMg)_{0.5}Mo_3O_{12}$, also has the highest stiffness. It is interesting to note that these correlations relate the elastic properties in the room temperature monoclinic phase with the thermal expansion in the high-temperature orthorhombic phase for $x \leq 0.75$.

The bulk moduli of several $A_2M_3O_{12}$ materials have been reported to decrease significantly following a pressure-induced phase transition into a monoclinic phase, and it has been surmised that a similar increase in compliance follows thermally induced orthorhombic-monoclinic phase transitions.[204] However, it is seen here that the elastic moduli of $HfMgMo_3O_{12}$ are close to those of the monoclinic members of the series. Additionally, the elastic moduli of the two near-zero thermal expansion materials $In(HfMg)_{0.5}Mo_3O_{12}$ and of $ZrMgMo_3O_{12}$ fall within the margin of error of each other (see Section 5.3.3), despite $ZrMgMo_3O_{12}$ being in a orthorhombic phase at room temperature. The decrease in stiffness seen following a pressure-induced orthorhombic-monoclinic phase transition could be related to the tendency of thermomiotic materials to become more compliant upon compression (see Equation 1.14 above and related discussion). $SrTiO_3$ is an example of a material that undergoes a similar displacive phase transition which involves rotation of corner-linked coordination polyhedra,[8,291] but the transition does not cause a large change in the elastic properties.[291]

6.3.2. $Sc_{2-2x}Al_{2x}W_3O_{12}$

6.3.2.1. Lattice Constants

Lattice constants of $Sc_{2-2x}Al_{2x}W_3O_{12}$ materials as determined from XRD refinement are shown in Table 6.3 and Figure 6.8. All of the refinements were performed in the orthorhombic *Pnca* setting. The diffractograms are presented in Appendix A, Figures A11–A15. The lattice constants are consistent with those previously reported in the literature.[149,203,220,285,286] A steady increase in each of the lattice constants was observed as Al^{3+} (ionic radius 67.5 pm)[138] is replaced with Sc^{3+} (88.5 pm).[138] In contrast to the molybdate materials presented in the previous section, considerable reduction of

Table 6.3: Lattice constants of $Sc_{2-2x}Al_{2x}W_3O_{12}$ materials (*Pnca* setting), goodness-of-fit values, and mean densities, expressed as % of the theoretical density, for sintered pellets. Literature results are shown in italics for comparison.[286]

Material	*a* / Å	*b* / Å	*c* / Å	χ^2	Mean density / % theoretical
$Al_2W_3O_{12}$	9.1407(4)	12.6167(4)	9.0575(4)	1.392	92.6
Reference 286	*9.1499*	*12.6117*	*9.0685*		
$Al_{1.5}Sc_{0.5}W_3O_{12}$	9.2348(4)	12.7452(6)	9.1487(5)	1.069	87.0
Reference 286	*9.2638*	*12.7699*	*9.1799*		
$AlScW_3O_{12}$	9.3423(5)	12.8929(7)	9.2538(5)	1.114	91.2
Reference 286	*9.3952*	*12.9559*	*9.3204*		
$Al_{0.5}Sc_{1.5}W_3O_{12}$	9.5056(7)	13.0872(9)	9.4155(7)	1.064	88.2
Reference 286	*9.5463*	*13.1318*	*9.4458*		
$Sc_2W_3O_{12}$	9.6627(4)	13.3218(6)	9.5728(4)	2.282	79.7
Reference 286	*9.6801*	*13.3211*	*9.5832*		
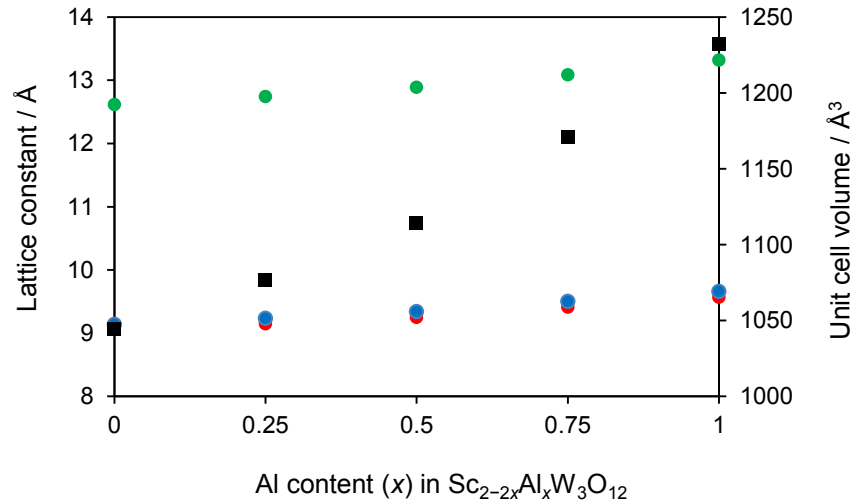
Figure 6.8: Lattice constants of the *a*- (•), *b*- (•), and *c*- (•) axes and unit cell volumes (■) of $Sc_{2-2x}Al_{2x}W_3O_{12}$ materials (*Pna*2_1 setting). Error bars corresponding to estimated standard deviations are smaller than the symbols.

porosity was achievable through sintering due to the absence of decomposition prior to melting. This reduction presents a major advantage of tungstate $A_2M_2O_{12}$ materials in comparison to molybdates in terms of potential applications.

148

6.3.2.1. Thermal Expansion

Dilatometric curves of $Sc_{2-2x}Al_{2x}W_3O_{12}$ materials are shown in Figure 6.9, and the CTEs of the members of the series as a function of composition are summarized in Figure 6.9 and Table 6.4. Dilatometry was performed between room temperature and 500 °C, or 700 °C, at a heating and cooling rate of 5 K min^{-1}. The thermal expansion of these materials was consistent with the values previously reported in the literature.[149,203,220,285] The bulk CTEs are closer to the reported intrinsic CTEs than in several previous dilatometric studies of $Sc_{2-2x}Al_{2x}W_3O_{12}$ materials ($0 \leq x \leq 1$),[53,218,285] indicating that microstructural effects on the CTE are relatively small. The microstructural effects can also be evaluated by the (relatively small) amount of hysteresis in the curves due to microcracking. $Sc_2W_3O_{12}$ was found to have a bulk CTE significantly more negative than the intrinsic CTE ($\alpha_\ell = -2.2 \times 10^{-6}$ K^{-1}),[149] presumably due to microstructural effects. This is not unexpected, as bulk CTEs of $Sc_2W_3O_{12}$ as low as -11×10^{-6} K^{-1} have been reported.[149]
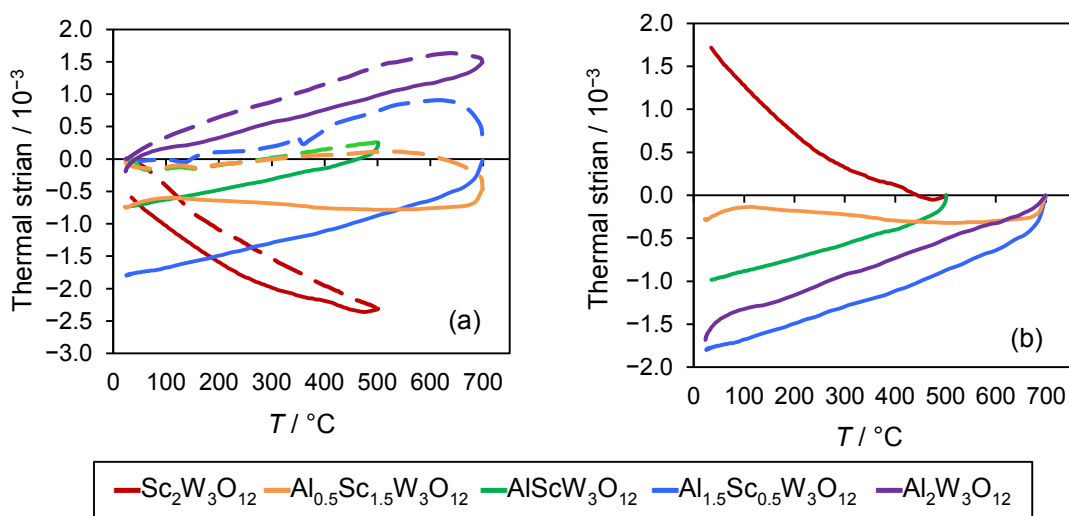
Figure 6.9: Thermal expansion in $Sc_{2-2x}Al_{2x}W_3O_{12}$ materials shown as (a) heating (dashed lines) and cooling (solid lines) curves and (b) as cooling curves only. The zero points of thermal strain in (b) have been set at the start of the cooling curves for ease of comparison.

149
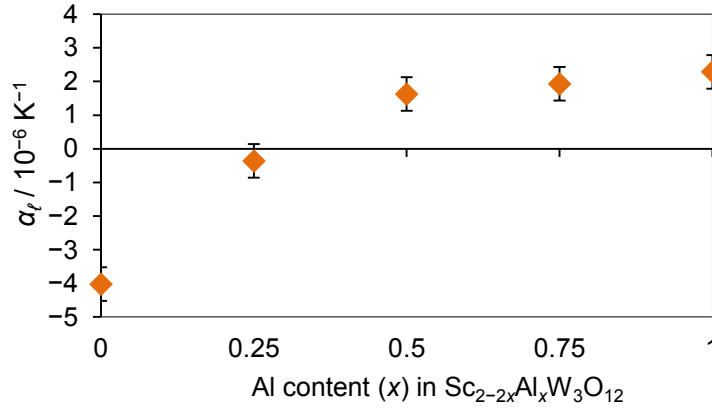
Figure 6.10: Thermal expansion in $Sc_{2-2x}Al_{2x}W_3O_{12}$ materials as measured here by dilatometry on cooling, presented as a function of composition. Estimated uncertainties are included.

Table 6.4: Coefficients of thermal expansion over given temperature ranges as determined from linear regression of dilatometric cooling curves of $Sc_{2-2x}Al_{2x}W_3O_{12}$ materials. Literature values are included in italics for comparison. Estimated uncertainties are also included.

Material	α_ℓ / 10^{-6} K^{-1}	Temperature range / °C	Measurement method
$Sc_2W_3O_{12}$	-4.0 ± 0.5	35 to 500	Dilatometry
Reference 149	*−2.2*	*−263 to 176*	*XRD*
$Sc_{1.5}Al_{0.5}W_3O_{12}$	-0.4 ± 0.5	55 to 600	Dilatometry
Reference 285	*−0.32*	*30 to 600*	*XRD*
$ScAlW_3O_{12}$	1.6 ± 0.5	35 to 460	Dilatometry
Reference 286	*−1.02*	*30 to 600*	*Dilatometry*
$Sc_{0.5}Al_{1.5}W_3O_{12}$	1.9 ± 0.5	35 to 600	Dilatometry
Reference 286	*0.05*	*30 to 600*	*Dilatometry*
$Al_2W_3O_{12}$	2.3 ± 0.5	25 to 700	Dilatometry
Reference 203	*2.1*	*50 to 550*	*Dilatometry (single crystal)*

Unusually, the CTEs were largely invariant to Al/Sc substitution up to $x = 0.5$. This invariance could be related to a nonlinear variation of the axial CTEs with composition, as the axial CTEs of $x = 0.75$ and $x = 0.85$ materials were reported to all be negative,[285] whereas in $Sc_2W_3O_{12}$ thermal expansion along the b-axis was reported to be

highly positive.[149] However, the axial CTEs in Reference 285 were determined by interpolation between only three data points, making their reliability questionable. Reference 286 reported a similar behaviour to what is seen here in a dilatometric study, although they did not report axial CTEs.

6.3.2.2.   Mechanical Properties

The velocities of sound, and bulk and shear moduli of $Sc_{2-2x}Al_{2x}W_3O_{12}$ materials, following correction for porosity (see Appendix B for uncorrected values), are shown in Figure 6.11. This series showed a looser correlation of the elastic moduli with the CTE than did the $In_{2-2x}(HfMg)_xMo_3O_{12}$ series, even though in this series measurements could be performed directly on the orthorhombic phases. However, an increase in stiffness, especially of the shear component, can be seen from $x = 0$ to $x = 1$ in Figure 6.11(b). In this series, the increase in density from $x = 0$ to $x = 1$ has a significant effect because the variations in the velocity of sound are small. Unfortunately, the relative uncertainties of the measurements for the $x = 0.75$ and, to a lesser extent, $x = 1$ materials were quite large. The large uncertainties can be traced to the fact that while the measured densities between the three pelletized samples varied somewhat, the measured velocities did not, indicating that microstructural factors such as microcracking influenced the results. The additional microstructural effects could be due in part to the large degree of densification achieved during sintering, as an increased pore fraction could reduce thermal stress (see Chapter 3). However, the bulk modulus result for $x = 1$ can be corroborated by comparison to the experimental value from variable-pressure XRD (48 GPa).[26]
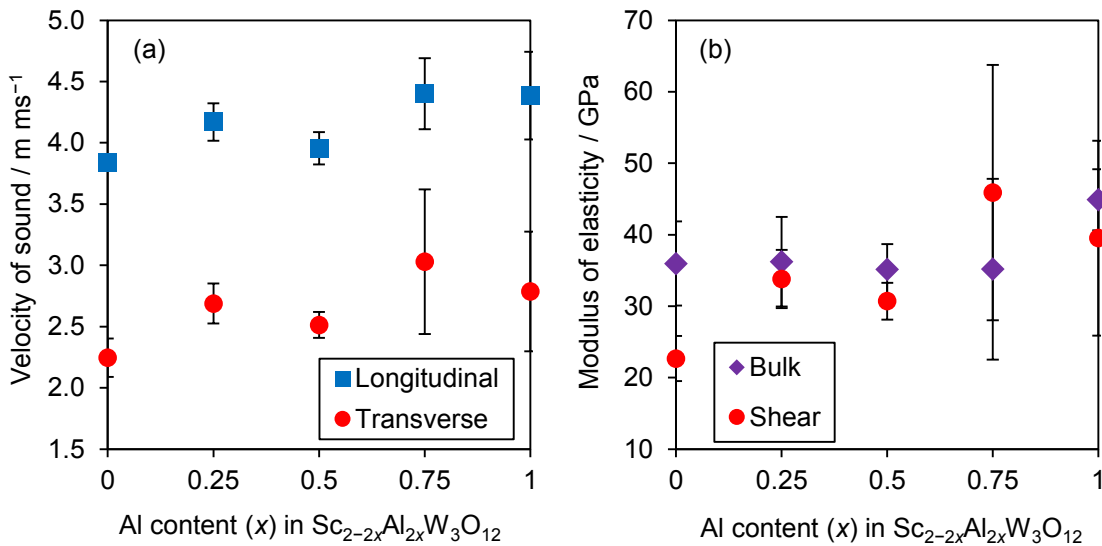
Figure 6.11: (a) Longitudinal and transverse velocities of sound and (b) bulk and shear moduli of $Sc_{2-2x}Al_{2x}W_3O_{12}$. All measurements were performed at room temperature on orthorhombic phases.

6.3.3. $Cr_{2-2x}(HfMg)_xW_3O_{12}$

6.3.3.1. Lattice Constants

Lattice constants of $Cr_{2-2x}(HfMg)_xW_3O_{12}$ materials are presented in Table 6.5 and Figure 6.12; diffractograms are presented in Appendix A, Figures A16–A20. Due to the delayed contraction following cooling in these materials (*vide infra*), the diffractograms were acquired after the samples remained at room temperature for a period of one year. All of the diffractograms were refined in the monoclinic $P2_1/a$ setting. No additional phases were detected in any of the materials. $HfMgW_3O_{12}$ has been reported by different authors to exist in a monoclinic[91] or orthorhombic[250] phase at room temperature; the current results unambiguously show that it is the monoclinic phase. A switch in the relative lengths of the *a*- and *c*-axes was seen between $x = 0.5$ and $x = 0.75$, as was the case in $In_{2-2x}(HfMg)_xMo_3O_{12}$ (see Section 6.3.1.1). Additionally, the change in cell volume is not monotonic as the smaller Cr^{3+} (ionic radius 75.5 pm)[138] ion is replaced by larger Hf^{4+} (85 pm)[138] and Mg^{2+} (86 pm)[138] ions; $Cr_{0.5}(HfMg)_{0.75}W_3O_{12}$ actually has the

152

Table 6.5: Lattice constants of $Cr_{2-2x}(HfMg)_xW_3O_{12}$ materials ($P2_1/a$ setting), goodness-of-fit values, and mean densities, expressed as % of the theoretical density, for sintered pellets. The literature result for $HfMgW_3O_{12}$ is included in italics.

Material	a / Å	b / Å	c / Å	β / °	χ^2	Mean density / % theoretical
$Cr_2W_3O_{12}$	16.0585(2)	9.3070(2)	19.4079(3)	125.534(1)	1.007	88.5
$Cr_{1.5}(HfMg)_{0.25}W_3O_{12}$	15.9777(4)	9.4179(2)	19.3255(4)	124.867(1)	0.728	89.9
$Cr(HfMg)_{0.5}W_3O_{12}$	15.9784(9)	9.2654(5)	19.339(1)	125.849(5)	1.393	93.9
$Cr_{0.5}(HfMg)_{0.75}W_3O_{12}$	18.908(1)	9.3191(5)	16.031(1)	125.895(5)	0.815	76.1
$HfMgW_3O_{12}$	18.9988(5)	9.6029(3)	16.231(2)	125.494(2)	0.360	89.0
Reference 91	*16.297*	*9.606*	*19.038*	*125.639*		
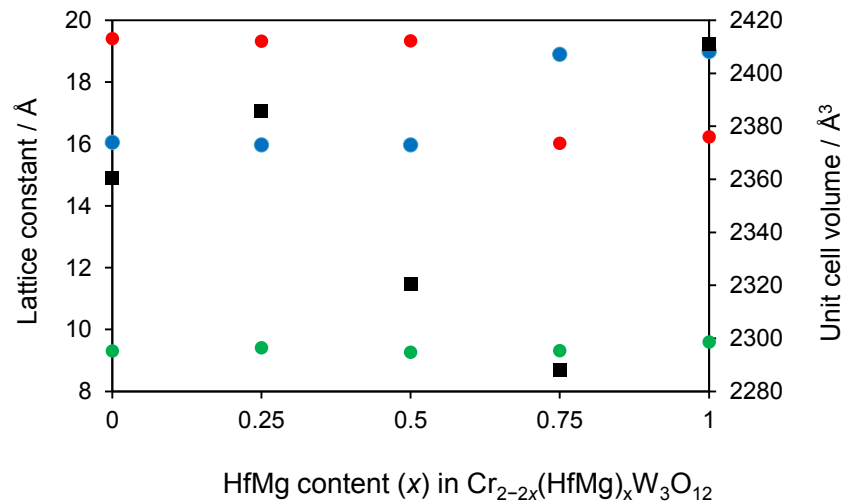
Figure 6.12: Lattice constants of the a- (●), b- (●), and c- (●) axes and unit cell volumes (■) of $Cr_{2-2x}(HfMg)_xW_3O_{12}$ materials ($P2_1/a$ setting). Error bars corresponding to estimated standard deviations are smaller than the symbols.

smallest molar volume of this series. It was possible to sinter this series of tungstate materials well enough to obtain considerable reduction of porosity.

6.3.3.2.   Thermal Expansion

An initial attempt to measure the CTEs of $Cr_{2-2x}(HfMg)_xW_3O_{12}$ materials revealed an unexpected result: while the solid solution materials ($x = 0.25$, 0.5, 0.75) showed a large volume increase upon heating followed by a decreased magnitude of the CTE,

typical of a monoclinic-orthorhombic phase transition, no reversal of this behaviour was seen subsequently on cooling. In order to examine this phenomenon, the samples were re-measured by dilatometry after they had been left at room temperature for five months. Measurements were then performed using a temperature ramp of 10 K min^{-1} to 500 °C or 700°C, followed by cooling at a rate of 5 K min^{-1} to room temperature. Following cooling, measurement continued at room temperature for 10 h.

The results for the three solid solutions are shown in Figure 6.13. The absence of a phase transition on cooling is evident; in fact there was not a significant change in the CTE upon crossing the phase transition temperature (*ca.* 100 °C). Possibly, an orthorhombic phase persists upon cooling, however XRD results (Figure 6.14) indicate that the materials are monoclinic immediately following cooling. This result implies that, for example, $Cr_{0.5}(HfMg)_{0.25}W_3O_{12}$ displays NTE in its monoclinic structure during cooling, a highly unusual phenomenon for such materials.

Upon reaching room temperature the materials contracted very slowly, indicating relaxation of their structures towards the equilibrium volume. This contraction was approximately linear as a function of time (from 180 min to 770 min as shown in Figure 6.13). The delayed volume change was investigated further using XRD. A powdered sample of $Cr_{0.5}(HfMg)_{0.75}W_3O_{12}$ was heated to 500 °C for one hour and then cooled to room temperature and immediately examined using XRD. Additional X-ray diffractograms were acquired after allowing the material to remain at room temperature (Figure 6.14). These showed increases in the positions of the peaks in 2θ, corresponding to contraction of the unit cell. This trend can be seen in the refined cell parameters in Figure 6.15 and Table 6.6. The contraction, expressed in terms of
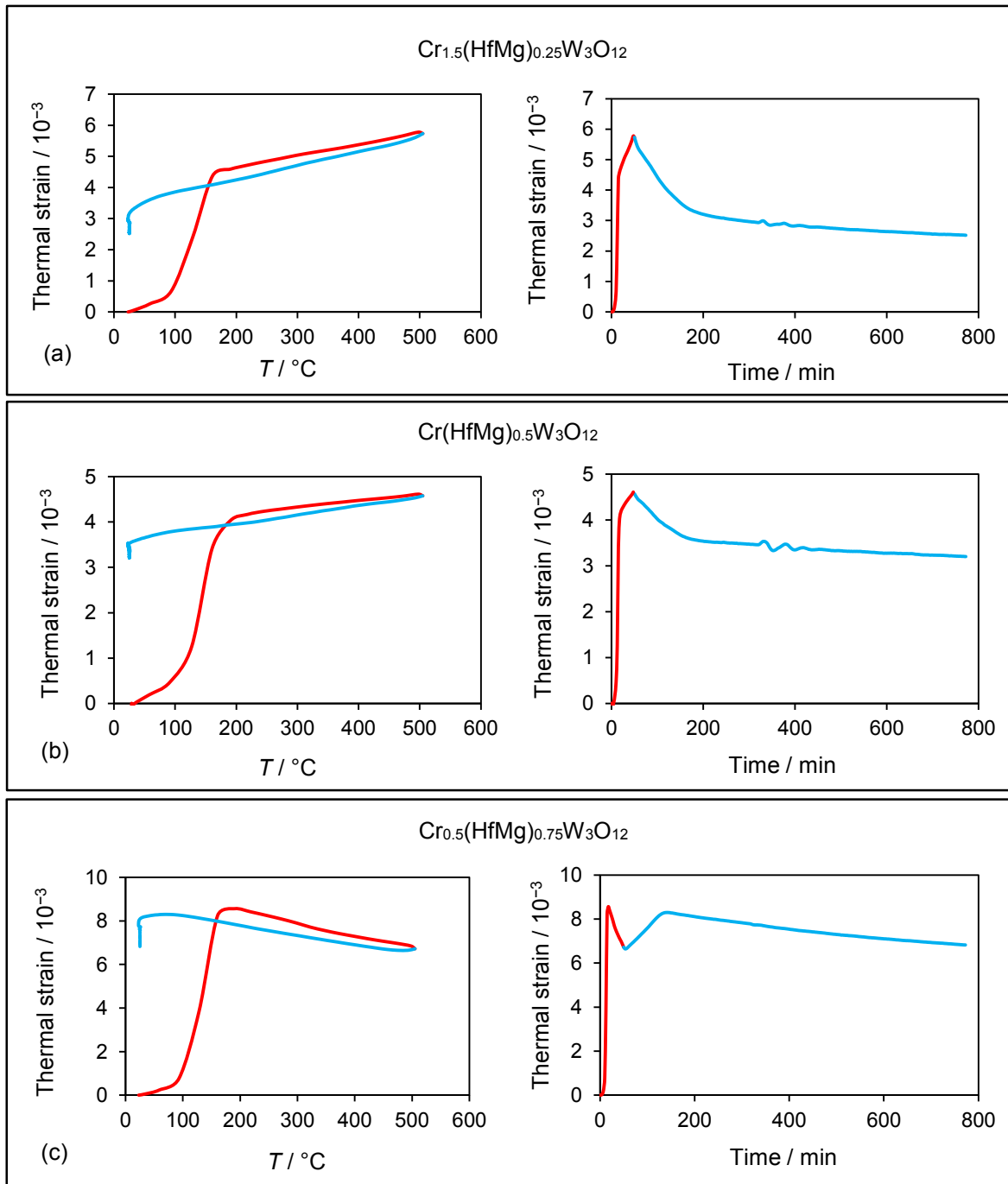
Figure 6.13: Dilatometric heating (red lines) and cooling (blue lines) curves for (a) $Cr_{1.5}(HfMg)_{0.25}W_3O_{12}$, (b) $Cr(HfMg)_{0.5}W_3O_{12}$, and (c) $Cr_{0.5}(HfMg)_{0.25}W_3O_{12}$, after the samples had been left at room temperature for five months prior to the experiment. Thermal strain is shown as a function of temperature (left column) and time (right column) in order to visualize the absence of the phase transition and delayed contraction upon cooling.
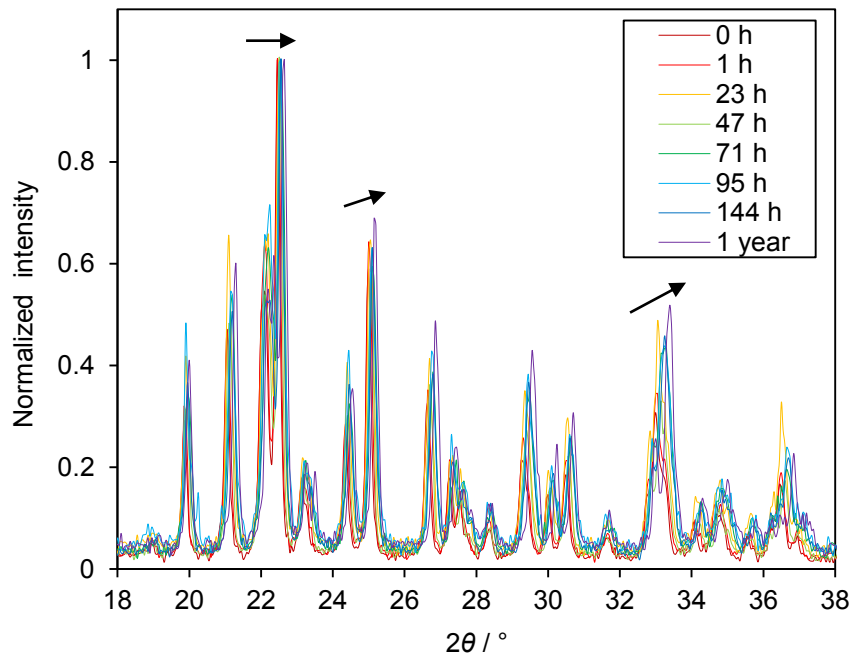
Figure 6.14: Portions of overlaid X-ray diffractograms of $Cr_{0.5}(HfMg)_{0.75}W_3O_{12}$ at various times (indicated in the legend) following cooling to room temperature from above the phase transition temperature. Arrows indicate the movement of peaks over time.
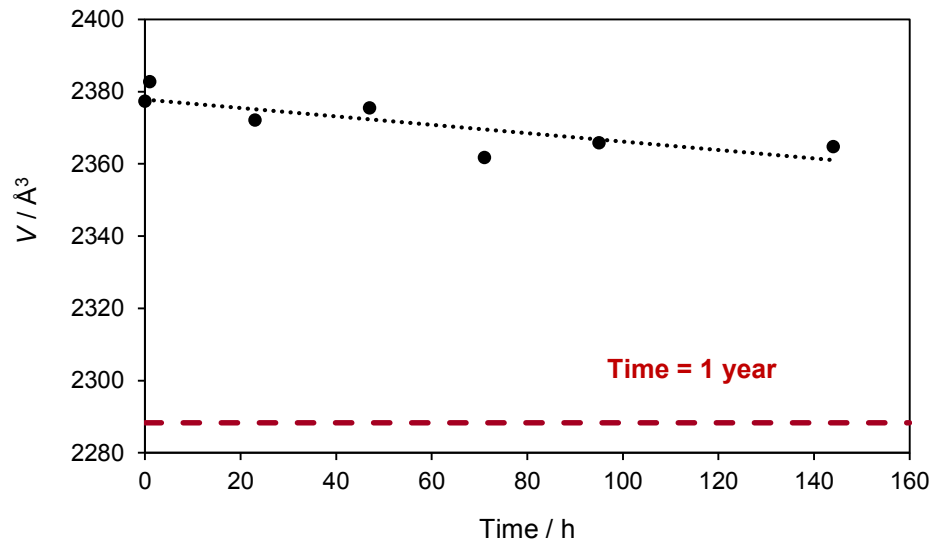
Figure 6.15: Unit cell volume of $Cr_{0.5}(HfMg)_{0.75}W_3O_{12}$ as determined from XRD as a function of time following cooling to room temperature from above the phase transition temperature. The dotted black line is a linear fit to the data intended as a guide to the eye. The dashed red line represents the unit cell volume after the sample was left for one year at room temperature.

Table 6.6: Lattice constants of $Cr_{0.5}(HfMg)_{0.75}W_3O_{12}$ and goodness-of-fit values as a function of time following cooling from above the phase transition temperature.

Time from cooling	a / Å	b / Å	c / Å	β / °	χ^2
0 h	19.192(1)	9.3866(6)	16.1492(7)	125.196(5)	1.097
1 h	19.320(1)	9.3589(4)	16.1452(6)	125.291(6)	0.905
23 h	19.300(1)	9.3543(7)	16.114(1)	125.372(6)	1.025
47 h	19.3067(9)	9.3447(4)	16.1257(6)	125.261(4)	0.981
71 h	19.2467(7)	9.3274(4)	16.0891(7)	125.143(3)	0.810
95 h	19.254(1)	9.3374(5)	16.1041(9)	125.199(5)	0.941
1 year	18.908(1)	9.3191(5)	16.031(1)	125.895(5)	0.815

volumetric strain, observed from XRD was an order of magnitude slower than that observed from dilatometry (-6×10^{-7} min^{-1} *vs.* -6×10^{-6} min^{-1}) and a larger volume difference was observed by XRD between the fully relaxed material and the material immediately following heating (4 % *vs.* 2 %). The differences in contraction rates and volume changes suggests a difference between the bulk and powdered samples, possibly related to nucleation or the sintered crystallites placing mechanical constraints on each other. In addition to changes in the positions of the Bragg peaks, changes in their normalized intensities were also seen in the diffractograms. This could be related to changes in atomic positions which cannot be elucidated from the Le Bail refinements.

Dilatometric curves of the end members of the series, $Cr_2W_3O_{12}$ and $HfMgW_3O_{12}$, are shown in Figure 6.16, and the dilatometric thermal expansion behaviours of all the members of the series are summarized in Figure 6.17 and Table 6.7. These end-member materials showed no change in length when they were held at room temperature following cooling. $Cr_2W_3O_{12}$ shows no evidence of a phase transition in the temperature range studied, contrary to a previous report.[287] However, its thermal expansivity over the full temperature range still falls in line with those of the three solid solution materials of
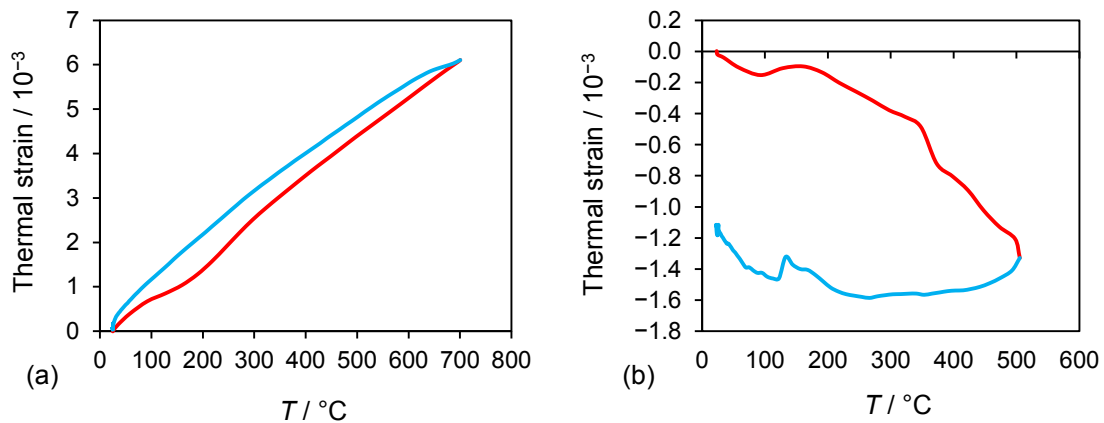
Figure 6.16: Dilatometric heating (red lines) and cooling (blue lines) curves of (a) $Cr_2W_3O_{12}$ and (b) $HfMgW_3O_{12}$.
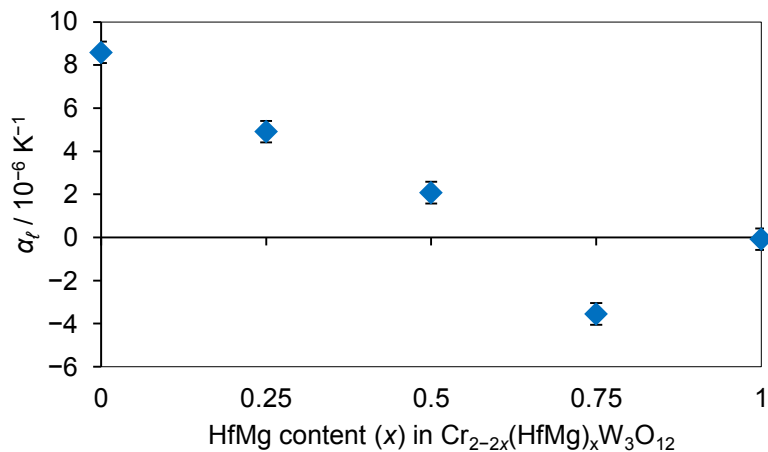
Figure 6.17: Thermal expansion in $Cr_{2-2x}(HfMg)_xW_3O_{12}$ materials as measured by dilatometry on cooling, presented as a function of composition. Estimated uncertainties are included.

Table 6.7: Coefficients of thermal expansion over given temperature ranges as determined from linear regression of dilatometric cooling curves of $Cr_{2-2x}(HfMg)_xW_3O_{12}$ materials. The literature result for $HfMgW_3O_{12}$ (from variable-temperature XRD) is included in italics. Estimated uncertainties are included.

Material	α_ℓ / 10^{-6} K^{-1}	Temperature range / °C
$Cr_2W_3O_{12}$	8.6 ± 0.5	25 to 700
$Cr_{1.5}(HfMg)_{0.25}W_3O_{12}$	4.9 ± 0.5	25 to 500
$Cr(HfMg)_{0.5}W_3O_{12}$	2.1 ± 0.5	25 to 500
$Cr_{0.5}(HfMg)_{0.75}W_3O_{12}$	-3.6 ± 0.5	25 to 500
$HfMgW_3O_{12}$	-0.1 ± 0.5	150 to 500
Reference 91	*−1.2*	*200 to 600*

this series (Figure 6.17). $HfMgW_3O_{12}$ has previously been reported to have a second-order monoclinic-orthorhombic phase transition between 125 °C and 200 °C,[91] and a small feature is seen in the dilatometric curve in that temperature range. The CTE of $HfMgW_3O_{12}$ as measured from the cooling curve is slightly higher than the literature value (-0.1×10^{-6} K^{-1} *vs.* -1.2×10^{-6} K^{-1}),[91] indicating some microstructural effects on the bulk CTE.

The overall thermal expansion behaviour of the $Cr_{2-2x}(HfMg)_xW_3O_{12}$ series of materials shows some similarities to that of the $In_{2-2x}(HfMg)_xMo_3O_{12}$ series, most notably an anomaly in the thermal expansivity at $x = 0.75$. In combination with the change in lattice constants between $x = 0.5$ and $x = 0.75$ in both series discussed above, the presence of two anomalies in this compositional range suggests that substitution of trivalent cations into a *Pna*2_1 material leads to a decrease in thermal expansivity up to the point that the Hf^{4+} and Mg^{2+} cations become disordered, leading to a *Pnca* phase with disordered A sites. This hypothesis could be tested by variable-temperature XRD.

6.3.3.3.   Mechanical Properties

The elastic properties of $Cr_{2-2x}(HfMg)_xW_3O_{12}$ materials, corrected for porosity (see Appendix B for uncorrected velocities of sound), are shown in Figure 6.18. With the exception of $Cr_2W_3O_{12}$, the materials followed a trend in their stiffness as a function of composition opposite to that of their CTE (*cf.* Figure 6.17), with one increasing as the other decreases and *vice versa*. This is similar to the behaviour of the $In_{2-2x}(HfMg)_xMo_3O_{12}$ materials (Section 6.3.1.3), which showed a decrease in stiffness with increasingly negative, rather than positive, thermal expansion. However in the $Cr_{2-2x}(HfMg)_xW_3O_{12}$ case the $x = 0.75$ material with anomalously low thermal expansion
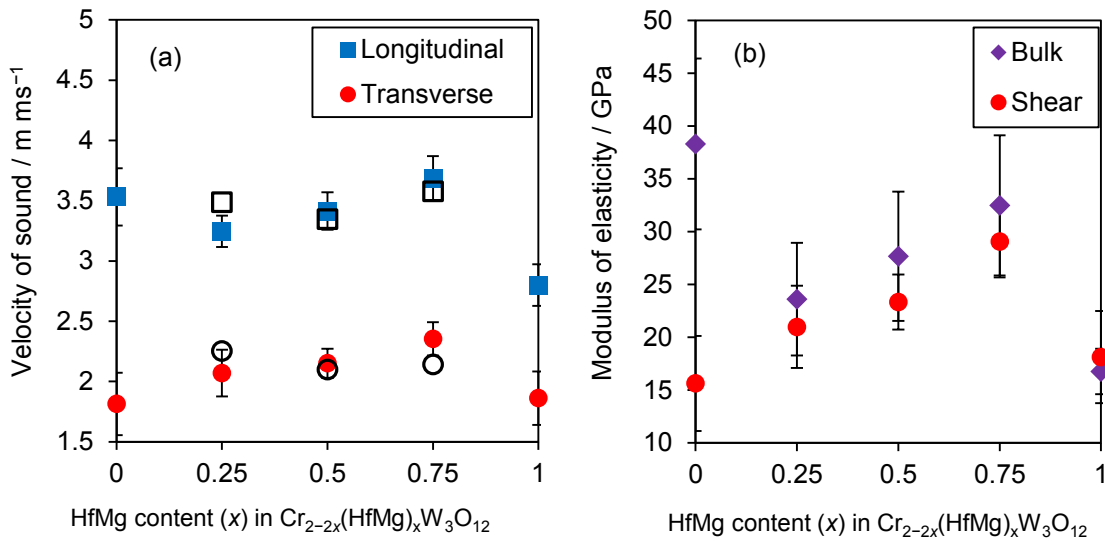
Figure 6.18: (a) Longitudinal and transverse velocities of sound and (b) bulk and shear moduli of $Cr_{2-2x}(HfMg)_xW_3O_{12}$. All measurements were performed at room temperature on monoclinic phases; data points marked as open symbols were measured on samples immediately following cooling from above the phase transition temperature.

has increased, rather than decreased stiffness relative to the other members of the series.

The shear modulus of $Cr_2W_3O_{12}$ fell in line with the trend, however its bulk modulus was significantly higher than expected based on the trend of the solid solution materials. This increase in the bulk modulus could be related to the apparent lack of a monoclinic-orthorhombic phase transition upon heating in this material; it behaves more like a conventional ceramic in its thermal expansion and mechanical properties.[16]

An additional set of measurements of the velocity of sound was acquired on the solid solution materials immediately following cooling from 350 °C in order to see if the mechanical properties changed during the delayed contraction of the material, and these are shown in Figure 6.18. These measurements showed only minor differences from those determinations performed on materials that had been stored at room temperature, even though the CTEs immediately following cooling are considerably lower than those of the relaxed monoclinic structure (see Figure 6.13). This, to some extent, validates the

comparison of the CTEs of the orthorhombic phases at elevated temperature to the mechanical properties of the monoclinic phases at room temperature.

6.4. Conclusions

Three series of solid solutions were studied in this chapter ($In_{2-2x}(HfMg)_xMo_3O_{12}$, $Sc_{2-2x}Al_{2x}W_3O_{12}$, and $Cr_{2-2x}(HfMg)_xW_3O_{12}$) and all were shown to vary from positive to negative thermal expansion as a function of composition. Anomalously negative thermal expansion was found in $In_{2-2x}(HfMg)_xMo_3O_{12}$ and $Cr_{2-2x}(HfMg)_xW_3O_{12}$ for $x = 0.75$, possibly related to a compositional phase transition between *Pnca* and *Pna2$_1$* phases. The elastic constants of the materials studied also varied significantly with composition, a finding that implies that selection of a material from the $A_2M_3O_{12}$ or $AMgM_3O_{12}$ family for a particular application must take into account its mechanical properties as well as its thermal expansion properties. The variations of the shear moduli were similar to those of the bulk moduli.

The bulk thermal expansion and elastic constants within a given series appeared to be correlated, although the nature of these correlations varied from series to series. Overall, the shear moduli tended to decrease with increasing magnitude of the CTE, while the relationship between the bulk moduli and the CTE was more complicated. This is perhaps to be expected given the influence of factors such as monoclinic-orthorhombic phase transitions, differences between molybdates and tungstates and *Pnca* and *Pna2$_1$* phases, and the absence of information regarding the axial properties of these anisotropic materials. Some of these problems are avoided in the computational study of elastic tensors presented in Chapter 8.

Upon cooling $Cr_{2-2x}(HfMg)_xW_3O_{12}$ solid solutions below their (presumed) orthorhombic-monoclinic transition temperatures no volume contraction or change in the CTE was observed. Subsequently, a contraction was shown to occur very slowly at room temperature. This phenomenon has not been previously reported in any $A_2M_3O_{12}$ or AMgM_3O_{12} materials; further study would be required to determine structural changes during and after cooling, and to understand the origin of this phenomenon.

Chapter 7: The Heat Capacities of Thermomiotic ScF$_3$ and ScF$_3$-YF$_3$ Solid Solutions[xix]

7.1. Background

The coefficient of thermal expansion of scandium trifluoride (ScF$_3$) has been reported to be negative over a wide temperature range (10 K to 1100 K).[292] ScF$_3$ has the cubic ReO$_3$ structure, which consists of corner-sharing ScF$_6$ octahedra (Figure 7.1). NTE in ScF$_3$ arises from transverse vibrations of the F atoms, which shorten the average Sc—Sc distance.[30,292] Recently, the thermal expansivities and compressibilities of a series of Y-substituted solid solutions of ScF$_3$ have been reported;[283] these materials are cubic and thermomiotic at room temperature but transition *via* cooperative static rotations of the ScF$_6$ octahedra into rhombohedral phases with positive thermal expansion upon cooling.

It has previously been suggested that materials with the ReO$_3$ structure are generally unstable with respect to distortion, largely due to dipole-dipole interactions.[293] Phase transitions potentially related to this instability have been reported in ScF$_3$ under *ca.* 0.1 GPa of pressure at 50 K[292] as well as in Sc$_{1-x}$Y$_x$F$_3$, and Sc$_{1-x}$Ti$_x$F$_3$.[294] The phenomenon of transition from a thermomiotic phase to a phase with positive thermal expansion is also seen in many thermomiotic materials from the $A_2M_3O_{12}$ and ABM_3O_{12} families (see Section 1.6), and represents a major challenge to the use of thermomiotic materials in applications where a large temperature range of dimensional stability is

---
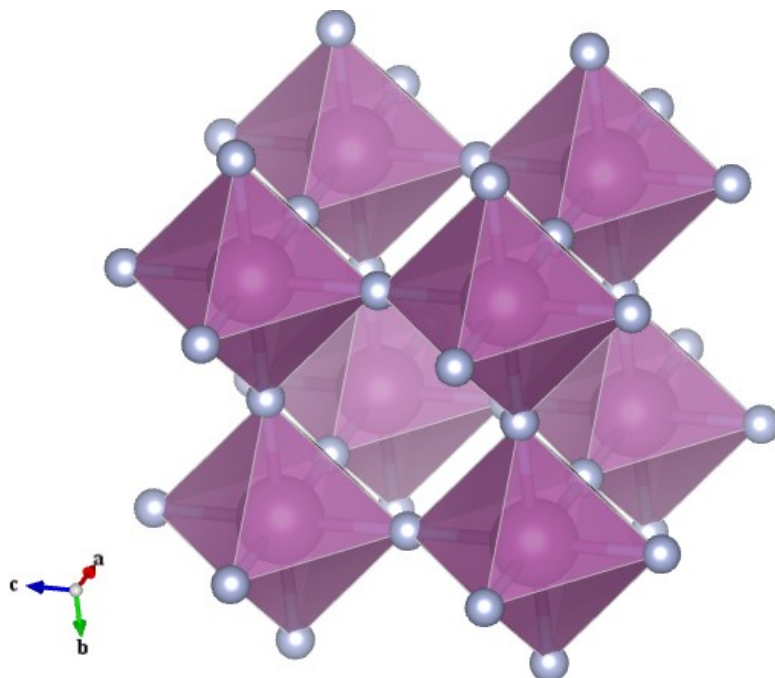
Figure 7.1: The cubic ($Fm\bar{3}m$) structure of ScF_3,[292] with ScF_6 octahedra shown in purple and F atoms shown as grey spheres.

required. A primary goal of this investigation was to examine the phase transitions in Y-substituted ScF_3 using relaxation calorimetry and definitively determine whether a similar transition in ScF_3 occurs in the absence of applied pressure.

This chapter reports a low-temperature calorimetric study of ScF_3 and Y-substituted ScF_3 ($Sc_{1-x}Y_xF_3$, $0.05 \leq x \leq 0.25$). The heat capacity of ScF_3 has not previously been reported below room temperature; the current results present insight into the phononic and thermodynamic properties of ScF_3. Specifically, the low-frequency modes which lead to negative thermal expansion have been shown to lead to a peak in the heat capacity expressed as $C_P\,T^{-3}$ which is absent from conventional, positive thermal expansion materials.[1]

DFT calculations were used to determine the heat capacity of ScF_3 for comparison, as well as the elastic tensor. The heat capacity calculated using the whole

Brillouin zone (BZ) was compared with that calculated knowing only the phonon frequencies at the Γ point. This comparison was performed in order to assess the potential of using a simplifying assumption: that a reasonable estimate of the heat capacity of thermomiotic materials can be obtained using the Einstein equation to predict the heat capacity of the optic modes based on their frequencies at Γ and the Debye equation to predict the heat capacity of the acoustic modes. This assumption could be useful, for example, in situations where the heat capacity must be estimated to convert thermal diffusivity into thermal conductivity,[3] and would require significantly less computational expense for large systems. The effect of dispersion on heat capacity was previously investigated in $Y_2Mo_3O_{12}$ and was found to play a small but significant role.[274]

7.2. Procedures

Dr. Cody Morelock at the Georgia Institute of Technology prepared samples of $Sc_{1-x}Y_xF_3$ ($x = 0.05, 0.10, 0.20,$ and 0.25) by the solid-state reaction of ScF_3 and YF_3,[294] and assessed their lattice constants and sample purity by XRD.[295]

The heat capacities of ScF_3, $Sc_{0.95}Y_{0.05}F_3$, $Sc_{0.90}Y_{0.10}F_3$, $Sc_{0.80}Y_{0.20}F_3$, and $Sc_{0.75}Y_{0.25}F_3$ were measured by relaxation calorimetry following the procedure described in Section 2.3.3. Data tables and sample masses are presented in Appendix D.

DFT calculations of the phononic structure, elastic constants, and heat capacity of ScF_3 were carried out in ABINIT (see Section 2.8).[186,190,191] Norm-conserving pseudopotentials generated by the OPIUM code[296] were used as received from the Bennett and Rappe Pseudopotential Library.[297] Perdew–Burke–Ernzerhof (PBE) GGA exchange-correlation functionals were used.[298] These functionals were compared to LDA functionals and found to give a value of the bulk modulus of ScF_3 closer to the

experimental value ($\approx$ 60 GPa).[283,292] This point of comparison was chosen because

experimental results suggest that the bulk modulus of ScF_3 is largely independent of

temperature between 300 and 500 K[283] (unlike some other thermomiotic materials such as

ZrW_2O_8[25] and HfW_2O_8[299] for which the bulk modulus is strongly temperature dependent),

which would facilitate direct comparison with first-principles calculations. Additionally,

the temperature-dependent phonon spectrum experimentally obtained by inelastic neutron

scattering shows little change in the energy of the low-energy phonons with

temperature.[30]

The experimental lattice constant (the only structural parameter of ScF_3

unrestricted by symmetry) was relaxed until the maximum stress in the cell was below

10^{-7} hartree/bohr^3, resulting in a 1.4 % increase of the lattice constant and a final internal

pressure of 1.06×10^{-3} GPa. Calculation of the electronic structure of ScF_3 was then

performed using a 50 hartree plane-wave-energy cut-off and a $6 \times 6 \times 6$ shifted

Monkhorst–Pack grid[192] of **k**-points. This grid size corresponds to a spacing of points of

0.042 Å^{-1}. Subsequently, the responses to electric fields, atomic displacements and

strains were computed using the response-function functionality of ABINIT;[195,196,197] the

atomic displacements were computed over a $6 \times 6 \times 6$ grid of **q**-points. The dynamical

matrices resulting from these calculations were then used to calculate the stiffness tensor

and interpolated over an $80 \times 80 \times 80$ grid of **q**-points to compute the phonon dispersion

relation and the heat capacity (see Appendix D for data). The stiffness tensor was

calculated to determine the Debye temperature, to compare the bulk modulus (K) to

experiment, and to determine the heretofore unreported shear modulus (G), Young's

modulus (Y), and Poisson ratio (μ) of ScF_3.

166

For comparison, the heat capacity was also calculated using only the phonon frequencies at Γ and the Debye characteristic temperature (θ_D). The heat capacity of the optic bands was calculated treating each optic mode, with frequency v_i, as an independent Einstein oscillator, *i.e.*, as:[3]

$$C_V = \sum_i g_i N k \left(\frac{h v_i}{kT}\right)^2 \frac{e^{\frac{h v_i}{kT}}}{\left(e^{\frac{h v_i}{kT}} - 1\right)^2},$$ (7.1)

where N is the number of atoms in a mole of formula units and g_i is the degeneracy of the ith mode. The heat capacity due to the acoustic bands was calculated using the Debye equation, *i.e.*, as:[3]

$$C_V = 9 \left(\frac{\theta_D}{T}\right)^3 \int_0^{\theta_D/T} \frac{x^4 e^x}{(e^x - 1)^2} dx.$$ (7.2)

The Debye temperature (which is defined as $\frac{h}{2k}\left(\frac{1}{3v_l^3} + \frac{2}{3v_t^3}\right)^{-1/3} \sqrt[3]{\frac{6N}{\pi V}}$ for an elastically isotropic material) was obtained from the elastic constants using a geometric Voigt–Reuss–Hill (VRH) average,[300] which generally produces the most accurate estimates of the Debye temperature for polycrystalline aggregates.[300]

7.3. Results and Discussion

The calculated stiffness tensor, $\mathbf{c}$, of ScF$_3$ has the following unique elements: $c_{11} =$ 230 GPa, $c_{12} = 17.3$ GPa, $c_{44} = 18.0$ GPa. The geometric VRH values for the isotropic elastic constants are $K = 88.4$ GPa, $G = 38.0$ GPa, $Y = 99.1$ GPa and $\mu = 0.30$.[300] This leads to a value of 505 K for the Debye temperature, θ_D. Interestingly, there is a large difference between the Voigt (uniform strain) and Reuss (uniform stress) values for the shear modulus, with $G_V = 53.4$ GPa and $G_R = 27.1$ GPa. Because $G_V = G_R$ for an isotropic solid, the large difference can be interpreted as an indication of elastic

167

anisotropy in this cubic material. This can be expressed numerically as the universal

anisotropy (so named because of its applicability to any space group), A_U, defined as:[301]

$$A_U = 5\frac{G_V}{G_R} + \frac{K_V}{K_R} - 6,$$ (7.3)

where K_V and K_R are the Voigt and Reuss bulk moduli. For ScF_3, $A_U = 4.9$, which is

larger than, for example, almost all cubic elemental metals.[301] The origin of this

anisotropy can be understood by considering the difference between a force applied along

[100], where there are Sc–F–Sc chains, and a force applied along [111], where there are

isolated Sc^{3+} ions. This result is consistent with the large role dispersion plays in the

thermal properties of ScF_3 (*vide infra*).

The calculated phonon dispersion relation and the phonon DOS of ScF_3 are

presented in Figure 7.2 and Figure 7.3. The DFT-calculated phonon dispersion and DOS

have been previously reported and compared to inelastic neutron scattering results;[30]

similar calculations have been carried out here of the heat capacity and elastic properties

of ScF_3, not previously reported.

The molar heat capacity at constant pressure (C_P) of ScF_3, as measured

experimentally, was converted to molar heat capacity at constant volume (C_V) using

literature values for the compressibility and temperature-dependent CTE[283] as:[3]

$$C_V = C_P - \alpha_V{}^2 T K V_m.$$ (7.4)

The result is plotted along with the DFT C_V result in Figure 7.4. The molar volumes for

the C_V value from DFT and the experimental C_V are normally slightly different: the

former is constant, and the latter allows for different volumes at different temperatures.

Nevertheless, C_V values can be directly compared in this case because the compressibility

and CTE of ScF_3 are largely invariant with volume.[283] The full-BZ DFT calculations of
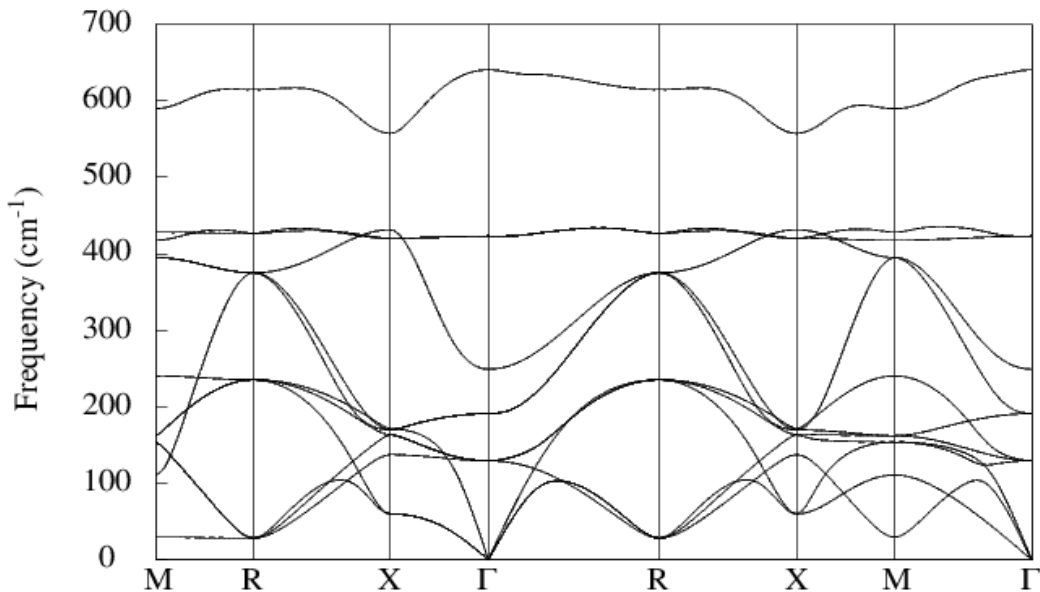
Figure 7.2: The calculated phonon dispersion relation for ScF$_3$. Special points in the Brillouin zone are marked as M ($\mathbf{q}$ = [0.5 0.5 0]), R ($\mathbf{q}$ = [0.5 0.5 0.5]), X ($\mathbf{q}$ = [0 0.5 0]), and Γ ($\mathbf{q}$ = [0 0 0]).
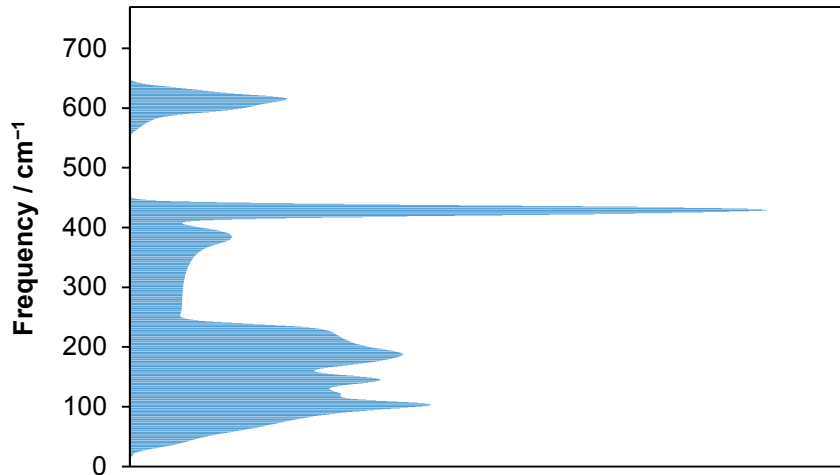
Figure 7.3: The calculated phonon density of states of ScF$_3$. 1 cm^{-1} bins were used.

the heat capacity provide an excellent match to the experiment in the temperature range

from 15 to 400 K, but diverge significantly below this temperature (Figure 7.4).

Comparison of the calculated phonon DOS (Figure 7.3) with the experimental DOS

reported from inelastic neutron scattering[30] shows that there are fewer states in the
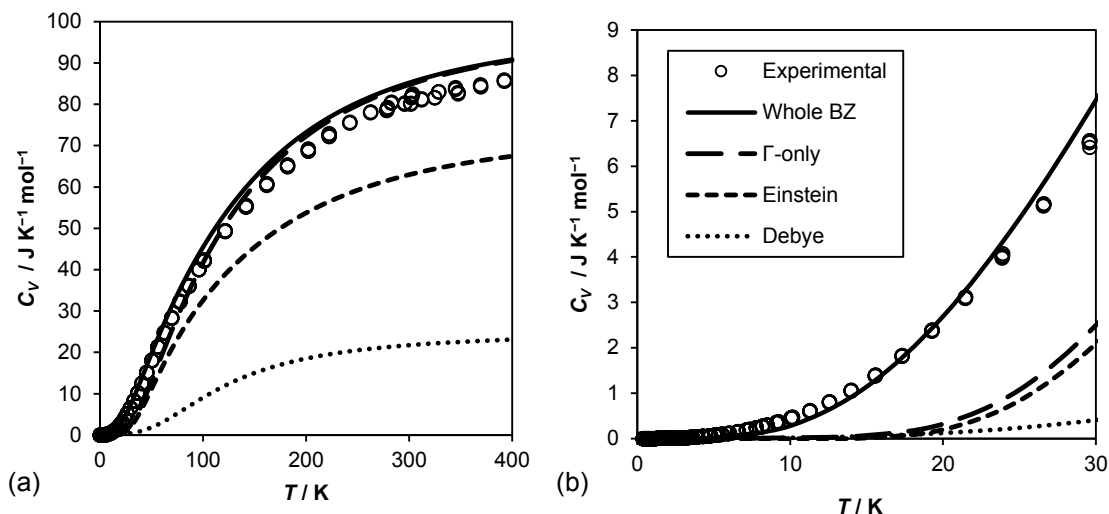
Figure 7.4: The molar constant-volume molar heat capacity of ScF_3 as a function of temperature as determined from experiment, as calculated using the whole Brillouin zone, and as calculated using the sum of the Einstein models of the phonon frequencies at the Γ point and the Debye contribution from the acoustic modes (a) over a wide temperature range, and (b) at low temperature. The Einstein calculation of the heat capacity of the optic modes and the Debye calculation of the heat capacity of the acoustic modes are also shown. Adapted from Reference 295 with permission.

calculated DOS at the lowest energies. The differences between experiment and the full-BZ calculation in the heat capacity below 15 K could possibly be due to quartic anharmonicity of transverse motions of the F atoms, which has been reported to significantly influence the low-temperature thermal expansion of ScF_3,[30] since the DFT calculations are confined to the harmonic approximation. Previously reported frozen-phonon calculations showed softening of the potential of the R4+ mode when a quartic model was used.[30] Since this anharmonic behaviour is expected to be general to the low-energy rigid-unit modes near R,[30] the reduction in their energies would lead to an increase in the low-temperature heat capacity above that predicted by the harmonic approximation. In order to investigate this discrepancy further, additional frozen-phonon or molecular dynamics calculations on supercells should be performed to better

understand the effect of anharmonicity on the low-temperature phononic properties of ScF_3.

Additionally, the acoustic band between R and M was calculated to be nearly dispersionless (see Figure 7.2). The calculated energy of the acoustic band at R is higher than that reported in Reference 30. If the present calculations overestimate the energy of the acoustic band at R it would lead to an underestimation of the low-temperature heat capacity.

The low-temperature heat capacity of ScF_3 is of interest because the presence of low-dispersion low-frequency modes is highly correlated with negative thermal expansion, for example in HfW_2O_8[21] and $Zn(CN)_2$,[11] as these modes often correspond to coordinated rotations of rigid units. Many thermomiotic materials have low-energy vibrational modes that are not well-described by the Debye model, which manifest as a low-temperature peak in $C_P\ T^{-3}$ (Figure 7.5). Similar peaks have previously been reported in other thermomiotic materials, although they are usually attributed more to the contribution of low-energy optic bands than to the non-Debye-like behaviour of the acoustic bands.[85,126,270,274,275] When expressed per mole of atoms rather than per mole of formula units, the height of the peak in $C_P\ T^{-3}$ of ScF_3 is similar in magnitude to reports for other thermomiotic materials (0.15 mJ K^{-4} mol^{-1} for ScF_3; *cf.* $Y_2Mo_3O_{12}$, 0.4 mJ K^{-4} mol^{-1};[274] ZrW_2O_8, 0.3 mJ K^{-4} mol^{-1};[126] $HfMo_2O_8$, 0.2 mJ K^{-4} mol^{-1};[85] and $Sc_2W_3O_{12}$, 0.2 mJ K^{-4} mol^{-1}),[275] indicating directly from experimental heat capacity data that there are low-energy vibrational states with negative Grüneisen parameters available in ScF_3.

The Γ-only calculations dramatically underestimate the heat capacity at low temperatures (especially $T < 100$ K), indicating that dispersion plays an important role in
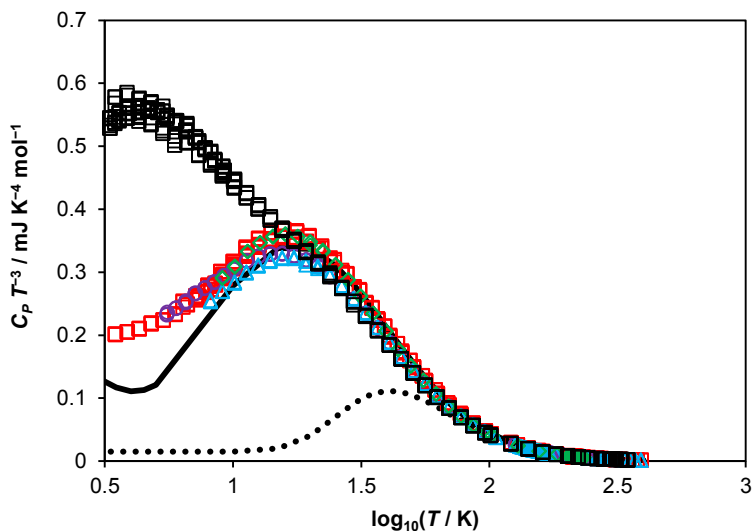
Figure 7.5: The experimental molar heat capacity of ScF_3 ($\square$), $Sc_{0.95}Y_{0.05}F_3$ ($\circ$), $Sc_{0.9}Y_{0.1}F_3$ ($\triangle$), $Sc_{0.8}Y_{0.2}F_3$ ($\diamond$), and $Sc_{0.75}Y_{0.25}F_3$ ($\square$), expressed as $C_P T^{-3}$, as a function of temperature, and for ScF_3 as calculated using the whole Brillouin zone (solid black line), and as calculated without dispersion using the optic phonon frequencies at the Γ point and the Debye temperature (dotted black line). Adapted from Reference 295 with permission.

the low-temperature heat capacity of ScF_3. The Debye contribution underestimates the acoustic modes at low temperatures due to their unusually low energies near the R and M points (Figure 7.2). Additionally, there are low-frequency optic modes with negative Grüneisen parameters that contribute to the heat capacity at low temperature.[30] Therefore, ScF_3 behaves thermally at low temperatures as if the lattice is much less stiff than is implied by the elastic constants, due to the vibrational modes that are responsible for NTE.

Experimentally determined heat capacities of four $Sc_{1-x}Y_xF_3$ solid solutions are shown in Figures 7.5 and 7.6; complete data tables are available in Appendix D. The molar heat capacities of Y-substituted ScF_3 are close to that of ScF_3 in their cubic (room temperature) phases; however, upon cooling, they transition between 250 K and 100 K (transition temperature varies with composition) to rhombohedral phases,[283] at which

172
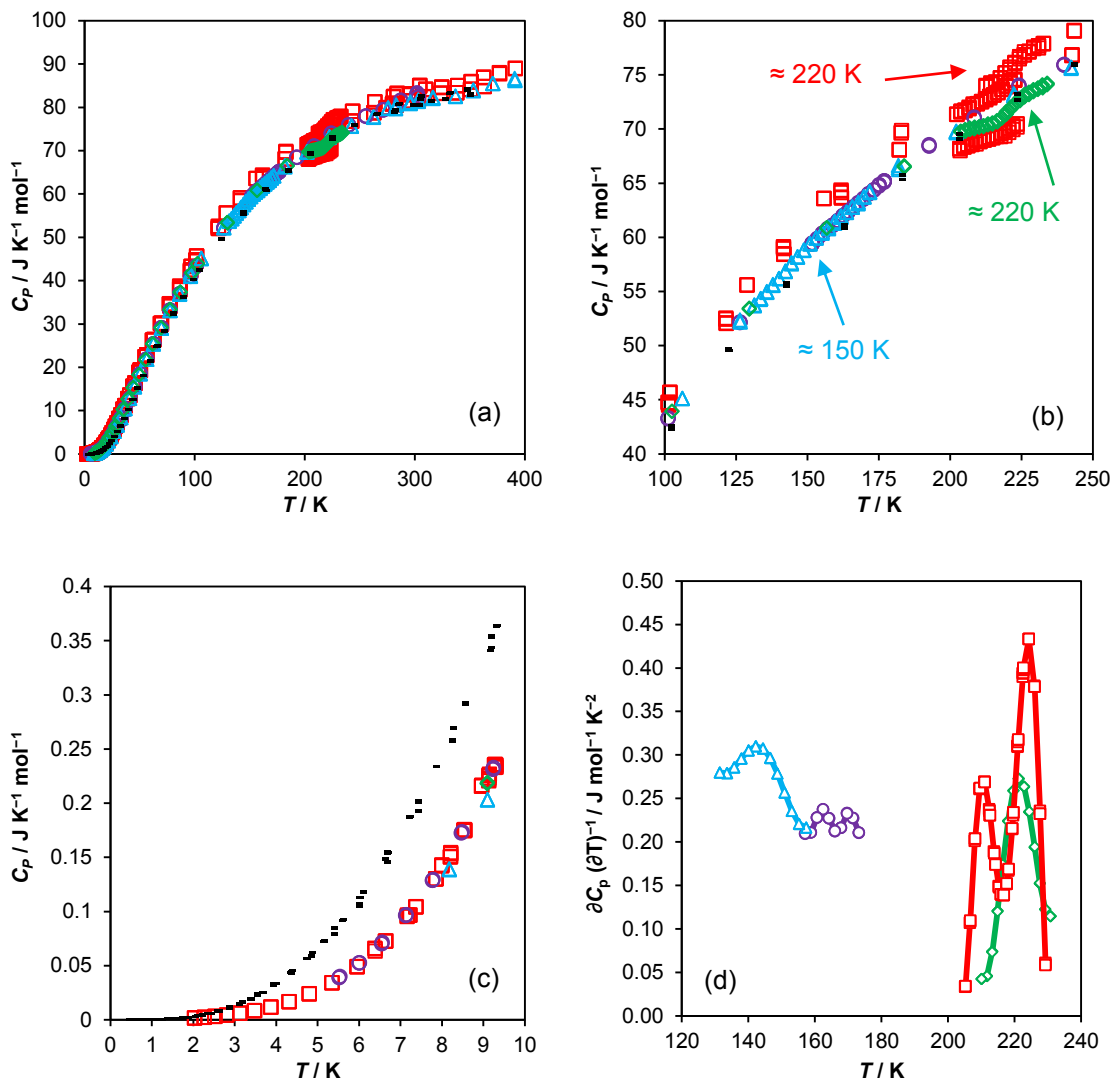
Figure 7.6: The experimentally measured molar heat capacities of $Sc_{0.95}Y_{0.05}F_3$, ($\circ$) $Sc_{0.9}Y_{0.1}F_3$, ($\triangle$) $Sc_{0.8}Y_{0.2}F_3$ ($\diamond$), $Sc_{0.75}Y_{0.25}F_3$ ($\square$), and ScF_3 (-) as a function of temperature: (a) full temperature range view; (b) phase-transition temperature region (with estimated cubic-rhombohedral phase transition temperatures indicated), (c) low-temperature region, and (d) temperature derivatives in the phase transition region (lines are included as a guide to the eye). Adapted from Reference 295 with permission.

point their heat capacities begin to diverge from that of ScF_3. The low-temperature heat

capacities of the Y-substituted materials are smaller than for ScF_3 (Figures 7.5 and

7.6(c)), a finding which correlates with the positive thermal expansion of the

rhombohedral phases.

Although the heat capacity of ScF_3 is larger than that of the Y-substituted materials at low temperature, significant peaks are visible in the heat capacities of the latter expressed as $C_P T^{-3}$ (Figure 7.5), which is atypical for positive thermal expansion materials.[1] However, a similar result was previously reported in the heat capacity of the framework material $HfMgMo_3O_{12}$, which has low positive thermal expansion at room temperature, undergoes a pseudo-second-order transition into a monoclinic phase upon cooling, but still shows a significant peak in $C_P T^{-3}$ in this low-temperature phase.[270]

$Sc_2Mo_3O_{12}$, a thermomiotic material at room temperature, also undergoes a transition to a positive thermal expansion phase upon cooling and shows a peak in $C_P T^{-3}$ at low temperature.[275] Presumably, some of the low-frequency modes with negative Grüneisen parameters can persist following low-energy displacive phase transitions of framework materials even when the material as a whole exhibits a positive CTE. Experimental identification of the changes in the phononic structure related to the phase transition in the solid solutions and their influence on the thermal expansion would require variable-pressure, variable-temperature inelastic neutron scattering. Although computational investigation of such a disordered system is possible in principle, for example using a special quasirandom structure model[302] to determine the phononic structure of rhombohedral $Sc_{1-x}Y_xF_3$, in practical terms to incorporate the Y-doping and the subsequent structural distortions would require the use of a unit cell much larger than that of ScF_3, considerably increasing the resources required.

Cubic-rhombohedral phase transitions can be observed (Figure 7.6) in the heat-capacity data for $Sc_{0.8}Y_{0.2}F_3$ and $Sc_{0.75}Y_{0.25}F_3$ at approximately 220 K and very weakly for $Sc_{0.9}Y_{0.1}F_3$ at 150 K. These temperatures are somewhat higher than those reported from

variable-temperature XRD;[283] however, they are close to the inflection point in the reported volume-temperature curve. The small anomalies in heat capacity are consistent with second-order phase transitions, as suggested by the XRD data.[283] A phase transition was not observed in the heat capacity of $Sc_{0.95}Y_{0.05}F_3$; possibly it was below the detection limit. A low enthalpy change is consistent with the low-temperature heat capacity results: the relatively high values of the low-temperature heat capacity suggest that the Y-doped ScF_3 solid solutions have considerable vibrational entropy in their rhombohedral phases,[15] stabilizing them with respect to the cubic phase, which in the case of ScF_3 also has considerable vibrational entropy.

There is no experimental evidence of a phase transition in ScF_3 at any point in the temperature range studied (0.38 K to 390 K). The low-temperature heat capacity of ScF_3 is significantly higher than that of the Y-substituted materials down to the lowest temperature measured for those samples (2.03 K for $Sc_{0.75}Y_{0.25}F_3$). This finding is consistent with the absence of negative-frequency vibrational modes in the DFT $T = 0$ K phonon structure, which would be indicative of structural instability. The present experimental and theoretical results, in combination with previously reported low-temperature diffraction experiments,[30,283,292] suggest that ScF_3, in the absence of applied pressure, is not susceptible to the distortional instability identified in other ReO_3 structures.[293]

7.4. Conclusions

The experimental heat capacity of ScF_3 from 0.38 to 390 K shows no evidence of a phase transition. The low-temperature heat capacity of ScF_3 shows significant deviation from the Debye model, which was shown from the calculated phonon dispersion to be

due to the low-energy phonon modes that are responsible for negative thermal expansion in ScF_3. The heat capacities of $Sc_{0.95}Y_{0.05}F_3$, $Sc_{0.9}Y_{0.1}F_3$, $Sc_{0.8}Y_{0.2}F_3$, and $Sc_{0.75}Y_{0.25}F_3$ were reported; the last three show evidence of a cubic-rhombohedral phase transition as previously reported. The low-temperature heat capacities of the Y-doped rhombohedral phases have a smaller low-temperature anomaly, in terms of $C_P\,T^{-3}$, than ScF_3.

Chapter 8: Calculated Elastic Tensors and Γ-point Phonon Energies of $A_2Mo_3O_{12}$ Materials and $ZrMgMo_3O_{12}$

8.1. Background

Materials from the $A_2M_3O_{12}$ and $AMgM_3O_{12}$ families are known to display highly anisotropic thermal expansion properties.[1] This anisotropic thermal expansion can cause large thermal stresses and subsequently microcracking in polycrystalline materials with randomly oriented grains.[205] As will be demonstrated in Chapter 9, the anisotropy of the elastic constants affects the thermal stress distributions. The anisotropy of the elastic properties of these materials is generally unknown, and more difficult to determine experimentally than the CTE anisotropy. Therefore, the elastic tensors of $Al_2Mo_3O_{12}$, $Sc_2Mo_3O_{12}$, and $ZrMgMo_3O_{12}$ have been calculated here. Together with that of $Y_2Mo_3O_{12}$ (calculated by Dr. Josef Zwanziger),[274] this provides elastic constants of materials ranging from low positive to large negative thermal expansion.

As discussed in Chapter 6, examination of elastic properties of these materials has previously been limited to determination of bulk moduli by variable-pressure XRD. This experiment can yield information about directional compressibilities; for example in $Sc_2W_3O_{12}$[26] and $Sc_2Mo_3O_{12}$[27] the compressibility along an axis was shown to be positively correlated with the thermal expansion along that axis. However, the technique has limitations, for example the compressibilities in orthorhombic $Al_2W_3O_{12}$ could not be accurately determined due to a pressure-induced phase transition,[27] and no information about shear elasticity is obtained. The use of ultrasonic measurement to obtain shear moduli of bulk polycrystalline samples (Chapter 6) contributes some additional

information, but experimental determination of the full elastic tensor would require single crystals for Brillouin spectroscopy or resonant ultrasound spectroscopy.

Therefore, computational methods are, for practical reasons, the best choice to study the full elastic anisotropy of $A_2M_3O_{12}$ materials. In the present work, the materials studied were limited to molybdates because of the increased computational expense that would be required to include the $4f$ orbitals of tungsten. There is an associated drawback: the DFT calculations were performed without inclusion of thermal effects (*i.e.*, at $T = 0$ K). Since $A_2Mo_3O_{12}$ materials (except $Y_2Mo_3O_{12}$) transition into a monoclinic phase upon cooling, the calculations were performed on a phase which is not stable at absolute zero. Therefore the phononic structures will contain vibrational modes with negative energy that cause the instability of the orthorhombic structure.[9,141,303] However, since the orthorhombic-monoclinic phase transition involves rotation of the coordination polyhedra,[150] the unstable mode will be located away from the Γ point[293,304] and is not caused by an instability of acoustic modes near Γ.[305] Additionally, because many thermomiotic materials have highly temperature-dependent bulk moduli,[8,25,31,299] DFT results will not necessarily match room-temperature elastic constants.

The energies of the optic phonons at Γ were also calculated using DFT, as calculation of the full dispersion relationship would be too computationally expensive. Low-energy optic phonon modes in $A_2M_3O_{12}$ materials corresponding to polyhedral distortions can have large negative Grüneisen parameters,[46,47,143] and therefore their energies play an important role in the thermal expansion behaviour. Determination of optic phonon frequencies also allows further validation of the calculations by comparison to experimental Raman spectra.

8.2. Procedures

Elastic tensors and Γ-point phonons were calculated using density functional perturbation theory in ABINIT[186,190,191] following the procedures described in Section 2.8. The structures of $Al_2Mo_3O_{12}$[140] and $Sc_2Mo_3O_{12}$[277] were taken from the literature, while the structure of $ZrMgMo_3O_{12}$ is given in Table 5.1. PBE GGA exchange-correlation functionals were used in all cases.[298] In the cases of $Al_2Mo_3O_{12}$ and $Sc_2Mo_3O_{12}$, norm-conserving pseudopotentials generated using the OPIUM code[296] from the Bennet and Rappe pseudopotential library[297] were used. For $ZrMgMo_3O_{12}$, two-projector optimized norm-conserving Vanderbilt pseudopotentials[306] provided by Dr. Josef Zwanziger were used. These pseudopotentials were tested by comparison of calculated bulk moduli to experimental values for MgO (-7.2 % deviation),[307] ZrO_2 (-1.6 % deviation),[232] and Mo (-3.4 % deviation),[xx,308] yielding reasonable results.[185] Computational parameters determined following convergence studies and structure optimization are listed in Table 8.1. Shifted Monkhorst-Pack **k**-point grids were used.[192]

Table 8.1: Parameters determined by convergence studies and volume changes and final pressures following structural relaxation.

Material	Plane wave cut-off energy / Hartree	**k**-point grid dimensions	**k**-point grid spacing / $Å^{-1}$	Volume change relative to experiment / %	Pressure / GPa
$Al_2Mo_3O_{12}$	30	$2 \times 2 \times 2$	0.094	6.4	1×10^{-4}
$ZrMgMo_3O_{12}$	35	$2 \times 3 \times 3$	0.063	7.5	9×10^{-4}
$Sc_2Mo_3O_{12}$	35	$2 \times 3 \times 3$	0.107	7.3	2×10^{-4}

[xx] Mo was chosen as the test material because MoO_3 has a layered structure and therefore is an unsuitable point of comparison,[185] and the bulk modulus of MoO_2 has not been reported in the literature.

Experimental results regarding elastic properties of $Al_2Mo_3O_{12}$ (albeit in the monoclinic phase) are presented in Section 3.5, and those of $ZrMgMo_3O_{12}$ in Section 5.3.3. Attempts were made to synthesize $Sc_2Mo_3O_{12}$ in order to measure its elastic properties and Raman spectrum, however no synthesis temperature was found where sufficient densification occurred without decomposition of the material, even when sintering times as long as 96 h were used. However, the bulk modulus of $Sc_2Mo_3O_{12}$ has previously been reported from variable-pressure XRD (32 ± 2 GPa).[27]

Y$_2$Mo$_3$O$_{12}$ was synthesized in order to compare its bulk elastic constants to DFT-calculated values.[274] Samples were prepared using the solid-state reaction method described in Section 2.1 with Y_2O_3 (Acros Organics, 99.99 %) and MoO_3 (Sigma Aldrich, $\geq$ 99.5 %) as reagents. Sintering was performed for 24 h at 950 °C using a temperature ramp up of 5 K min^{-1} and natural cooling. Under ambient conditions, $Y_2Mo_3O_{12}$ readily absorbs moisture from the air; this water is incorporated into the lattice, inhibits the rocking motion of the tetrahedra, and destroys the *Pbcn* framework responsible for thermomiotic behaviour.[145,309] To avoid hydration of the samples, they were sintered in Ar atmosphere and then immediately placed in a desiccator. The phase purity of the $Y_2Mo_3O_{12}$ synthesized was confirmed as $\gtrsim$ 99 % by XRD (Siemens D-500 powder diffractometer, collected by Andy George, see Appendix A, Figure A21 for pattern).

The longitudinal and transverse velocities of sound of $Y_2Mo_3O_{12}$ were determined by ultrasonic measurement of three sintered $Y_2Mo_3O_{12}$ pellets (see Reference 274 for further description) as described in Section 2.5. The measurements were performed in dry N_2 atmosphere. The samples measured had an average density of 86 % of the theoretical density.

Raman spectra of $Y_2Mo_3O_{12}$ and $Al_2Mo_3O_{12}$ were measured following the procedure described in Section 2.6. $Y_2Mo_3O_{12}$ was measured in a sealed glass tube. The Raman spectrum of $ZrMgMo_3O_{12}$ is described in Chapter 5. The Raman spectrum of $Sc_2Mo_3O_{12}$ was not acquired due to the problems involving decomposition described above, however it has been reported in the literature.[310,311]

8.3. Results and Discussion

8.3.1. Elastic Tensors

The bulk velocities of sound of $Y_2Mo_3O_{12}$, following correction for porosity (see Appendix B for uncorrected values), were determined to be $v_l = 3.4 \pm 0.1$ m ms^{-1} and $v_t = 2.0 \pm 0.1$ m ms^{-1}. These values correspond to a bulk modulus of 21 ± 3 GPa and a shear modulus of 12 ± 1 GPa, both considerably smaller than the calculated values ($K = 47$ GPa and $G = 19$ GPa).[274] This difference is possibly due to a large temperature dependence of the elastic constants such as that reported for ZrW_2O_8.[25]

The calculated elastic stiffness tensor (*c*) of orthorhombic $Al_2Mo_3O_{12}$ (*Pbcn* setting) is given by:

$$c = \begin{bmatrix} 79.1 & 19.3 & 19.3 & 0 & 0 & 0 \\ 19.3 & 128 & 51.3 & 0 & 0 & 0 \\ 19.3 & 51.3 & 126 & 0 & 0 & 0 \\ 0 & 0 & 0 & 45.7 & 0 & 0 \\ 0 & 0 & 0 & 0 & 29.8 & 0 \\ 0 & 0 & 0 & 0 & 0 & 29.4 \end{bmatrix} \times \text{GPa} \quad (8.1)$$

and the corresponding directional elastic moduli are shown in Table 8.2. The thermal expansion tensor (*α*) from the literature[159] is shown for comparison:

$$\alpha = \begin{array}{|c|c|c|} \hline 7 & 0 & 0 \\ \hline 0 & 0.5 & 0 \\ \hline 0 & 0 & -1 \\ \hline \end{array} \times 10^{-6}\,\text{K}^{-1}. \qquad (8.2)$$

Table 8.2: Directional elastic moduli of $Al_2Mo_3O_{12}$.

Young's modulus / GPa		Shear modulus / GPa		Compressibility / GPa^{-1}		Poisson ratio			
Y_{11}	74.8	G_{23}	45.7	β_{11}	1.05×10^{-2}	μ_{23}	0.38	μ_{32}	0.15
Y_{22}	105	G_{13}	29.8	β_{22}	4.43×10^{-3}	μ_{13}	0.15	μ_{31}	0.15
Y_{33}	104	G_{12}	29.4	β_{33}	4.52×10^{-3}	μ_{12}	0.11	μ_{21}	0.15

$Al_2Mo_3O_{12}$ showed similar elastic anisotropic properties to that of its thermal expansion, with only a small difference between the b- and c-axes. The overall elastic anisotropy of $Al_2Mo_3O_{12}$, expressed as A_U (see Equation 7.3) is equal to 1.9. By comparison. $Y_2Mo_3O_{12}$ has $A_U = 3.9$.[274] Unlike in the case of $Y_2Mo_3O_{12}$,[274] the Young's modulus and directional compressibilities followed the expected trends and were inversely proportional to each other. The VRH values[300] for the bulk elastic constants were determined to be $K = 35.3$ GPa and $G = 36.2$ GPa. These stiffnesses are roughly twice as large as those determined experimentally for monoclinic $Al_2Mo_3O_{12}$ ($K = 13.5 \pm$ 1.3 GPa, $G = 18.2 \pm 0.7$ GPa, see Section 3.5). A similar discrepancy was seen in the case of $Y_2Mo_3O_{12}$ (*vide supra*), obscuring whether the difference is due to temperature dependence of the elastic constants or the difference between the monoclinic and orthorhombic phases.

The calculated elastic stiffness tensor of orthorhombic $ZrMgMo_3O_{12}$ ($P2_1nb$ setting) is given by:

$$c = \begin{bmatrix} 56.3 & 16.8 & 14.2 & 0 & 0 & 0 \\ 16.8 & 85.2 & 43.6 & 0 & 0 & 0 \\ 14.2 & 43.6 & 88.4 & 0 & 0 & 0 \\ 0 & 0 & 0 & 33.9 & 0 & 0 \\ 0 & 0 & 0 & 0 & 20.1 & 0 \\ 0 & 0 & 0 & 0 & 0 & 18.0 \end{bmatrix} \times \text{GPa} \quad (8.3)$$

and the corresponding directional elastic moduli are shown in Table 8.3. The experimental thermal expansion tensor (see Section 5.3.2) is shown for comparison:

$$\alpha = \begin{bmatrix} 7.6 & 0 & 0 \\ 0 & -2.5 & 0 \\ 0 & 0 & -4.7 \end{bmatrix} \times 10^{-6}\,\text{K}^{-1}. \quad (8.4)$$

Like $Al_2Mo_3O_{12}$, $ZrMgMo_3O_{12}$ shows increased stiffness along its thermomiotic axes both in terms of Young's modulus and compressibility. The stiffnesses of the b- and c-axes were similar even though their CTEs are quite different in magnitude. The overall elastic anisotropy of $ZrMgMo_3O_{12}$ was very similar to that of $Al_2Mo_3O_{12}$; both have $A_U = 1.9$. The VRH bulk and shear moduli were 26.5 GPa and 23.8 GPa, respectively. These values are relatively close to those obtained through experimental measurements ($K = 31 \pm 3$ GPa, $G = 22 \pm 1$ GPa, see Section 5.3.3).

Table 8.3: Directional elastic moduli of $ZrMgMo_3O_{12}$.

Young's modulus / GPa		Shear modulus / GPa		Compressibility / GPa^{-1}		Poisson ratio			
Y_{11}	52.5	G_{23}	33.9	β_{11}	1.45×10^{-2}	μ_{23}	0.46	μ_{32}	0.49
Y_{22}	61.9	G_{13}	20.1	β_{22}	5.72×10^{-3}	μ_{13}	0.11	μ_{31}	0.49
Y_{33}	65.6	G_{12}	18.0	β_{33}	6.16×10^{-3}	μ_{12}	0.18	μ_{21}	0.15

The calculated elastic stiffness tensor of orthorhombic $Sc_2Mo_3O_{12}$ (*Pbcn* setting) is given by:

$$c = \begin{vmatrix} 53.1 & 14.9 & 16.7 & 0 & 0 & 0 \\ 14.9 & 88.1 & 49.3 & 0 & 0 & 0 \\ 16.7 & 49.3 & 92.2 & 0 & 0 & 0 \\ 0 & 0 & 0 & 31.8 & 0 & 0 \\ 0 & 0 & 0 & 0 & 15.8 & 0 \\ 0 & 0 & 0 & 0 & 0 & 18.5 \end{vmatrix} \times \text{GPa.} \quad (8.5)$$

and the corresponding directional elastic moduli are shown in Table 8.4. The experimental thermal expansion tensor[149] is shown for comparison:

$$\alpha = \begin{vmatrix} 11 & 0 & 0 \\ 0 & -8.7 & 0 \\ 0 & 0 & -8.4 \end{vmatrix} \times 10^{-6}\,\text{K}^{-1}. \quad (8.6)$$

The elastic anisotropy of $Sc_2Mo_3O_{12}$ ($A_U = 2.9$) was larger than that of $Al_2Mo_3O_{12}$ and $ZrMgMo_3O_{12}$, which would perhaps be expected given its larger CTE anisotropy. The VRH values for the bulk and shear moduli were $K = 24.0$ GPa and $G = 22.3$ GPa; unlike in the cases of $Al_2Mo_3O_{12}$ and $Y_2Mo_3O_{12}$ the calculated bulk modulus is significantly smaller than the experimental value ($K = 32 \pm 2$ GPa from variable-pressure XRD).[27]

Table 8.4: Directional elastic moduli of $Sc_2Mo_3O_{12}$.

Young's modulus / GPa		Shear modulus / GPa		Compressibility / GPa^{-1}		Poisson ratio			
Y_{11}	49.5	G_{23}	31.8	β_{11}	1.57×10^{-2}	μ_{23}	0.51	μ_{32}	0.12
Y_{22}	60.9	G_{13}	15.8	β_{22}	6.00×10^{-3}	μ_{13}	0.13	μ_{31}	0.16
Y_{33}	63.1	G_{12}	18.5	β_{33}	4.80×10^{-3}	μ_{12}	0.10	μ_{21}	0.12

In order to visualize correlations of axial elastic properties with axial thermal expansion, axial Young's moduli (Y_{ii}), axial compressibilities (β_{ii}), and directional shear moduli (G_{jk}) are shown as a function of the axial CTEs (α_{ii})[149,159] for the three materials described above and $Y_2Mo_3O_{12}$[142,274] in Figure 8.1(a)–(c). The elastic behaviour of the thermomiotic b- and c-axes appear to be related to their axial CTEs whereas the elastic
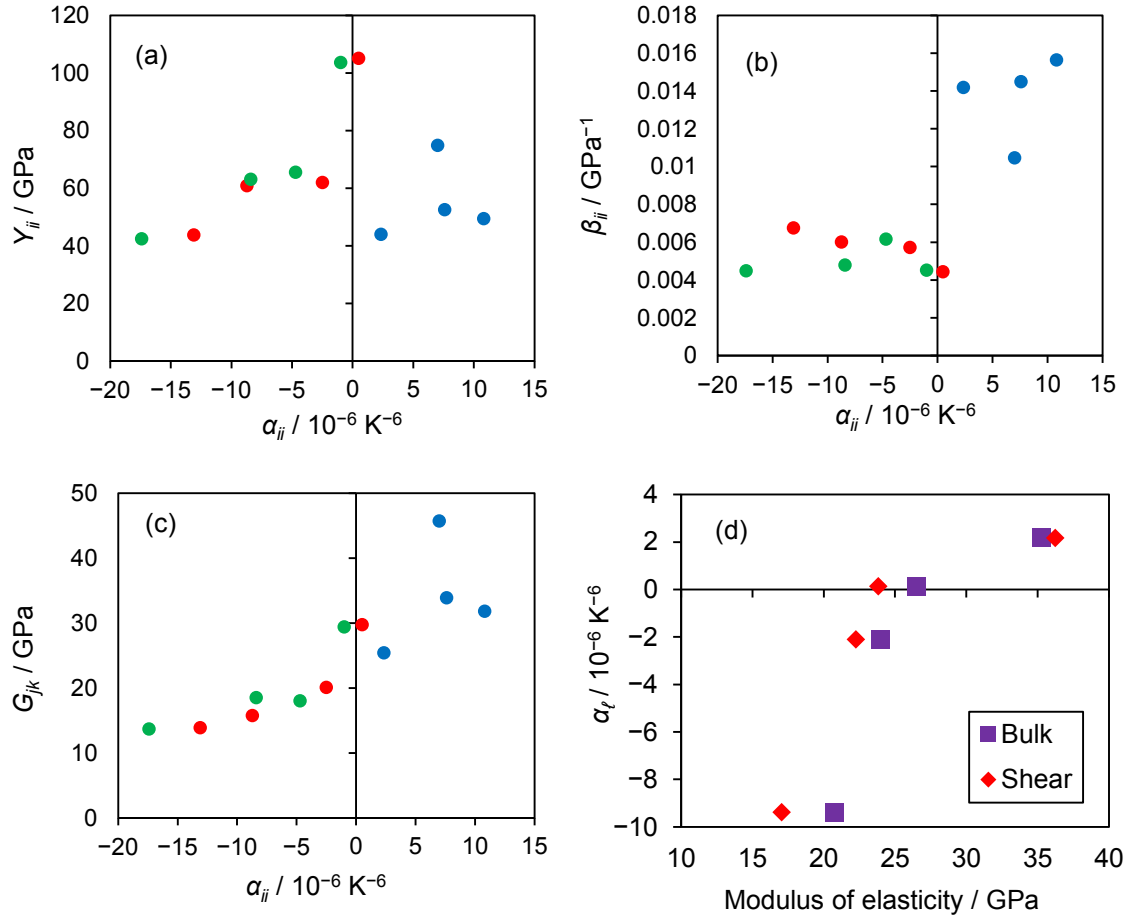
Figure 8.1: Calculated directional elastic moduli ((a) Young's moduli, (b) compressibilities, (c) shear moduli) shown as a function of axial thermal expansion along the a- (●), b- (●), and c- (●) axes for orthorhombic $Al_2Mo_3O_{12}$, $ZrMgMo_3O_{12}$, $Sc_2Mo_3O_{12}$, and $Y_2Mo_3O_{12}$ in the *Pbcn* or *P2$_1$nb* setting. (d) Volumetric thermal expansion shown as a function of calculated VRH bulk and shear moduli for orthorhombic $Al_2Mo_3O_{12}$, $ZrMgMo_3O_{12}$, $Sc_2Mo_3O_{12}$, and $Y_2Mo_3O_{12}$. Axial CTEs and the elastic tensor of $Y_2Mo_3O_{12}$ were taken from the literature—see text for references.

behaviour of the a-axis does not show a strong correlation. The b- and c-axes are stiffer

than the a-axis except in the case of $Y_2Mo_3O_{12}$, in which the a-axis has a higher Young's

modulus but also higher compressibility. Stiffer thermomiotic axes could lead to a

negative effect on the bulk CTE of a polycrystal, as the stiffer thermomiotic axes would

have a larger contribution to the bulk expansion (*cf.* the behaviours discussed for

composites in Chapter 4). This effect is discussed further in Chapter 9.

The materials studied show significantly different behaviour when subjected to different stress conditions. The *b*- and *c*-axes show a decrease in uniaxial stiffness (Figure 8.1 (a)) with increasingly negative thermal expansion. However, when subjected to isotropic pressure (Figure 8.1 (b)), a smaller and less constant variation in the stiffness is seen. These differences illustrate the importance of computational studies of the full elastic tensor, as only β_{ii} is obtained from experimental variable-pressure XRD measurements on polycrystalline samples. The directional shear moduli show generally increased stiffness for G_{23} by comparison to G_{13} and G_{12}, which is consistent with the increased stiffness of the *b*- and *c*-axes in comparison to the *a*-axis. This trend leads to the shear modulus in a plane (G_{jk}) increasing with the thermal expansion of the axis perpendicular to the plane (α_{ii}). The variations in the axial elastic constants with axial CTEs are a possible explanation as to why correlations between the elastic moduli and CTEs of the materials presented in Chapter 6 could only be found within each series of solid solutions; two materials with similar bulk CTEs do not necessarily have similar axial CTEs.

The correlation between the calculated VRH bulk and shear moduli and the bulk CTE is shown in Figure 8.1 (d). A decrease in overall stiffness with increasingly negative thermal expansion can be seen clearly. The trend relating the elastic moduli to the CTE is very similar to that relating the *A* site ionic force to the CTE, which was shown previously (Figure 5.17), suggesting that polyhedral distortability is a common factor between thermal expansion and elastic properties in this group of materials. The axial CTEs of $A_2M_3O_{12}$ materials and $ZrMgMo_3O_{12}$ are shown in Figure 8.2, as a function of the *A* site ionic force. Figure 8.2 shows that the relationship between axial CTEs and the
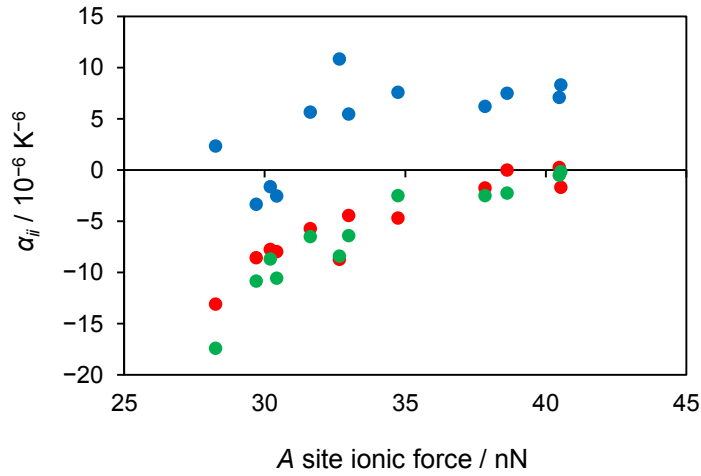
Figure 8.2: CTEs along the *a*- (●), *b*- (●), and *c*- (●) axes of $A_2M_3O_{12}$ materials and ZrMgMo$_3$O$_{12}$ in their orthorhombic phases (*Pbcn* or *P2$_1$nb* setting) are shown as a function of the *A* site ionic force (an average is used for ZrMgMo$_3$O$_{12}$). Information regarding $A_2M_3O_{12}$ materials was taken from the literature; see Table 5.2 for references.

A site ionic force is similar to that between axial CTEs and the elastic constants: the thermomiotic *b*- and *c*-axes follow a well-defined trend, while the thermal expansion along the *a*-axis does not.

With the anisotropic elastic constants, axial Grüneisen parameters could be determined, defined as: [12]

$$\gamma_{ii} = \frac{V_m}{C_V}(c_{ii}\alpha_{ii} + c_{ij}\alpha_{jj} + c_{ik}\alpha_{kk}). \qquad (8.7)$$

Here, C_V was calculated using the Einstein and Debye models following the procedure described in Chapter 7 using the calculated elastic tensors and Γ-point phonon frequencies.[274] The axial Grüneisen parameters were determined at a temperature of 300 K for ZrMgMo$_3$O$_{12}$, Sc$_2$Mo$_3$O$_{12}$, and Y$_2$Mo$_3$O$_{12}$,[142,274] and at a temperature of 550 K for Al$_2$Mo$_3$O$_{12}$. The results are shown in Figure 8.3 and Table 8.5.

Thermal expansion along the *b*- and *c*-axes is largely determined by the Grüneisen parameter along that axis, showing that vibrational modes with negative Grüneisen

187
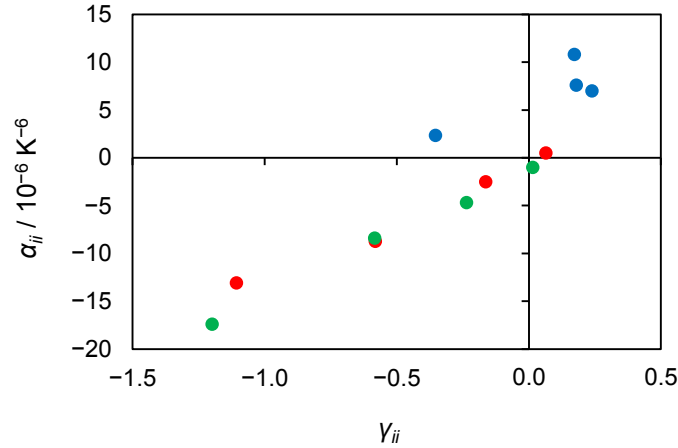
Figure 8.3: Axial CTEs shown as a function of axial Grüneisen parameters along the a- (●), b- (●), and c- (●) axes for orthorhombic $Al_2Mo_3O_{12}$, $ZrMgMo_3O_{12}$, $Sc_2Mo_3O_{12}$, and $Y_2Mo_3O_{12}$ in the $Pbcn$ or $P2_1nb$ setting. Axial CTEs and the elastic tensor of $Y_2Mo_3O_{12}$ are taken from the literature—see text for references.

Table 8.5: Axial Grüneisen parameters of orthorhombic $Al_2Mo_3O_{12}$, $ZrMgMo_3O_{12}$, $Sc_2Mo_3O_{12}$, and $Y_2Mo_3O_{12}$ in the $Pbcn$ or $P2_1nb$ setting.

Material	γ_{11}	γ_{22}	γ_{33}
$Al_2Mo_3O_{12}$	0.24	0.07	0.02
$ZrMgMo_3O_{12}$	0.18	−0.16	−0.23
$Sc_2Mo_3O_{12}$	0.17	−0.58	−0.58
$Y_2Mo_3O_{12}$	−0.35	−1.11	−1.20

parameters along those axes are directly responsible for NTE. Essentially, this high

degree of correlation is because the $c_{ij}\alpha_{jj}$ and $c_{ik}\alpha_{kk}$ terms in Equation 8.7 have opposite

signs and nearly cancel. These terms are due to the Poisson effect, where a (thermal)

strain along one axis causes a corresponding strain along the axes perpendicular to it.[6] As

shown in Tables 8.2 to 8.4, some of the axial Poisson ratios in these materials are quite

large, close to the theoretical limit of 0.5 for stable isotropic materials.[312] However, NTE

along the b- and c-axes increases the CTE along the a-axis due to the Poisson effect. The

PTE along the a-axis in $Y_2Mo_3O_{12}$ is caused entirely by this effect, as γ_{11} is negative.

Similarly, the increase in thermal expansion along the a-axis in $Sc_2Mo_3O_{12}$ relative to

ZrMgMo$_3$O$_{12}$ and Al$_2$Mo$_3$O$_{12}$ is due to its larger NTE along the *b*- and *c*- axes, as all three materials have similar values of γ_{11}. Therefore, the Poisson effect is responsible for some of the thermal expansion anisotropy which causes microcracking in sintered bodies of *A*$_2$*M*$_3$O$_{12}$ materials.[205] This interaction could explain some of the otherwise unexplained variation in the CTE along the *a*-axis seen in Figure 8.2.

8.3.2. Γ-point Phonon Energies

Γ-point optic phonon frequencies calculated in ABINIT are presented in tabular form in Appendix C, and visually in Figure 8.4 (along with the previously reported phonon spectrum of Y$_2$Mo$_3$O$_{12}$).[274] Figure 8.4 shows the common features of the phonon spectra of the four materials studied: a band of low-energy librational, translational, and bending modes separated from stretching modes with higher energy, with asymmetric stretches at lower energies than symmetric stretches.[180,181] As discussed in Chapter 5, ZrMgMo$_3$O$_{12}$ has a larger spread of stretching mode energies due to the splitting of the *A* site into a Zr site and Mg site, but otherwise its Γ-point phonon spectrum is similar to that of the *A*$_2$Mo$_3$O$_{12}$ materials. Of particular interest is a mode at 26 cm^{-1} in Al$_2$Mo$_3$O$_{12}$ which is anomalously low in energy by comparison to the other translational and librational modes in this material. This mode could be the "soft" mode with negative frequency at some point in the Brillouin zone which causes the orthorhombic-monoclinic phase transition, as discussed above.

The energies of the low-energy phonons can be compared more easily in Figure 8.5, which shows the cumulative distribution function of the modes below 500 cm^{-1}. The phonons below *ca.* 200 cm^{-1} are expected to have negative mode Grüneisen parameters and contribute to NTE, while those of higher energies are expected to have positive[47] or
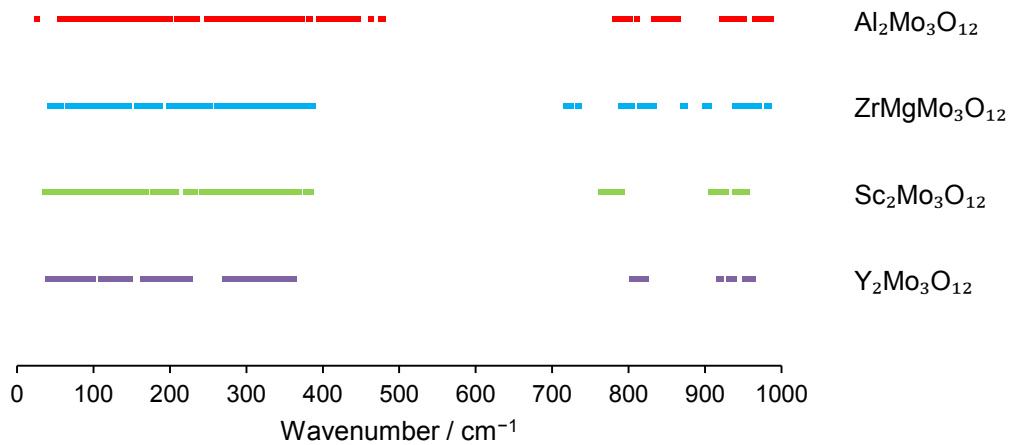
Figure 8.4: Calculated Γ-point optic phonon frequencies of $A_2Mo_3O_{12}$ materials (including $Y_2Mo_3O_{12}$)[274] and $ZrMgMo_3O_{12}$.
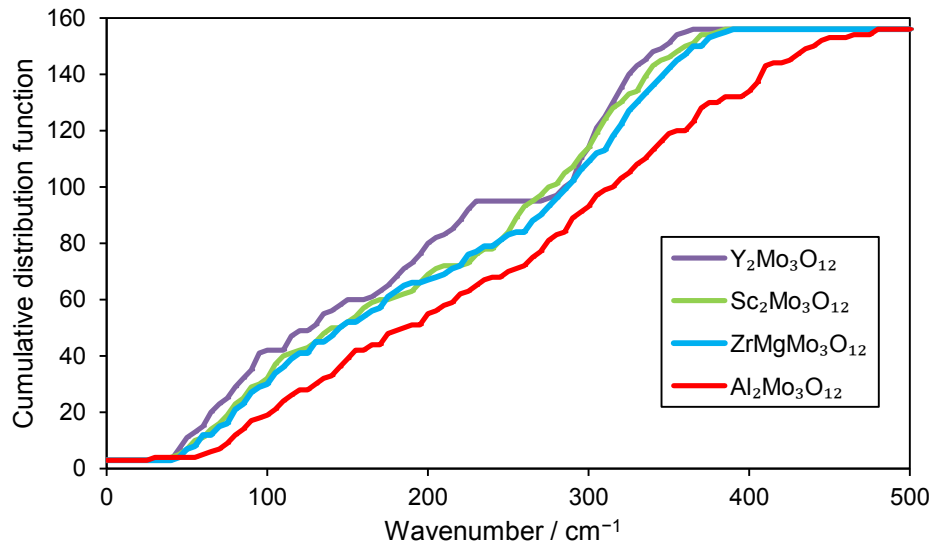
Figure 8.5: Calculated Γ-point phonon frequencies (in the region below 500 cm^{-1} where the modes most relevant to thermal expansion exist) of $A_2Mo_3O_{12}$ materials (including $Y_2Mo_3O_{12}$)[274] and $ZrMgMo_3O_{12}$ are shown as the cumulative number of modes with an energy less than or equal to a given wavenumber.

near-zero Grüneisen parameters.[46] Figure 8.5 shows that $Y_2Mo_3O_{12}$ has significantly more modes with energies below 200 cm^{-1} and has generally lower phonon energies in this region, which is consistent with its observed NTE over a wide temperature range.[45,46] Conversely, $Al_2Mo_3O_{12}$ has considerably fewer modes below 200 cm^{-1}, with a much

broader distribution of its phonon frequencies in the region below 500 cm^{-1}. The mode distributions for $Sc_2Mo_3O_{12}$ and $ZrMgMo_3O_{12}$ are very similar, especially in the region below 200 cm^{-1}. Since $Sc_2Mo_3O_{12}$ has a negative CTE while $ZrMgMo_3O_{12}$ displays zero thermal expansion, this implies that the mode Grüneisen parameters of $Sc_2Mo_3O_{12}$ are more negative. Interestingly, the inherent distortions of the AO_6 polyhedra of $Sc_2Mo_3O_{12}$ and (on average) $ZrMgMo_3O_{12}$ are also very similar (see Figure 5.13), however their distortabilites (expressed in terms of the A site ionic force, see Figure 5.17) are quite different.

The calculated Γ-point phonon frequencies of $Al_2Mo_3O_{12}$, $ZrMgMo_3O_{12}$, $Sc_2Mo_3O_{12}$ and $Y_2Mo_3O_{12}$ are compared to experimental Raman spectra (measured at room temperature) in Figure 8.6 and Figure 8.7. $Al_2Mo_3O_{12}$ shows significant differences between the calculated and experimental Raman spectra because the experimental spectrum includes additional peaks due to the lower symmetry of the room-temperature monoclinic phase.[313] However, the energies of the band below 500 cm^{-1} are well-reproduced. The calculated Γ-point phonon spectrum of $ZrMgMo_3O_{12}$ matches well with the experimental Raman spectrum, especially the positions of the stretching peaks, which were less well-reproduced in the CASTEP results (see Figure 5.8). A small underestimation of the mode energies can be attributed to the choice of PBE GGA functionals,[184,185] whose underbinding also contributes to the reduction of the calculated elastic moduli below their experimental values. This slight underestimation is also seen in the cases of $Sc_2Mo_3O_{12}$ and $Y_2Mo_3O_{12}$. As discussed above, a Raman spectrum of $Sc_2Mo_3O_{12}$ was not acquired, however, the Γ-point phonon spectrum is compared to the

Al₂Mo₃O₁₂

Wavenumber / cm⁻¹

ZrMgMo₃O₁₂

Wavenumber / cm⁻¹

Y₂Mo₃O₁₂

Wavenumber / cm⁻¹
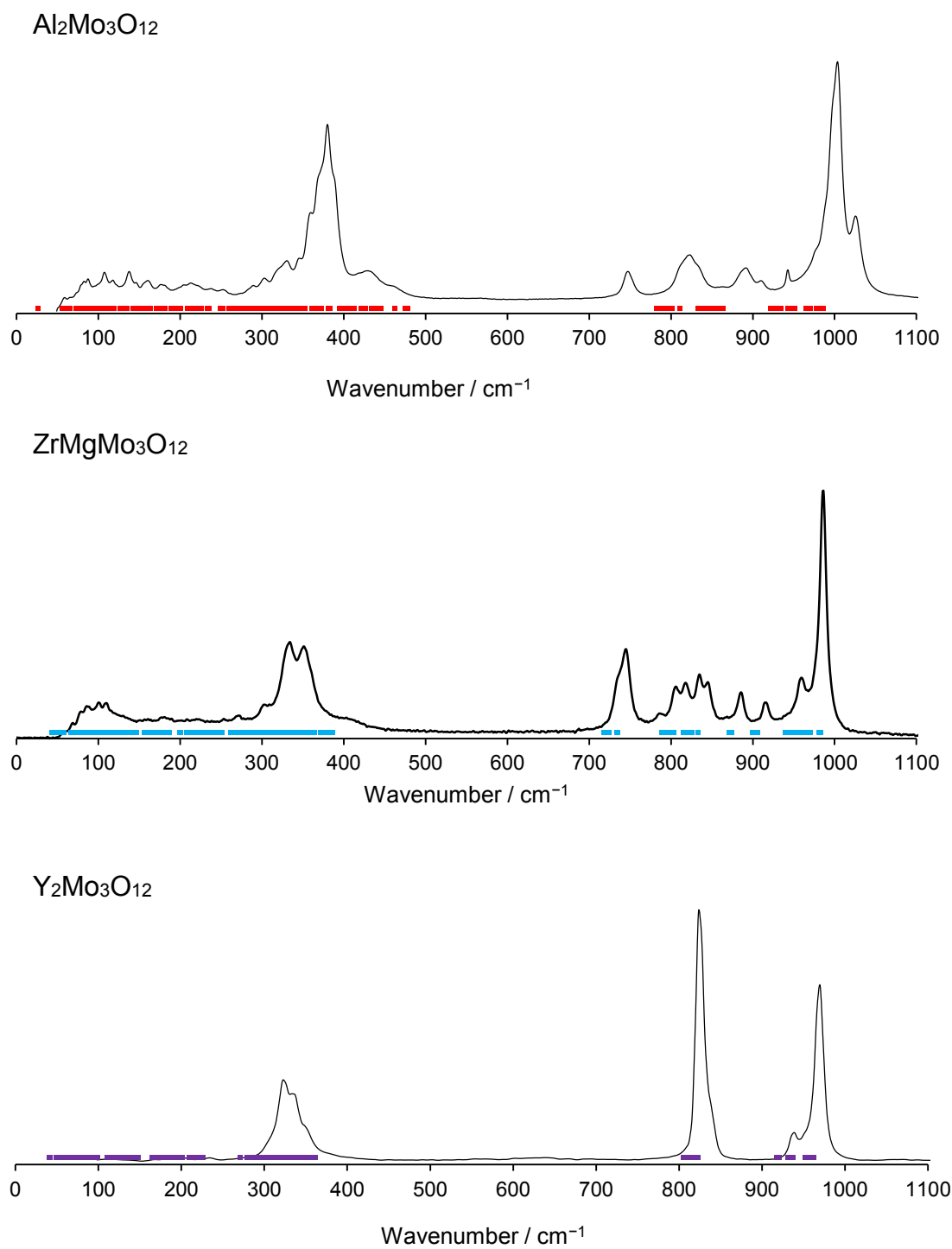
Figure 8.6: Experimental Raman spectra (black line) compared to calculated Γ-point optic phonon frequencies of Al₂Mo₃O₁₂, ZrMgMo₃O₁₂, and Y₂Mo₃O₁₂.[274]
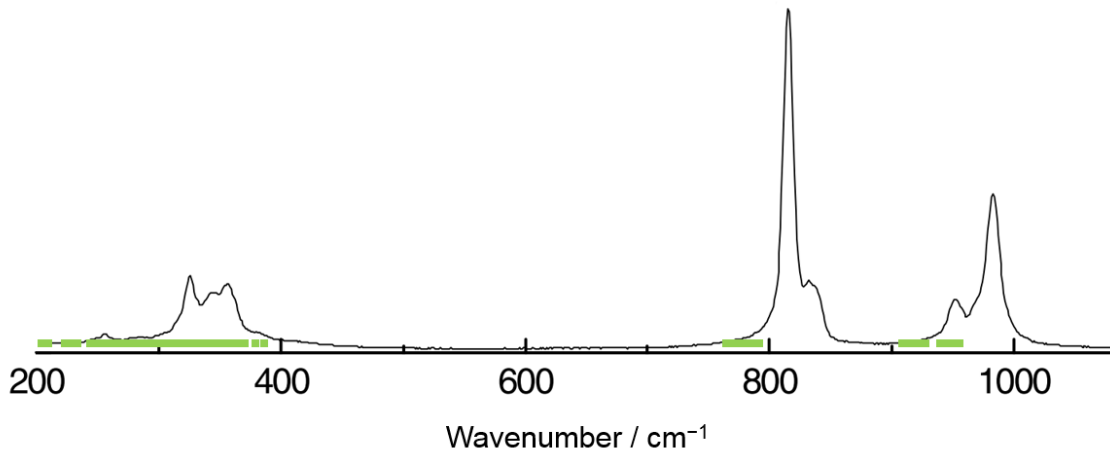
Figure 8.7: Experimental Raman spectrum (black line) from the literature[311] compared to calculated Γ-point optic phonon frequencies of $Sc_2Mo_3O_{12}$. Adapted from Reference 311 with permission.

Raman spectrum reported in Reference 311 (Figure 8.7), showing generally good agreement with the calculated data. Overall, the results of this comparison, in addition to the comparison of experimental elastic moduli to calculated values performed above, show that the calculated elastic and phononic properties of these materials, while not quantitatively accurate, have a reasonable agreement with the experimental data.

8.4. Conclusions

Materials in the $A_2Mo_3O_{12}$ and $AMgMo_3O_{12}$ families were shown to have significant elastic anisotropy, a finding consistent with their characteristically large CTE anisotropy. The thermomiotic axes of these materials were shown to be stiffer than the PTE axes, which could act to decrease their bulk CTEs. However, the stiffness along the thermomiotic axes decreases with increasingly negative thermal expansion. The stiffness along the PTE axes did not show a strong correlation with their CTEs. However, $Al_2Mo_3O_{12}$, $ZrMgMo_3O_{12}$, and $Sc_2Mo_3O_{12}$ were shown to have similar axial Grüneisen parameters along their PTE axes, with differences in thermal expansion being driven by

elastic factors. Calculated Γ-point optic phonon frequencies showed differences between the materials in the low-energy region which correlate to their thermal expansion behaviour, and were used to validate the results by comparison to experimental Raman spectra.

Chapter 9: Thermal Stress in Polycrystalline $A_2Mo_3O_{12}$ Materials

9.1. Finite Element Analysis of Randomly Oriented Polycrystals

9.1.1. Background

The thermal expansion properties of $A_2M_3O_{12}$ materials are typically highly anisotropic and as a result considerable thermal stress can occur in polycrystalline sintered bodies (see Chapter 1). In order to determine the thermal stress due to CTE anisotropy and to examine the effect of varying stiffness along various crystal axes on the bulk CTE, thermal stress following cooling in a polycrystalline body with randomly oriented crystallites was modeled using FEM (see Section 2.7). Two materials were studied, $Al_2Mo_3O_{12}$ and $Y_2Mo_3O_{12}$. At the time that the calculations involving $Al_2Mo_3O_{12}$ were performed, the elastic tensor presented in Chapter 9 had not been calculated, so the material was treated as elastically isotropic. In the case of $Y_2Mo_3O_{12}$, the elastic tensor reported in Reference 274 was used. This provided the opportunity to determine the effects of elastic anisotropy by comparison of the two analyses.

The simulated polycrystal was a cube subdivided into smaller cubic crystallites. Due to computational limitations, the number of crystallites included in the polycrystal was limited to 64. Each crystallite has a randomized orientation, determined by three random Euler angles ϑ, φ, and ψ (angles by which the **x**, **y**, and **z** axes are rotated). The Euler angles determine the rotation tensor $\boldsymbol{R}$, which rotates the thermal expansion tensor $\boldsymbol{\alpha}$ into a tensor $\boldsymbol{\alpha}'$ with a new basis as follows:[119]

$$\boldsymbol{\alpha}' = \boldsymbol{R}\boldsymbol{\alpha}\boldsymbol{R}^{-1}, \tag{9.1}$$

where $\boldsymbol{R}$ can be expressed in matrix form as the product:

$$R = \begin{bmatrix} \cos\vartheta & 0 & \sin\vartheta \\ 0 & 1 & 0 \\ -\sin\vartheta & 0 & \cos\vartheta \end{bmatrix} \begin{bmatrix} 1 & 0 & 0 \\ 0 & \cos\varphi & -\sin\varphi \\ 0 & \sin\varphi & \cos\varphi \end{bmatrix} \begin{bmatrix} \cos\psi & -\sin\psi & 0 \\ \sin\psi & \cos\psi & 0 \\ 0 & 0 & 1 \end{bmatrix}. \tag{9.2}$$

However, determination of R using random Euler angles will not result in a truly random final orientation of the basis vectors of α. In order to achieve that goal, the order in which the three matrices above were multiplied together (*i.e.*, the order in which rotations of each of the three axes occur) was randomized, as was the starting orientation of α (*i.e.*, α_a etc. were randomly selected to correspond to the thermal expansion along the **x**, **y**, or **z** axis prior to the rotation being applied). This leads to a total of 72 possible ways to randomly reorient α. This complicated procedure was necessary to mitigate the problem of gimbal lock, where if φ is equal to 0 or π a degree of freedom of the other rotations is lost, causing the final random orientation to be biased towards having the **z′** axis aligned with the **z** axis. The problem could have been avoided more elegantly by the use of quaternions, however this is unfortunately precluded by the limitations of the software package used (COMSOL Multiphysics v. 4).

The stiffness tensor c can also be reoriented using the random Euler angles in a way similar to the procedure for α. Again, a rotation tensor, T, was used to rotate c:[119]

$$c' = TcT^{-1}. \tag{9.3}$$

T, like c, is a fourth-rank tensor. Its matrix representation is related to the entries of the second-rank rotation tensor R as follows:[119]

$$T_1 = \begin{bmatrix} R_{11}^2 & R_{12}^2 & R_{13}^2 \\ R_{21}^2 & R_{22}^2 & R_{23}^2 \\ R_{31}^2 & R_{32}^2 & R_{33}^2 \end{bmatrix} \tag{9.4a}$$

$$T_2 = \begin{bmatrix} R_{12}R_{13} & R_{11}R_{13} & R_{11}R_{12} \\ R_{22}R_{33} & R_{21}R_{23} & R_{21}R_{22} \\ R_{32}R_{33} & R_{31}R_{33} & R_{31}R_{32} \end{bmatrix} \tag{9.4b}$$

$$\boldsymbol{T}_3 = \begin{bmatrix} R_{21}R_{31} & R_{22}R_{32} & R_{23}R_{33} \\ R_{11}R_{31} & R_{12}R_{32} & R_{13}R_{33} \\ R_{11}R_{21} & R_{12}R_{22} & R_{13}R_{23} \end{bmatrix} \tag{9.4c}$$

$$\boldsymbol{T}_4 = \begin{bmatrix} R_{23}R_{32} + R_{22}R_{33} & R_{23}R_{31} + R_{21}R_{33} & R_{22}R_{31} + R_{21}R_{32} \\ R_{13}R_{32} + R_{12}R_{33} & R_{13}R_{31} + R_{11}R_{33} & R_{12}R_{31} + R_{11}R_{32} \\ R_{13}R_{22} + R_{12}R_{23} & R_{13}R_{21} + R_{11}R_{23} & R_{12}R_{21} + R_{11}R_{22} \end{bmatrix} \tag{9.4d}$$

$$\boldsymbol{T} = \begin{bmatrix} \boldsymbol{T}_1 & 2\boldsymbol{T}_2 \\ \boldsymbol{T}_3 & \boldsymbol{T}_4 \end{bmatrix}. \tag{9.4e}$$

The second-rank rotation tensor $\boldsymbol{R}$ is defined as in the previous case.

Because the crystallites were randomly oriented, many models must be created and their results averaged in order to give a final result that can be considered statistically representative of a real polycrystal containing billions of crystallites. To determine how many models were required, a convergence study was performed. Convergence was achieved for all examined variables (α_{ij}, σ_{ij}, and ε_{ij}) after about 400 models were averaged. The mesh used on the simulated polycrystal consisted of swept cubic elements subdivided into tetrahedral elements so that the mesh in the homogenous region could be made much coarser. The mesh size chosen was checked by a mesh convergence study. An example simulated polycrystal of $Y_2Mo_3O_{12}$ is shown in Figure 9.1.
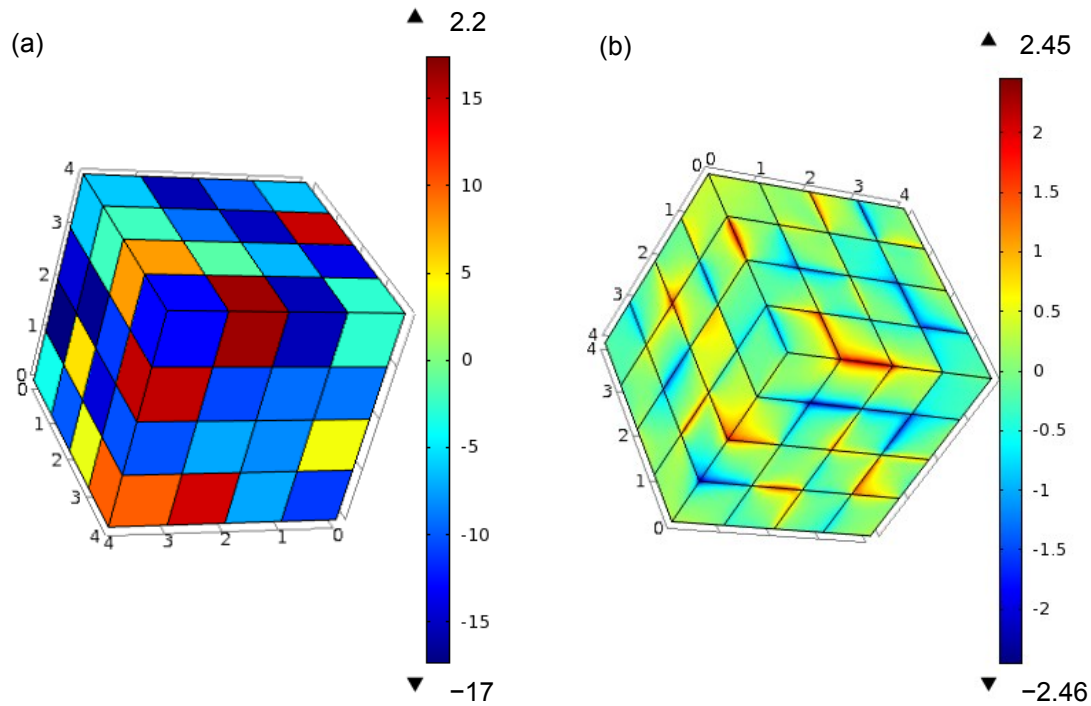
Figure 9.1: An example FE modeled polycrystal of $Y_2Mo_3O_{12}$, showing (a) coefficient of thermal expansion along the $\mathbf{x'}$ direction of each grain in units of $10^{-6}\ K^{-1}$ and (b) the first principal invariant of stress in units of GPa following cooling by 700 K.

9.1.2. $Al_2Mo_3O_{12}$[xxi]

In the case of $Al_2Mo_3O_{12}$, the simulated polycrystalline material was bound by a homogenous isotropic medium, and a temperature drop of 700 K was imposed at the boundaries of the model, to be indicative of thermal stresses on cooling after sintering. The axial CTEs of $Al_2Mo_3O_{12}$ used were the literature values for the orthorhombic (high-temperature) form.[159] Measurements and calculations of the elastic properties of $Al_2Mo_3O_{12}$ had not been performed at the time of this study,[xxii] so the Young's modulus

---

[xxi] This section was adapted with permission from Prisco, L. P.; Romao, C. P.; White, M. A.; Marinkovic, B. A. *J. Mater. Sci.* **2013**, *48*, 2986–2996. The author's contributions included finite element analysis and writing the relevant portions of the manuscript.

[xxii] A study using a larger simulated polycrystal, more realistic microstructure, and the full calculated elastic tensor is presented in Section 9.2.

was estimated to be 22 GPa based on other similar structures,[270] and its Poisson ratio was estimated[25] to be 0.3 (*c.f.* the DFT-calculated VRH values $Y = 79.4$ GPa and $\mu = 0.12$).

The finite element model used was validated by comparison of the calculated average strain energy density over all 400 models (53 kJ m^{-3}), to the value predicted by the analytical solution given by Kreher (77 kJ m^{-3}).[314,315] The difference can be ascribed to the boundary conditions used for the study, as the stress at the boundary between the polycrystal and the homogenous medium is lower on average than if the polycrystal continued indefinitely. Increasing the size of the modeled polycrystal would increase the strain energy density; however computational restrictions prohibited making a model of a size such that the results could be considered quantitatively similar to the analytically derived average values. Furthermore, average values of stress are not presented because analytical solutions for them exist (*vide infra*). The present finite element analysis is focused mainly on the local maximum stresses in the material, and whether they would be sufficiently prevalent and of sufficient magnitude to cause widespread microcracking which could lead to a noticeable effect on the bulk CTE. Inaccuracy introduced by the boundary conditions used would be expected to have a small effect on the maximum stress.

It should be noted that the low rigidity of materials similar to $Al_2Mo_3O_{12}$ reduces the thermal stress of the material compared with many ceramics, but it also reduces its material strength.

The distributions of the maxima and minima of the three principal stresses (σ_1, σ_2, and σ_3) are shown in histogram form in Figure 9.2 for the 400 models. It can be seen that the maximum σ_1 (*i.e.*, the largest unidirectional tensile stress in the model) and the
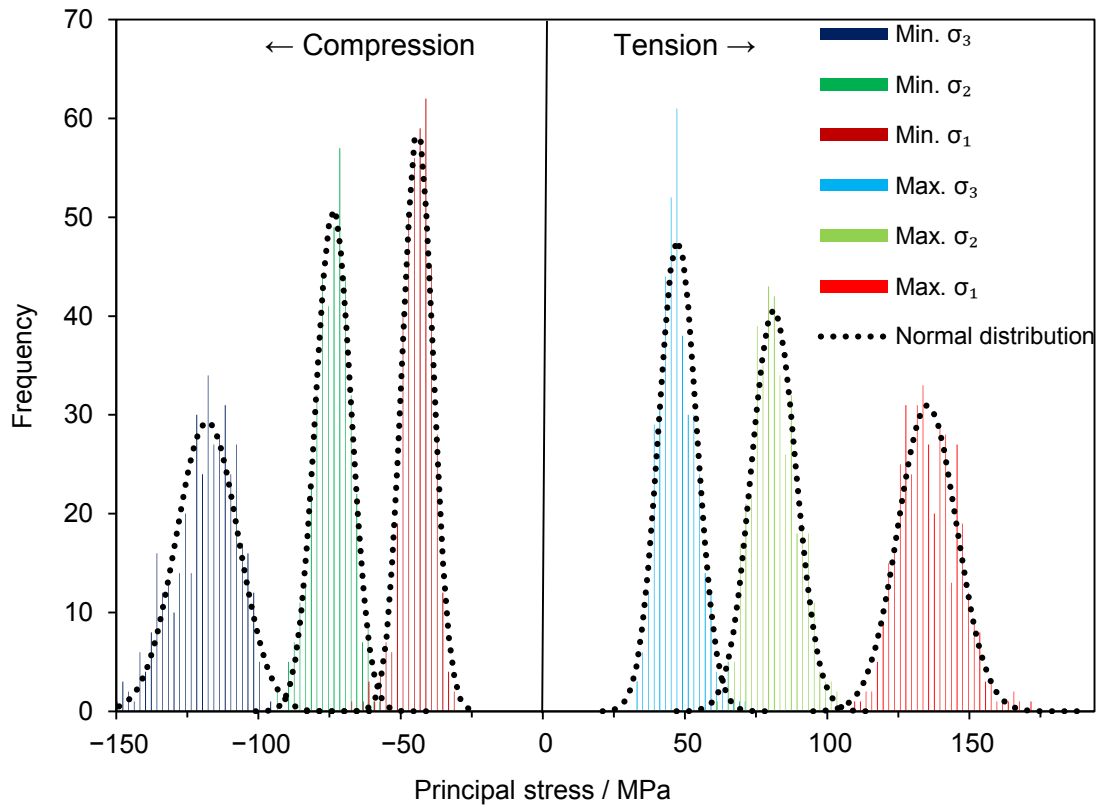
Figure 9.2: This histogram shows the maximum and minimum values of each principal stress (σ_1, σ_2, and σ_3; where the principal axes are defined such that $\sigma_1 > \sigma_2 > \sigma_3$; in this case, σ_1 and σ_2 are tensile on average, and σ_3 is compressive on average) in each of the 400 modeled $Al_2Mo_3O_{12}$ polycrystals. Normal distributions of each principal stress are included for comparison. Adapted from Reference 205 with permission.

minimum σ_3 (*i.e.*, the largest unidirectional compressive stress) were not well represented by normal distribution functions, with some significant outliers present in the distribution of σ_1. The other principal stresses fit normal distributions more closely, with the compressive stresses being on average somewhat greater and more tightly distributed than the tensile stresses.

According to Kreher,[314,315] on average the principal stresses will be aligned with the crystallographic axes within a crystallite. The average principal stresses were calculated following Kreher's method to be $\sigma_1 = 6.0$ MPa, $\sigma_2 = 4.3$ MPa, and $\sigma_3 = -8.5$ MPa. On cooling the two crystallographic axes with positive thermal expansion (*a*-axis

and b-axis, in the *Pbcn* setting used herein, see Equation 8.2 above) are in tension, and the c-axis (which shows NTE), is in compression, on average. The larger magnitude of σ_3 compared with σ_1 gives rise to maximum compressive principal stresses from the finite element analysis that are slightly larger than the maximum tensile principal stresses (Figure 9.2). The wider distribution of maximum principal tensile stresses could be a consequence of two of the average principal stresses being tensile.

Taken together, these results show that while the maximum thermal expansion mismatch (between the a- and c-axes in $Al_2Mo_3O_{12}$) is the main driver of thermal stress in $Al_2Mo_3O_{12}$ and related materials, the mismatch between the other pairs of axes also plays a noticeable role in shaping the thermal stress distribution. For example, when Cr^{3+} is substituted for Al^{3+} in $Al_2Mo_3O_{12}$ the difference between all three crystallographic CTEs is reduced, whereas when Fe^{3+} is substituted for Al^{3+} the difference between α_a and α_c decreases but the difference between α_b and α_c increases.[159] Consequently, the addition of Cr^{3+} could reduce microcracking in $Al_2Mo_3O_{12}$ to a greater extent than addition of Fe^{3+}.

The maximum total tensile stress, which equals the maximum first invariant of stress, is shown in Figure 9.3. Assuming that $Al_2Mo_3O_{12}$ behaves like a typical brittle material and is much stronger under compression than tension, tensile stress is likely to cause failure. The physical interpretation of Figure 9.3 is that the maximum tensile stress in a given 64-crystallite segment of a polycrystal is likely to be $\approx$ 220 MPa. This level of stress is expected to be larger than the tensile strength of $Al_2Mo_3O_{12}$ (the tensile strength of sintered bodies of Al_2O_3, a much stiffer material, falls between 200 and 600 MPa),[316]
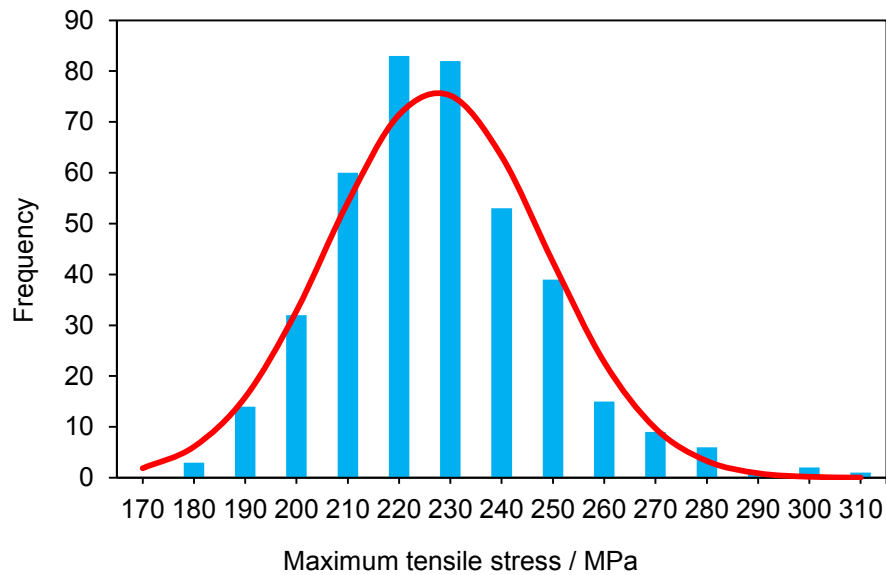
Figure 9.3: The maximum local tensile stress in each of 400 simulated $Al_2Mo_3O_{12}$ polycrystals. A normal distribution with a mean of 222 MPa and a standard deviation of 20 MPa is included for comparison. Adapted from Reference 205 with permission.

and therefore the presence of many microcracks in microparticulate samples can be understood.[205]

It is important to note that the bulk strength of a material cannot be directly compared to the microstructural stresses because the growth of microcracks, as described by Griffith's theory,[317] occurs when the strain energy (which depends on the crystallite volume) released from crack formation, due to the relaxation of stress, is greater than the surface energy required to propagate the crack. Therefore, decreasing the grain size of the material can increase its resistance to thermal stress, although the thermal stress itself is unchanged. With this in mind, the maximum strain energy density for each model is plotted in Figure 9.4. The strain energy density is poorly represented by a normal distribution, as there are several extreme outliers, as for the maximum tensile stress (Figure 9.3). The outliers can be understood as points of random but severe mismatch between several adjacent grains.
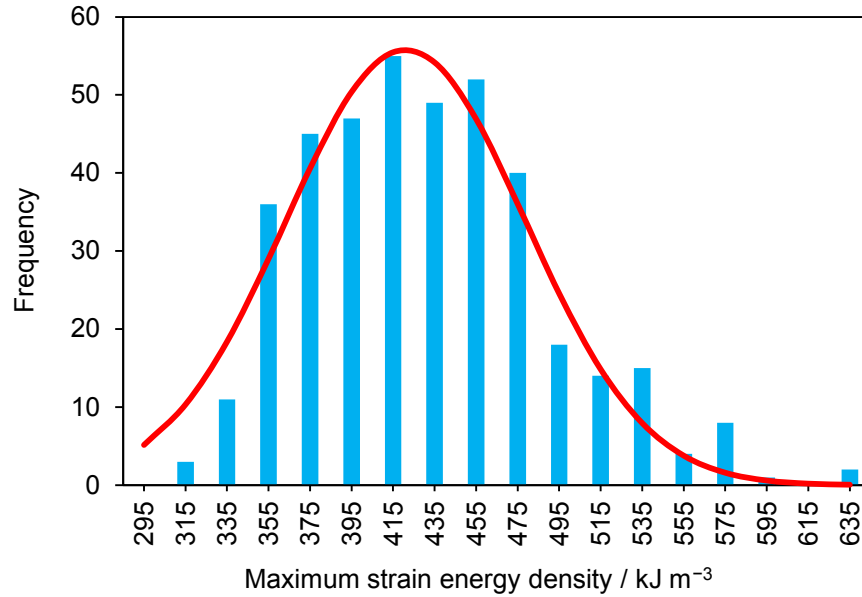
Figure 9.4: The maximum strain energy density in each of 400 simulated $Al_2Mo_3O_{12}$ polycrystals. A normal distribution of mean 421 kJ m^{-3} and standard deviation of 56 kJ m^{-3} is included for comparison. Adapted from Reference 205 with permission.

The maximum total compressive stress in each model is shown in Figure 9.5, which is well represented by a normal distribution. Compressive stress in $Al_2Mo_3O_{12}$ would be unlikely to cause failure, as the tensile stresses are larger and a brittle ceramic withstands much higher compressive stresses, however many open-framework compounds with structures similar to $Al_2Mo_3O_{12}$ have been found to undergo pressure-induced phase transitions and/or amorphization at relatively low pressures.[99] For example, $Al_2W_3O_{12}$ and $Sc_2Mo_3O_{12}$ undergo pressure-induced phase transitions at compressive stresses of 0.3 GPa and 0.75 GPa, respectively, and $Sc_2Mo_3O_{12}$ becomes amorphous at a compressive stress of 24 GPa.[27] No high-pressure study of $Al_2Mo_3O_{12}$ has been reported, but one could speculate that the local maximum compressive stress, being on the order of 200 MPa, could potentially be enough to initiate a phase change in some regions of the material if a high-pressure crystalline phase exists, although thermal stress probably would not lead to pressure-induced amorphization.
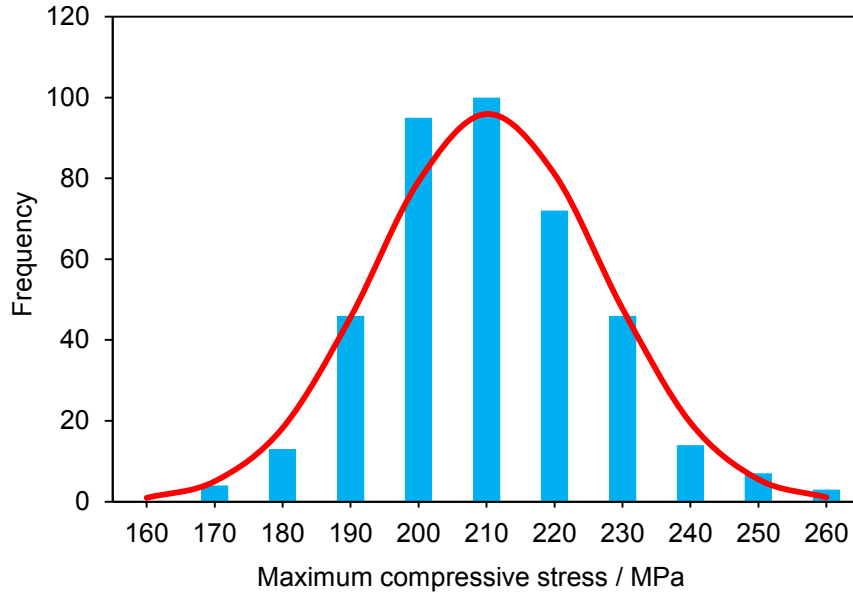
Figure 9.5: The maximum compressive local stress in each of 400 simulated $Al_2Mo_3O_{12}$ polycrystals. A normal distribution with a mean of 205 MPa and a standard deviation of 16 MPa is included for comparison. Adapted from Reference 205 with permission.

9.1.3. $Y_2Mo_3O_{12}$[xxiii]

The DFT stiffness tensor[xxiv] and experimental thermal expansion tensor of

$Y_2Mo_3O_{12}$:[142]

$$\alpha = \begin{array}{|c|c|c|} \hline 2.3 & 0 & 0 \\ \hline 0 & -13 & 0 \\ \hline 0 & 0 & -17 \\ \hline \end{array} \times 10^{-6}\,\text{K}^{-1} \quad (9.5)$$

were used to perform a finite-element analysis of the thermal stresses arising upon

cooling a polycrystalline sample of $Y_2Mo_3O_{12}$. Roller boundary conditions were applied

along three orthogonal sides of the polycrystal, while the other three sides of the cube

---

[xxiii] This section was adapted with permission from Romao, C. P.; Miller, K. J.; Johnson, M. B.; Zwanziger, J. W.; Marinkovic, B. A.; White, M. A. *Phys. Rev. B* **2014**, *90*, 024305. The author's contributions included measurement of velocities of sound, analysis of the elastic tensor in terms of axial elastic moduli, finite element analysis and writing the relevant portions of the manuscript.
[xxiv] The elastic tensor used in the finite element analysis presented here was calculated using pseudopotentials generated with the OPIUM code and is presented in the Supplemental Material of Reference 274.

were left unconstrained. A 700 K temperature drop was imposed at these boundaries of the model to mimic thermal stress in the material. In the model of $Al_2Mo_3O_{12}$ presented above it was determined that the unconstrained sides reduce the average stress in the polycrystal (hence the use of a homogenous medium surrounding the polycrystal), however this approach was required to determine the effect of elastic anisotropy on the thermal expansion.

In the 400 randomly oriented samples studied, three related quantities, the first principal invariant of stress (Figure 9.6(a)), the strain energy density (Figure 9.6(b)), and the volumetric strain (shown in a different form in Figure 9.7) were found to be normally distributed, as would be the case if elastic anisotropy were not included in the model (see Section 9.1.2 above).
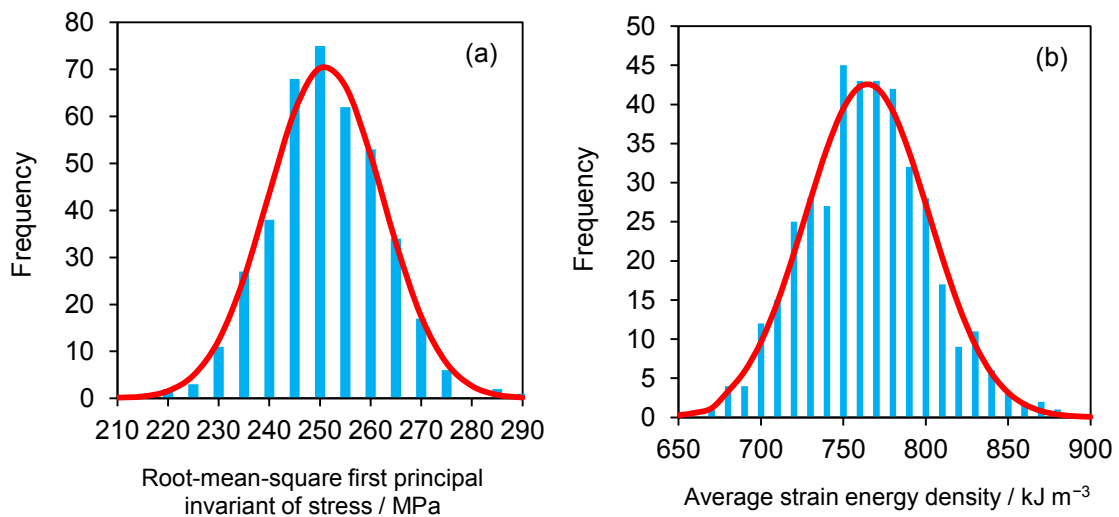
Figure 9.6: (a) Root-mean-square first principal invariant of stress and (b) average strain energy density for each of the 400 simulated $Y_2Mo_3O_{12}$ polycrystals. Normal distributions are included for comparison

The normal distribution of the stress leads to a normal distribution of the strain, and therefore a normal distribution of the effective CTE (Figure 9.7). The effective CTE
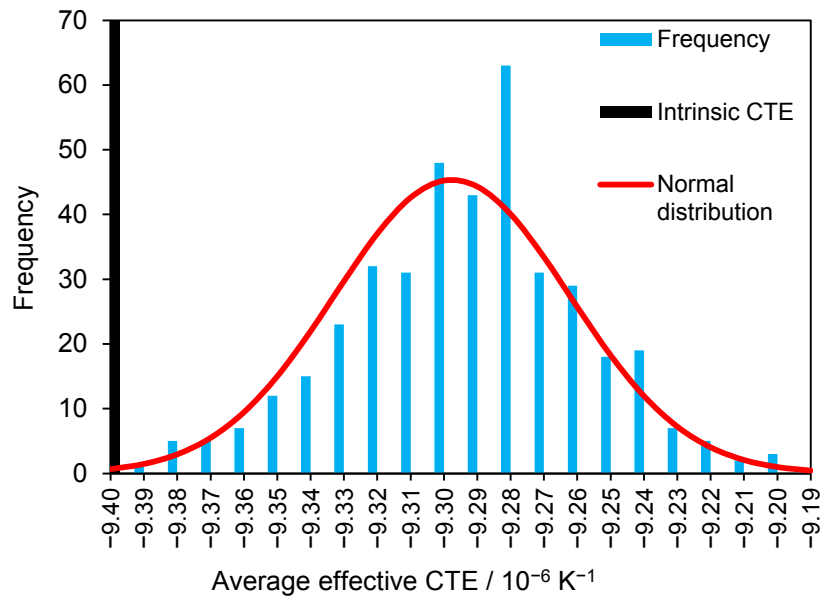
Figure 9.7: Distribution of the average effective linear CTE for each of the 400 simulated $Y_2Mo_3O_{12}$ polycrystals. A normal distribution is included for comparison. The intrinsic coefficient of thermal expansion is the experimental value from XRD over the temperature range 100 to 900 K.[45,142] Adapted from Reference 274 with permission.

is what would be measured experimentally for a bulk sample, if that sample were free of other influences on the CTE such as microcracking.

A small increase in CTE relative to the experimental intrinsic CTE[45,142] due to coupling of elastic anisotropy with thermal expansion anisotropy can be seen in Figure 9.7. Since the experimental CTE tensor was used as an input parameter to the model, if there were no elastic anisotropy then the effective CTE would equal the experimental CTE. It can be inferred that the increase in CTE is due to the axes with more positive thermal expansion having higher Young's moduli. It is interesting that this effect outweighs that due to the decrease of the axial compressibilities with increasing axial CTE, showing that the crystallites are on average in a state closer to uniaxial stress than isotropic stress.

This finding has consequences regarding the experimental measurement of the elastic properties: because the relation between the axial compressibilities (which can be measured by variable-pressure X-ray diffraction) did not in this case predict the relation between the axial Young's moduli, and because the axial Young's moduli were in this case a better predictor of the effective CTE, it is necessary to know the full stiffness tensor to predict the thermoelastic properties of the bulk material.

The expectation values of the various stress measures can be calculated following the method of Kreher,[314,315] but it is more instructive to look at the maxima of various stress measures, as these conditions can lead to microcracking and fracture. The maximum and minimum principal stresses are shown in Figure 9.8. The principal stress extrema distributions were fitted using Minitab[318] to three-parameter Weibull distributions with the probability distribution function:

$$p(\sigma) = \zeta \beta^{-\zeta}(\sigma - \sigma_0)^{\zeta-1}e^{-\left(\frac{\sigma-\sigma_0}{\beta}\right)^{\zeta}} \tag{9.6}$$

for $\sigma > \sigma_0$, where σ_0 is the location parameter, β is the scale parameter, and ζ is the shape parameter. Weibull distributions are commonly used to describe properties such as maximum stress, strength, and time to failure in cases where some stochastic effect causes them to vary.[319,320,321] When extrema of the principal stresses are fit, it is appropriate to set σ_0 equal to the smallest value of $|\sigma|$.[320]

The principal stress extrema distributions of Figure 9.8 can be compared to those calculated for $Al_2Mo_3O_{12}$ in Section 9.1.2 above using the same method but with isotropic elastic constants. The largest change is in the distributions of the stress extrema from approximately normal to Weibull distributions with $\zeta \approx 2$. A Weibull distribution with $\zeta = 1$ is a normal distribution, while one with $\zeta = 2$ is a Rayleigh distribution. This
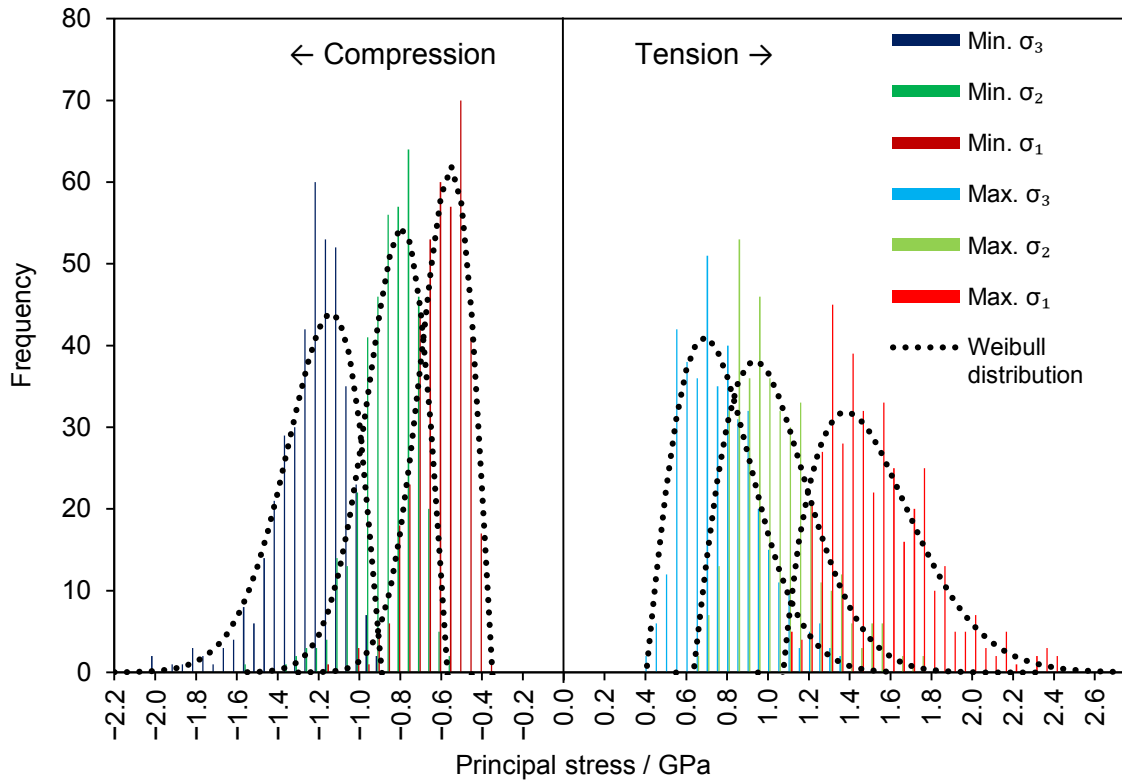
Figure 9.8: Maxima and minima of the three principal stresses in each of the 400 simulated $Y_2Mo_3O_{12}$ polycrystals. The principal stresses are defined so that $\sigma_1 > \sigma_2 > \sigma_3$. Fitted three-parameter Weibull distributions are shown as dotted lines. Adapted from Reference 274 with permission.

change in distribution shows that the level of elastic anisotropy in the material will affect the failure behavior of the material.[320]

As in $Al_2Mo_3O_{12}$, the distribution of the tensile stresses is broader than that of the compressive stresses. In $Al_2Mo_3O_{12}$, the difference was attributed to two of the crystallographic axes being in tension and one in compression, on average, upon cooling; however, in the case of $Y_2Mo_3O_{12}$ the opposite is true.[45,142] The broadness of the maximum tensile principal stress distribution in $Y_2Mo_3O_{12}$ must be due to another factor, probably the elastic anisotropy. Possibly the high shear modulus in the plane between the two NTE axes reduces the stress anisotropy in that plane.

The maximum tensile and compressive thermal stresses are defined as the maximum and minimum, respectively, of the first principal invariant of stress in each model. Both average about 3 GPa, with the maximum tensile stress being more broadly distributed and reaching an ultimate value of 5.5 GPa (Figure 9.9).[xxv] These values are very large due to the large amount of CTE anisotropy present in $Y_2Mo_3O_{12}$. Huge tensile stresses of approximately 3 GPa would be enough to cause significant microcracking in the material, while compressive stresses above 2.4 GPa might be sufficient to cause pressure-induced amorphization.[27] The problem of microcracking caused by huge tensile stresses could be mitigated and the strength of the material increased by appropriate control of the particle size and the microstructure of polycrystalline bodies.[205]
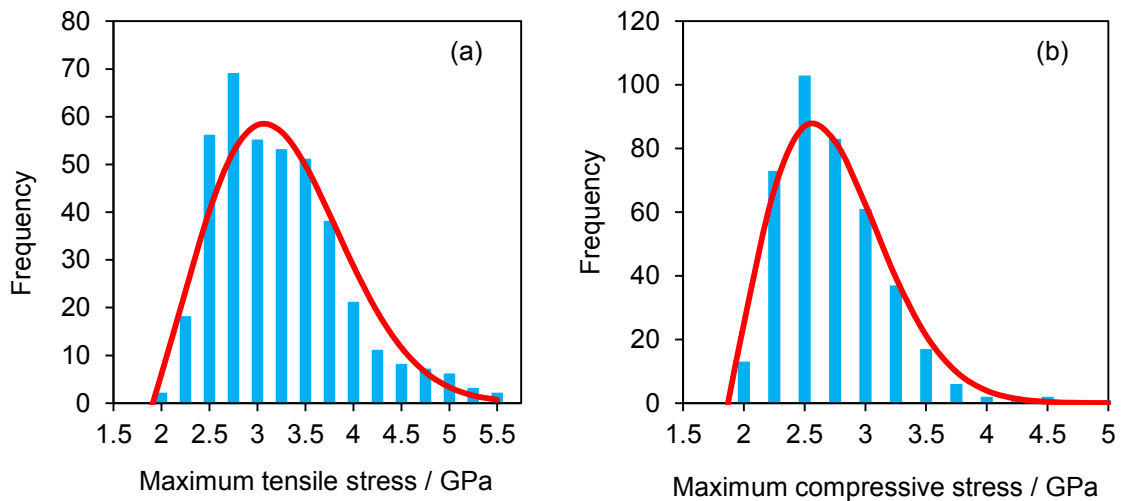
Figure 9.9: The maximum (a) tensile and (b) compressive thermal stresses in each of the 400 simulated $Y_2Mo_3O_{12}$ polycrystals. Fitted three-parameter Weibull distributions are shown. Each set of data was fitted to a three-parameter Weibull distribution; in this case σ_0 was determined as part of the fit.

[xxv] The Minitab software used for the fitting uses a maximum likeliness estimation method, which is not ideal when all three parameters of the Weibull distribution must be determined.[321] However, because the fitted Weibull parameters are not used quantitatively, this introduces an acceptable uncertainty.

The thermal stress analysis presented herein has its origins in CTE anisotropy in polycrystalline $Y_2Mo_3O_{12}$; it is proportional to the change in temperature of the material, but not the rate of change. If the temperature changes suddenly, additional stress will be present due to thermal shock. The thermal shock a material can withstand decreases with its stiffness and CTE, and increases with its fracture strength and thermal conductivity (see Section 1.1.2). These properties are all connected to the thermomiotic nature of $Y_2Mo_3O_{12}$.[1] The high degree of CTE anisotropy can be expected to lead to microcracking in a polycrystalline body, which in turn would reduce its fracture strength. $Y_2Mo_3O_{12}$ is relatively compliant for an oxide ceramic, which reduces the amount of thermal stress it experiences but also reduces its strength. Many of these factors are shared with other thermomiotic materials and underscore the challenges involved in their applications.

The effects of elastic anisotropy and its potential connections to CTE anisotropy in thermomiotic materials have not previously been examined closely. In the case of $Y_2Mo_3O_{12}$ the directional shear moduli and compressibilities are strongly anisotropic; however, their effects to some degree cancel, resulting in a different trend in the directional Young's moduli than the compressibilities. The high shear stiffness in the plane between the two axes with large negative CTEs is somewhat surprising given the usual connection between vibrational anharmonicity, thermal expansion, and compliance. This trait can be seen as desirable in applications where a large negative CTE is needed as it could decrease the material's effective CTE. Whether the trends in the elastic anisotropy seen in $Y_2Mo_3O_{12}$ are shared with other anisotropic thermomiotic materials remains to be seen.

9.2. Thermal Stress Analysis *via* Fast Fourier Transforms

The elastic and CTE tensors of $Al_2Mo_3O_{12}$ (see Section 8.3.1) and $Y_2Mo_3O_{12}$[274] were used by Dr. Sean Donegan (at the time, a Ph.D. student at Carnegie Mellon University under the supervision of Dr. Anthony Rollett) to create models of thermal stress in polycrystals following cooling by 700 K. The data sets generated by these models, including the stress and strain at each point, were then analysed by the author. The method used to create the models uses a fast Fourier transform approach to iteratively solve the constituent equations of thermoelasticity.[322] This resulted in considerable computational time savings by comparison to FEM, allowing much larger models to be studied. The polycrystalline models consisted of 1190 randomly-oriented grains with a synthetic microstructure embedded in a compliant buffer layer. The buffer layer was used to avoid constraining the material on its sides so that the effect of elastic anisotropy on the volume thermal expansion could be determined.

The models showed significant thermal stress in both $Y_2Mo_3O_{12}$ and $Al_2Mo_3O_{12}$ following cooling. Thermal stress extrema in both materials reached hundreds of MPa, levels expected to be sufficient to cause significant microcracking. An example cross section of the thermal stress distribution in $Y_2Mo_3O_{12}$ can be seen in Figure 9.10. Stresses from the finite element results were considerably higher, with maxima greater than 2 GPa. This difference can be attributed to the differences in the modeled microstructures. The finite element model was limited by computational constraints to cubic crystallites, which led to larger stresses since as many as eight misaligned grains could meet at a vertex. This effect is evidently greater than the stress decrease caused by the small size and unrestrained boundary conditions used in the finite element model of $Y_2Mo_3O_{12}$. The
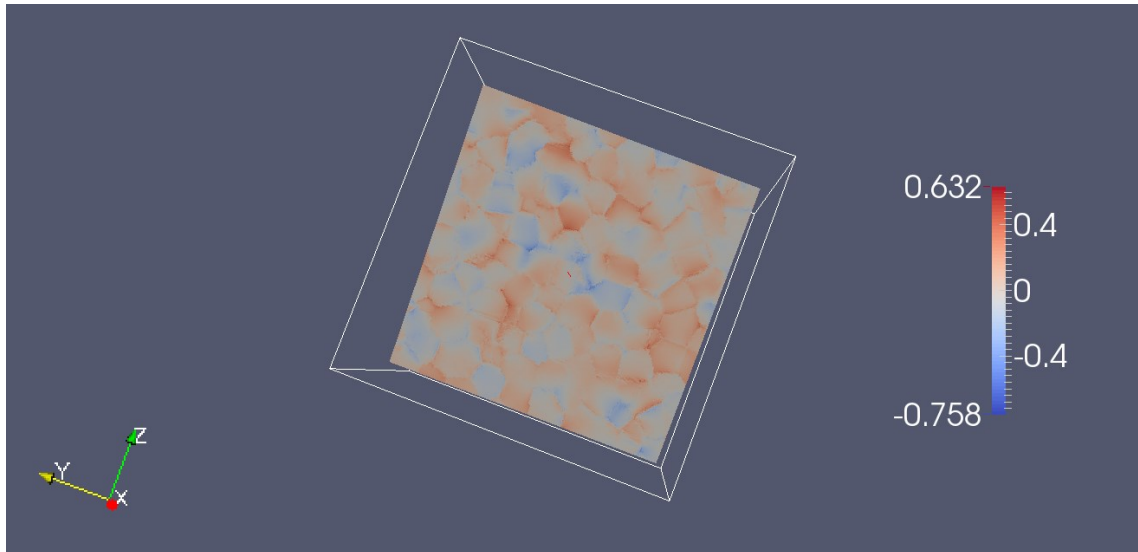
Figure 9.10: Thermal stress (GPa) in the **x** direction in a modelled $Y_2Mo_3O_{12}$ polycrystal following cooling by 700 K. The stress results can be compared to those obtained from finite element modelling in Section 9.1.

current model uses a more realistic microstructure which entails fewer grains meeting at

each grain edge and boundary, and subsequently less thermal expansion mismatch on

average per grain.

A primary way which the finite element analyses presented in Section 9.1 were

validated was by comparison to the predicted average strain energy density obtained by

the method of Kreher (excluding the effect of elastic anisotropy).[314,315] In the

cases of $Al_2Mo_3O_{12}$ and $Y_2Mo_3O_{12}$ the average strain energy density was less than the

predicted value, which was attributed to the small size of the models (64 crystallites).

However, the average strain energy densities of the present models are similarly lower

than the predicted values (659 kJ m^{-3} *vs*. 837 kJ m^{-3} for $Y_2Mo_3O_{12}$ and 222 kJ m^{-3} *vs*.

311 kJ m^{-3} for $Al_2Mo_3O_{12}$). In this case, the number of grains in the microstructure

should be large enough that the surface effects on the average strain energy density are

minimal. The difference can now be attributed to Kreher's assumptions, which were that

the average stress in the material is zero and the average strain is equal to the thermal strain.[314,315] However, the second condition is not true when the coupling of elastic anisotropy and thermal expansion isotropy is considered; the thermal expansion of the stiffer axes would be slightly more expressed than that of the more compliant axes. This effect is seen in the models, as $Y_2Mo_3O_{12}$ and $Al_2Mo_3O_{12}$ show net non-zero strains which can be expressed as deviations from the intrinsic linear CTE of $-1.3 \times 10^{-7} \, K^{-1}$ and $-2.5 \times 10^{-7} \, K^{-1}$, respectively.

The spatially resolved thermal stress data were analysed following two separate local coordinate transformations performed using MATLAB:[323] one to the principal stresses (σ_1, σ_2, and σ_3) and one to the unit cell axes (σ_{aa}, σ_{bb}, σ_{cc}, σ_{bc}, σ_{ac}, and σ_{ab}). Statistical analysis of the resulting distributions using univariate distribution functions was subsequently attempted using R.[324] Several functions (normal, Cauchy, and logistic distributions) were trialed. The normal and logistic distributions showed reasonable fits to the data near the mean, but poorly predicted the extremal stresses. This method of fitting the data directly, while rigorous, was limited by two factors: the large size of the data set ($\approx 13 \times 10^6$ data points), and that the distribution function used must be able to handle negative and positive inputs (which excludes, for example, the Rayleigh, gamma, two-parameter Weibull, and two-parameter lognormal distributions). To avoid these limitations a different method was adopted.

Using MATLAB, the thermal stress data points were sorted into histograms, with 500 kPa bin sizes. This allowed more functions and combinations of functions to be trialed because of the large reduction in the size of the data set to be analysed, at the expense of some added granularity. The use of histograms shifts the problem from a

univariate fitting of statistical distributions to a two-dimensional problem of finding functions that fit the histograms, thusly estimating the underlying distributions. Curve-fitting was carried out using the program Fityk.[325,326]

The stress distributions and fits in the unit cell axis basis are shown in Figures 9.11 and 9.12. The distributions in $Al_2Mo_3O_{12}$ and $Y_2Mo_3O_{12}$ were qualitatively very similar, with the stresses in $Y_2Mo_3O_{12}$ being somewhat larger in magnitude. The increased thermal expansion anisotropy in $Y_2Mo_3O_{12}$ relative to $Al_2Mo_3O_{12}$, which leads to increased thermal stress, is somewhat compensated for by its reduced stiffness. Compressive and tensile thermal stresses reach levels up to 0.5 GPa in both materials, which would be expected to cause microcracking in real polycrystals, as is seen experimentally in $Al_2Mo_3O_{12}$.

No single function was found to fit the stress distributions in the eigenbasis or the unit cell axis basis. Instead, multiple curves were required. In both materials, the uniaxial stress distributions showed significant skewness while shoulders were visible in the shear stress distributions (particularly σ_{ac} and σ_{ab}). The four-parameter lognormal distribution[327] was determined to provide high-quality fits to the stress distributions in the eigenbasis (shown in Appendix E) and the unit cell basis (Figures 9.11 and 9.12) using only two curves, while the normal distribution required three to avoid underestimation of the extremal stresses. The use of two curves is more justifiable than three since thermal stress is caused by interactions of one axis with the thermal expansion of the other two. The uniaxial stresses were particularly well suited to the lognormal distribution in both materials. These stresses were almost completely fit by one lognormal function, with only a small second curve required. $Al_2Mo_3O_{12}$, for which thermoelastic properties are close to
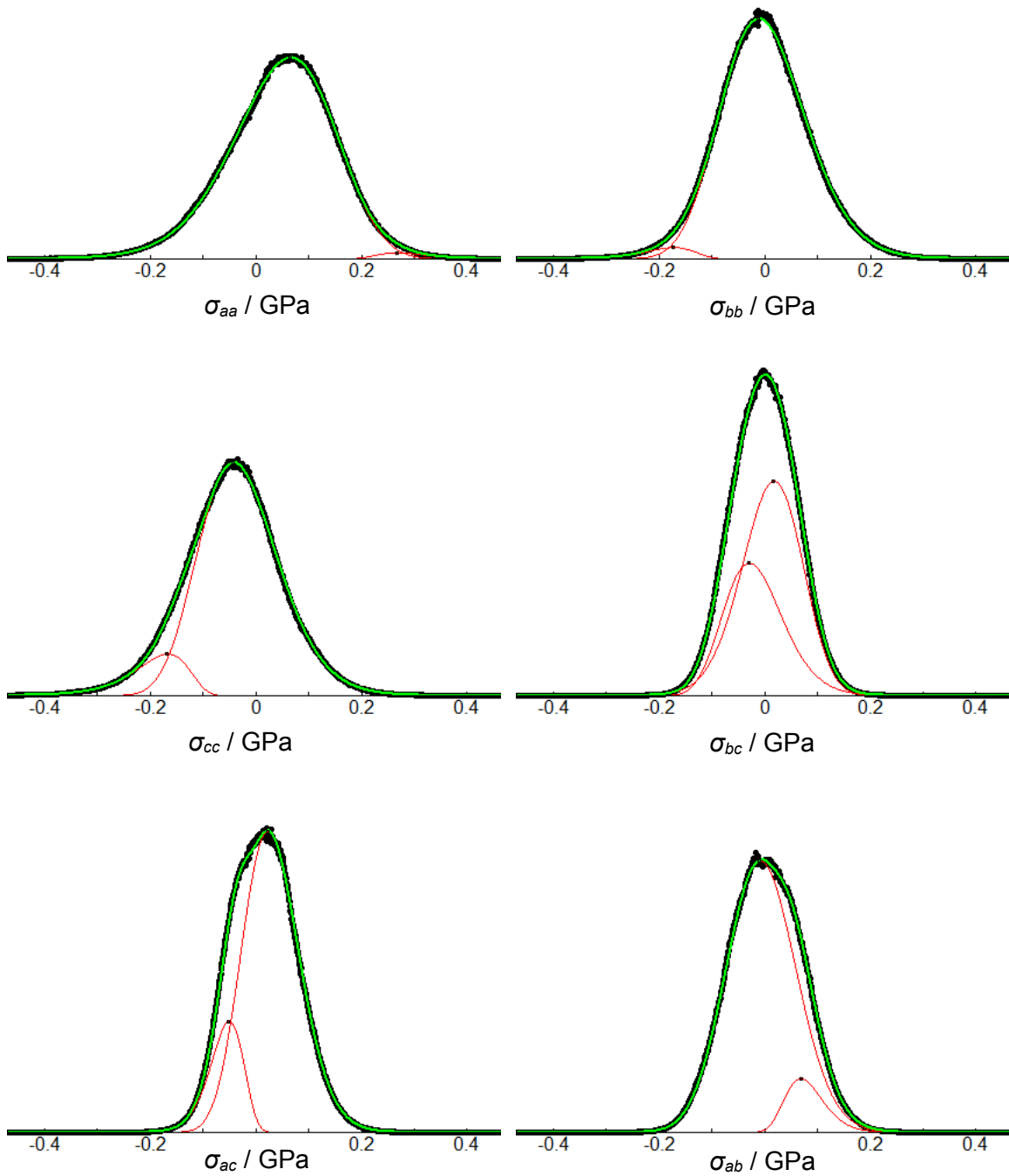
Figure 9.11: Thermal stress distributions in the unit cell axis basis in a modeled $Y_2Mo_3O_{12}$ polycrystal following cooling by 700 K. Black points are data, green curves are fits to the data, and red curves are lognormal functions.
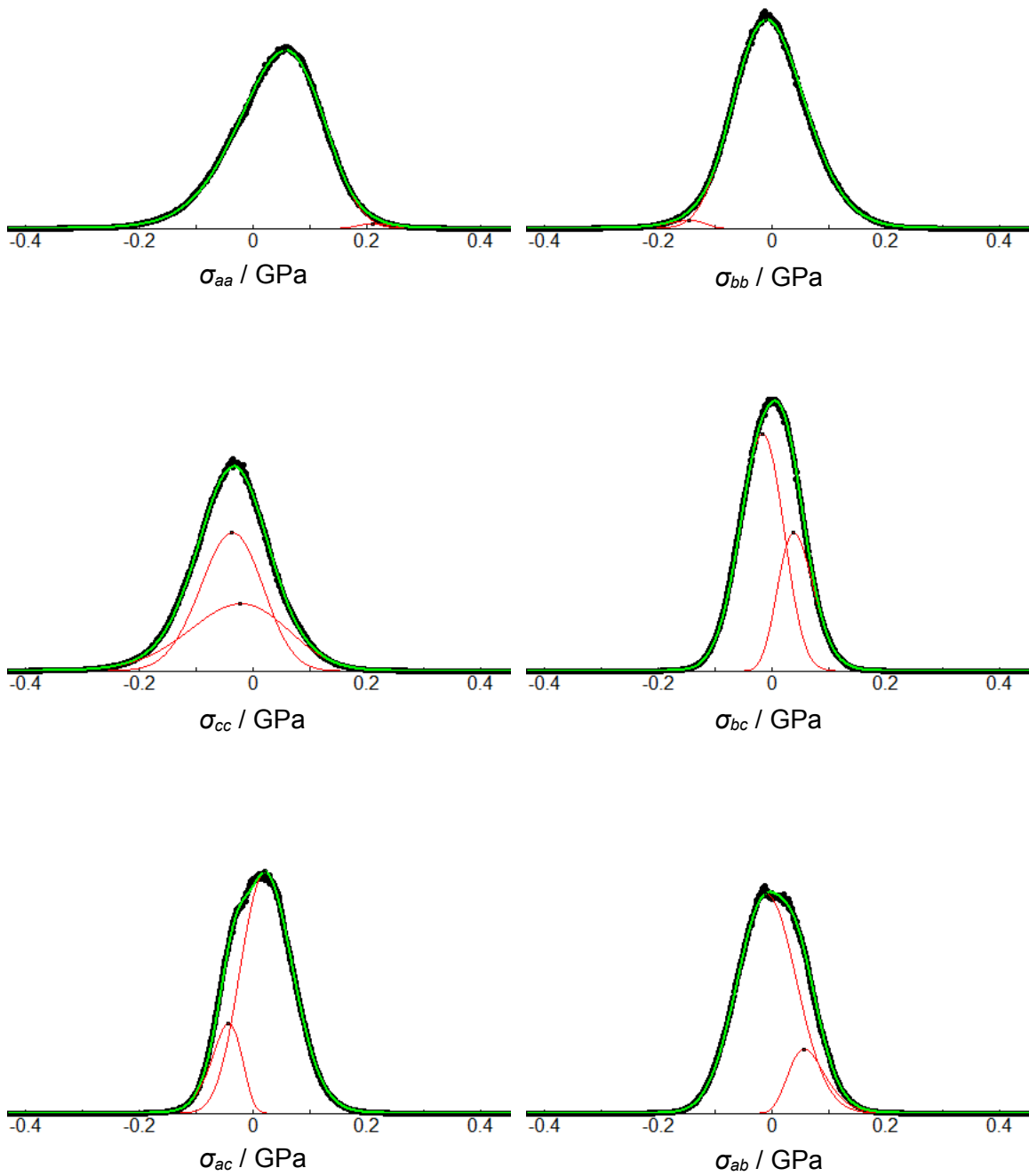
Figure 9.12: Thermal stress distributions in the unit cell axis basis in a modeled Al$_2$Mo$_3$O$_{12}$ polycrystal following cooling by 700 K. Black points are data, green curves are fits to the data, and red curves are lognormal functions.

transverse isotropy in the *bc* plane, requires an especially small contribution from the second function, suggesting a possible relation between the regularity of the stress distributions and the degree of anisotropy of the material. The shear stresses required two lognormal functions of significant magnitude to fit the data. The difference can perhaps be explained by the greater anisotropy of the shear elastic constants relative to the uniaxial elastic constants.

The utility of the lognormal distribution in fitting the data likely is connected to some underlying physical phenomenon. The lognormal distribution is known to arise as a result of multiplication of a series of random variables, whereas the normal distribution arises from summation of a series of random variables.[328] Therefore, the lognormal fit to the stress distribution could imply some multiplicative character to their origin. In anisotropic polycrystalline materials thermal expansion mismatches cause strains in the material, and consequently reaction forces and stresses. In elastically isotropic materials the interactions of reaction forces throughout the material are isotropic. This isotropy results in the stresses at any point being related to the strains caused by thermal expansion anisotropy throughout the remainder of material additively, and the normal thermal stress distribution is a logical result. However, in a material where the elastic constants are anisotropic, the transfer of stresses through the material is not so simple. The elastic anisotropy leads to the grains reacting differently to the applied strains based on their orientations, with increased stress in stiffer directions and *vice versa*. Therefore, elastic anisotropy introduces a multiplicative factor into the thermal stress distributions, since the relationship between the stress at a point and the strain at another point is modified by the variations in the stiffness tensor. While this additive and multiplicative

combination of random variables would not be expected to result in a lognormal

distribution, similar distributions have been studied previously and appear similar to the

stress distributions seen see here.[329]

9.3. Conclusions

The thermal stress distributions calculated in this chapter show that thermal

expansion anisotropy can cause large thermal stresses in $A_2M_3O_{12}$ materials, enough to

cause significant microcracking upon heating and cooling. The distributions of the

thermal stresses are affected by the properties of the CTE and elastic tensors.

Interestingly, the results shown in Section 9.2 indicate that the stress distributions in the

two extremal members of the $A_2Mo_3O_{12}$ family are quite similar. In both cases, maximum

tensile and compressive thermal stresses on the order of 0.5 GPa can be expected. The

elastic tensors of $Al_2Mo_3O_{12}$ and $Y_2Mo_3O_{12}$ were found to couple with the thermal

expansion tensors to produce small deviations in the bulk CTE. The thermal stress

distributions could be fit with lognormal distributions in both cases, indicating the

presence of some multiplicative effect due to elastic anisotropy. However, due to the

large number of variables in play, the current data set is insufficient to identify

quantitatively how the thermoelastic properties of $Y_2Mo_3O_{12}$ and $Al_2Mo_3O_{12}$ affect the

stress distributions. Therefore, in the future calculations will be performed on $Sc_2Mo_3O_{12}$

and $ZrMgMo_3O_{12}$, since their elastic tensors have been calculated (see Chapter 8).

Chapter 10: Conclusion

Interactions between thermal expansion and mechanical properties have been investigated in this thesis in order to obtain a more complete picture of the thermoelastic behaviour of thermomiotic materials. Computational and experimental investigations were performed in order to probe thermoelastic properties of composites containing thermomiotic components and bulk polycrystalline thermomiotic materials.

Large thermal stresses in composite materials containing thermomiotic components had been previously predicted in the literature; initial investigations explored potential methods to alleviate this problem. Pressure-induced phase transitions and inclusion of a phase of intermediate thermal expansion were identified as potentially effective means of thermal stress reduction. Additionally, thermal stress was found to be considerably lower in composites that included a compliant material such as a polymer, even when the CTE mismatch was much larger. These ideas were implemented in the synthesis of a series of ceramic composite materials combining the thermomiotic materials ZrW_2O_8 and $Al_2W_3O_{12}$ with ATZ, a material with phase-transition enhanced toughness, and the synthesis of lamellar ZrW_2O_8 *via* freeze-casting and its impregnation with PMMA. Characterization of the prepared composites revealed large differences between the CTEs predicted by the rule of mixtures and the measured CTEs, which were related to the large differences in stiffnesses between the components. This finding firmly established the relevance of the elastic properties of thermomiotic materials to their ability to counteract positive thermal expansion.

Due to their chemical flexibility, the $A_2M_3O_{12}$ and $AMgM_3O_{12}$ families offered an opportunity to study the elastic properties of a range of structurally related thermomiotic

materials in conjunction with their thermal expansion. However, no structure of an orthorhombic AMgM_3O$_{12}$ material had been reported, and thus the mechanism of thermal expansion reduction in this family was unknown. Therefore, the structure of ZrMgMo$_3$O$_{12}$, a material that was determined to have zero thermal expansion, was solved using NMR crystallography. The structure was revealed to be similar to that of the A_2M_3O$_{12}$ family, but with larger polyhedral distortions than expected based on its CTE. The thermal expansion of ZrMgMo$_3$O$_{12}$ was explained and related to that of the A_2M_3O$_{12}$ family through the strength of the ionic interaction between the Zr^{4+} and Mg^{2+} cations and their coordinate O^{2-} anions, indicating a common mechanism of CTE reduction between the two families and furthering the connection between the rigidity of coordination polyhedra and thermal expansion in these materials.

Three series of solid solutions (In$_{2-2x}$(HfMg)$_x$Mo$_3$O$_{12}$, Sc$_{2-2x}$Al$_{2x}$W$_3$O$_{12}$, and Cr$_{2-2x}$(HfMg)$_x$W$_3$O$_{12}$) were synthesized and their bulk elastic moduli and CTEs measured. Within each series, correlations between thermal expansion and stiffness were shown; in general stiffness decreased with an increasing magnitude of the CTE. This result implies that the materials studied with more negative thermal expansion would be less useful than expected at counteracting PTE, especially in combination with stiff PTE materials. Additionally, this investigation revealed an interesting property of Cr$_{2-2x}$(HfMg)$_x$W$_3$O$_{12}$ solid solution materials: upon cooling through the orthorhombic-monoclinic phase transition temperature, the expected decrease in volume and change in CTE was not observed. Instead, a very gradual contraction occurred while the material remained at room temperature. The measurements of velocities of sound used to determine the elastic moduli were affected by microcracks in the polycrystalline samples

due to thermal stress from their anisotropic thermal expansion. This presented another avenue of research concerning thermoelasticity: how anisotropic thermal expansion and elasticity couple to influence thermal stress in polycrystalline bodies.

Computational methods were used to investigate anisotropic elasticity and Γ-point phonon energies in $Al_2Mo_3O_{12}$, $Sc_2Mo_3O_{12}$, and $ZrMgMo_3O_{12}$, and elasticity and the full phonon dispersion relationship in ScF_3. In the case of ScF_3, the computational results were paired with experimental measurement of low-temperature heat capacity. All the materials studied were determined to have significant elastic anisotropy. The elastic tensors were related to the axial thermal expansion in the anisotropic materials by the axial Grüneisen parameters, showing how the large CTE anisotropy is driven in part by coupling of the axial CTEs through the Poisson effect. Interestingly, the thermomiotic axes were generally found to be stiffer than the axes with positive thermal expansion.

The calculated elastic tensors of $Al_2Mo_3O_{12}$ and $Y_2Mo_3O_{12}$ were used to produce models of thermal stress in polycrystals. These models showed significant thermal stresses due to thermal expansion anisotropy, at levels sufficient to cause microcracking when the material is cooled to room temperature following sintering. Elastic anisotropy was found to couple with CTE anisotropy, influencing the stress distributions in a way that increased the extremal stresses.

The overall goals of the research presented herein were to examine the thermoelastic relationships between thermal expansion, elasticity, and thermal stress in thermomiotic materials, and to find ways to ameliorate the mechanical shortcomings of thermomiotic materials and protect them from thermal stress. Experimental and computational results showed significant correlations between thermal expansion and

elastic stiffness in the $A_2M_3O_{12}$ and $AMgM_3O_{12}$ material families; materials with more negative thermal expansion were found to generally be more compliant both in terms of their bulk and axial properties. This finding can be related to the proposed mechanism for NTE in these materials involving polyhedral distortion, as well as the general thermodynamic relationship between the CTE, the elastic tensor, and the Grüneisen parameter. The influence of coupled elastic and CTE anisotropy on thermal stress distributions demonstrated that the intrinsic axial properties effect the thermoelastic behaviour of the bulk material.

Microstructural control, use of non-Hookean materials, and use of compliant materials were identified as promising approaches to overcome the mechanical shortcomings and propensity to thermal stress of thermomiotic materials. By using experimental methods to characterize the elastic properties as well as the thermal expansivity of thermomiotic materials, it was shown to be possible to obtain useful predictions of the thermoelastic behaviour of bulk composite materials.

Research concerning the full thermoelastic properties of thermomiotic materials was shown to be important both to understand the origins of negative thermal expansion and to predict the properties of bulk monophasic and composite materials. However, since this topic has not been extensively studied previously for most thermomiotic materials, considerable future work remains. Comprehensive characterization of the elastic properties of thermomiotic materials would allow more general conclusions concerning the links between elastic properties and thermal expansion. As no experimental method is available to determine the elastic tensor from a polycrystalline sample, further computational research is required as well. Computations also offer the

ability to estimate thermal stresses in bulk materials, which would be important in order for thermomiotic materials to find applications.

While much is known about the vibrational origins of NTE in materials composed of rigid coordination polyhedra with connectivities that are amenable to RUMs, the mechanisms of NTE in materials with distortable polyhedra are less well understood. Further studies of the phononic structures of these materials are necessary in order to elucidate their connections to polyhedral distortion and to elastic properties.

There are many potential methods to compensate for mechanical deficiencies of thermomiotic materials, only several of which were explored in this thesis. There are many potential routes to microstructural control that could be used to reduce thermal stress and tailor thermal expansivity. While the utility of non-Hookean materials at stress management has been explored in other systems, the potential non-Hookean behaviour of many thermomiotic materials (through pressure-induced phase transitions and amorphization) under thermal stress could be investigated. An important component of compensation for thermoelastic deficiencies must be consideration of the stiffnesses of the materials involved.

Appendix A: X-ray Diffractograms

A1. Al₂Mo₃O₁₂
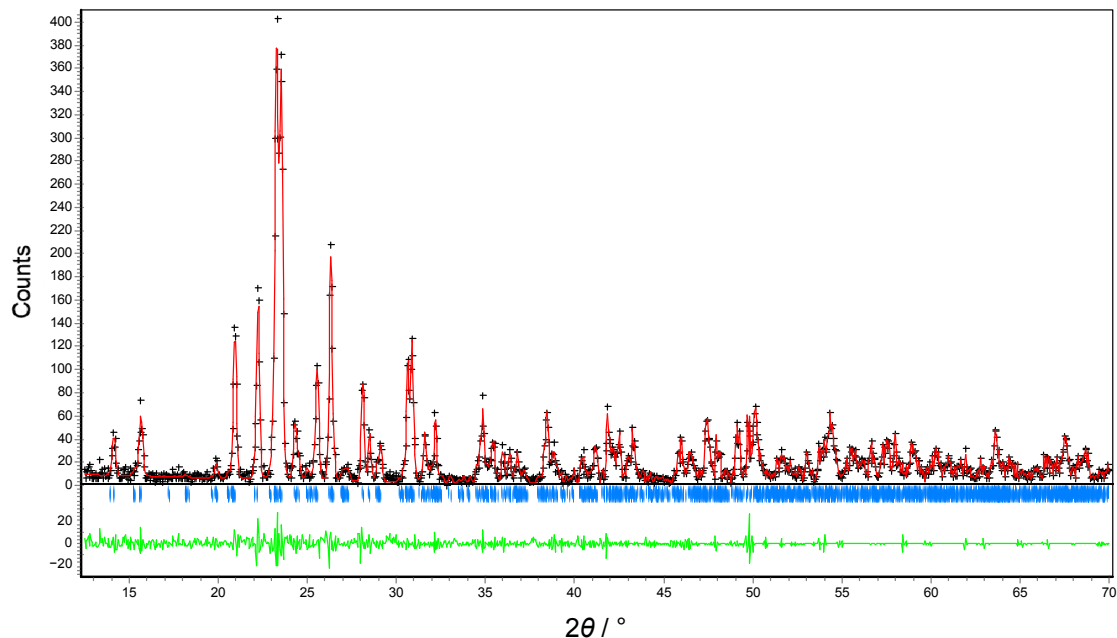
Figure A1: X-ray diffractogram of $Al_2Mo_3O_{12}$ (see Chapter 3) with experimental data shown as black crosses, the Le Bail fit to the data ($\chi^2 = 0.564$) as a red line, the peak positions shown as blue ticks,[xxvi] and the residual (measured intensity minus predicted intensity) shown as a green line.

[xxvi] Two sets of marks are shown for each Bragg peak in the diffractograms presented herein due to the presence of $K\alpha_1$ ($\lambda = 1.54016$ Å) and $K\alpha_2$ ($\lambda = 1.54398$ Å) radiation from the Cu X-ray source.

A2. ZrW_2O_8/$Al_2W_3O_{12}$/ATZ Composite
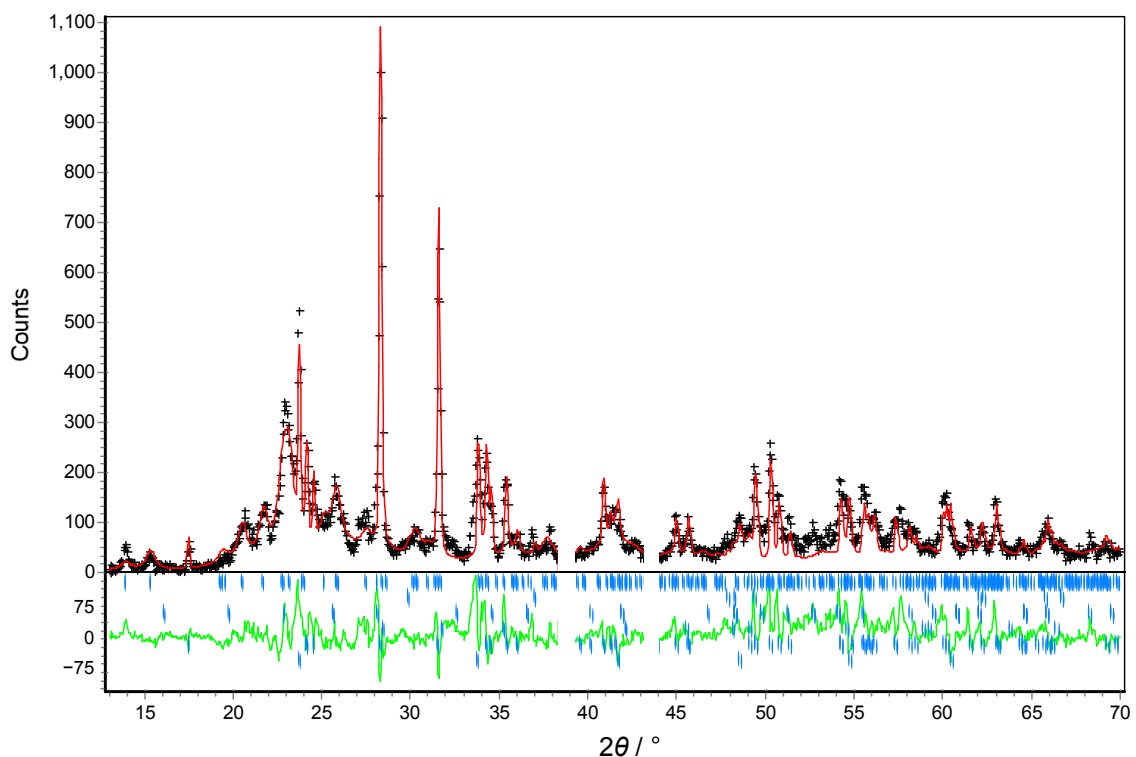
Figure A2: X-ray diffractogram of a ZrW_2O_8/$Al_2W_3O_{12}$/ATZ composite material (Sample 7, see Chapter 4). Measured data are shown in black, a Rietveld fit to the data is shown in red, the residual is shown in green, and the peak positions of the phases included in the Rietveld fit are shown in blue (from top to bottom: $Al_2W_3O_{12}$, Al_2O_3, ZrW_2O_8, tetragonal ZrO_2, monoclinic ZrO_2, and cubic WO_3.) Two peaks from the sample holder at 38° and 44° 2θ were excluded from the refinement.

A3. Lamellar ZrW$_2$O$_8$
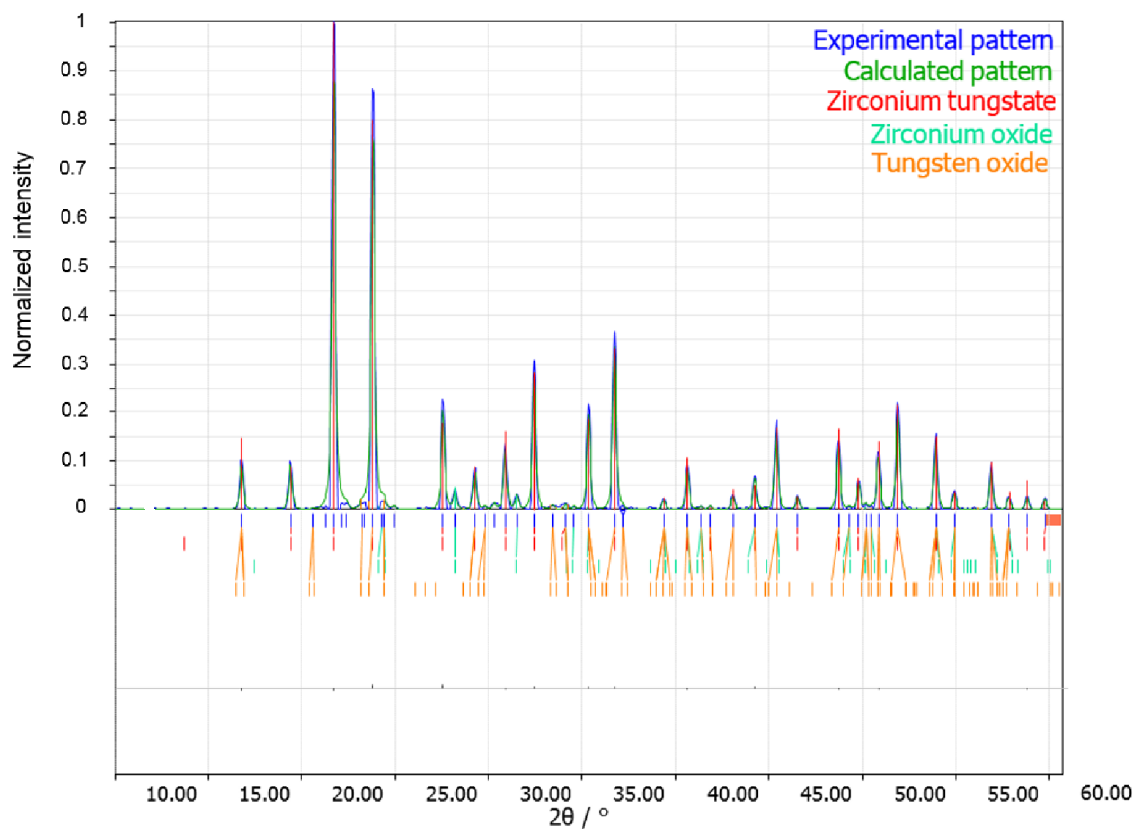
Figure A3: X-ray diffractogram of lamellar ZrW$_2$O$_8$ (see Chapter 4), showing the presence of ZrO$_2$ and WO$_3$ due to decomposition.

A4. ZrMgMo₃O₁₂
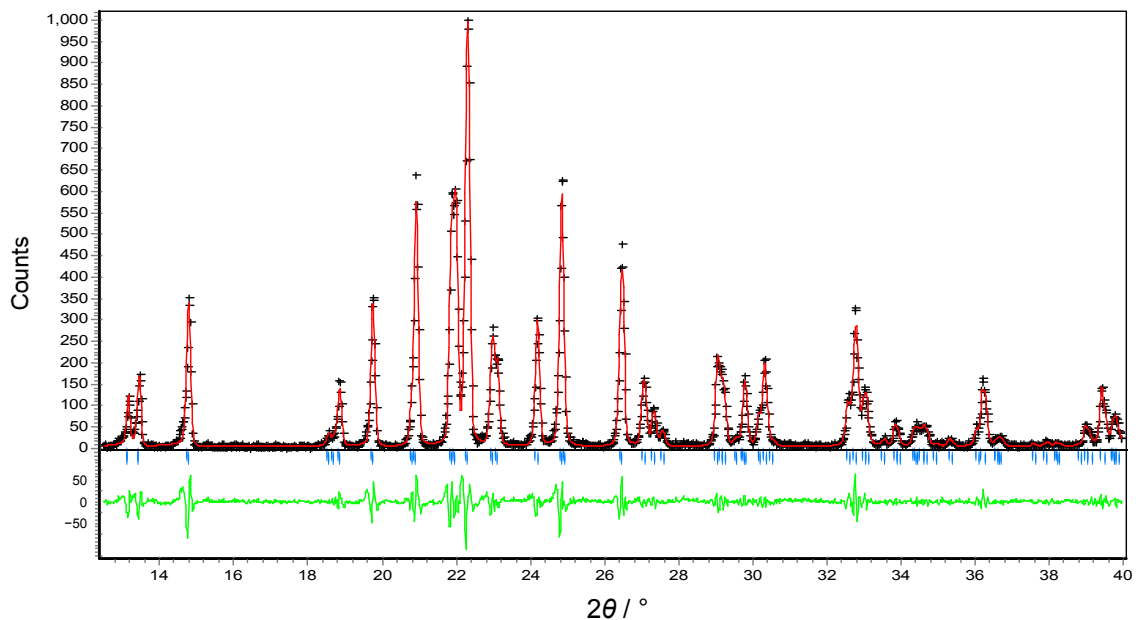
Figure A4: X-ray diffractogram of ZrMgMo$_3$O$_{12}$ (see Chapter 5) with experimental data shown as black crosses, the Le Bail fit to the data ($\chi^2 = 1.946$) shown as a red line, the peak positions shown as blue ticks, and the residual shown as a green line.
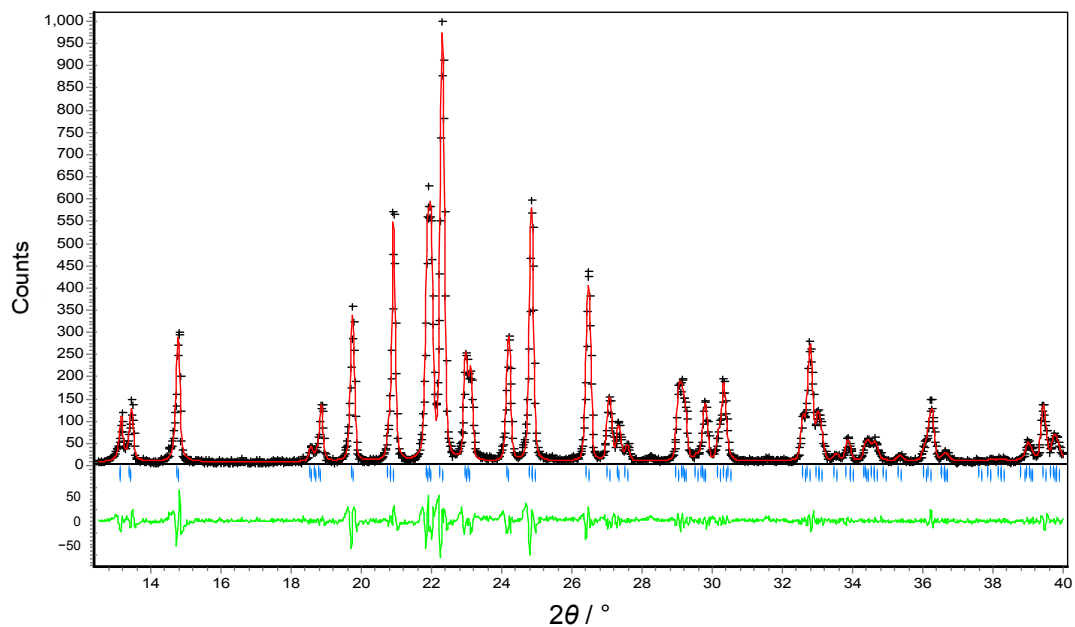
Figure A5: X-ray diffractogram of ^{17}O-enriched ZrMgMo$_3$O$_{12}$ (see Chapter 5) with experimental data shown as black crosses, the Le Bail fit to the data ($\chi^2 = 1.314$) shown as a red line, the peak positions shown as blue ticks, and the residual shown as a green line.

A5. $In_{2-2x}(HfMg)_xMo_3O_{12}$
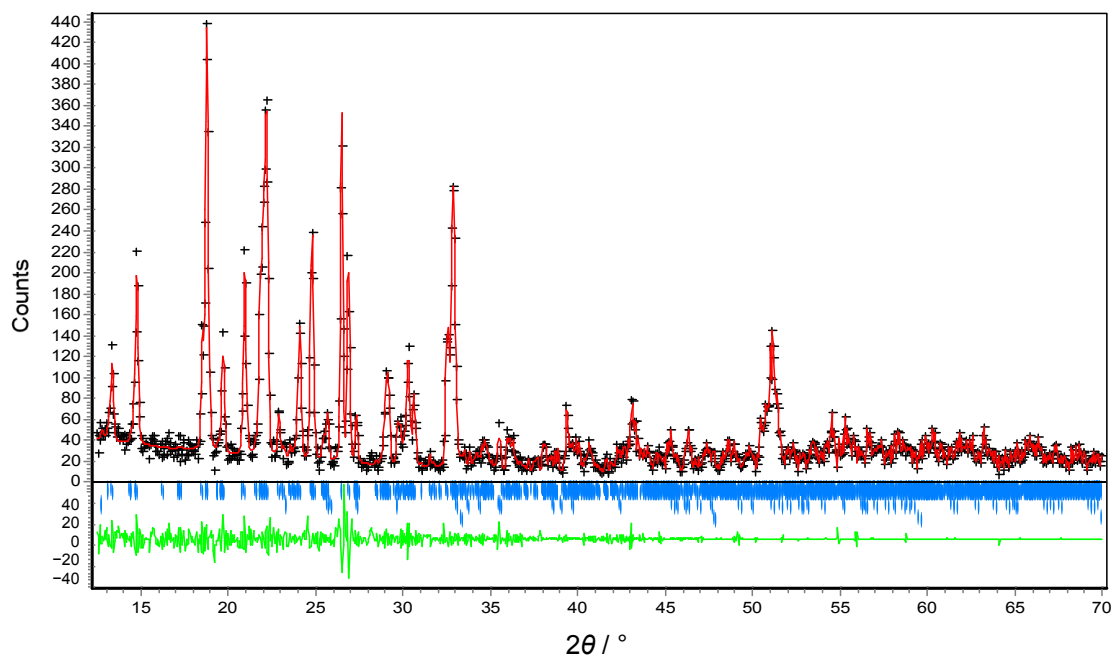
Figure A6: X-ray diffractogram of $In_2Mo_3O_{12}$ (see Chapter 6) with experimental data shown as black crosses, the Le Bail fit to the data ($\chi^2 = 0.514$) shown as a red line, the peak positions shown as blue ticks (top row, $In_2Mo_3O_{12}$, second row MoO_3, bottom row In_2O_3), and the residual shown as a green line.
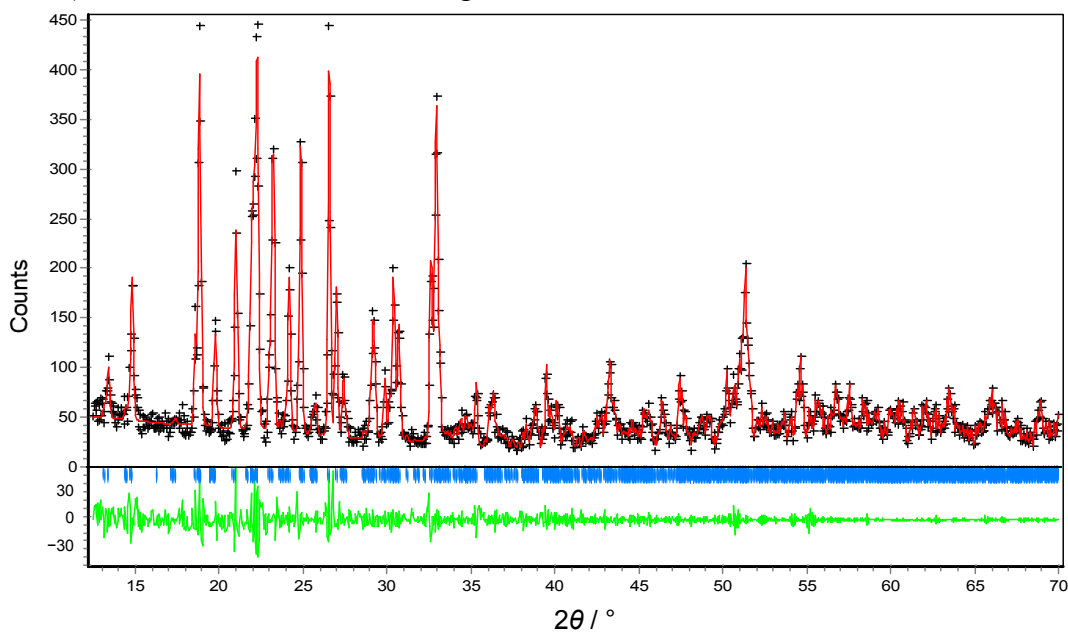
Figure A7: X-ray diffractogram of $In_{1.5}(HfMg)_{0.25}Mo_3O_{12}$ (see Chapter 6) with experimental data shown as black crosses, the Le Bail fit to the data ($\chi^2 = 0.633$) shown as a red line, the peak positions shown as blue ticks, and the residual shown as a green line.
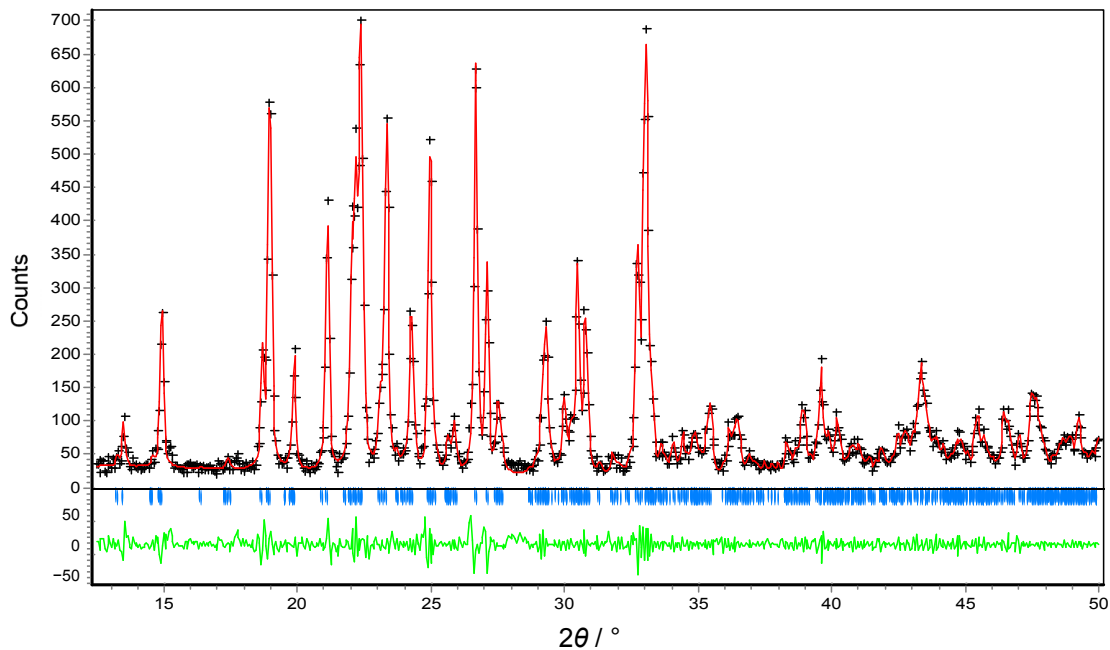
Figure A8: X-ray diffractogram of $In(HfMg)_{0.5}Mo_3O_{12}$ (see Chapter 6) with experimental data shown as black crosses, the Le Bail fit to the data ($\chi^2 = 0.873$) shown as a red line, the peak positions shown as blue ticks, and the residual shown as a green line.
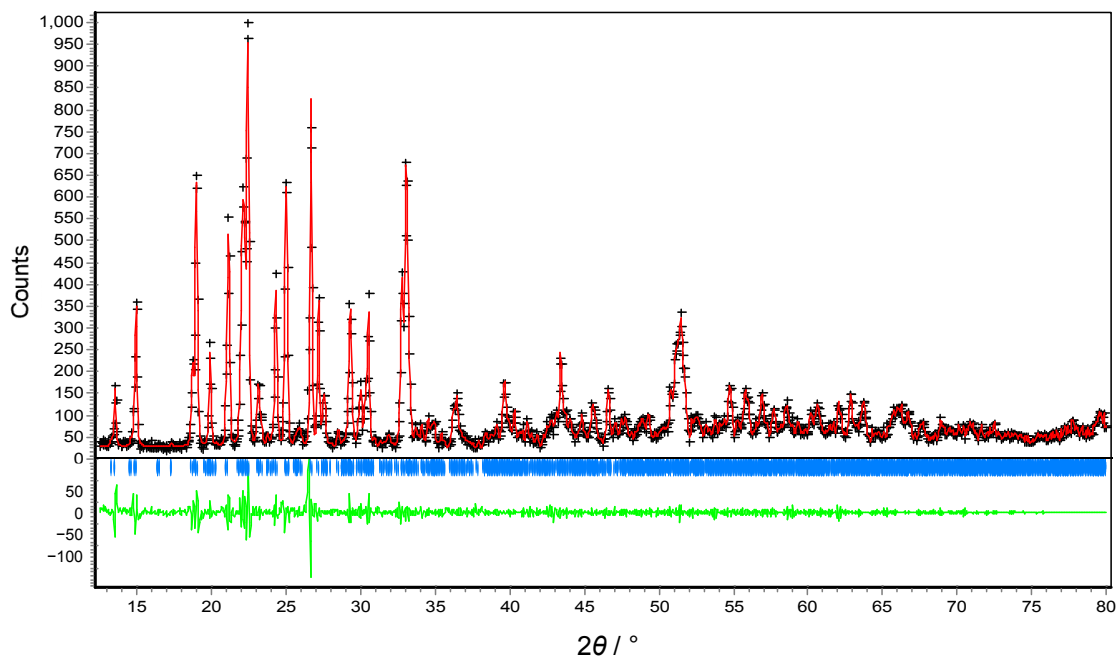
Figure A9: X-ray diffractogram of $In_{0.5}(HfMg)_{0.75}Mo_3O_{12}$ (see Chapter 6) with experimental data shown as black crosses, the Le Bail fit to the data ($\chi^2 = 0.869$) shown as a red line, the peak positions shown as blue ticks, and the residual shown as a green line.
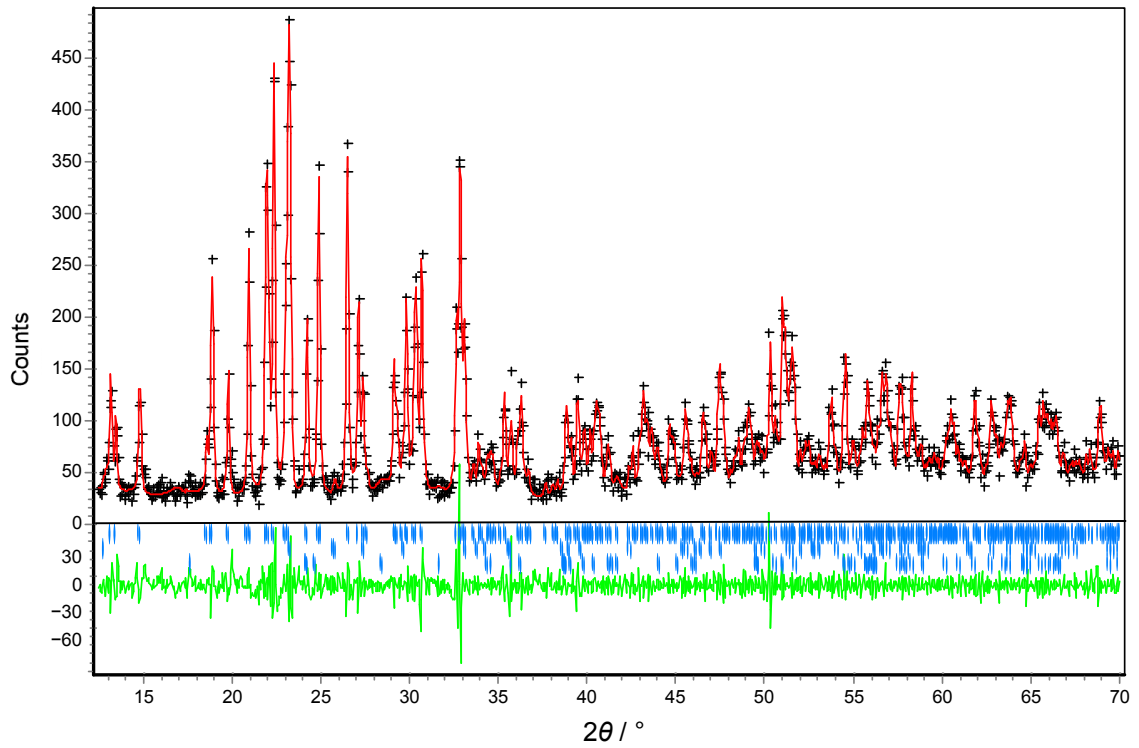
Figure A10: X-ray diffractogram of HfMgMo$_3$O$_{12}$ (see Chapter 6) with experimental data shown as black crosses, the Le Bail fit to the data ($\chi^2 = 1.086$) shown as a red line, the peak positions shown as blue ticks (top row, In$_2$Mo$_3$O$_{12}$, second row MoO$_3$, bottom row HfO$_2$), and the residual shown as a green line.

A6. $Sc_{2-2x}Al_{2x}W_3O_{12}$
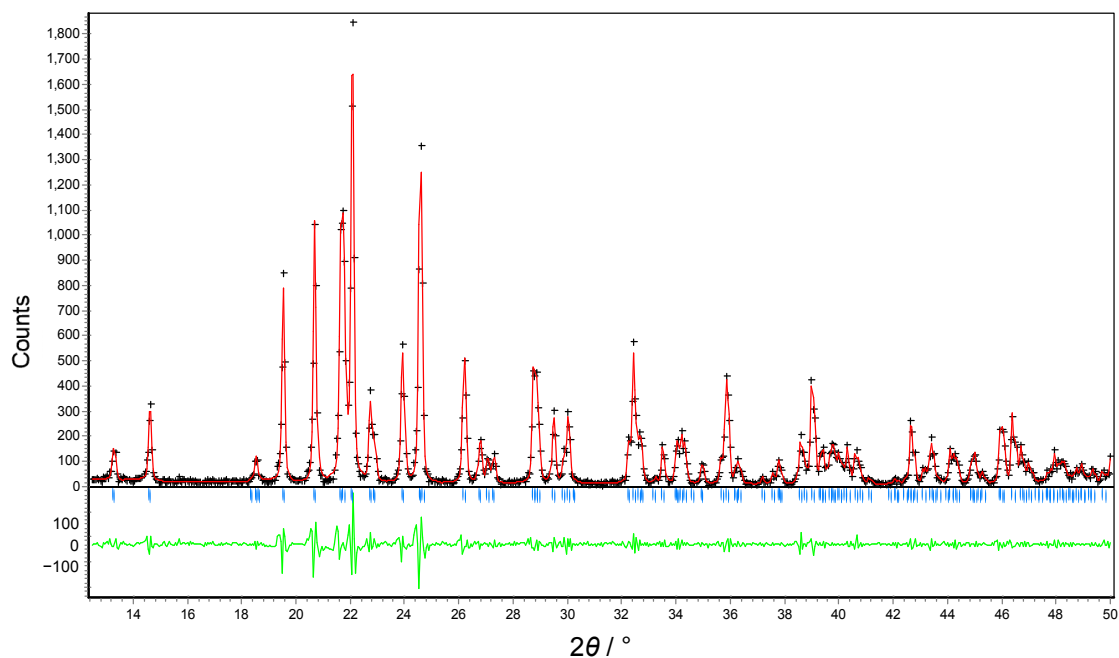
Figure A11: X-ray diffractogram of $Sc_2W_3O_{12}$ (see Chapter 6) with experimental data shown as black crosses, the Le Bail fit to the data ($\chi^2 = 2.282$) shown as a red line, the peak positions shown as blue ticks, and the residual shown as a green line.
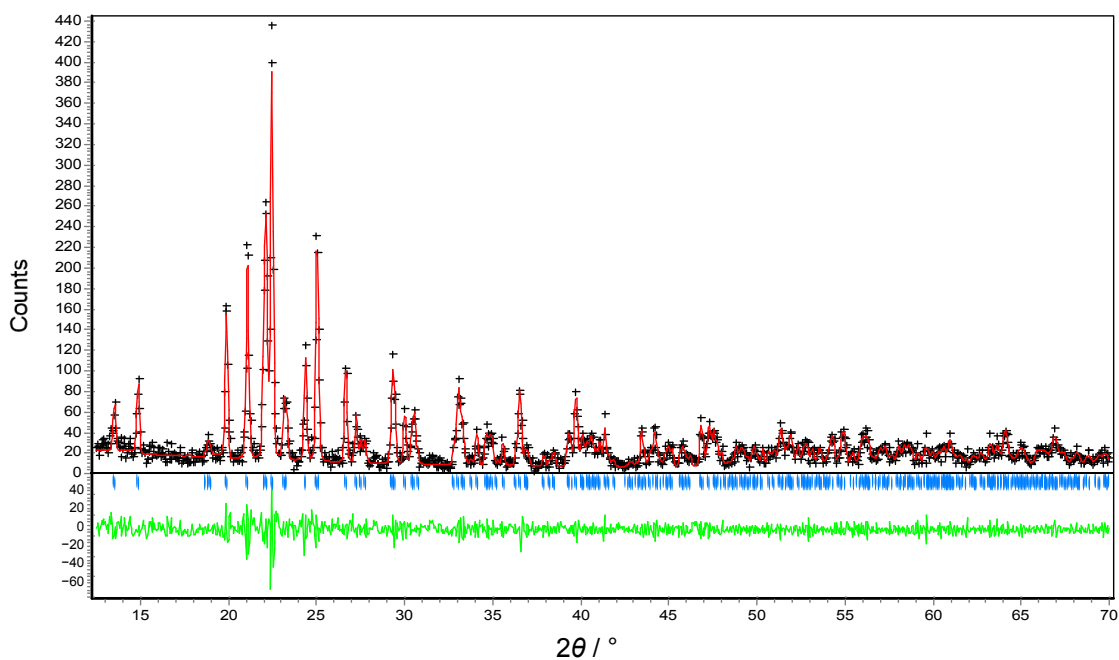
Figure A12: X-ray diffractogram of $Al_{0.5}Sc_{1.5}W_3O_{12}$ (see Chapter 6) with experimental data shown as black crosses, the Le Bail fit to the data ($\chi^2 = 1.064$) shown as a red line, the peak positions shown as blue ticks, and the residual shown as a green line.
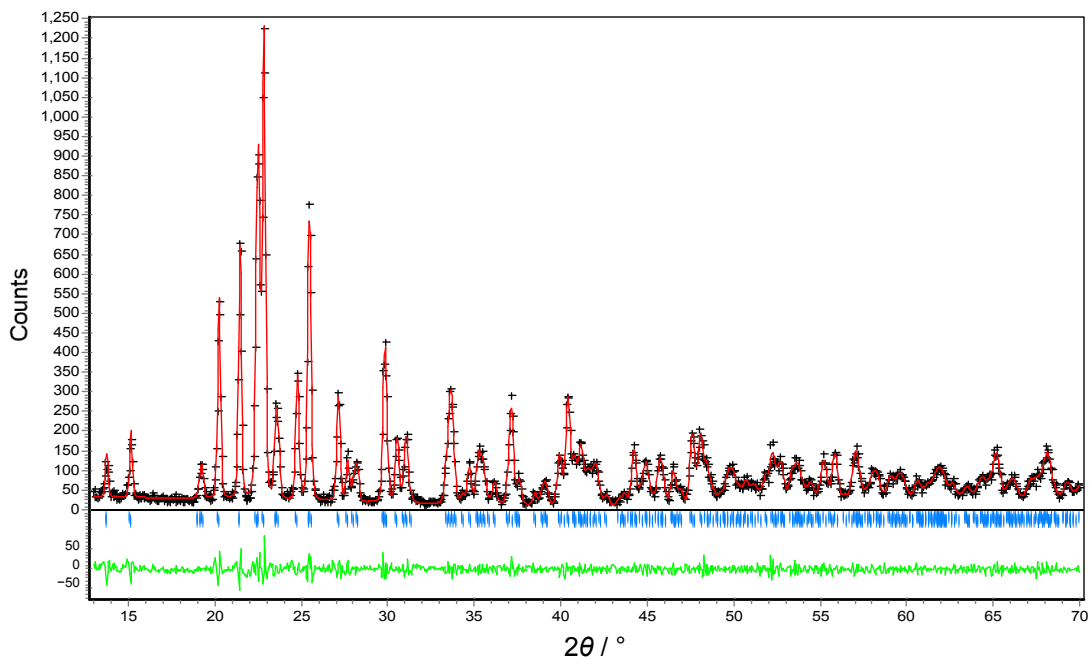
Figure A13: X-ray diffractogram of $AlScW_3O_{12}$ (see Chapter 6) with experimental data shown as black crosses, the Le Bail fit to the data ($\chi^2 = 1.114$) shown as a red line, the peak positions shown as blue ticks, and the residual shown as a green line.
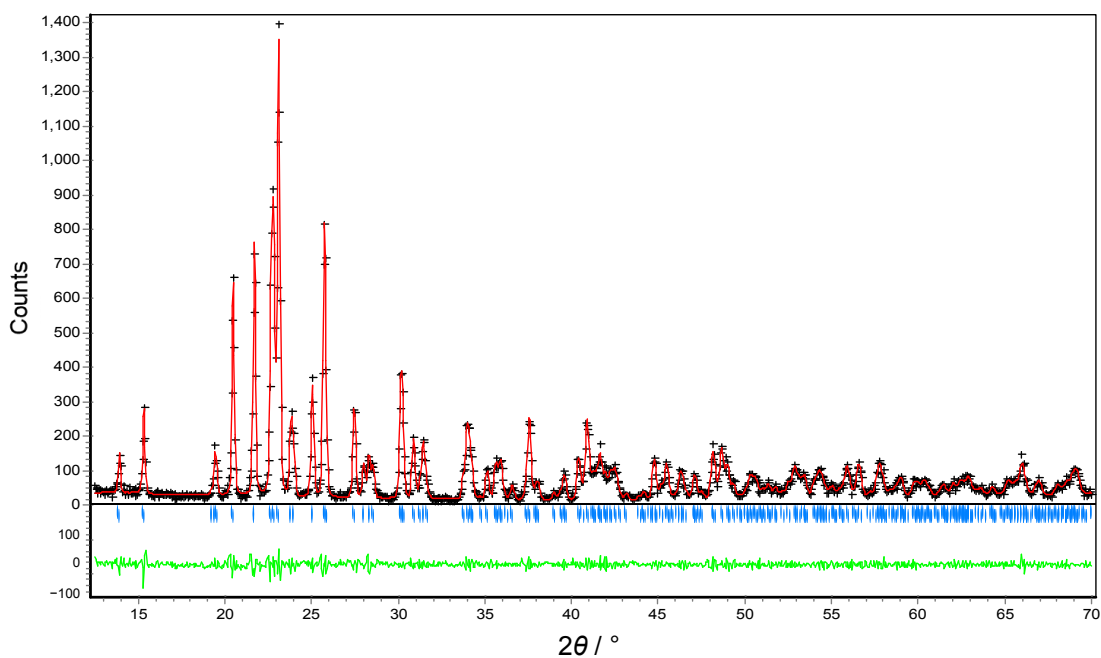
Figure A14: X-ray diffractogram of $Al_{1.5}Sc_{0.5}W_3O_{12}$ (see Chapter 6) with experimental data shown as black crosses, the Le Bail fit to the data ($\chi^2 = 1.069$) shown as a red line, the peak positions shown as blue ticks, and the residual shown as a green line.
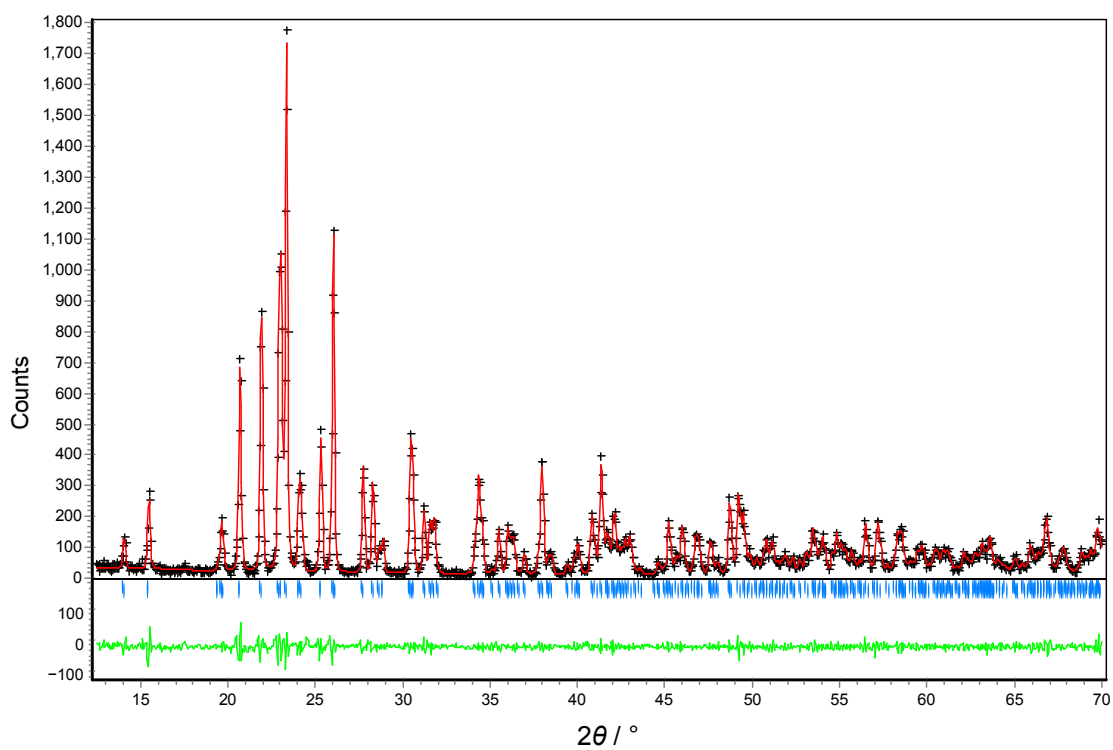
Figure A15: X-ray diffractogram of $Al_2W_3O_{12}$ (see Chapter 6) with experimental data shown as black crosses, the Le Bail fit to the data ($\chi^2 = 1.392$) shown as a red line, the peak positions shown as blue ticks, and the residual shown as a green line.

A7. Cr$_{2-2x}$(HfMg)$_x$W$_3$O$_{12}$
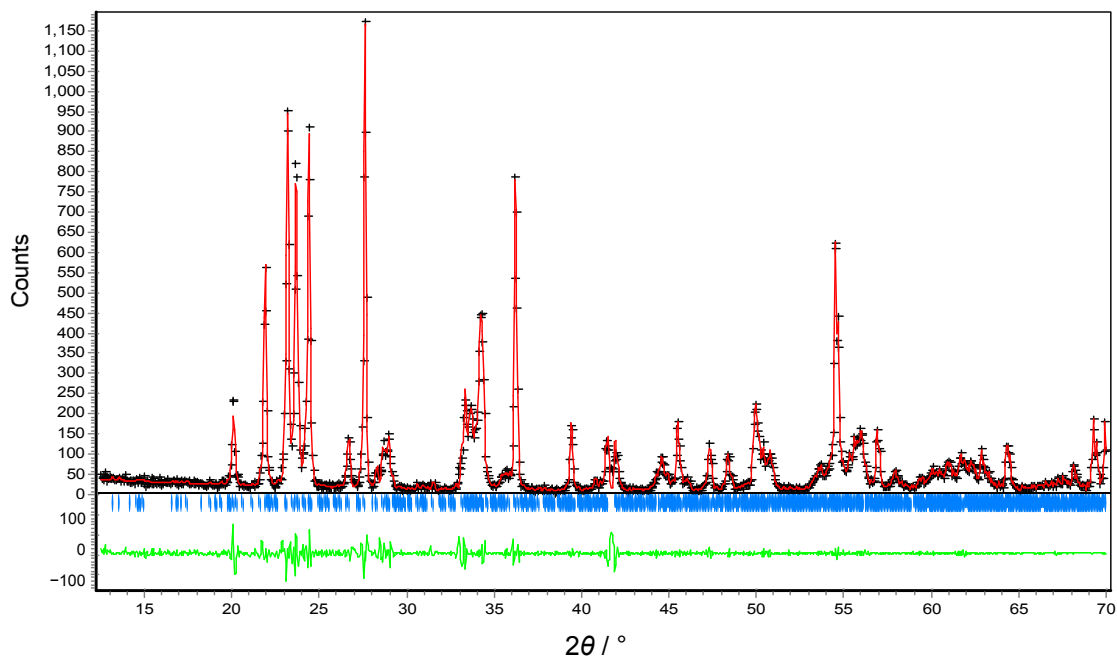
Figure A16: X-ray diffractogram of Cr$_2$W$_3$O$_{12}$ (see Chapter 6) with experimental data shown as black crosses, the Le Bail fit to the data ($\chi^2 = 1.007$) shown as a red line, the peak positions shown as blue ticks, and the residual shown as a green line.
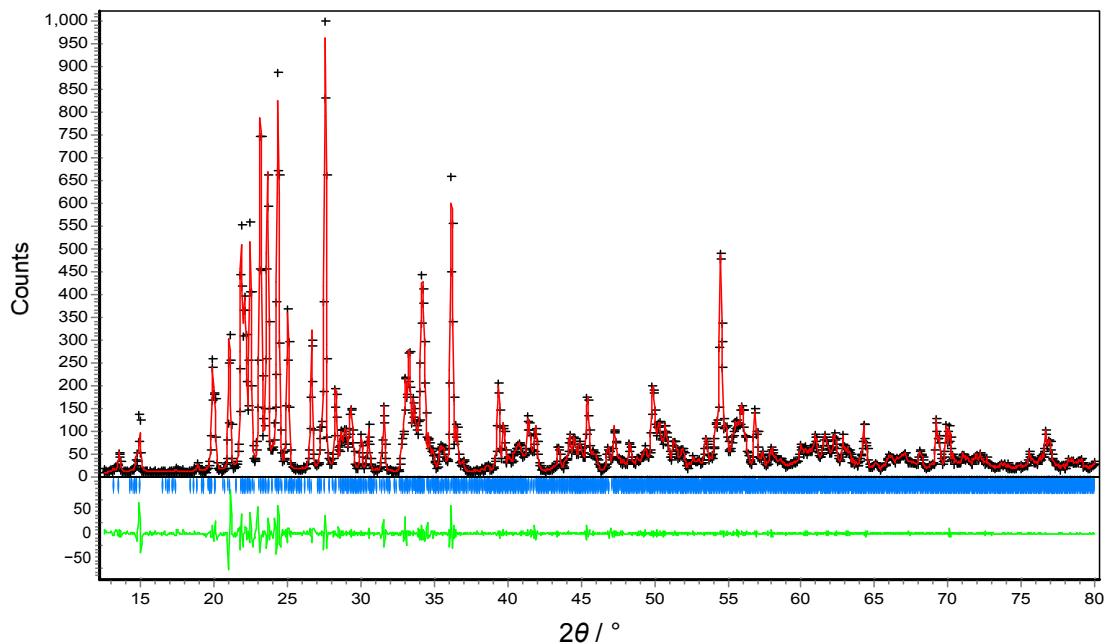
Figure A17: X-ray diffractogram of Cr$_{1.5}$(HfMg)$_{0.25}$W$_3$O$_{12}$ (see Chapter 6) with experimental data shown as black crosses, the Le Bail fit to the data ($\chi^2 = 0.728$) shown as a red line, the peak positions shown as blue ticks, and the residual shown as a green line.
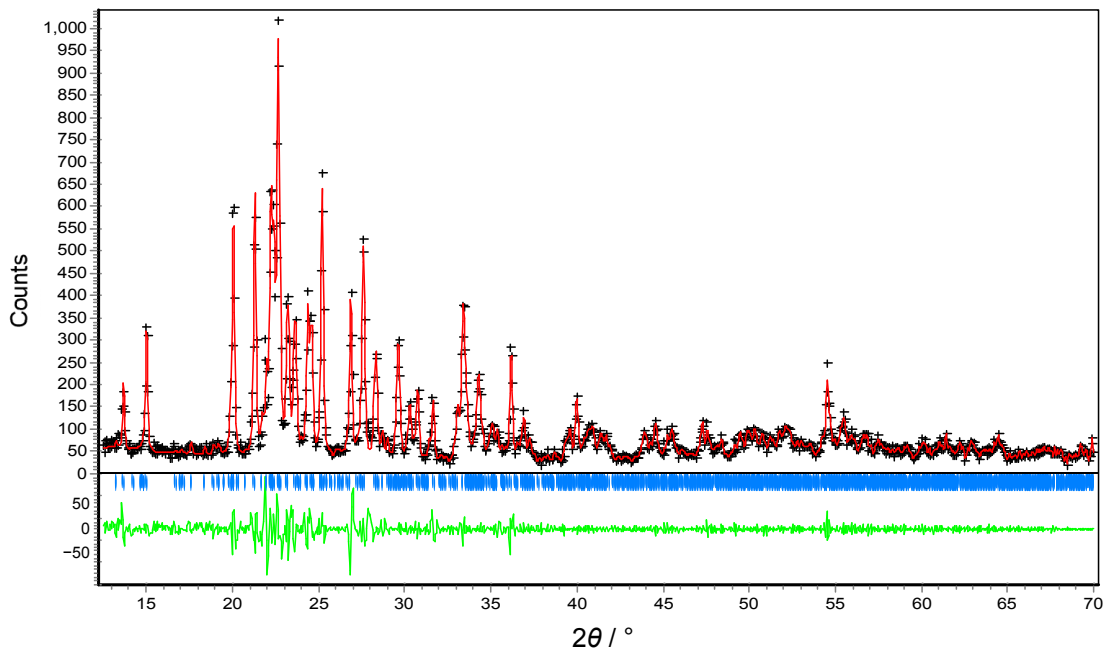
Figure A18: X-ray diffractogram of $Cr(HfMg)_{0.5}W_3O_{12}$ (see Chapter 6) with experimental data shown as black crosses, the Le Bail fit to the data ($\chi^2 = 1.393$) shown as a red line, the peak positions shown as blue ticks, and the residual shown as a green line.
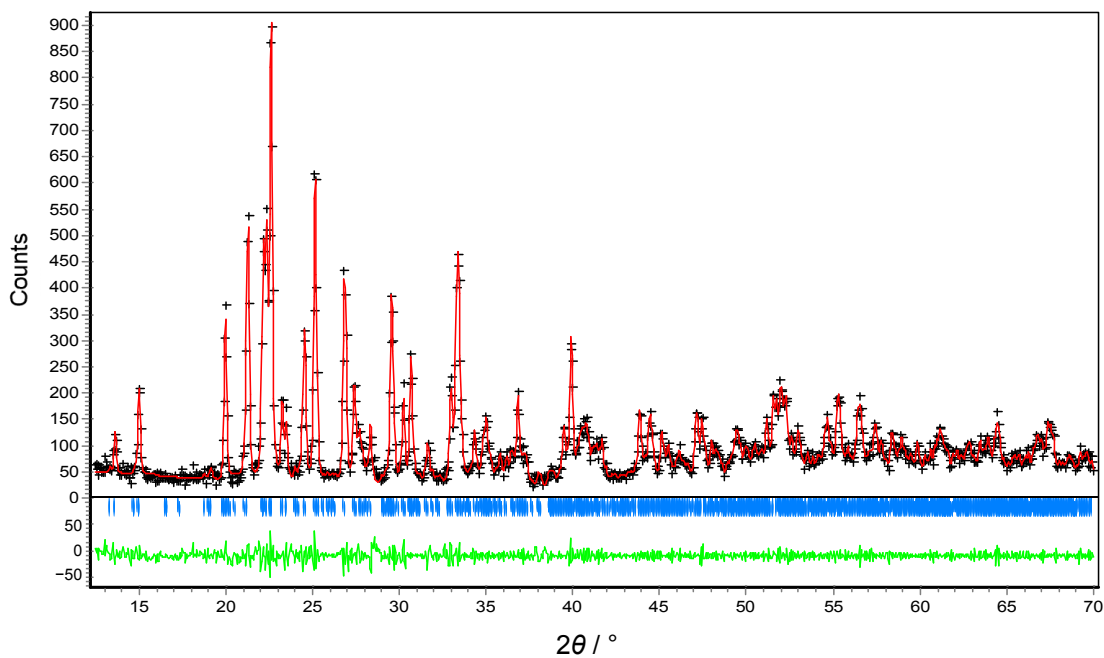
Figure A19: X-ray diffractogram of $Cr_{0.5}(HfMg)_{0.75}W_3O_{12}$ (see Chapter 6) with experimental data shown as black crosses, the Le Bail fit to the data ($\chi^2 = 0.815$) shown as a red line, the peak positions shown as blue ticks, and the residual shown as a green line.
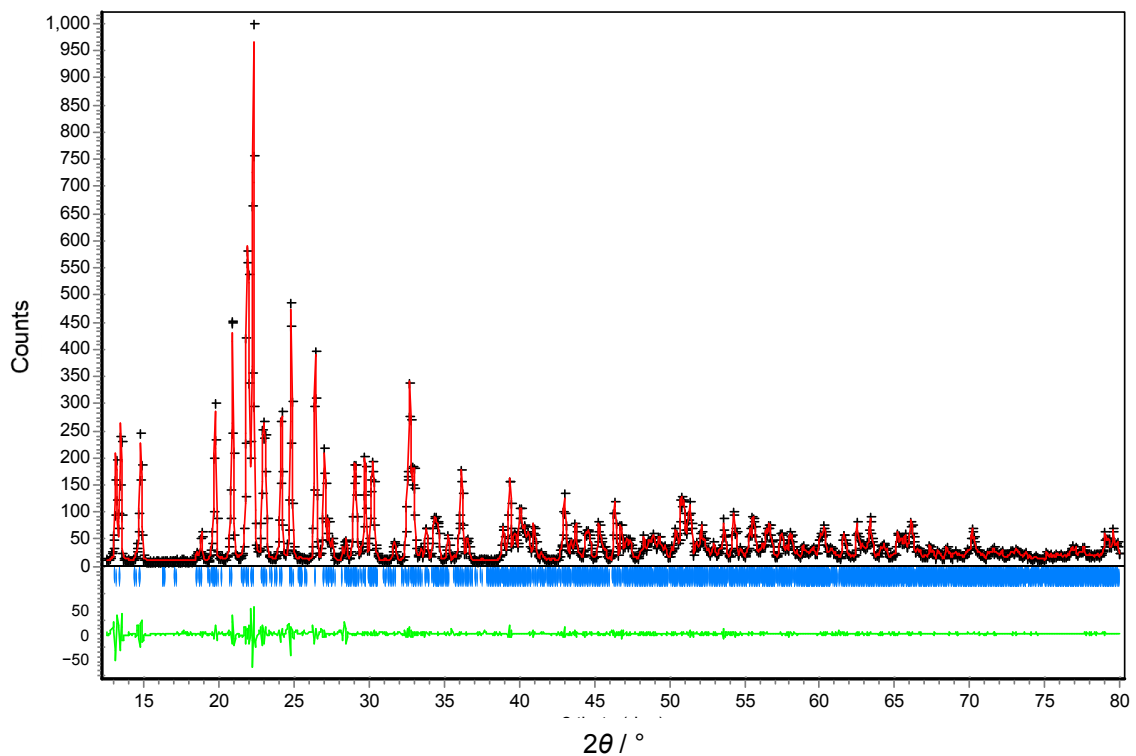
Figure A20: X-ray diffractogram of HfMgW$_3$O$_{12}$ (see Chapter 6) with experimental data shown as black crosses, the Le Bail fit to the data ($\chi^2 = 0.360$) shown as a red line, the peak positions shown as blue ticks, and the residual shown as a green line.

A8. $Y_2Mo_3O_{12}$
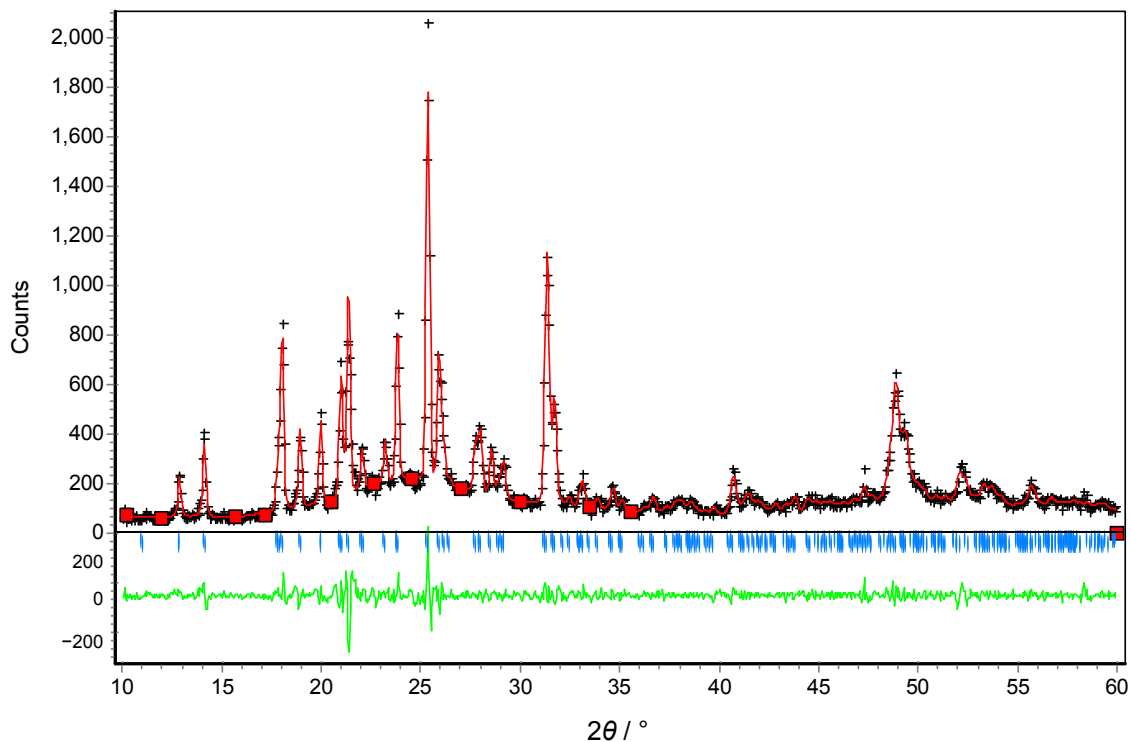
Figure A21: X-ray diffractogram of $Y_2Mo_3O_{12}$ (see Chapter 8) with experimental data shown as black crosses, the Le Bail fit to the data ($\chi^2 = 1.721$) shown as a red line, the peak positions shown as blue ticks, and the residual shown as a green line. Because the measurement was performed under ambient conditions, some hydration of the sample occurred during the experiment, leading to a large background. For this reason, background points were input manually (red boxes) rather than by refinement of a polynomial.

Appendix B: Velocities of Sound

B1. Al$_2$Mo$_3$O$_{12}$

Table B1: Measured longitudinal and transverse velocities of sound of Al$_2$Mo$_3$O$_{12}$ (see Chapter 3), uncorrected for porosity.

Sample	v_l / m ms^{-1}	v_t / m ms^{-1}	Density / % theoretical
1	3.63(2)	2.43(7)	85.6
2	3.45(2)	2.2(1)	86.0
3	3.9(1)	2.5(1)	86.1

B2. ZrMgMo$_3$O$_{12}$

Table B2: Measured longitudinal and transverse velocities of sound of ZrMgMo$_3$O$_{12}$ (see Chapter 5), uncorrected for porosity.

Sample	v_l / m ms^{-1}	v_t / m ms^{-1}	Density / % theoretical
1	3.56(7)	2.11(9)	85.6
2	3.6(1)	2.3(1)	85.2
3	3.5(2)	2.17(4)	79.8

B3. In$_{2-2x}$(HfMg)$_x$Mo$_3$O$_{12}$

Table B3: Measured longitudinal and transverse velocities of sound of In$_2$Mo$_3$O$_{12}$ (see Chapter 6), uncorrected for porosity.

Sample	v_l / m ms^{-1}	v_t / m ms^{-1}	Density / % theoretical
1	2.1(1)	1.23(4)	73.2
2	2.21(9)	1.52(4)	77.8
3	2.0(3)	1.37(6)	73.7

Table B4: Measured longitudinal and transverse velocities of sound of In$_{1.5}$(HfMg)$_{0.25}$Mo$_3$O$_{12}$ (see Chapter 6), uncorrected for porosity.

Sample	v_l / m ms^{-1}	v_t / m ms^{-1}	Density / % theoretical
1	2.7(1)	1.71(7)	72.5
2	2.7(1)	1.71(7)	71.8
3	2.99(3)	1.99(3)	75.6

Table B5: Measured longitudinal and transverse velocities of sound of In(HfMg)$_{0.5}$Mo$_3$O$_{12}$ (see Chapter 6), uncorrected for porosity.

Sample	v_l / m ms^{-1}	v_t / m ms^{-1}	Density / % theoretical
1	2.8(2)	1.7(1)	68.1
2	2.8(1)	1.7(1)	68.1
3	2.9(1)	1.84(6)	67.8

Table B6: Measured longitudinal and transverse velocities of sound of In$_{0.5}$(HfMg)$_{0.75}$Mo$_3$O$_{12}$ (see Chapter 6), uncorrected for porosity.

Sample	v_l / m ms^{-1}	v_t / m ms^{-1}	Density / % theoretical
1	3.16(3)	2.106(6)	91.5
2	2.99(2)	2.00(4)	91.5
3	2.38(1)	1.72(6)	73.9

Table B7: Measured longitudinal and transverse velocities of sound of HfMgMo$_3$O$_{12}$ (see Chapter 6), uncorrected for porosity.

Sample	v_l / m ms^{-1}	v_t / m ms^{-1}	Density / % theoretical
1	2.59(4)	1.7(1)	73.1
2	3.3(1)	2.16(9)	88.1
3	3.33(6)	2.1(1)	90.0

B4. Sc$_{2-2x}$Al$_{2x}$W$_3$O$_{12}$

Table B8: Measured longitudinal and transverse velocities of sound of Sc$_2$W$_3$O$_{12}$ (see Chapter 6), uncorrected for porosity.

Sample	v_l / m ms^{-1}	v_t / m ms^{-1}	Density / % theoretical
1	3.8(1)	2.2(1)	78.7
2	3.8(3)	2.31(2)	77.7
3	3.9(1)	2.18(6)	79.4

Table B9: Measured longitudinal and transverse velocities of sound of $Sc_{1.5}Al_{0.5}W_3O_{12}$ (see Chapter 6), uncorrected for porosity.

Sample	v_l / m ms^{-1}	v_t / m ms^{-1}	Density / % theoretical
1	3.6(2)	2.34(7)	86.2
2	3.63(3)	2.3(1)	85.6
3	3.8(4)	2.4(1)	92.7

Table B10: Measured longitudinal and transverse velocities of sound of $ScAlW_3O_{12}$ (see Chapter 6), uncorrected for porosity.

Sample	v_l / m ms^{-1}	v_t / m ms^{-1}	Density / % theoretical
1	3.75(7)	2.382(9)	93.4
2	3.56(6)	2.29(2)	90.7
3	3.52(6)	2.21(4)	89.6

Table B11: Measured longitudinal and transverse velocities of sound of $Sc_{0.5}Al_{1.5}Mo_3O_{12}$ (see Chapter 6), uncorrected for porosity.

Sample	v_l / m ms^{-1}	v_t / m ms^{-1}	Density / % theoretical
1	3.8(4)	2.57(2)	85.2
2	3.7(5)	2.74(3)	83.2
3	3.9(2)	2.6(1)	92.5

Table B12: Measured longitudinal and transverse velocities of sound of $Al_2W_3O_{12}$ (see Chapter 6), uncorrected for porosity.

Sample	v_l / m ms^{-1}	v_t / m ms^{-1}	Density / % theoretical
1	4.05(3)	2.7(1)	90.4
2	3.98(5)	2.42(6)	94.3
3	4.15(2)	2.6(2)	93.2

B5. $Cr_{2-2x}(HfMg)_xW_3O_{12}$

Table B13: Measured longitudinal and transverse velocities of sound of $Cr_2W_3O_{12}$ (see Chapter 6), uncorrected for porosity.

Sample	v_l / m ms^{-1}	v_t / m ms^{-1}	Density / % theoretical
1	3.2(3)	1.54(3)	89.0
2	3.19(5)	1.7(2)	88.8
3	3.0(2)	1.56(2)	87.7

Table B14: Measured longitudinal and transverse velocities of sound of $Cr_{1.5}(HfMg)_{0.25}W_3O_{12}$ (see Chapter 6), uncorrected for porosity.

Sample	v_l / m ms^{-1}	v_t / m ms^{-1}	Density / % theoretical
1	3.18(7)	2.1(4)	96.4
2	2.8(2)	1.7(2)	86.4
3	2.78(4)	1.81(8)	86.9

Table B15: Measured longitudinal and transverse velocities of sound of $Cr(HfMg)_{0.5}W_3O_{12}$ (see Chapter 6), uncorrected for porosity.

Sample	v_l / m ms^{-1}	v_t / m ms^{-1}	Density / % theoretical
1	3.09(1)	1.94(3)	92.0
2	3.20(5)	2.07(2)	93.8
3	3.33(4)	2.04(2)	95.8

Table B16: Measured longitudinal and transverse velocities of sound of $Cr_{0.5}(HfMg)_{0.75}W_3O_{12}$ (see Chapter 6), uncorrected for porosity.

Sample	v_l / m ms^{-1}	v_t / m ms^{-1}	Density / % theoretical
1	3.0(3)	1.8(1)	79.8
2	2.8(6)	1.82(8)	77.7
3	2.65(4)	1.71(2)	70.8

Table B17: Measured longitudinal and transverse velocities of sound of $HfMgW_3O_{12}$ (see Chapter 6), uncorrected for porosity.

Sample	v_l / m ms^{-1}	v_t / m ms^{-1}	Density / % theoretical
1	2.48(4)	1.7(2)	86.2
2	2.50(2)	1.7(2)	91.1
3	2.50(1)	1.61(3)	89.7

B6. $Y_2Mo_3O_{12}$

Table B18: Measured longitudinal and transverse velocities of sound of $Y_2Mo_3O_{12}$ (see Chapter 8), uncorrected for porosity.

Sample	v_l / m ms^{-1}	v_t / m ms^{-1}	Density / % theoretical
1	2.99(8)	1.74(6)	87.0
2	2.9(3)	1.7(1)	84.6
3	2.97(3)	1.7(1)	87.1

Appendix C: Γ-point Phonon Frequencies

Table C1: Calculated Γ-point vibrational frequencies of $ZrMgMo_3O_{12}$ from CASTEP (see Chapter 5).

v / cm^{-1}

21.11	85.72	124.79	185.07	244.21	280.04	349.56	426.46	894.35	994.62
22.51	85.98	126.00	187.69	245.69	281.49	352.80	431.13	904.87	994.99
29.17	87.20	131.82	192.75	245.98	285.84	357.86	451.05	909.10	998.10
36.08	89.65	133.93	196.71	250.67	288.98	361.79	461.32	909.30	998.17
38.08	91.21	135.54	198.74	250.87	293.07	363.04	462.26	909.72	1009.41
42.77	91.78	136.71	201.31	252.54	293.59	367.22	462.44	928.91	1016.12
48.66	93.06	141.09	214.02	254.71	294.27	374.23	812.68	929.57	1023.06
50.04	96.62	142.12	218.01	254.87	294.80	390.93	813.83	935.61	1026.19
52.77	96.98	145.43	218.38	256.20	301.93	391.17	816.34	951.45	1027.11
53.87	98.38	152.10	219.61	257.70	302.19	393.24	817.64	952.06	1031.22
55.17	98.46	152.87	222.43	259.11	308.46	393.45	823.75	952.47	1031.75
57.28	101.13	157.98	223.97	260.80	313.40	398.34	824.52	957.75	1033.45
63.20	104.38	161.67	225.03	262.06	319.62	400.21	841.86	963.95	
63.63	106.09	163.87	227.36	265.03	321.25	402.92	845.09	966.59	
67.81	109.44	164.41	227.81	266.65	323.86	403.75	847.13	978.80	
72.42	113.19	166.88	230.26	267.62	324.36	419.38	871.47	988.59	
76.20	113.51	178.92	230.73	270.74	327.31	419.49	873.03	989.59	
78.10	115.88	179.36	235.77	271.60	335.10	420.41	882.56	991.17	
78.48	117.41	182.47	239.18	274.03	335.24	420.69	884.06	992.47	
81.14	119.01	182.74	240.82	278.31	337.62	424.69	889.14	993.05	
85.71	120.17	184.46	241.16	279.50	348.75	425.71	891.22	994.54	

Table C2: Calculated Γ-point vibrational frequencies of $Al_2Mo_3O_{12}$ from ABINIT (see Chapter 8).

v / cm^{-1}

25.96	110.11	170.52	234.35	287.27	331.63	373.06	441.15	843.82	946.97
55.52	114.64	171.16	235.35	287.89	334.86	381.19	443.73	846.83	948.57
61.39	115.71	174.70	248.59	290.30	338.57	383.41	445.56	848.33	950.10
65.54	119.44	175.18	249.40	292.83	339.14	395.08	462.33	849.18	950.83
72.13	125.94	180.97	252.03	298.91	339.30	398.72	475.26	850.55	965.11
74.17	127.97	188.63	259.95	299.21	342.26	402.66	477.97	850.57	968.23
75.87	130.31	195.48	260.80	300.20	342.88	403.34	782.36	852.98	970.29
78.15	134.98	197.60	261.84	302.37	343.68	404.96	783.82	853.17	977.53
78.19	135.62	199.00	264.77	303.97	346.93	405.78	785.27	853.86	979.73
80.89	142.03	199.02	265.45	304.97	347.10	406.79	787.34	856.40	981.60
84.19	142.27	200.12	269.32	306.72	349.03	407.60	787.89	860.59	984.13
85.63	143.97	209.23	270.78	307.60	352.32	408.44	790.89	861.10	985.50
89.13	147.95	209.74	271.28	312.55	360.82	408.58	793.92	862.96	
89.35	148.08	214.27	273.26	315.43	361.12	408.58	796.97	863.96	
91.98	148.54	218.39	273.57	319.35	361.58	412.42	799.76	922.02	
95.87	151.00	218.98	277.29	319.78	366.21	420.82	801.17	922.91	
100.36	153.81	219.88	278.09	321.99	366.93	425.19	810.93	929.65	
103.50	154.25	223.85	283.50	322.66	367.84	426.27	832.54	932.28	
106.12	160.49	225.74	286.30	326.71	368.06	434.33	836.55	934.50	
106.32	163.32	225.92	286.45	328.14	368.26	434.41	840.12	943.18	
106.69	170.50	233.39	286.70	328.46	372.98	437.26	842.50	944.95	

Table C3: Calculated Γ-point vibrational frequencies of $ZrMgMo_3O_{12}$ from ABINIT (see Chapter 8).

v / cm^{-1}

43.18	88.24	135.13	199.01	262.55	298.59	327.30	371.65	815.60	955.54
46.47	89.32	136.47	200.63	266.27	300.50	330.50	371.67	821.76	955.61
46.84	89.64	141.49	208.19	268.75	301.44	333.12	372.41	824.53	956.05
48.13	92.01	141.90	214.36	271.65	303.95	334.47	378.56	825.06	957.03
54.67	92.80	143.36	214.84	273.90	309.75	336.21	380.25	832.72	960.60
55.24	95.87	145.85	216.11	274.83	311.18	338.08	386.19	871.21	966.06
56.24	101.18	146.33	221.48	275.85	312.28	338.68	717.69	871.85	968.55
57.74	101.41	156.17	222.15	279.45	312.65	340.60	719.29	873.79	969.09
57.96	102.58	158.04	223.06	279.88	313.37	340.90	719.50	899.93	970.50
66.48	103.15	160.28	224.46	280.43	313.74	340.91	722.45	901.28	980.58
66.57	107.93	162.16	228.48	283.80	316.37	346.26	723.96	901.89	980.80
66.77	108.47	165.50	233.86	284.79	317.01	346.50	724.20	903.15	983.22
71.19	110.36	171.38	234.75	286.94	318.90	346.55	733.11	904.77	
76.11	110.44	173.51	240.09	288.73	319.41	351.37	734.30	905.41	
76.56	111.61	173.74	244.72	289.87	320.30	352.39	735.08	939.41	
78.19	118.33	174.29	245.97	291.10	320.54	352.68	788.97	941.50	
78.72	119.60	178.58	249.63	292.03	321.13	356.54	792.89	948.20	
78.74	125.08	179.10	251.51	294.20	324.03	356.90	793.88	949.22	
83.03	126.36	182.32	261.60	294.36	324.23	363.55	798.10	949.41	
84.38	127.12	183.29	262.08	295.07	326.37	363.93	803.49	953.92	
87.26	129.18	186.43	262.35	297.28	326.47	364.59	814.97	955.07	

Table C4: Calculated Γ-point vibrational frequencies of $Sc_2Mo_3O_{12}$ from ABINIT (see Chapter 8).

v / cm^{-1}									
21.11	85.72	124.79	185.07	244.21	280.04	349.56	426.46	894.35	994.62
22.51	85.98	126.00	187.69	245.69	281.49	352.80	431.13	904.87	994.99
29.17	87.20	131.82	192.75	245.98	285.84	357.86	451.05	909.10	998.10
36.08	89.65	133.93	196.71	250.67	288.98	361.79	461.32	909.30	998.17
38.08	91.21	135.54	198.74	250.87	293.07	363.04	462.26	909.72	1009.41
42.77	91.78	136.71	201.31	252.54	293.59	367.22	462.44	928.91	1016.12
48.66	93.06	141.09	214.02	254.71	294.27	374.23	812.68	929.57	1023.06
50.04	96.62	142.12	218.01	254.87	294.80	390.93	813.83	935.61	1026.19
52.77	96.98	145.43	218.38	256.20	301.93	391.17	816.34	951.45	1027.11
53.87	98.38	152.10	219.61	257.70	302.19	393.24	817.64	952.06	1031.22
55.17	98.46	152.87	222.43	259.11	308.46	393.45	823.75	952.47	1031.75
57.28	101.13	157.98	223.97	260.80	313.40	398.34	824.52	957.75	1033.45
63.20	104.38	161.67	225.03	262.06	319.62	400.21	841.86	963.95	
63.63	106.09	163.87	227.36	265.03	321.25	402.92	845.09	966.59	
67.81	109.44	164.41	227.81	266.65	323.86	403.75	847.13	978.80	
72.42	113.19	166.88	230.26	267.62	324.36	419.38	871.47	988.59	
76.20	113.51	178.92	230.73	270.74	327.31	419.49	873.03	989.59	
78.10	115.88	179.36	235.77	271.60	335.10	420.41	882.56	991.17	
78.48	117.41	182.47	239.18	274.03	335.24	420.69	884.06	992.47	
81.14	119.01	182.74	240.82	278.31	337.62	424.69	889.14	993.05	
85.71	120.17	184.46	241.16	279.50	348.75	425.71	891.22	994.54	

Appendix D: Heat Capacity Data Tables

See Chapter 7 for further details regarding these results.

D1. Calculated Heat Capacity of ScF₃

Table D1: Heat capacity of ScF_3 calculated by DFT using the phonon dispersion relation shown in Figure 7.2.

T / K	C_P / J K^{-1} mol^{-1}	T / K	C_P / J K^{-1} mol^{-1}	T / K	C_P / J K^{-1} mol^{-1}	T / K	C_P / J K^{-1} mol^{-1}
0.5	0.0000804	75	34.113	190	71.525	310	86.009
1.0	0.000439	80	36.645	195	72.447	315	86.368
1.5	0.000908	85	39.068	200	73.331	320	86.714
2.0	0.00152	90	41.386	205	74.179	325	87.047
2.5	0.00245	95	43.604	210	74.991	330	87.369
3.0	0.00355	100	45.726	215	75.771	335	87.680
3.5	0.00501	105	47.757	220	76.519	340	87.980
4.0	0.00710	110	49.701	225	77.237	345	88.269
4.5	0.0103	115	51.562	230	77.926	350	88.549
5.0	0.0151	120	53.342	235	78.588	355	88.819
10	0.276	125	55.045	240	79.224	360	89.081
15	1.143	130	56.675	245	79.836	365	89.333
20	2.697	135	58.233	250	80.423	370	89.577
25	4.862	140	59.725	255	80.989	375	89.814
30	7.481	145	61.152	260	81.533	380	90.042
35	10.396	150	62.517	265	82.056	385	90.263
40	13.479	155	63.823	270	82.560	390	90.477
45	16.627	160	65.072	280	83.514	395	90.685
50	19.765	165	66.268	285	83.965	400	90.886
55	22.843	170	67.413	290	84.399		
60	25.829	175	68.509	295	84.819		
65	28.706	180	69.558	300	85.223		
70	31.468	185	70.563	305	85.636		

D2. Experimental Heat Capacity Data for ScF₃

N.B.: Only data points that met the reliability criteria ($\geq$ 90 % thermal coupling constant between sample and platform and $\geq$ 40 % sample contribution to the total heat capacity) are included.

Table D2: ScF$_3$ Heat Capacity Data: 15.46 mg sample; in order of data collection.

T / K	C_P / J K^{-1} mol^{-1}	T / K	C_P / J K^{-1} mol^{-1}	T / K	C_P / J K^{-1} mol^{-1}	T / K	C_P / J K^{-1} mol^{-1}
303.35	82.806	69.70	28.524	15.58	1.401	3.47	0.024
302.98	82.421	69.69	28.506	15.57	1.393	3.47	0.024
303.01	82.417	69.69	28.494	15.57	1.394	3.47	0.024
282.68	80.628	62.61	24.941	14.01	1.066	3.12	0.017
282.84	80.853	62.60	24.908	13.99	1.063	3.11	0.017
282.84	80.804	62.60	24.899	13.99	1.060	3.11	0.017
262.59	78.323	56.26	21.481	12.58	0.811	2.80	0.012
262.70	78.490	56.25	21.448	12.57	0.806	2.80	0.012
262.70	78.512	56.25	21.445	12.57	0.808	2.80	0.012
242.43	75.863	50.54	18.150	11.30	0.616	2.52	0.008
242.52	76.080	50.53	18.119	11.30	0.613	2.51	0.008
242.51	75.941	50.53	18.111	11.29	0.614	2.51	0.008
222.29	73.158	45.41	15.237	10.15	0.469	2.26	0.006
222.37	73.276	45.40	15.210	10.15	0.467	2.26	0.006
222.36	73.235	45.40	15.194	10.15	0.466	2.26	0.006
202.13	69.510	40.81	12.563	9.11	0.354	2.03	0.004
202.18	69.563	40.80	12.535	9.11	0.353	2.03	0.004
202.18	69.506	40.80	12.534	9.11	0.354	2.03	0.004
181.94	65.727	36.67	10.269	8.19	0.270		
181.98	65.753	36.66	10.247	8.19	0.269		
181.98	65.660	36.66	10.244	8.19	0.269		
161.75	61.112	32.95	8.282	7.35	0.202		
161.76	61.098	32.93	8.262	7.35	0.202		
161.76	61.205	32.94	8.259	7.35	0.201		
141.55	55.828	29.61	6.577	6.62	0.155		
141.55	55.868	29.59	6.569	6.61	0.154		
141.55	55.869	29.59	6.574	6.61	0.155		
121.36	49.661	26.60	5.168	5.94	0.113		
121.35	49.699	26.59	5.183	5.94	0.113		
121.35	49.735	26.59	5.180	5.95	0.113		
101.18	42.518	23.91	4.082	5.33	0.085		
101.17	42.577	23.89	4.036	5.33	0.084		
101.16	42.454	23.89	4.025	5.33	0.084		
96.13	40.190	21.47	3.129	4.79	0.063		
96.12	40.191	21.47	3.106	4.79	0.063		
96.12	40.187	21.46	3.119	4.79	0.062		
86.29	36.246	19.30	2.395	4.30	0.046		
86.28	36.288	19.28	2.389	4.30	0.045		
86.28	36.264	19.28	2.393	4.30	0.046		
77.57	32.478	17.34	1.836	3.86	0.034		
77.56	32.517	17.32	1.825	3.86	0.032		
77.56	32.481	17.32	1.825	3.86	0.033		

Table D3: ScF$_3$ Heat Capacity Data: 6.41 mg sample; in order of data collection.

T / K	C_P / J K^{-1} mol^{-1}	T / K	C_P / J K^{-1} mol^{-1}	T / K	C_P / J K^{-1} mol^{-1}	T / K	C_P / J K^{-1} mol^{-1}
222.34	72.616	45.40	15.165	10.13	0.453	2.26	0.006
222.42	72.614	45.38	15.131	10.13	0.450	2.26	0.006
222.42	72.737	45.38	15.138	10.13	0.451	2.26	0.006
202.16	69.073	40.79	12.500	9.10	0.344	2.03	0.004
202.21	69.047	40.77	12.477	9.10	0.341	2.03	0.004
202.21	69.145	40.77	12.480	9.10	0.341	2.03	0.004
181.97	65.322	36.65	10.192	8.18	0.259		
182.00	65.313	36.63	10.202	8.17	0.257		
181.99	65.368	36.64	10.186	8.18	0.257		
161.78	60.781	32.93	8.199	7.35	0.193		
161.79	60.867	32.91	8.223	7.34	0.192		
161.78	60.866	32.91	8.220	7.35	0.193		
141.60	55.407	29.59	6.426	6.61	0.146		
141.57	55.583	29.56	6.536	6.60	0.146		
141.57	55.543	29.57	6.537	6.60	0.146		
121.41	49.547	26.59	5.170	5.93	0.108		
121.36	49.538	26.57	5.134	5.93	0.106		
121.35	49.535	26.57	5.143	5.93	0.105		
101.22	42.322	23.88	4.019	5.33	0.079		
101.16	42.272	23.87	3.981	5.32	0.079		
101.16	42.357	23.87	4.016	5.33	0.080		
96.09	40.258	21.46	3.101	4.79	0.059		
96.10	40.232	21.44	3.099	4.78	0.060		
96.10	40.252	21.45	3.089	4.79	0.059		
86.31	36.143	19.27	2.374	4.30	0.043		
86.27	36.187	19.26	2.369	4.30	0.043		
86.27	36.383	19.26	2.368	4.30	0.043		
77.58	32.333	17.32	1.817	3.86	0.031		
77.55	32.277	17.31	1.811	3.86	0.031		
77.56	32.324	17.31	1.811	3.86	0.031		
69.70	28.384	15.57	1.382	3.47	0.023		
69.68	28.365	15.56	1.380	3.47	0.022		
69.68	28.384	15.56	1.379	3.47	0.022		
62.61	24.828	13.99	1.048	3.12	0.016		
62.58	24.799	13.98	1.046	3.11	0.016		
62.59	24.775	13.98	1.046	3.11	0.017		
56.25	21.377	12.57	0.795	2.80	0.012		
56.23	21.361	12.56	0.793	2.79	0.012		
56.23	21.361	12.56	0.793	2.80	0.012		
50.53	18.067	11.28	0.601	2.52	0.008		
50.51	18.037	11.28	0.599	2.51	0.008		
50.51	18.028	11.28	0.600	2.51	0.008		

Table D4: ScF_3 Heat Capacity Data: 10.30 mg sample; in order of data collection. Note that heat capacity units here are mJ K^{-1} mol^{-1}, whereas J K^{-1} mol^{-1} are used in Tables C2 and C3.

T / K	C_P / mJ K^{-1} mol^{-1}	T / K	C_P / mJ K^{-1} mol^{-1}	T / K	C_P / mJ K^{-1} mol^{-1}	T / K	C_P / mJ K^{-1} mol^{-1}
10.09	455.91	3.31	19.82	1.09	0.50	0.38	0.09
10.07	453.95	3.31	19.79	1.09	0.50	0.38	0.09
10.07	454.43	3.31	19.67	1.09	0.50	0.38	0.09
9.26	363.59	3.04	15.02	1.00	0.40		
9.25	363.04	3.04	14.92	1.00	0.40		
9.24	363.49	3.04	14.86	1.00	0.40		
8.50	292.81	2.79	11.22	0.92	0.33		
8.49	291.46	2.79	11.18	0.92	0.32		
8.49	292.65	2.79	11.19	0.92	0.33		
7.79	234.36	2.56	8.27	0.85	0.26		
7.78	234.06	2.56	8.17	0.85	0.27		
7.79	234.38	2.56	8.20	0.85	0.27		
7.14	187.07	2.35	6.25	0.78	0.23		
7.14	186.66	2.35	6.18	0.78	0.23		
7.14	186.92	2.35	6.26	0.78	0.22		
6.57	148.49	2.14	4.61	0.72	0.19		
6.56	148.03	2.15	4.62	0.72	0.19		
6.56	147.87	2.15	4.64	0.71	0.19		
6.03	118.06	1.97	3.36	0.66	0.17		
6.02	117.94	1.97	3.39	0.66	0.17		
6.02	118.05	1.97	3.41	0.66	0.17		
5.53	92.94	1.81	2.53	0.60	0.15		
5.53	92.74	1.81	2.52	0.60	0.14		
5.53	93.03	1.81	2.50	0.60	0.15		
5.08	73.16	1.67	1.92	0.56	0.14		
5.07	72.78	1.67	1.90	0.56	0.14		
5.07	72.66	1.67	1.91	0.56	0.13		
4.66	56.83	1.53	1.44	0.51	0.12		
4.66	56.57	1.53	1.43	0.51	0.11		
4.66	56.65	1.53	1.42	0.51	0.12		
4.28	44.05	1.41	1.09	0.47	0.11		
4.28	43.84	1.41	1.07	0.47	0.11		
4.27	43.92	1.41	1.08	0.47	0.11		
3.93	34.10	1.29	0.83	0.44	0.10		
3.93	34.00	1.29	0.83	0.44	0.09		
3.93	33.94	1.29	0.82	0.44	0.10		
3.60	25.81	1.19	0.64	0.41	0.08		
3.60	25.70	1.19	0.64	0.41	0.09		
3.60	25.73	1.19	0.64	0.41	0.09		

Table D5: ScF$_3$ Heat Capacity Data: 8.136 mg sample; in order of data collection. Note that heat capacity units here are mJ K^{-1} mol^{-1}, whereas J K^{-1} mol^{-1} are used in Tables C2 and C3.

T / K	C_P / mJ K^{-1} mol^{-1}	T / K	C_P / mJ K^{-1} mol^{-1}	T / K	C_P / mJ K^{-1} mol^{-1}
302.20	82013.24	3.59	25.13	0.92	0.35
302.27	82053.52	3.59	25.11	0.92	0.34
302.30	81869.41	3.60	25.14	0.92	0.35
10.09	457.63	3.32	19.42	0.85	0.28
10.07	456.60	3.31	19.23	0.85	0.27
10.07	455.81	3.31	19.20	0.85	0.30
9.26	364.64	3.04	14.56	0.78	0.24
9.24	364.43	3.04	14.46	0.78	0.24
9.24	364.03	3.04	14.45	0.78	0.25
8.49	292.56	2.79	10.85	0.72	0.20
8.48	292.18	2.79	10.74	0.72	0.22
8.48	291.81	2.79	10.80	0.66	0.18
7.80	234.27	2.56	7.91	0.66	0.17
7.78	234.42	2.56	7.86	0.66	0.18
7.78	234.42	2.56	7.84	0.60	0.16
7.15	187.64	2.35	5.97	0.60	0.13
7.14	187.25	2.35	5.93	0.60	0.15
7.14	187.67	2.35	5.96	0.56	0.17
6.57	148.21	2.15	4.43	0.56	0.16
6.56	147.65	2.15	4.39	0.51	0.14
6.55	147.69	2.15	4.38	0.51	0.13
6.55	147.96	1.97	3.23	0.51	0.14
6.56	147.99	1.97	3.23	0.47	0.12
6.56	148.24	1.97	3.24	0.47	0.11
5.54	92.34	1.81	2.41	0.47	0.12
5.52	92.24	1.81	2.40	0.44	0.10
5.52	92.29	1.81	2.41	0.44	0.11
5.08	72.69	1.67	1.84	0.40	0.08
5.08	72.61	1.67	1.83	0.40	0.09
5.08	72.46	1.67	1.78	0.40	0.10
4.67	56.51	1.53	1.38	0.38	0.10
4.66	56.33	1.53	1.37	0.38	0.10
4.66	56.35	1.53	1.34	0.38	0.10
4.28	43.49	1.41	1.05		
4.28	43.43	1.41	1.04		
4.28	43.33	1.41	1.06		
3.93	33.68	1.29	0.80		
3.93	33.45	1.29	0.87		
3.93	33.44	1.29	0.81		

Table D6: ScF$_3$ Heat Capacity Data: 8.62 mg sample; in order of data collection.

T / K	C_P / J K^{-1} mol^{-1}
279.29	79.616
279.00	79.456
279.01	79.398
295.61	80.640
295.63	80.431
295.62	80.384
312.14	81.615
312.16	81.436
312.15	81.415
329.06	83.359
328.62	83.311
328.65	83.262
345.04	84.306
345.04	84.099

Table D7: ScF$_3$ Heat Capacity Data: 12.78 mg sample; in order of data collection.

T / K	C_P / J K^{-1} mol^{-1}	T / K	C_P / J K^{-1} mol^{-1}
278.75	79.087	369.45	84.613
278.38	78.936	392.44	86.112
278.39	78.859	392.47	85.806
301.62	80.588	392.43	85.849
301.65	80.457		
301.64	80.326		
324.89	81.951		
324.91	81.842		
324.90	81.837		
347.49	83.120		
347.52	82.730		
347.51	82.982		
369.34	84.964		
369.48	84.476		

D3. Experimental Heat Capacity Data for $Sc_{0.95}Y_{0.05}F_3$

N.B.: Only data points that met the reliability criteria (≥ 90 % thermal coupling constant between sample and platform and ≥ 40 % sample contribution to the total heat capacity) are included.

Table D8: $Sc_{0.95}Y_{0.05}F_3$ Heat Capacity Data: 13.86 mg sample; in order of data collection.

T / K	C_P / J K^{-1} mol^{-1}	T / K	C_P / J K^{-1} mol^{-1}	T / K	C_P / J K^{-1} mol^{-1}	T / K	C_P / J K^{-1} mol^{-1}
303.32	82.437	166.03	62.752	77.60	33.194	17.34	1.701
302.87	82.314	166.06	62.822	77.57	33.237	17.33	1.696
302.88	82.399	166.07	62.742	77.57	33.227	17.33	1.695
287.00	81.564	164.23	62.333	69.74	29.159	15.58	1.247
287.14	81.647	164.26	62.385	69.71	29.139	15.57	1.243
287.14	81.620	164.25	62.397	69.71	29.140	15.57	1.242
271.30	79.389	162.43	61.977	62.64	25.482	14.00	0.904
271.41	79.453	162.46	61.976	62.61	25.454	13.99	0.900
271.42	79.427	162.45	62.019	62.61	25.462	13.99	0.901
255.57	77.936	160.63	61.487	56.30	21.857	12.58	0.649
255.67	78.049	160.65	61.535	56.26	21.879	12.58	0.647
255.67	77.949	160.65	61.564	56.26	21.886	12.58	0.646
239.82	75.915	158.82	61.160	50.59	18.503	11.30	0.460
239.92	75.973	158.85	61.100	50.55	18.515	11.30	0.458
239.91	75.902	158.85	61.120	50.55	18.518	11.30	0.458
224.11	73.919	157.02	60.775	45.45	15.500		
224.19	74.064	157.05	60.771	45.42	15.489		
224.19	74.014	157.04	60.812	45.42	15.499		
208.38	70.984	155.21	60.365	40.84	12.797		
208.44	71.038	155.24	60.375	40.81	12.774		
208.44	71.117	155.24	60.300	40.81	12.781		
192.62	68.426	153.42	59.835	36.69	10.457		
192.67	68.483	153.44	59.869	36.67	10.441		
192.66	68.555	153.44	59.909	36.67	10.437		
176.85	65.084	151.61	59.372	32.96	8.408		
176.89	65.186	151.64	59.452	32.95	8.386		
176.89	65.168	151.64	59.416	32.94	8.387		
176.98	65.216	151.69	59.394	29.62	6.675		
176.89	65.156	151.63	59.476	29.61	6.653		
176.88	65.219	151.64	59.429	29.61	6.649		
175.05	64.733	126.39	52.131	26.62	5.214		
175.08	64.848	126.40	52.189	26.60	5.208		
175.09	64.856	126.40	52.145	26.61	5.206		
173.25	64.398	101.18	43.317	23.90	4.024		
173.29	64.367	101.17	43.253	23.90	4.000		
173.28	64.409	101.16	43.308	23.90	4.004		
171.45	64.013	96.13	41.000	21.48	3.086		
171.48	63.982	96.13	41.027	21.46	3.056		
171.48	64.034	96.13	41.080	21.48	3.055		
169.64	63.524	86.33	37.006	19.30	2.299		
169.68	63.546	86.31	36.962	19.29	2.292		
169.67	63.608	86.31	36.972	19.28	2.285		

Table D9: $Sc_{0.95}Y_{0.05}F_3$ Heat Capacity Data: 8.58 mg sample; in order of data collection.

T / K	C_P / mJ K^{-1} mol^{-1}	T / K	C_P / mJ K^{-1} mol^{-1}	T / K	C_P / mJ K^{-1} mol^{-1}
301.82	82900.71	8.47	172.66	6.00	52.50
302.02	83182.42	7.78	129.76	6.00	52.49
302.02	83369.99	7.77	128.96	5.54	40.17
10.08	312.34	7.77	128.68	5.53	39.40
10.06	311.16	7.14	97.07	5.52	39.08
10.06	311.04	7.13	96.30		
9.24	233.24	7.13	96.53		
9.23	231.75	6.56	71.71		
9.22	231.42	6.55	70.76		
8.48	173.64	6.54	70.44		
8.47	173.22	6.01	52.86		

D4. Experimental Heat Capacity Data for $Sc_{0.9}Y_{0.1}F_3$

N.B.: Only data points that met the reliability criteria (≥ 90 % thermal coupling constant between sample and platform and ≥ 40 % sample contribution to the total heat capacity) are included.

Table D10: $Sc_{0.9}Y_{0.1}F_3$ Heat Capacity Data: 13.86 mg sample; in order of data collection.

T / K	C_P / J K^{-1} mol^{-1}	T / K	C_P / J K^{-1} mol^{-1}	T / K	C_P / J K^{-1} mol^{-1}	T / K	C_P / J K^{-1} mol^{-1}
303.23	81.350	148.71	58.788	69.68	29.068	15.55	1.216
302.90	81.410	148.73	58.823	69.69	29.001	15.55	1.212
302.91	81.421	148.73	58.836	69.69	29.002	15.55	1.210
283.06	80.583	146.55	58.154	62.58	25.448	13.97	0.869
282.74	79.854	146.57	58.233	62.59	25.393	13.97	0.868
282.74	79.706	146.56	58.184	62.59	25.400	13.97	0.866
262.51	77.692	144.38	57.652	56.24	21.875	12.55	0.616
262.60	77.850	144.41	57.551	56.24	21.842	12.55	0.613
262.60	77.851	144.40	57.597	56.23	21.849	12.55	0.613
242.37	75.674	142.22	56.845	50.53	18.535	11.28	0.431
242.43	75.714	142.24	56.867	50.53	18.511	11.28	0.429
242.43	75.604	142.24	56.895	50.53	18.501	11.28	0.429
222.26	73.051	140.05	56.170	45.40	15.534	10.14	0.297
222.29	73.262	140.08	56.206	45.40	15.495	10.13	0.295
222.29	73.172	140.07	56.196	45.39	15.494	10.14	0.294
202.11	69.658	137.89	55.549	40.78	12.845	9.10	0.204
202.10	69.800	137.91	55.638	40.79	12.795	9.10	0.203
202.10	69.741	137.91	55.564	40.78	12.796	9.10	0.203
181.94	66.264	135.78	54.987	36.64	10.486	8.18	0.139
181.91	66.410	135.75	54.912	36.65	10.462	8.18	0.139
181.91	66.639	135.76	54.944	36.65	10.453	8.18	0.139
161.75	61.848	133.57	54.256	32.92	8.427	303.24	81.739
161.71	61.897	133.59	54.337	32.92	8.404	171.88	64.182
161.71	61.845	133.58	54.349	32.92	8.404	171.82	64.226
161.75	61.988	131.40	53.772	29.58	6.694	171.82	64.134
161.70	61.915	131.42	53.730	29.58	6.667	169.79	63.758
161.70	61.884	131.41	53.681	29.58	6.666	169.81	63.760
159.52	61.294	126.41	52.191	26.57	5.236	169.81	63.732
159.54	61.424	126.36	52.360	26.57	5.224	167.77	63.119
159.53	61.477	126.37	52.208	26.58	5.219	167.79	63.240
157.36	60.931	106.14	45.128	23.85	4.014	167.78	63.109
157.38	60.894	106.17	45.116	23.87	3.996	165.75	62.810
157.38	60.792	106.16	45.126	23.87	4.012	165.76	62.792
155.19	60.373	95.90	41.762	21.43	3.009	165.76	62.767
155.22	60.495	96.08	41.086	21.44	3.047	163.72	62.302
155.22	60.500	96.09	40.982	21.45	3.051	163.74	62.332
153.04	59.964	86.25	36.979	19.27	2.276	163.74	62.301
153.05	59.939	86.28	36.871	19.27	2.230		
153.05	59.943	86.27	36.954	19.25	2.269		
150.87	59.387	77.52	33.165	17.31	1.678		
150.89	59.419	77.54	33.083	17.31	1.672		
150.89	59.427	77.54	33.134	17.31	1.670		

Table D11: $Sc_{0.9}Y_{0.1}F_3$ Heat Capacity Data: 15.05 mg sample; in order of data collection.

T / K	C_P / J K^{-1} mol^{-1}	T / K	C_P / J K^{-1} mol^{-1}	T / K	C_P / J K^{-1} mol^{-1}
276.06	79.917	336.92	82.601	390.97	86.308
275.75	79.846	336.91	82.513		
275.76	79.783	353.35	83.845		
296.09	81.214	353.34	84.032		
296.13	80.986	370.77	85.550		
296.12	80.884	370.94	85.545		
316.48	82.316	370.96	85.500		
316.52	82.052	390.85	86.711		
316.51	82.294	390.99	86.166		

D5. Experimental Heat Capacity Data for $Sc_{0.8}Y_{0.2}F_3$

N.B.: Only data points that met the reliability criteria ($\geq$ 90 % thermal coupling constant between sample and platform and $\geq$ 40 % sample contribution to the total heat capacity) are included.

Table D12: $Sc_{0.8}Y_{0.2}F_3$ Heat Capacity Data: 7.72 mg sample; in order of data collection.

T / K	C_P / J K^{-1} mol^{-1}	T / K	C_P / J K^{-1} mol^{-1}	T / K	C_P / J K^{-1} mol^{-1}	T / K	C_P / J K^{-1} mol^{-1}
234.06	74.240	211.68	70.207	61.97	25.427	12.77	0.722
233.98	74.087	211.70	70.299	61.97	25.423	12.77	0.723
233.97	74.188	211.69	70.310	55.37	21.803	11.42	0.495
232.36	74.079	210.08	70.199	55.36	21.772	11.41	0.494
232.39	73.914	210.11	70.182	55.36	21.764	11.41	0.494
232.39	73.796	210.10	70.199	49.46	18.298	10.17	0.324
230.77	73.656	208.49	70.026	49.45	18.265	10.18	0.326
230.80	73.754	208.51	70.072	49.45	18.262	10.18	0.327
230.79	73.805	208.51	70.175	44.18	15.311	9.10	0.220
229.18	73.642	206.90	69.939	44.18	15.274	9.09	0.218
229.21	73.582	206.92	70.093	44.18	15.264	9.09	0.219
229.20	73.437	206.92	69.975	39.47	12.705		
227.58	73.403	205.31	69.770	39.46	12.670		
227.62	73.309	205.33	69.961	39.46	12.674		
227.61	73.188	205.33	69.937	35.24	10.274		
225.99	72.975	203.72	69.781	35.24	10.264		
226.02	73.189	203.74	69.735	35.25	10.260		
226.02	73.004	203.73	69.818	31.48	8.183		
224.40	72.811	184.00	66.492	31.48	8.177		
224.43	72.626	183.90	66.621	31.49	8.174		
224.42	72.715	183.90	66.530	28.13	6.422		
222.81	72.286	156.75	60.869	28.13	6.418		
222.84	72.279	156.77	60.884	28.13	6.409		
222.83	72.393	156.76	60.853	25.13	4.954		
221.21	71.919	129.62	53.381	25.13	4.943		
221.24	71.845	129.62	53.410	25.13	4.950		
221.24	71.982	129.62	53.455	22.46	3.779		
219.63	71.377	102.52	43.959	22.45	3.792		
219.65	71.592	102.48	43.909	22.46	3.769		
219.65	71.378	97.38	41.782	20.05	2.769		
218.04	71.058	97.40	41.781	20.05	2.807		
218.06	70.979	97.40	41.780	20.06	2.807		
218.06	71.115	86.95	37.358	17.91	2.053		
216.45	70.782	86.92	37.364	17.91	2.049		
216.48	70.673	86.92	37.350	17.92	2.051		
216.47	70.676	77.71	33.317	16.00	1.479		
214.86	70.507	77.68	33.366	16.00	1.475		
214.88	70.561	77.68	33.377	16.01	1.475		
214.88	70.466	69.42	29.154	14.31	1.046		
213.26	70.497	69.40	29.151	14.30	1.041		
213.29	70.410	69.40	29.141	14.30	1.043		
213.29	70.395	61.99	25.439	12.78	0.724		

D6. Experimental Heat Capacity Data for $Sc_{0.75}Y_{0.25}F_3$

N.B.: Only data points that met the reliability criteria (≥ 90 % thermal coupling constant between sample and platform and ≥ 40 % sample contribution to the total heat capacity) are included.

Table D13: $Sc_{0.75}Y_{0.25}F_3$ Heat Capacity Data: 5.40 mg sample; in order of data collection.

T / K	C_P / J K^{-1} mol^{-1}	T / K	C_P / J K^{-1} mol^{-1}	T / K	C_P / J K^{-1} mol^{-1}	T / K	C_P / J K^{-1} mol^{-1}
234.06	74.240	211.68	70.207	61.97	25.427	12.77	0.722
233.98	74.087	211.70	70.299	61.97	25.423	12.77	0.723
233.97	74.188	211.69	70.310	55.37	21.803	11.42	0.495
232.36	74.079	210.08	70.199	55.36	21.772	11.41	0.494
232.39	73.914	210.11	70.182	55.36	21.764	11.41	0.494
232.39	73.796	210.10	70.199	49.46	18.298	10.17	0.324
230.77	73.656	208.49	70.026	49.45	18.265	10.18	0.326
230.80	73.754	208.51	70.072	49.45	18.262	10.18	0.327
230.79	73.805	208.51	70.175	44.18	15.311	9.10	0.220
229.18	73.642	206.90	69.939	44.18	15.274	9.09	0.218
229.21	73.582	206.92	70.093	44.18	15.264	9.09	0.219
229.20	73.437	206.92	69.975	39.47	12.705		
227.58	73.403	205.31	69.770	39.46	12.670		
227.62	73.309	205.33	69.961	39.46	12.674		
227.61	73.188	205.33	69.937	35.24	10.274		
225.99	72.975	203.72	69.781	35.24	10.264		
226.02	73.189	203.74	69.735	35.25	10.260		
226.02	73.004	203.73	69.818	31.48	8.183		
224.40	72.811	184.00	66.492	31.48	8.177		
224.43	72.626	183.90	66.621	31.49	8.174		
224.42	72.715	183.90	66.530	28.13	6.422		
222.81	72.286	156.75	60.869	28.13	6.418		
222.84	72.279	156.77	60.884	28.13	6.409		
222.83	72.393	156.76	60.853	25.13	4.954		
221.21	71.919	129.62	53.381	25.13	4.943		
221.24	71.845	129.62	53.410	25.13	4.950		
221.24	71.982	129.62	53.455	22.46	3.779		
219.63	71.377	102.52	43.959	22.45	3.792		
219.65	71.592	102.48	43.909	22.46	3.769		
219.65	71.378	97.38	41.782	20.05	2.769		
218.04	71.058	97.40	41.781	20.05	2.807		
218.06	70.979	97.40	41.780	20.06	2.807		
218.06	71.115	86.95	37.358	17.91	2.053		
216.45	70.782	86.92	37.364	17.91	2.049		
216.48	70.673	86.92	37.350	17.92	2.051		
216.47	70.676	77.71	33.317	16.00	1.479		
214.86	70.507	77.68	33.366	16.00	1.475		
214.88	70.561	77.68	33.377	16.01	1.475		
214.88	70.466	69.42	29.154	14.31	1.046		
213.26	70.497	69.40	29.151	14.30	1.041		
213.29	70.410	69.40	29.141	14.30	1.043		
213.29	70.395	61.99	25.439	12.78	0.724		

Table D14: $Sc_{0.75}Y_{0.25}F_3$ Heat Capacity Data: 10.60 mg sample; in order of data collection.

T / K	C_P / J K^{-1} mol^{-1}	T / K	C_P / J K^{-1} mol^{-1}	T / K	C_P / J K^{-1} mol^{-1}	T / K	C_P / J K^{-1} mol^{-1}	T / K	C_P / J K^{-1} mol^{-1}
303.62	81.879	206.67	71.879	40.89	13.513	6.65	0.073	209.11	68.624
303.25	81.557	205.19	71.743	40.89	13.515	6.63	0.073	210.44	68.917
303.26	81.658	205.23	71.691	36.77	11.128	6.63	0.073	210.49	68.861
282.91	80.514	205.23	71.713	36.75	11.111	5.96	0.049	210.50	68.829
283.08	80.631	203.75	71.571	36.75	11.114	5.95	0.049	211.86	69.123
283.07	80.531	203.79	71.660	33.04	9.016	5.95	0.049	211.95	68.983
262.76	78.746	203.79	71.609	33.02	8.997	5.35	0.034	211.94	68.982
262.91	78.768	202.30	71.373	33.02	8.997	5.35	0.034	213.39	69.236
262.89	78.783	202.34	71.346	29.69	7.201	5.35	0.034	213.47	69.093
242.59	76.776	202.35	71.357	29.67	7.184	4.80	0.024	213.46	69.072
242.72	76.865	182.25	68.131	29.67	7.180	4.80	0.024	214.83	69.348
242.71	76.801	182.14	68.089	26.68	5.672	4.80	0.024	214.91	69.184
222.45	74.552	182.14	68.071	26.66	5.662	4.31	0.017	214.90	69.209
222.55	74.531	161.89	63.645	26.67	5.660	4.31	0.017	216.30	69.294
222.54	74.622	161.93	63.631	23.97	4.376	4.31	0.017	216.33	69.385
222.69	74.563	161.92	63.703	23.95	4.371	3.87	0.012	216.35	69.368
222.54	74.523	141.72	58.440	23.96	4.374	3.87	0.012	217.77	69.313
222.54	74.508	141.73	58.476	21.53	3.363	3.87	0.012	217.75	69.650
221.05	74.270	141.73	58.443	21.52	3.340	3.48	0.008	217.80	69.581
221.10	74.270	121.53	52.091	21.52	3.348	3.48	0.008	219.24	69.362
221.09	74.199	121.52	52.039	19.34	2.527	3.48	0.008	219.18	69.858
219.60	73.910	121.52	52.074	19.34	2.516	3.13	0.006	219.23	69.812
219.66	74.037	101.36	44.607	19.34	2.512	3.12	0.006	220.60	69.689
219.66	73.924	101.34	44.505	17.37	1.867	3.12	0.006	220.55	70.059
218.16	73.655	101.33	44.534	17.37	1.859	2.81	0.004	220.60	70.003
218.22	73.675	96.29	42.220	17.38	1.847	2.81	0.004	222.04	69.961
218.21	73.665	96.30	42.138	15.61	1.359	2.81	0.004	222.00	70.305
216.73	73.386	96.29	42.152	15.60	1.353	2.52	0.003	222.04	70.226
216.77	73.403	86.46	38.029	15.61	1.354	2.52	0.003	223.48	70.196
216.77	73.359	86.46	37.879	14.04	0.976	2.52	0.003	223.44	70.481
215.28	73.154	86.45	37.912	14.03	0.971	2.27	0.002	223.48	70.465
215.34	73.130	77.72	34.209	14.03	0.971	2.26	0.002	209.11	68.624
215.33	73.167	77.70	34.147	12.62	0.691	2.26	0.002	210.44	68.917
213.84	73.038	77.70	34.121	12.61	0.688	2.03	0.002	210.49	68.861
213.90	72.876	69.86	30.016	12.61	0.688	2.03	0.002	210.50	68.829
213.88	72.986	69.83	29.996	11.33	0.481	2.03	0.002	211.86	69.123
212.40	72.780	69.83	30.002	11.33	0.478	203.53	68.002	211.95	68.983
212.45	72.712	62.76	26.329	11.33	0.479	203.35	68.167	211.94	68.982
212.44	72.762	62.72	26.312	10.18	0.330	203.35	68.221	213.39	69.236
210.96	72.510	62.73	26.309	10.17	0.329	204.73	68.476	213.47	69.093
211.01	72.515	56.40	22.756	10.18	0.329	204.81	68.350	213.46	69.072
211.00	72.544	56.37	22.732	9.14	0.227	204.81	68.327	214.83	69.348
209.51	72.349	56.37	22.732	9.13	0.225	206.17	68.605	214.91	69.184
209.57	72.344	50.69	19.338	9.14	0.226	206.25	68.474	214.90	69.209
209.56	72.359	50.65	19.352	8.21	0.155	206.25	68.435	216.30	69.294
208.07	72.229	50.65	19.342	8.21	0.153	207.61	68.698	216.33	69.385
208.12	72.315	45.55	16.259	8.21	0.154	207.69	68.629	216.35	69.368
208.12	72.225	45.50	16.285	7.38	0.105	207.69	68.573	217.77	69.313
206.64	71.942	45.51	16.291	7.37	0.104	209.02	69.043	217.75	69.650
206.68	72.013	40.93	13.512	7.37	0.104	209.10	68.981	217.80	69.581

Table D15: $Sc_{0.75}Y_{0.25}F_3$ Heat Capacity Data: 9.37 mg sample; in order of data collection.

T / K	C_P / J K^{-1} mol^{-1}	T / K	C_P / J K^{-1} mol^{-1}	T / K	C_P / J K^{-1} mol^{-1}	T / K	C_P / J K^{-1} mol^{-1}
304.68	85.048	215.94	74.342	43.77	15.666	8.96	0.217
304.30	85.073	215.97	74.303	43.77	15.621	8.95	0.216
304.32	84.885	215.96	74.309	43.76	15.628	8.96	0.217
283.86	83.064	214.27	74.136	39.09	12.822	8.00	0.143
284.04	83.269	214.30	74.180	39.09	12.786	8.00	0.142
284.04	83.152	214.29	74.272	39.08	12.788	8.00	0.143
263.68	81.240	212.60	73.905	34.91	10.368	7.17	0.097
263.83	81.236	212.62	74.023	34.90	10.327	7.16	0.096
263.82	81.336	212.62	73.967	34.90	10.327	7.16	0.095
243.45	79.106	182.96	69.868	31.16	8.251	6.39	0.066
243.57	79.064	182.82	69.666	31.17	8.210	6.38	0.066
243.56	79.058	182.82	69.655	31.17	8.204	6.39	0.064
232.79	77.909	155.77	63.587	27.85	6.433		
232.68	77.899	155.79	63.600	27.84	6.419		
232.68	77.878	155.78	63.576	27.84	6.400		
230.98	77.707	128.78	55.578	24.87	4.859		
231.01	77.691	128.76	55.614	24.85	4.916		
231.01	77.482	128.76	55.598	24.86	4.916		
229.32	77.550	101.79	45.645	22.20	3.699		
229.35	77.532	101.76	45.698	22.19	3.731		
229.34	77.426	101.76	45.705	22.20	3.731		
227.64	77.105	96.69	43.291	19.82	2.793		
227.67	77.188	96.71	43.242	19.81	2.771		
227.67	77.164	96.70	43.309	19.82	2.772		
225.98	76.860	86.30	38.637	17.70	2.028		
226.00	77.138	86.29	38.662	17.69	2.017		
226.00	76.838	86.29	38.740	17.70	2.019		
224.30	76.477	77.08	34.680	15.80	1.452		
224.33	76.677	77.08	34.616	15.80	1.447		
224.33	76.673	77.08	34.571	15.80	1.445		
222.63	76.162	68.83	30.148	14.11	1.022		
222.66	76.077	68.84	30.116	14.11	1.017		
222.65	76.056	68.84	30.106	14.11	1.018		
220.96	75.464	61.46	26.260	12.60	0.708		
220.98	75.694	61.45	26.251	12.60	0.707		
220.98	75.720	61.45	26.251	12.60	0.705		
219.29	75.168	54.89	22.443	11.25	0.484		
219.31	75.189	54.88	22.396	11.25	0.480		
219.30	75.156	54.88	22.400	11.25	0.481		
217.62	74.727	49.01	18.855	10.04	0.321		
217.64	74.688	49.02	18.808	10.03	0.320		
217.63	74.719	49.01	18.801	10.04	0.320		

Table D16: $Sc_{0.75}Y_{0.25}F_3$ Heat Capacity Data: 8.98 mg sample; in order of data collection.

T / K	C_P / J K^{-1} mol^{-1}
274.06	79.969
273.77	79.827
273.77	79.872

Table D17: $Sc_{0.75}Y_{0.25}F_3$ Heat Capacity Data: 9.84 mg sample; in order of data collection.

T / K	C_P / J K^{-1} mol^{-1}	T / K	C_P / J K^{-1} mol^{-1}	T / K	C_P / J K^{-1} mol^{-1}
280.88	82.540	324.49	84.696	362.57	86.964
280.55	82.426	324.49	84.526	362.67	86.842
280.56	82.387	324.48	84.674	362.65	86.911
295.17	83.105	339.14	85.070	376.95	88.064
295.18	83.118	339.15	84.988	377.07	87.704
295.18	82.875	339.15	85.002	377.07	87.918
309.82	84.079	351.22	85.786	391.37	89.069
309.83	84.152	351.22	85.970	391.43	88.888
309.83	84.221	351.23	85.987		

Table D18: $Sc_{0.75}Y_{0.25}F_3$ Heat Capacity Data: 11.05 mg sample; in order of data collection.

T / K	C_P / J K^{-1} mol^{-1}	T / K	C_P / J K^{-1} mol^{-1}	T / K	C_P / J K^{-1} mol^{-1}
280.05	80.991	323.49	83.258	363.28	84.858
279.67	80.727	323.47	83.258	363.28	84.778
279.67	80.813	323.48	83.279		
294.27	81.446	338.14	83.382		
294.26	81.517	338.11	83.360		
294.26	81.469	338.11	83.367		
308.88	82.492	350.70	84.133		
308.86	82.449	350.69	84.193		
308.86	82.436	350.69	84.216		

Table D19: $Sc_{0.75}Y_{0.25}F_3$ Heat Capacity Data: 6.28 mg sample; in order of data collection.

T / K	C_P / J K^{-1} mol^{-1}	T / K	C_P / J K^{-1} mol^{-1}
10.09	0.319	7.87	0.130
10.07	0.317	7.85	0.130
10.07	0.317	7.85	0.130
9.29	0.236	7.23	0.097
9.27	0.236	7.22	0.097
9.27	0.236	7.22	0.096
8.55	0.176		
8.53	0.175		
8.53	0.175		

Table D20: $Sc_{0.75}Y_{0.25}F_3$ Heat Capacity Data: 4.44 mg sample; in order of data collection.

T / K	C_P / J K^{-1} mol^{-1}	T / K	C_P / J K^{-1} mol^{-1}
10.11	0.316	9.30	0.235
10.10	0.315	9.29	0.235
10.09	0.315	9.28	0.235
9.31	0.233	8.56	0.175
9.29	0.234	8.55	0.175
9.29	0.233	8.54	0.175
10.11	0.317		
10.09	0.318		
10.09	0.317		

Appendix E: Thermal Stress Distributions in $Y_2Mo_3O_{12}$ and $Al_2Mo_3O_{12}$

Figure E1: Thermal stress distributions in the eigenbasis in a modeled $Y_2Mo_3O_{12}$ polycrystal following cooling by 700 K (see Chapter 9). Black points are data, green curves are fits to the data, and red curves are lognormal functions.
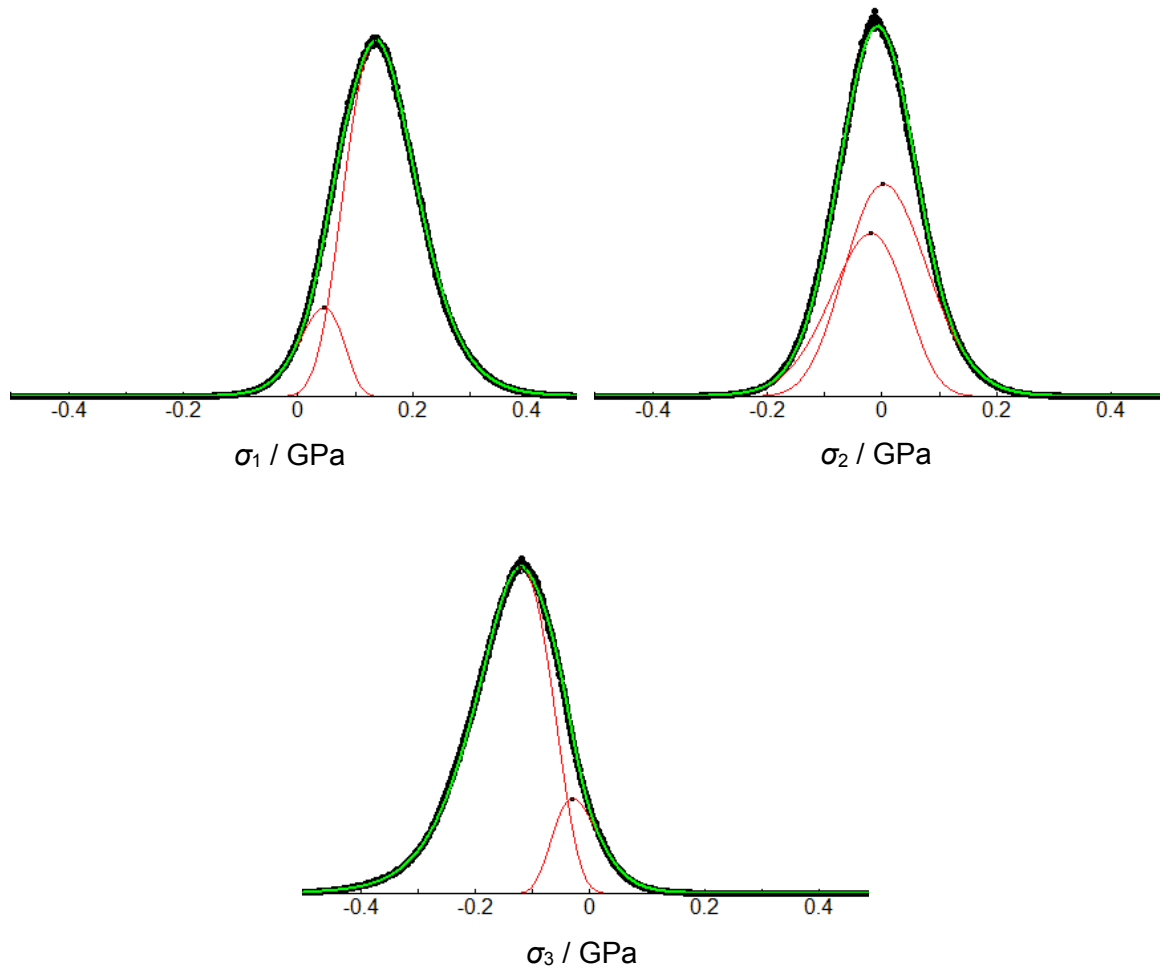
Figure E2: Thermal stress distributions in the eigenbasis in a modeled $Al_2Mo_3O_{12}$ polycrystal following cooling by 700 K (see Chapter 9). Black points are data, green curves are fits to the data, and red curves are lognormal functions.
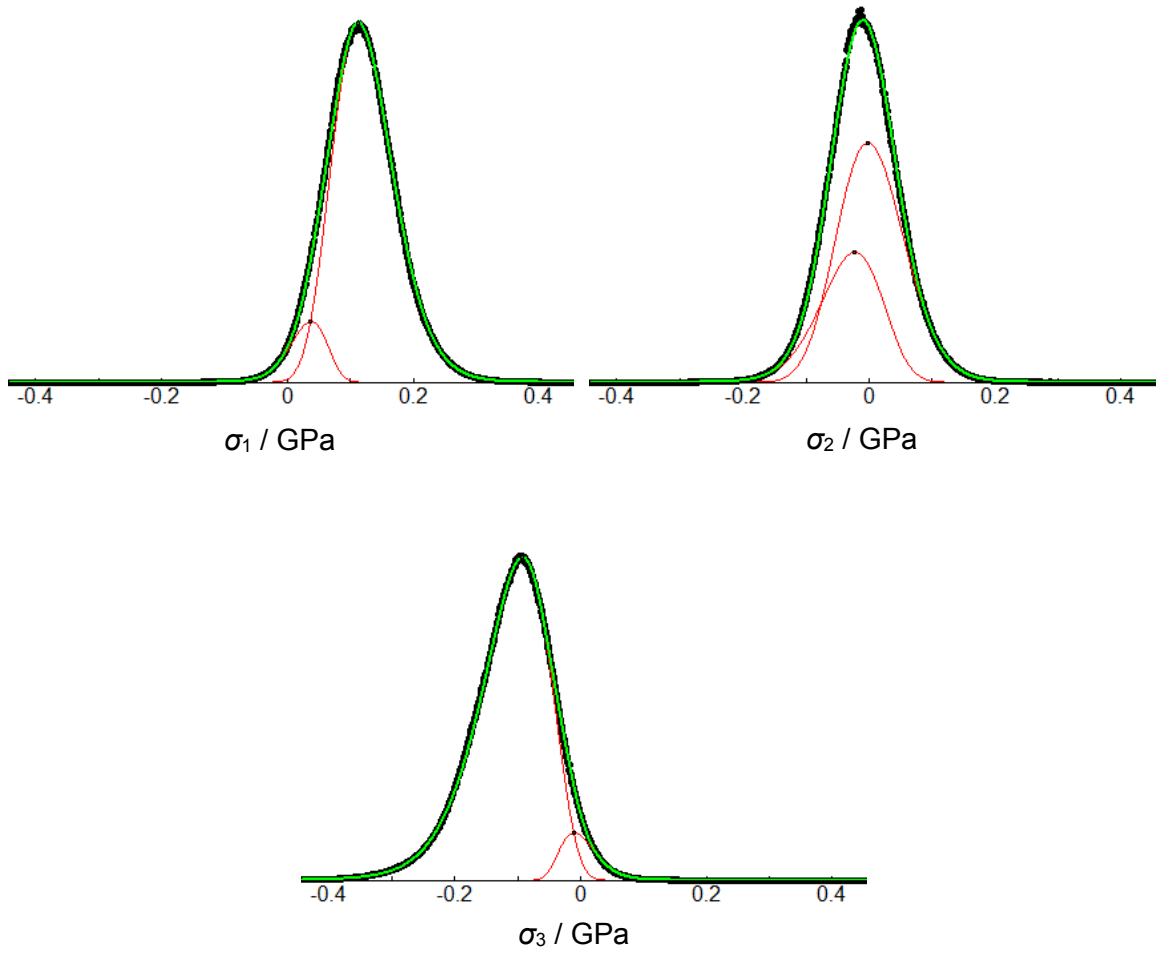
Appendix F: Copyright Agreements

F1. Permissions for Chapter 1 and Chapter 2

3. Rights

The Contributor hereby grants, transfers and assigns to the Publisher to the maximum extent possible each and every right in and to the Contribution and any revision throughout the world for any media (including electronic media such as optical or magnetic media) to sell, license and otherwise distribute the Contribution or any part of the Contribution, for the full term of copyright, including, without limitation, the copyright therein. The Contributor acknowledges that any work made by the Contributor shall have been made as a contribution to a collective work. This exclusive grant of rights means that the Contributor has no independent right to assign or license the Contribution in whole or in part to third parties or to directly exploit the Contribution. In the event the Contributor wishes to utilize material contained in the Contribution in the Contributor's other works or presentations, the Contributor shall request permission from the Publisher, which permission shall not be unreasonably withheld for proposed uses that do not materially interfere with the rights granted to the Publisher hereunder.

Notwithstanding for foregoing, the *Contributor and any Co-contributors* shall be entitled to use the material contained in the Contribution without obtaining the Publisher's permission in preparing articles for publication in scholarly or professional journals, in contributions to symposia, in a single

chapter in a book, for the Contributor's classroom lectures (and may use and make copies of excerpts up to ten percent (10%) of the Contribution for this purpose) and for presentations or lectures at professional meetings, may place a summary of the Contribution online and may use portions or excerpts in a graduate thesis, provided that the Publisher and the Work are appropriately identified. The Contributor understands and agrees that the Publisher may, but is under no obligation to use its services in any subsequent edition of the Work and the Publisher may use all or any of the Contribution, including in any such editions, derivatives and ancillaries, without additional compensation than expressly provided in this Agreement, and the Publisher shall give credit to the Contributor in such manner which, in the judgment of the Publisher, fairly reflects the contribution to the new work.

F2. Permissions for Figure 1.2

License Number	3584440564335
License date	Mar 08, 2015
Licensed content publisher	Royal Society of Chemistry
Licensed content publication	Journal of the Chemical Society Dalton Transactions
Licensed content title	Negative thermal expansion materials †
Licensed content author	John S. O. Evans
Licensed content date	Dec 31, 1969
Issue number	19
Type of Use	Thesis/Dissertation
Requestor type	academic/educational
Portion	figures/tables/images
Number of figures/tables/images	2
Format	electronic
Distribution quantity	100
Will you be translating?	no
Order reference number	None
Title of the thesis/dissertation	Thermoelastic Properties of Thermomiotic (Negative Thermal Expansion) Materials
Expected completion date	May 2015

F3. Permissions for Figure 1.4

F4. Permissions for Section 3.5

License Number	3611590873237
License date	Apr 17, 2015
Licensed content publisher	Springer
Licensed content publication	Journal of Materials Science (full set)
Licensed content title	Al2Mo3O12/polyethylene composites with reduced coefficient of thermal expansion
Licensed content author	Alexandre Roberto Soares
Licensed content date	Jan 1, 2014
Volume number	49
Issue number	22
Type of Use	Book/Textbook
Requestor type	Publisher
Publisher	Dalhousie University
Portion	Full text
Format	Electronic
Will you be translating?	No
Print run	100
Author of this Springer article	Yes and you are the sole author of the new work
Order reference number	None
Title of new book	Thermoelastic Properties of Thermomiotic (Negative Thermal Expansion) Materials
Author of new book	Carl P Romao
Expected publication date of new book	May 2015
Estimated size of new book (pages)	300

F5. Permissions for Chapter 5

F6. Permissions for Chapter 7

License Number	3611571318673
License date	Apr 17, 2015
Licensed content publisher	Springer
Licensed content publication	Journal of Materials Science (full set)
Licensed content title	The heat capacities of thermomiotic ScF3 and ScF3–YF3 solid solutions
Licensed content author	Carl P. Romao
Licensed content date	Jan 1, 2015
Volume number	50
Issue number	9
Type of Use	Book/Textbook
Requestor type	Publisher
Publisher	Dalhousie University
Portion	Full text
Format	Electronic
Will you be translating?	No
Print run	100
Author of this Springer article	Yes and you are the sole author of the new work
Order reference number	None
Title of new book	Thermoelastic Properties of Thermomiotic (Negative Thermal Expansion) Materials
Author of new book	Carl P Romao
Expected publication date of new book	May 2015
Estimated size of new book (pages)	300

F7. Permissions for Figure 8.7

Supplier	Elsevier Limited The Boulevard,Langford Lane Kidlington,Oxford,OX5 1GB,UK
Registered Company Number	1982084
Customer name	Carl P Romao
Customer address	6274 Coburg Road
	Halifax, NS B3H 4R2
License number	3610441056823
License date	Apr 15, 2015
Licensed content publisher	Elsevier
Licensed content publication	Solid State Communications
Licensed content title	Two-stage amorphization of scandium molybdate at high pressure
Licensed content author	None
Licensed content date	January 2004
Licensed content volume number	129
Licensed content issue number	1
Number of pages	5
Start Page	9
End Page	13
Type of Use	reuse in a thesis/dissertation
Intended publisher of new work	other
Portion	figures/tables/illustrations
Number of figures/tables/illustrations	1
Format	electronic
Are you the author of this Elsevier article?	No
Will you be translating?	No
Original figure numbers	Figure 1
Title of your thesis/dissertation	Thermoelastic Properties of Thermomiotic (Negative Thermal Expansion) Materials
Expected completion date	May 2015
Estimated size (number of pages)	250
Elsevier VAT number	GB 494 6272 12

F8. Permissions for Section 9.1.2

License Number	3611580122442
License date	Apr 17, 2015
Licensed content publisher	Springer
Licensed content publication	Journal of Materials Science (full set)
Licensed content title	The effect of microstructure on thermal expansion coefficients in powder-processed Al2Mo3O12
Licensed content author	Luciana Prates Prisco
Licensed content date	Jan 1, 2012
Volume number	48
Issue number	7
Type of Use	Book/Textbook
Requestor type	Publisher
Publisher	Dalhousie University
Portion	Full text
Format	Electronic
Will you be translating?	No
Print run	100
Author of this Springer article	Yes and you are the sole author of the new work
Order reference number	None
Title of new book	Thermoelastic Properties of Thermomiotic (Negative Thermal Expansion) Materials
Author of new book	Carl P Romao
Expected publication date of new book	May 2015
Estimated size of new book (pages)	300

F9. Permissions for Section 9.1.3

References

1. Romao, C. P.; Miller, K. J.; Whitman, C. A.; White, M. A.; Marinkovic, B. A. Negative Thermal Expansion (Thermomiotic) Materials. In *Comprehensive Inorganic Chemistry II*; Reedijk, J.; Poeppelmeier, K., Ed.; Elsevier: Oxford, UK, 2013; Vol. 4, p 128–151. doi:10.1016/b978-0-08-097774-4.00425-3.

2. White, G. K. *Contemp. Phys.* **1993**, *34*, 193–204. doi:10.1080/00107519308213818.

3. White, M. A. *Physical Properties of Materials*; CRC Press: Boca Raton, FL, 2012.

4. Kittel, C. *Introduction to Solid State Physics*; Wiley: Hoboken, NJ, 2005.

5. Barker Jr., R. E. *J. Appl. Phys.* **1963**, *34*, 107–116. doi:10.1063/1.1729049.

6. Barrera, G. D.; Bruno, J. A. O. Barron, T. H. K.; Allan, N. L. *J. Phys.: Condens. Matter* **2005**, *17*, R217–R252. doi:10.1088/0953-8984/17/4/R03.

7. Evans, J. S. O. *J. Chem. Soc. Dalton Trans.* **1999**, 3317–3326. doi:10.1039/A904297K.

8. Dove, M. T.; Fang, H. Lattice dynamics, negative thermal expansion, and associated anomalous physical properties of materials. Submitted to *Rep. Prog. Phys.*, 2015.

9. Miller, W.; Smith, C. W.; Mackenzie, D. S. Evans, K. E. *J. Mater. Sci.* **2009**, *44*, 5441–5451. doi:10.1007/s10853-009-3692-4.

10. Hofmeister, A. M.; Mao, H.-k. *Proc. Natl. Acad. Sci. U. S. A.* **2002**, *99*, 559–564. doi:10.1073/pnas.241631698.

11. Zwanziger, J. W. *Phys. Rev. B* **2007,** *76,* 052102. doi:10.1103/PhysRevB.76.052102.

12. Key, S. W. *J. Appl. Phys.* **1967**, *38*, 2923–2928. doi:10.1063/1.1710025.

13. Choy, C. L.; Wong, S. P.; Young, K. *Phys. Rev. B* **1984**, *29*, 1741–1747. doi:10.1103/physrevb.29.1741.

14. Parsons, B. J. *Proc. R. Soc. Lond. A* **1977**, *352,* 397–417. doi:10.1098/rspa.1977.0006.

15. Fultz, B. *Prog. Mater. Sci.* **2010,** *55,* 257–352. doi:10.1016/j.pmatsci.2009.05.002.

16. Kingery, W. D.; Bowen, H. K.; Uhlmann, D. R. *Introduction to Ceramics*; John Wiley & Sons: New York, 1960.

17. Barker Jr., R. E. *J. Appl. Phys.* **1967**, *38*, 4234–4242. doi:10.1063/1.1709110.

18. Zerilli, F. J.; Kuklja, M. M. *J. Phys. Chem. A* **2007**, *111*, 1721–1725. doi:10.1021/jp067709y.

19. White, M. A.; Meingast, C.; David, W. I. F.; Matsuo, T. *Solid State Commun.* **1995**, *94*, 481–484. doi:10.1016/0038-1098(94)00902-3.

20. Watanabe, H.; Tani, J.; Kido, H.; Mizuuchi, K. *Mater. Sci. Eng., A* **2008**, *494*, 291–298. doi:10.1016/j.msea.2008.04.037.

21. Mittal, R.; Chaplot, S. L.; Schober, H.; Kolesnikov, A. I.; Loong, C.-K.; Lind, C.; Wilkinson, A. P. *Phys. Rev. B* **2004**, *70*, 214303. doi:10.1103/PhysRevB.70.214303.

22. Arora, A. K.; Yagi, T.; Miyajima, N.; Mary, T. A. *J. App. Phys.* **2005**, *97*, 013508. doi:10.1063/1.1819975.

23. Han, S. S.; Goddard III, W. A. *J. Phys. Chem. C* **2007**, *111*, 15185–15191. doi:10.1021/jp075389s.

24. Chapman, K. W.; Chupas, P. J. *J. Am. Chem. Soc.* **2007**, *129*, 10090–10091. doi:10.1021/ja073791e.

25. Drymiotis, F.R.; Ledbetter, H.; Betts, J. B.; Kimura, T.; Lashley, J. C.; Migliori, A.; Ramirez, A. P.; Kowach, G. R.; Van Duijn, J. *Phys. Rev. Lett.* **2004,** *93,* 025502. doi:10.1103/PhysRevLett.93.025502.

26. Varga, T.; Wilkinson, A. P.; Lind, C.; Bassett, W. A.; Zha, C.-S. *Phys. Rev. B* **2005**, *71*, 214106. doi:10.1103/physrevb.71.214106.

27. Varga, T.; Wilkinson, A. P.; Lind, C.; Bassett, W. A.; Zha, C.-S. *J. Phys.: Condens. Matter* **2005**, *17*, 4271–4283. doi:10.1088/0953-8984/17/27/004.

28. Karmakar, S.; Deb, S. K.; Tyagi, A. K.; Sharma, S. M. *J. Solid State Chem* **2004**, *177*, 4087–4092. doi:10.1016/j.jssc.2004.08.020.

29. Fang, H.; Phillips, A. E.; Dove, M. T.; Tucker, M. G.; Goodwin, A. L. *Phys. Rev. B* **2014**, *88*, 144103. doi:10.1103/PhysRevB.88.144103.

30. Li, C. W.; Tang, X.; Muñoz, J. A.; Keith, J. B.; Tracy, S. J.; Abernathy, D. L.; Fultz, B. *Phys. Rev. Lett.* **2011**, *107*, 195504. doi:10.1103/physrevlett.107.195504.

31. Fang, H.; Dove, M. T.; Phillips, A. E. *Phys. Rev. B* **2014**, 214103. doi:10.1103/physrevb.89.214103.

32. Pryde, A. K. A.; Hammonds, K. D.; Dove, M. T.; Heine, V.; Gale, J. D.; Warren, M. C. *J. Phys.: Condens. Matter* **1996**, *8*, 10973–10982. doi:10.1088/0953-8984/8/50/023.

33. Dove, M. T.; Trachenko, K. O.; Tucker, M. G.; Keen, D. A. *Rev. Mineral. Geochem.* **2000**, *39*, 1–33. doi:10.2138/rmg.2000.39.01.

34. Dove, M. T.; Giddy, A. P.; Heine, V. *Trans. Am. Crystallogr. Assoc.* **1991**, *27*, 65–75.

35. Dove, M. T.; Gambhir, M.; Heine, V. *Phys. Chem. Miner.* **1999,** *26*, 344–353. doi:10.1007/s002690050194.

36. Dove, M. T.; Heine, V.; Hammonds, K. D. *Mineral. Mag.* **1995**, *59*, 629–639. doi:10.1180/minmag.1995.059.397.07.

37. Hammonds, K. D.; Dove, M. T.; Giddy, A. P.; Heine, V.; Winkler, B. *Am. Mineral.* **1996**, *81*, 1057–1079.

38. Welche, P. R. L., Heine, V.; Dove , M. T. *Phys. Chem. Miner.* **1998**, *26*, 63–77. doi:10.1007/s002690050161.

39. Evans, J. S. O.; David, W. I. F.; Sleight, A. W. *Acta Crystallogr., Sect. B: Struct. Sci.* **1999**, *55*, 333–340. doi:10.1107/s0108768198016966.

40. Heine, V.; Welche, P. R. L., Dove, M. T. *J. Am. Ceram. Soc.* **1999**, *82*, 1793–1802. doi:10.1111/j.1151-2916.1999.tb02001.x.

41. Withers, R. L.; Tabira, Y.; Evans, J. S. O.; King, I. J.; Sleight, A. W. *J. Solid State Chem.* **2001**, *157*, 186–192. doi:10.1006/jssc.2000.9074.

42. Tao J. Z.; Sleight, A.W. *J. Solid State Chem.* **2003**, *173*, 442–448. doi:10.1016/s0022-4596(03)00140-3.

43. Hammonds, K. D.; Dove, M. T.; Giddy, A. P.; Heine, V. *Am. Mineral.* **1994**, *79*, 1207–1209.

44. Evans, J. S. O.; Mary, T. A.; Sleight, A. W. *J. Solid State Chem.* **1997**, *133*, 580–583. doi:10.1006/jssc.1997.7605.

45. Marinkovic, B. A.; Ari, M.; de Avillez, R. R.; Rizzo, F.; Ferreira, F. F.; Miller, K. J.; Johnson, M. B.; White, M. A. *Chem. Mater.* **2009**, *21*, 2886–2894. doi:10.1021/cm900650c.

46. Wang, L.; Wang, F.; Yuan, P.-F.; Sun, Q.; Liang, E.-J.; Jia, Y.; Guo, Z.-X. *Mater. Res. Bull.* **2013**, *48*, 2724–2729. doi:10.1016/j.materresbull.2013.04.001.

47. Rimmer, L. H. N.; Dove, M. T. *J. Phys. Condens. Matter* **2015**, *27*, 185401. doi:10.1088/0953-8984/27/18/185401.

48. Petzoldt, J.; Pannhorst, W. *J. Non-Cryst. Solids* **1991**, *129*, 191–198. doi:10.1016/0022-3093(91)90095-n.

49. Pannhorst, W. *J. Non-Cryst. Solids* **1997**, *219,* 198–204. doi:10.1016/s0022-3093(97)00270-6.

50. Northover, J. P.; Groves, W. A. *J. Mater Sci.* **1981,** *16,* 1874–1880. doi:10.1007/bf00540635.

51. Bach, H., Ed. *Low Thermal Expansion Glass Ceramics*; Springer, Berlin, 1995.

52. Kobayashi, Y.; Imanaka, N.; Adachi, G. *J. Cryst. Growth* **1994,** *143*, 362–364. doi:10.1016/0022-0248(94)90078-7.

53. Mary, T. A.; Sleight, A. W. *J. Mater. Res.* **1999,** *14,* 912–915. doi:10.1557/jmr.1999.0122.

54. Liang, E.-J. *Recent Pat. Mater. Sci.* **2010**, *3*, 106–128. doi:10.2174/1874464811003020106.

55. Agostini, G.; Corvasce, F. G. Tire with Low Thermal Expansion Component. U.S. Patent 7,347,242, Mar 25, 2008.

56. Schlichter, S.; Herrmann, A. S. Apparatus at a Carding Machine having a Cylinder and Clothed and/or Unclothed Elements Located Opposite the Cylinder. U.S. Patent 7,694,393, Apr 13, 2010.

57. Dejneka, M. J.; Chapman, C. L.; Misture, S. T. *J. Am. Ceram. Soc.* **2011**, *94*, 2249–2261. doi:10.1111/j.1551-2916.2011.04730.x.

58. Merkel, G. A. Optical Device with Negative Thermal Expansion Substrate and Uses Therefor. U.S. Patent 6,377,729, Apr 23, 2002.

59. Bookbinder, D. C.; Carberry, J. P.; Danielson, P. S.; DeMartino, S. E.; Hagy, H. E.; Wedding, B. M. Athermal Optical Waveguide Grating Device. U.S. Patent 6,603,900, Aug 5, 2003.

60. Matano, T.; Yoshihara, S. Substrate for Optical Communication Device, Method for Production thereof and Optical Communication Device Using the Same. U.S. Patent 7,106,941, Sep 12, 2006.

61. Pedersen, J. E.; Beukema, M.; Poulsen, C. V.; Eskildsen, L. E. Packaging of an Optical Fiber Laser. U.S. Patent 6,603,779, Aug 5, 2003.

62. Jiang, T.; Wu, Z. Zero Insertion Force Sockets Using Negative Thermal Expansion Materials. U.S. Patent 6,264,486, July 24, 2001.

63. Suzuki, T.; Omote, A.; Kuwata, J. Zero Thermal Expansion Material and Practical Component Parts Making Use of the Same. U.S. Patent 6,844,283, Jan 18, 2005.

64. Hougham, G. G.; Chey, S. J.; Doyle, J. P.; Liu, X. H.; Jahnes, C. V.; Lauro, P. A.; LaBianca, N. C.; Rooks, M. J. Negative Thermal Expansion System (NTES) Device for TCE Compensation in Elastomer Composites and Conductive Elastomer Interconnects in Microelectronic Packaging. U.S. Patent 7,417,315, Aug 26, 2008.

65. Kohka, K. Negative Thermal Expansion Metal Electrically Connected to Motor Means for Microwave Oven. U.S. Patent 4,608,474, Aug 26, 1986.

66. McAvoy, G. J.; Lawlor, V. P.; Silverbrook, K. Thermal Bend Actuator Comprising Passive Element having Negative Thermal Expansion. U.S. Patent 7,735,970, Jun 15, 2010.

67. Jakubinek, M. B.; O'Neill, C.; Felix, C.; Price, R. B.; White, M. A. *Dent. Mater.* **2008**, *24,* 1468–1476. doi:10.1016/j.dental.2008.03.012.

68. Versluis, A.; Douglas, W. H., Sakaguchi, R. L. *Dent. Mater.* **1996,** *12,* 290–294. doi:10.1016/s0109-5641(96)80036-4.

69. Boyd, R. N.; Colin, L.; Kaufman, E. G. Dental Filling Composition of a Coefficient of Thermal Expansion Approximating that of Natural Tooth Enamel. U.S. Patent 3,503,128, Mar 31, 1970.

70. Limaye, S. Y.; Agrawal, D. K.; Roy, R.; Mehrotra, Y. *J. Mater. Sci.* **1991**, *26,* 93–98. doi:10.1007/bf00576037.

71. Morelock, C. R.; Greve, B. K.; Cetinkol, M.; Chapman, K. W.; Chupas, P. J.; Wilkinson, A. P. *Chem. Mater.* **2013**, *25*, 1900–1904. doi:10.1021/cm400536n.

72. Carey, T.; Tang, C. C.; Hriljac, J. A.; Anderson, P. A. *Chem. Mater.* **2014**, *26*, 1561–1566. doi:10.1021/cm403312q.

73. Margadonna, S.; Prassides, K.; Fitch, A. N. *J. Am. Chem. Soc.* **2004**, *126*, 15390–15391. doi:10.1021/ja044959o.

74. Chen, J.; Xing, X.; Sun, C.; Hu, P.; Yu, R.; Wang, X.; Li, L. *J. Am. Chem. Soc.* **2008**, *130*, 1144–1145. doi:10.1021/ja7100278.

75. Takenaka, K.; Takagi, H. *Appl. Phys. Lett.* **2009**, *94*, 131904. doi:10.1063/1.3110046.

76. Miller, K. J.; Romao, C. P.; Bieringer, M.; Marinkovic, B. A.; Prisco, L.; White, M. A. *J. Am. Ceram. Soc.* **2013,** *96*, 561–566. doi:10.1111/jace.12085.

77. Suzuki, T.; Omote, A. *J. Am. Ceram. Soc.* **2006**, *89*, 691–693. doi:10.1111/j.1551-2916.2005.00729.x.

78. Launay, S.; Wallez, G.; Quarton, M. *Chem. Mater.* **2001**, *13*, 2833–2837. doi:10.1021/cm010002y.

79. Phillips, A. E.; Halder, G. J.; Chapman, K. W.; Goodwin, A. L.; Kepert, C. J. *J. Am. Chem. Soc.* **2010**, *132*, 10–11. doi:10.1021/ja906895j.

80. Goodwin, A. L.; Chapman, K. W.; Kepert, C. J. *J. Am. Chem. Soc.* **2005**, *127*, 17980–17981. doi:10.1021/ja056460f.

81. Phillips, A. E.; Goodwin, A. L.; Halder, G. J.; Southton, P. D.; Kepert, C. J. *Angew. Chem. Int. Ed.* **2008**, *47*, 1396–1399.

82. Yano, H.; Sugiyama, J.; Nakagaito, A.; Nogi, M.; Matsuura, T.; Hikita, M.; Handa, K. *Adv. Mater.* **2005,** *17,* 153–155. doi:10.1002/adma.200400597.

83. Nye, J. F. *Physical Properties of Crystals, Their Representation by Tensors and Matrices*; Oxford University Press: New York, 1985.

84. Novikova, S. I. *Meas. Tech.* **1984,** *27*, 933–938. (transl. from *Izmeritel'naya Tekhnika* **1984**, *10*, 40–42.) doi:10.1007/bf00862316.

85. Jakubinek, M. B.; Whitman, C. A.; White, M. A. *J. Therm. Anal. Calorim.* **2010,** *99,* 165–172. doi:10.1007/s10973-009-0458-9.

86. Miller, W.; Smith, C. W.; Dooling, P.; Burgess, A. N.; Evans, K. E. *Compos. Sci. Technol.* **2010**, *70*, 318–327. doi:10.1016/j.compscitech.2009.11.003.

87. Mary, T. A.; Evans, J. S. O.; Vogt, T.; Sleight, A. W. *Science* **1996,** *272,* 90–92. doi:10.1126/science.272.5258.90.

88. Lewis, R. J., Sr., Ed. *Hawley's Condensed Chemical Dictionary*, 13th ed.; John Wiley & Sons: New York, 1997.

89. Ruml, V. *Tagungsband – Kammer Tech. Suhl* **1979**, *53*, 87.

90. Lind, C.; Gates, S. D; Pedoussaut; N. M.; Baiz, T. I. *Materials* **2010,** *3,* 2567–2587. doi:10.3390/ma3042567.

91. Gindhart, A. M.; Lind, C.; Green, M. *J. Mater. Res.* **2008**, *23*, 210–213. doi:10.1557/jmr.2008.0013.

92. Tyagi, A. K.; Achary, S. N.; Mathews, M. D. *J. Alloys Compd.* **2002,** *339,* 207–210. doi:10.1016/s0925-8388(01)02003-5.

93. Korthuis, V.; Khosrovani, N.; Sleight, A. W.; Roberts, N.; Dupree, R.; Warren Jr., W. W. *Chem. Mater.* **1995**, *7*, 412–417. doi:10.1021/cm00050a028.

94. Hannink, R. H. J.; Kelly, P. M.; Muddle, B. C. *J. Am. Ceram. Soc.* **2000**, *83*, 461–487. doi:10.1111/j.1151-2916.2000.tb01221.x.

95. De Buysser, K.; Van Driessche, I.; Vande Putte, B.; Vanhee, P.; Schaubroeck, J.; Hoste, S. *Inorg. Chem.* **2008**, *47*, 736–741. doi:10.1021/ic701660w.

96. Evans, J. S. O.; Hu, Z.; Jorgensen, J. D.; Argyriou, D. N.; Short, S.; Sleight, A. W. *Science* **1997,** *275,* 61–65. doi:10.1126/science.275.5296.61.

97. Varga, T.; Wilkinson, A. P.; Lind, C.; Bassett, W. A.; Zha, C.-S. *Solid State Commun.* **2005**, *135*, 739–744. doi:10.1016/j.ssc.2005.05.041.

98. Perottoni, C. A.; da Jornada, J. A. H. *Science* **1998**, *280,* 886–889. doi:10.1126/science.280.5365.886.

99. Sikka, S. K. *J. Phys.: Condens. Matter* **2004**, *16*, S1033–S1039. doi:10.1088/0953-8984/16/14/013.

100. Lommens, P.; De Meyer, C.; Bruneel, E.; De Buysser, K.; Van Driessche, I.; Hoste, S. *J. Eur. Ceram. Soc.* **2005**, *25*, 3605–3610. doi:10.1088/0953-8984/16/14/013.

101. Zhai, P.; Haussener, S.; Ager, J.; Sathre, R.; Walczak, K.; Greenblatt, J.; McKone, T. *Energy Environ. Sci.* **2013**, *6*, 2380–2390. doi:10.1039/c3ee40880a.

102. United States Geological Survey. *Minerals Commodity Summaries.* 2012.

103. Stevens, R.; Linford, J.; Woodfield, B. F.; Boerio-Goates, J.; Lind, C.; Wilkinson, A. P. *J. Chem. Thermodyn.* **2003**, *35*, 919–937. doi:10.1016/s0021-9614(03)00050-8.

104. Khosrovani, N.; Sleight, A. W.; Vogt, T. *J. Solid State Chem.* **1997,** *132*, 355–360. doi:10.1006/jssc.1997.7474.

105. Mills, S. J.; Petříček, V.; Kampf, A. R.; Herbst-Imer, R.; Raudsepp, A. *J. Solid State Chem.* **2011**, *184*, 2322–2388. doi:10.1016/j.jssc.2011.06.018.

106. Huang, C. Y.; Agrawal, D. K.; McKinstry, H. A. *J. Mater. Sci.* **1995**, *30*, 3509–3514. doi:10.1007/bf00349902.

107. Lind, C.; Coleman; M. R.; Kozy, L. C.; Sharma, G. R. *Phys. Status Solidi B* **2011**, *248*, 123–129. doi:10.1002/pssb.201083967.

108. Holliday, L.; Robinson, J. *J. Mater. Sci.* **1973**, *8*, 301–311. doi:10.1007/bf00550148.

109. Lakes, R. *J. Mater. Sci. Lett.* **1996,** *15*, 475–477.

110. Jefferson, G.; Parthasarathy, T. A.; Kerans, R. J. *Int. J. Solids Struct.* **2009**, *46,* 2372–2387. doi:10.1016/j.ijsolstr.2009.01.023.

111. Berger, J.; Mercer, C.; McMeeking, R. M.; Evans A. G. *J. Am. Ceram. Soc.* **2011,** *94,* s42–s54. doi:10.1111/j.1551-2916.2011.04503.x.

112. Grima, J. N.; Ellul, B.; Attard, D.; Gatt, R.; Attard, M. *Compos. Sci. Technol.* **2010,** *70,* 2248–2252. doi:10.1016/j.compscitech.2010.05.003

113. Lim, T.-C. *J. Mater. Sci.* **2012**, *47*, 368–373. doi:10.1016/j.compscitech.2010.05.003.

114. Sigmund, O.; Torquato, S. *J. Mech. Phys. Solids.* **1997,** *45,* 1037–1067. doi:10.1016/s0022-5096(96)00114-7.

115. Lu, T. J.; Fleck, N. A. *Acta Mater.* **1998**, *46,* 4755–4768. doi:10.1016/s1359-6454(98)00127-x.

116. Krupke, W. F.; Shinn, M. D.; Marion, J. E.; Caird, J. A.; Stokowski, S. E. *J. Opt. Soc. Am. B* **1986**, *3*, 102–114. doi:10.1364/JOSAB.3.000102.

117. Hofmeister, A. M. *J. Geophys. Res.* **1991,** *96,* 21893–21907. doi:10.1029/91JB02157.

118. Fang, H.; Dove, M. T. *Phys Rev. B* **2013**, *87*, 214109. doi:10.1103/PhysRevB.87.214109.

119. Ting, T. C.-t. *Anisotropic Elasticity: Theory and Applications*; Oxford University Press: New York, NY, 1996.

120. Duwez, P.; Brown, F. H., Jr.; Odell, F. *J. Electrochem. Soc.* **1951,** *98,* 356–362. doi:10.1149/1.2778219.

121. Wang, J.; Stevens, R. *J. Mater. Sci.* **1989,** *24,* 3421–3440. doi:10.1007/bf02385721.

122. Sun, L.; Sneller, A.; Kwon, P. *Compos. Sci. Technol.* **2008,** *68,* 3425–3430. doi:10.1016/j.compscitech.2008.09.032.

123. Meyers, M. A.; Lin, A. Y.-M.; Chen, P.-Y.; Muyco, J. *J. Mech. Behav. Biomed. Mater.* **2008,** *1,* 76–85. doi:10.1016/j.jmbbm.2007.03.001.

124. Barber, A. H.; Lu, D.; Pugno, N. M. *J. R. Soc. Interface* **2015**, *12*, 20141326. doi:10.1098/rsif.2014.1326.

125. Chang, L. L. Y.; Scroger, M. G.; Phillips, B. *J. Am. Chem. Soc.* **1967**, *50,* 211–215. doi:10.1111/j.1151-2916.1967.tb15084.x.

126. Kennedy, C. A.; White, M. A. *Solid. State. Commun.* **2005**, *134*, 271–276. doi:10.1016/j.ssc.2005.01.031.

127. Evans, J. S. O.; Mary, T. A.; Vogt, T.; Subramanian, M. A.; Sleight, A. W. *Chem. Mater.* **1996**, *8*, 2809–2823. doi:10.1021/cm9602959

128. Kozy, L. C.; Tahir, M. N.; Lind, C.; Tremel, W. *J. Mater. Chem.* **2009,** *19,* 2760–2765. doi:10.1039/b820014a.

129. Sun, X.; Yang, J.; Liu, Q.; Cheng, X. *J. Alloys. Compd.* **2009,** *481,* 668–672. doi:10.1016/j.jallcom.2009.03.061.

130. Zhang, L.; Howe, J. Y.; Zhang, Y.; Fong, H. *Cryst. Growth. Des.* **2009**, *9,* 667–670. doi:10.1021/cg801272m.

131. Sun, L.; Kwon, P. *Mater. Sci. Eng. A* **2009,** *527,* 93–97. doi:10.1016/j.msea.2009.07.050.

132. Yang, X.; Cheng, X.; Yan, X.; Yang, J.; Fu, T.; Qiu, J. *Compos. Sci. Technol.* **2007,** *67,* 1167–1171. doi:10.1016/j.compscitech.2006.05.012.

133. Yilmaz, S.; Dunand, D. C. *Compos. Sci. Technol.* **2004,** *64,* 1895–1898. doi:10.1016/j.compscitech.2004.02.002.

134. Sullivan, L. M.; Lukehart, C. M. *Chem. Mater.* **2005**, 2136–2141. doi:10.1021/cm0482737.

135. Yang, J.; Yang, Y.; Liu, Q.; Xu, G.; Cheng, X. *J. Mater. Sci. Technol.* **2010**, *26*, 665–668. doi:10.1016/S1005-0302(10)60103-X.

136. Lind, C. *Materials* **2012**, *5*, 1125–1154. doi:10.3390/ma5061125.

137. Miller, W.; Smith, C. W.; Dooling, P.; Burgess, A. N.; Evans, K. E. *Phys. Status Solidi B* **2008**, *245***,** 552–556. doi:10.1002/pssb.200777710.

138. Shannon, R. D. *Acta. Cryst. A* **1976**, *32*, 751–767. doi:10.1107/s0567739476001551.

139. Harrison, W.T.A.; Cheetham, A.K.; Faber Jr., J. *J. Solid State Chem.* **1988**, *76*, 328–333. doi:10.1016/0022-4596(88)90226-5.

140. Harrison, W. T. A. *Mater. Res. Bull.* **1995**, *30*, 1325–1331. doi:10.1016/0025-5408(95)00157-3.

141. Goodwin, A. L; Wells, S. A.; Dove, M. T. *Chem. Geol.* **2006**, *225*, 213–221. doi:10.1016/j.chemgeo.2005.08.015.

142. Marinkovic, B.M.; Jardim, P. M.; de Avillez, R. R.; Rizzo, F. *Solid State Sci.* **2005**, *7*, 1377–1383. doi:10.1016/j.solidstatesciences.2005.08.012.

143. Liang, E.; Huo, H.; Wang, J.; Chao, M. *J. Phys. Chem. C* **2008**, *112*, 6577–6581. doi:10.1021/jp8013332.

144. Li, Z. Y.; Song, W. B.; Liang, E. J. *J. Phys. Chem. C* **2011**, *115*, 17806–17811. doi:10.1021/jp201962b.

145. Sumithra, S.; Umarji, A. M. *Mater. Res. Bull.* **2005,** *40*, 167–176. doi:10.1016/j.materresbull.2004.09.009.

146. Sumithra, S.; Umarji, A. M. *Solid State Sci.* **2004**, *6*, 1313–1319. doi:10.1016/j.solidstatesciences.2004.07.023.

147. Evans, J. S. O.; Mary, T. A.; Sleight, A. W. *J. Solid State Chem.* **1995**, 120, 101–104. doi:10.1006/jssc.1995.1383.

148. Cheng, Y. G.; Liu, X. S.; Song, W. B.; Yuan, B. H.; Wang, X. L.; Chao, M. J.; Liang, E. J. *Mater. Res. Bull.* **2015**, *65*, 273–278. doi:10.1016/j.materresbull.2015.02.013.

149. Evans, J. S. O.; Mary, T. A.; Sleight, A. W. *J. Solid State Chem.* **1998**, *137*, 148–160. doi:10.1006/jssc.1998.7744.

150. Evans, J. S. O.; Mary, T. A. *Int. J. Inorg. Mater.* **2000,** *2*, 143–151. doi:10.1016/s1466-6049(00)00012-x.

151. Varga, T.; Moats, J. L.; Ushakov, S. V.; Navrotsky, A. *J. Mater. Res.* **2007**, *22*, 2512–2521. doi:10.1557/jmr.2007.0311.

152. Sivasubramanian, V.; Ravindran, T. R.; Nithya, R.; Arora, A. K. *J. Appl. Phys.* **2004**, *69*, 387. doi:10.1063/1.1757659.

153. Marinkovic, B. A.; Ari, M.; Jardim, P. M.; de Avillez, R. R.; Rizzo F.; Ferreira. F. F. *Thermochim. Acta* **2010**, 499, 48–53. doi:10.1016/j.tca.2009.10.021.

154. Makovicky, E.; Balić-Žunić, T. *Acta Crystallogr., Sect. B: Struct. Sci.* **1998**, *54*, 766–773. doi:10.1107/s0108768198003905.

155. Suzuki, T.; Omote, A. *J. Am. Ceram. Soc.* **2004**, *87*, 1365–1367. doi:10.1111/j.1151-2916.2004.tb07737.x.

156. Marinkovic, B. A.; Jardim, P. M.; Ari, M.; de Avillez, R. R.; Rizzo, F.; Ferreira, F. F. *Phys. Status Solidi B* **2008**, *245*, 2514–2519. doi:10.1002/pssb.200880262.

157. Baiz, T. I.; Gindhart, A. M.; Kraemer, S. K.; Lind, C. *J. Sol-Gel Sci. Technol.* **2008**, *47*, 128–130. doi:10.1007/s10971-008-1765-5.

158. Bradstreet, S. W. *Bull. Am. Ceram. Soc.* **1958,** *37,* 510.

159. Ari, M.; Jardim, P. M.; Marinkovic, B.A.; Rizzo, F.; Ferreira. F. F. *J. Solid State Chem.* **2008**, *181*, 1472–1479. doi:10.1016/j.jssc.2008.03.015.

160. Tkacová, K. *Mechanical Activation of Minerals*; Elsevier: New York, 1989.

161. Pourghahramani, P.; Forssberg, E. *Int. J. Miner. Process.* **2006**, *79*, 120–139. doi:10.1016/j.minpro.2006.01.010.

162. Klug, H. P.; Alexander, L. E. *X-ray Diffraction Procedures for Polycrystalline and Amorphous Materials*; Wiley: New York, NY, 1974.

163. Le Bail, A. The Profile of a Bragg Reflection for Extracting Intensities. In *Powder Diffraction: Theory and Practice*; Billinge, S. J. L.; Dinnebier, Robert E. Ed.; Royal Society of Chemistry: Cambridge, UK, 2008; p 134–165.

164. Rietveld, H. M. *J. Appl. Cryst.* **1969**, *2*, 65–71. doi:10.1107/s0021889869006558.

165. http://www.rietica.org.

166. Ypma, T. J. *SIAM Rev.* **1995**, *37*, 531–551. doi:10.1137/1037125.

167. Young, R. A.; Wiles, D. B. *J. Appl. Cryst.* **1982**, *15*, 430–438. doi:10.1107/S002188988201231X.

168. Davis, W. I. F. *J. Res. Natl. Inst. Stand. Technol.* **2004**, *109*, 107-123. doi:10.6028/jres.109.008.

169. PDF-2 Powder Diffraction Database, International Centre for Diffraction Data, Newton Square, PA, 2012.

170. http://www.crystalimpact.com/match.

171. Johnson, M. B.; White, M. A. Thermal Methods. In *Inorganic Materials: Multi Length-Scale Characterisation*; Bruce, D. W.; OHare, D.; Walton, R. I., Eds.; Wiley: New York, 2014; p 63–119.

172. James, J. D.; Spittle, J. A.; Brown, S. G. R.; Evans, R. W. *Meas. Sci. Technol.* **2001**, *12*, R1–R15. doi:10.1088/0957-0233/12/3/201.

173. Milliner, T.; Neugebauer, J. *Nature* **1949**, *163*, 601–602. doi:10.1038/163601b0.

174. Kennedy, C. A.; Stancescu, M.; Marriott, R. A.; White, M. A. *Cryogenics* **2007**, *47*, 107–112. doi:10.1016/j.cryogenics.2006.10.001.

175. Hwang, J. S.; Lin, K. J.; Tien, C. *Rev. Sci. Instrum.* **1997**, *68*, 94–101. doi:10.1063/1.1147722.

176. Goldstein, J.; Newbury, D.; Joy, D.; Lyman, C.; Echlin, P.; Lifshin, E.; Sawyer, L.; Michael, J. *Scanning Electron Microscopy and X-Ray Microanalysis*; Springer: New York, NY, 2003.

177. Asmani, M.; Kermel, C.; Leriche, A.; Ourak, M. *J. Eur. Ceram. Soc.* **2001**, *21*, 1081–1086. doi:10.1016/s0955-2219(00)00314-9.

178. http://www.gimp.org.

179. Instruction Manual, 25-DL. Panametrics. ftp://ftp.olympusndt.com/public/Thickness%20Gages/TG%20Operating%20Manuals/25DL/25DL_Manual.pdf.

180. Torres Dias, A. C.; Luz Lima, C.; Paraguassu, W.; Pereira da Silva, K.; Freire, P. T. C.; Mendes Filho, J.; Marinkovic , B.; Miller, K. J.; White, M. A.; Souza Filho, A. G. *Vib. Spectrosc.* 2013, *68*, 251–256. doi:10.1016/j.vibspec.2013.08.004.

181. Maczka, M.; Paraguassu, W.; Souza Filho, A. G.; Freire, P. T. C.; Mendes Filho, J.; Melo, F. E. A.; Hanuza, J. *J. Solid State Chem.* **2004***, 177*, 2002–2006. doi:10.1016/j.jssc.2004.01.021.

182. Zienkiewicz, O. C.; Taylor, R. L.; Zhu, J. Z. *The Finite Element Method: its Basis and Fundamentals*. Butterworth-Heinemann: Waltham, MA, 2013.

183. http://www.comsol.com.

184. Martin, R. M. *Electronic Structure: Basic Theory and Methods*. Cambridge University Press: Cambridge, UK, 2004.

185. Haas, P.; Tran, F.; Blaha, P. *Phys. Rev. B* **2009**, *79*, 085104. doi:10.1103/PhysRevB.79.085104.

186. http://www.abinit.org.

187. http://www.ace-net.ca.

188. https://www.westgrid.ca.

189. Bottin, F.; Leroux, S.; Knyazev, A. Zerah, G. *Comput. Mat. Science* **2008**, *42*, 329–336. doi:10.1016/j.commatsci.2007.07.019.

190. Gonze, X.; Amadon, B.; Anglade, P.-M.; *et al. Comput. Phys. Commun.* **2009**, *180*, 2582–2615. doi:10.1016/j.cpc.2009.07.007.

191. Gonze, X.; Beuken, J.-M.; Caracas, R.; *et al. Comp. Mater. Sci.* **2002**, *25*:478–492. doi:10.1016/s0927-0256(02)00325-7.

192. Monkhorst, H. J.; Pack, J. D. *Phys. Rev. B* **1976**, *13*, 5188–5192. doi:10.1103/physrevb.13.5188.

193. http://sourceforge.net/projects/cif2cell/.

194. Björkman, T. *Comput. Phys. Commun*. **2011**, *182*, 1183–1186. doi:10.1016/j.cpc.2011.01.013.

195. Gonze, X. *Phys. Rev. B* **1997**, *55*, 10337–10354. doi:10.1103/physrevb.55.10337.

196. Gonze, X.; Lee, C. *Phys. Rev. B* **1997**, *55*, 10355–10368. doi:10.1103/physrevb.55.10355.

197. Hamann, D. R.; Wu, X.; Rabe, K. M.; Vanderbilt, D. *Phys. Rev. B* **2005**, *71*, 035117. doi:10.1103/physrevb.71.035117.

198. Lee, C.; Gonze, X. *Phys. Rev. B* **1995**, *51*, 8610–8613. doi:10.1103/physrevb.51.8610.

199. Watts, J.; Hilmas, G.; Fahrenholtz, W. G.; Brown, D.; Clausen, B. *J. Eur. Ceram. Soc.* **2010**, *30*, 2165–2171. doi:10.1016/j.jeurceramsoc.2010.02.014.

200. COMSOL Multiphysics Users Guide, v.4.

201. Abeyaratne, R.; Bhattacharya, K.; Knowles, J. K. Stress-strain Functions With Multiple Local Minima: Modeling Phase Transformations Using Finite Thermo-elasticity. In *Nonlinear Elasticity: Theory and Applications*; Fu, Y. B.; Ogden, R. W., Eds.; Cambridge University Press: Cambridge, UK, 2001; p 433–490.

202. Zienkiewicz, O. C.; Taylor, R. L. *The Finite Element Method for Solid and Structural Mechanics*; Butterworth-Heinemann: Oxford, UK, 2013.

203. Imanaka, N.; Hiraiwa, M.; Adachi, G.; Dabkowska, H.; Dabkowski, A. 2000 *J. Cryst. Growth* **2000**, *149*, 176–179. doi:10.1016/s0022-0248(00)00771-5.

204. Soares, A. R.; Ponton, P. I.; Mancic, L.; d'Almeida, J. R. M.; Romao, C. P.; White, M. A.; Marinkovic, B. A. *J. Mater. Sci.* **2014**, *49*, 7870–7882. doi:10.1007/s10853-014-8498-3.

205. Prisco, L. P.; Romao, C. P.; White, M. A.; Marinkovic, B. A. *J. Mater. Sci.* **2013**, *48*, 2986–2996. doi:10.1007/s10853-012-7076-9.

206. Yan, X.; Cheng, X.; Xu, G.; Wang, C.; Sun, S.; Riedel, R. *Mat.-wiss. u. Werkstofftech.* **2008**, *39*, 649–653. doi:10.1002/mawe.200800322.

207. Wang, X.; Zhang, J.; Zhang, Y.; Zhang, J.; Lu, F.; Wang, X. *Rare Met.*, **2010**, *29*, 371–375. doi:10.1007/s12598-010-0132-1.

208. Wu, Y.; Liu, Q.; Wang, H. *J. Compos. Mater.* **2012**, *46*, 1453–1458. doi:10.1177/0021998311420603.

209. Holzer, H.; Dunand, D. C. *J. Mater. Res.* **1999**, *14*, 780–789. doi:10.1557/jmr.1999.0104.

210. Kofteros, M.; Rodriguez, S.; Tandon, V.; Murr, L. E. *Scr. Mater.* **2001**, *45,* 369–374. doi:10.1016/s1359-6462(01)01009-0.

211. De Buysser, K.; Lommens, P.; de Meyer, C.; Bruneel, E.; Hoste, S.; van Driessche, I. *Ceram.-Silik.* **2004**, *48*, 139–144.

212. De Meyer, C.; Vandeperre, L.; van Driessche, I.; Bruneel, E.; S. Hoste, S. *Cryst. Eng.* **2002**, *5*, 469–478. doi:10.1016/s1463-0184(02)00058-8.

213. Poowancum, A.; Matsumaru, K.; Ishizaki, K. *J. Am. Ceram. Soc.* **2011**, *94*, 1354–1356. doi:10.1111/j.1551-2916.2011.04520.x.

214. Tran, K. D.; Groshens, T. J.; Nelson, J. G. *Mater. Sci. Eng. A* **2001**, *303*, 234–240. doi:10.1016/s0921-5093(00)01906-7.

215. Wang, L. D.; Fei, W. D.; Yao, C. K. *Mater. Sci. Eng. A* **2002**, *336*, 110–116. doi:10.1016/s0921-5093(01)01981-5.

216. Ding, L.; Wang, C.; Na, Y.; Chu, L.; Yan, J. *Scr. Mater.* **2011**, *65*, 687–690. doi:10.1016/j.scriptamat.2011.07.008.

217. Chen, J. C.; Huang, G.-C.; Hu, C.; Weng, J.-P. *Scripta Mater.* **2003**, *49*, 261–266. doi:10.1016/s1359-6462(03)00213-6.

218. Hashimoto, T.; Sugimoto, T.; Omoto, K.; Kineri, N.; Ogata, Y.; Tsuda, K. *Phys. Status Solidi B* **2008,** *245*, 2504–2508. doi:10.1002/pssb.200880258.

219. Achary, S. N.; Mukherjee, G. D.; Tyagi, A. K.; Vaidya, S. N. *J. Mater. Sci.* **2002**, *37*, 2501–2509. doi:10.1023/a:1015487406446.

220. Woodcock, D. A.; Lightfoot, P.; Ritter, C. *Solid State Chem.* **2000**, *149*, 92–98. doi:10.1006/jssc.1999.8502.

221. Li, F.; Liu, X.; Song, W.; Yuan, B.; Cheng, Y.; Yuan, H.; Cheng, F.; Chao, M.; Liang, E. *J. Solid State Chem.* **2014**, *218*, 15–22. doi:10.1016/j.jssc.2014.06.009.

222. Ivanova, D.; Nikolov, V.; Peshev, P. *J. Alloys Compd.* **2007**, *430*, 356–60. doi:10.1016/j.jallcom.2006.05.028.

223. Esfahani, H.; Nemati, A.; Salahi, E. *Adv. Mater. Res.* **2010**, *93–94*, 695–698. doi:10.4028/www.scientific.net/amr.93-94.695.

224. Tsuji, T.; Yamamura, Y.; Nakajima, N. *Thermochim. Acta* **2004**, *416*, 93–98. doi:10.1016/j.tca.2003.04.001.

225. De Buysser, K.; van Driessche, I.; Vande Putte, B.; Schaubroeck, J.; Hoste, S.; *J. Solid State Chem.* **2007**, *180*, 2310–2315. doi:10.1016/j.jssc.2007.05.028.

226. Romao, C. P.; Marinkovic, B. A.; Werner-Zwanziger, U.; White, M. A. In press in *J. Am. Ceram. Soc.*. doi:10.1111/jace.13675.

227. Zhecheva, E.; Stoyanova, R.; Ivanova, S.; Nikolov, V. *Solid State Sci.* **2010**, *12* 2010–2014. doi:10.1016/j.solidstatesciences.2010.08.018.

228. Ayyappan, S.; Subbanna, G. N.; Rao, C. N. R. *Chem. Eur. J.* **1995**, *1*, 165–170. doi:10.1002/chem.19950010305.

229. Martorana, S.; Fedele, A.; Mazzocchi, M.; Bellosi, A. *Appl. Surf. Sci.* **2009**, *255*, 6679–6685. doi:10.1016/j.apsusc.2009.02.069.

230. Chan, S.-K.; Fang, Y.; Grimsditch, M.; Li, Z.; Nevitt, M. V.; Robertson, W. M.; Zoubolis, E. S.; *J. Am. Ceram. Soc.* **1991**, *74*, 1742–1744. doi:10.1111/j.1151-2916.1991.tb07177.x.

231. Hovis, D. B.; Reddy, A.; Heuer, A. H. *Appl. Phys. Lett.* **2006**, *88*, 131910. doi:10.1063/1.2189071**.**

232. Smith, C. F.; Crandall, W. B. *J. Am. Ceram. Soc.* **1964**, *47* 624–627. doi:10.1111/j.1151-2916.1964.tb13120.x.

233. Patil, R. N.; Subbarao, E. C. *J. Appl. Cryst.* **1969**, *2*, 281–288 (1969). doi:10.1107/s0021889869007217.

234. Tremblay, L. P.; Johnson, M. B.; Werner-Zwanziger, U.; White, M. A. *J. Mater. Res.* **2011**, *26,* 1216–1224. doi:10.1557/jmr.2011.76.

235. Munch, E.; Launey, M. E.; Alsem, D. H.; Saiz, E.; Tomsia, A. P.; Ritchie, R. O. *Science* **2008,** *322,* 1516–1520. doi:10.1126/science.1164865.

236. Deville, S.; Saiz, E.; Nalla, R. K.; Tomsia, A. P. *Science* **2006,** *311,* 515–518. doi:10.4028/www.scientific.net/ast.49.148.

237. Nayar, S.; Pramanick, A. K.; Guha, A.; Mahato, B. K.; Gunjan, M.; Sinha, A *Bull. Mater. Sci.* **2008,** *31*, 429–432. doi:10.1007/s12034-008-0067-4.

238. Chen, R.; Johnson, M. B.; Plucknett, K. P.; White, M. A. *J. Mater. Res.* **2012**, *27*, 1869–1876. doi:10.1557/jmr.2012.112

239. Mayer, G. *Science* **2005,** *310*, 1144–1147. doi:10.1126/science.1116994.

240. Quemada, D.; Berli, C. *Advances in Colloid and Interface Science* **2002**, *98*, 51–85. doi:10.1016/s0001-8686(01)00093-8.

241. Pozdnyakov, A. O.; Handge, U. A.; Konchits, A.; Altstädt, V. *Polym. Adv. Technol.* **2011**, *22*, 84–89. doi:10.1002/pat.1849.

242. Drotning, W. D.; Roth, E. P. *J. Mater. Sci.* **1989**, *24*, 3137–3140. doi:10.1007/bf01139031,

243. Sinha, M.; Buckley, D. J. Acoustic Properties of Polymers. In *Physical Properties of Polymers*; Mark, J. E., Ed.; Springer: New York, NY; p 1021–1031.

244. Koh, J.-H.; Sorge, E.; Wen, T.-C.; Shetty, D. K. *Ceram. Int.* **2013**, *39*, 8421–8427. doi:10.1016/j.ceramint.2013.04.024.

245. Xu, Y; Carlson, S.; Norrestam, R. *J. Solid. State Chem.* **1997**, *132*, 123–130. doi:10.1006/jssc.1997.7420.

246. Grima, J. N.; Oliveri, L.; Ellul, B.; Gatt, R.; Attard, D.; Cicala, G.; Recca, G. *Phys. Status Solidi RRL* **2010**, *4*, 133–135. doi:10.1002/pssr.201004076.

247. Lim, T.-C. *Phys. Status Solidi B* **2011**, *248*, 140–147. doi:10.1002/pssb.200983970.

248. Klemens, P. G. *Int. J. Thermophys.* **1986**, *7*, 197–206. doi:10.1007/bf00503810.

249. Tokoro, H.; Nakagawa, K.; Imoto, K.; Hakoe, F.; Okoshi, S.-I. *Chem. Mater.* **2012**, *24*, 1324–1330. doi:10.1021/cm203762k.

250. Suzuki, T.; Omote, A. *J. Am. Ceram. Soc.* **2004**, *87*, 1365–1367. doi:10.1111/j.1151-2916.2004.tb07737.x.

251. Song, W. B.; Liang, E.-J.; Liu, X.-S.; Li, Z.-Y.; Yuan, B.-H.; Wang, J.-Q. *Chin. Phys. Lett.* **2013** *30*, 126502-1–126502-4.

252. Omote, A.; Yotsuhashi, S.; Zenitani, Y.; Yamada, Y. *J. Am. Ceram. Soc.* **2011**, *94*, 2285–2288. doi:10.1111/j.1551-2916.2011.04644.x

253. Steele, B. C. H.; Heinzel, A. *Nature*, **2001**, *414*, 345–352. doi:10.1038/35104620.

254. Harris, R. K.; R. E. Wasylishen; M. J. Duer, *NMR Crystallography*, John Wiley & Sons, Chichester, UK, **2009**.

255. Martineau, C.; Senker, J.; Taulelle, F. *Annu. Rep. NMR Spectrosc.* **2014**, *82*, 1–57. doi:10.1016/b978-0-12-800184-4.00001-1.

256. Brouwer, D. H.; Darton, R. J.; Morris, R. E.; Levitt, M. H. *J. Am. Chem. Soc.* **2005**, *127*, 10365–10370. doi:10.1021/ja052306h.

257. Brouwer, D. H.; Cadars, S.; Eckert, J.; Liu, Z.; Terasaki, O.; Chmelka, B. F. *J. Am. Chem. Soc.* **2013**, *135*, 5641–5655. doi:10.1021/ja311649m.

258. Bouchevreau, B.; Martineau, C.; Mellot-Draznieks, C.; Tuel, A.; Suchomel, M. R.; Trébosc, J.; Lafon, O.; Amoureux, J.-P.; Taulelle, F. *Chem. Mater.* **2013**, *25*, 2227–2242. doi:10.1021/cm4004799.

259. Martineau, C.; Bouchevreau, B.; Tian, Z.; Lohmeier, S.-J.; Behrens, P.; Taulelle, F. *Chem. Mater.* **2011**, *23*, 4799–4809. doi:10.1021/cm2021033.

260. Bouchevreau, B.; Martineau, C.; Mellot-Draznieks, C.; Tuel, A.; Suchomel, M. R.; Trébosc, J.; Lafon, O.; Amoureux, J.-P.; Taulelle, F. *Chem. Eur. J.* **2013**, *19*, 5009–5013. doi:10.1002/chem.201203767.

261. Hampson, M. R.; Hodgkinson, P.; Evans, J. S. O.; Harris, R. K.; King, I. J.; Allen, S.; Fayon, F. *Chem. Commun.* **2004**, 392–393. doi:10.1039/b314076h.

262. Hampson, M. R.; Evans, J. O.; Hodgkinson, P. *J. Am. Chem. Soc.* **2005**, *127*, 15175–15181. doi:10.1021/ja054063z.

263. Hibble, S. J.; Chippindale, A. M.; Marelli, E.; Kroeker, S.; Michaelis, V. K.; Greer, B. J.; Aguiar, P. M.; Bilbé, E. J.; Barney, E. R.; Hannon, A. C. *J. Am. Chem. Soc.* **2013**, *135*, 16478–16489. doi:10.1021/ja406848s.

264. Werner-Zwanziger, U.; Chapman, K. W.; Zwanziger, J. W. *Zeit. Phys. Chem.* **2012**, *226*, 1205–1218. doi:10.1524/zpch.2012.0285.

265. Romao, C. P.; Perras, F. A.; Werner-Zwanziger, U.; Lussier, J. A.; Miller, K. J.; Calahoo, C. M.; Zwanziger, J. W.; Bieringer, M.; Marinkovic, B. A.; Bryce, D. L.; White, M. A. *Chem. Mater.* **2015**, *27*, 2633–26476. doi:10.1021/acs.chemmater.5b00429.

266. Epifani, M.; Imperatori, P.; Mirenghi, L.; Schioppa, M; Siciliano, P. *Chem. Mater.* **2004**, *16*, 5495–5501. doi:10.1021/cm048997i.

267. Imanaka, N.; Kobyashi, Y.; Tamura, S.; Adachi, G. *Solid State Ionics* **2000**, *136–137*, 319–324. doi:10.1016/s0167-2738(00)00464-1.

268. Adachi, G.; Imanaka, N.; Tamura, S. *J. Alloys Compd.* **2001**, *323–324*, 534–539. doi:10.1016/s0925-8388(01)01138-0.

269. Imanaka, N.; Kobayashi, Y.; Fujiwara, K.; Asano, T.; Okazaki, Y.; Adachi, G.-y. *Chem. Mater.* **1998**, *10*, 2006–2012. doi:10.1021/cm980157e.

270. Miller, K. J.; Johnson, M. B.; White, M. A.; Marinkovic, B. A. *Solid State Commun.* **2012**, *152*, 1748–1752. doi:10.1016/j.ssc.2012.06.022.

271. Kingery, W. D. *J. Am. Ceram. Soc.* **1955**, *38*, 3–15. doi:10.1111/j.1151-2916.1955.tb14545.x.

272. Carter, B.; Norton, M.G., *Ceramic Materials Science and Engineering*; Springer, New York, New York, 2007.

273. Roy, R.; Agrawal, D. K; McKinstry, H. A., *Ann. Rev. Mater. Sci.* **1989**, *19,* 59–81. doi:10.1146/annurev.ms.19.080189.000423.

274. Romao, C. P.; Miller, K. J.; Johnson, M. B.; Zwanziger, J. W.; Marinkovic, B. A.; White, M. A. *Phys. Rev. B* **2014**, *90*, 024305. doi:10.1103/physrevb.90.024305.

275. Yamamura, Y.; Ikeuchi, S.; Saito, K. *Chem. Mater.* **2009**, *21*, 3008–3016. doi:10.1021/cm900965p.

276. M. W. Barsoum, *Fundamentals of Ceramics*; CRC Press, Boca Raton, Florida, 2002.

277. Balamurugan, S.; Rodewald, U. C.; Harmening, T.; van Wuellen, L.; Mohr, D.; Eckert, H.; Poettgen, R. *Z. Naturforsch., B: Chem. Sci.* **2010**, *65*, 13–17. doi:10.1002/chin.201015017.

278. Guzmán-Afonso, C.; González-Silgo, C.; González-Platas, J.; Torres, M. E.; Lozano-Gorrín, A. D.; Sabalisck, N.; Sánchez-Fajardo, V.; Campo, J.; Rodríguez-Carvajal, J. *J. Phys.: Condens. Matter* **2011**, *23*, 325402:1–325402:9. doi:10.1088/0953-8984/23/32/325402.

279. Makovicky, E.; Balic-Žunić, T *J. Appl. Cryst.* **1996**, *29*, 305–306. doi:10.1107/s0021889895015081.

280. Nassau, K.; Levinstein, H. J.; Loiacono, G. M. *J. Phys. Chem. Solids.* **1965**, *26*, 1805–1816. doi:10.1016/0022-3697(65)90213-1.

281. Dietzel, A. *Z. Elektrochem.* **1948**, *48*, 9–23.

282. Altermatt, D.; Brown, I. D. *Acta Cryst. B* **1985**, *41*, 244–247. doi:10.1107/s0108768185002063.

283. Morelock, C. R.; Greve, B. K.; Gallington, L. C.; Chapman, K. W.; Wilkinson, A. P. *J. Appl. Phys.* **2013**, *114*, 213501. doi:10.1063/1.4836855.

284. Miller, K. J. Towards Near-Zero Coefficients of Thermal Expansion in $A_2Mo_3O_{12}$ Materials, Ph.D. thesis, Dalhousie University, 2012.

285. Dasgupta, N.; Sörge, E.; Butler, B.; Wen, T.-C.; Shetty, D. K.; Cambrea, L. R.; Harris, D. C. *J. Mater. Sci.* **2012**, *47*, 6286–6296. doi:10.1007/s10853-012-6548-2.

286. Zhu, J.; Yang, J.; Cheng, X. *Solid State Sci.* **2012**, *14*, 187–190. doi:10.1016/j.solidstatesciences.2011.11.023.

287. Yang, Y.-M.; Li, L.-C.; Feng, M. *Chin. J. Inorg. Chem.* **2007**, *23*, 382–386 (in Chinese).

288. Sitepu, H. *Powder Diffraction*, **2009**, *24*, 315–326. doi:10.1154/1.3257906.

289. Marezio, M. *Acta. Cryst.* **1966**, *20*, 723–728. doi:10.1107/s0365110x66001749.

290. Ruh, R.; Corfield, P. W. R. *J. Am. Ceram. Soc.* **1970**, *53*, 126–129. doi:10.1111/j.1151-2916.1970.tb12052.x.

291. Stirling, W. G. *J. Phys. C: Solid State Phys.* **1972**, *5*, 2711–2730. doi:10.1088/0022-3719/5/19/005.

292. Greve, B. K.; Martin, K. L.; Lee, P. L.; Chupas, P. J.; Chapman, K. W.; Wilkinson A. P. *J. Am. Chem. Soc.* **2010**, *132,* 15496–15498. doi:10.1021/ja106711v.

293. Allen, P. B.; Chen, Y. R.; Chaudhuri, S.; Grey, C. P. *Phys. Rev. B* **2006**, *73*, 172102. doi:10.1103/physrevb.73.172102.

294. Morelock, C. R.; Gallington, L. C.; Wilkinson, A. P. *Chem. Mater.* **2014**, *26*, 1936–1940. doi:10.1021/cm5002048.

295. Romao, C. P.; Morelock, C. R.; Johnson, M. B.; Zwanziger, J. W.; Wilkinson, A. P.; White, M. A. *J. Mater. Sci.* **2015**, *50*, 3409–3415. doi:10.1007/s10853-015-8899-y.

296. http://opium.sourceforge.net.

297. http://www.sasupenn.edu/rappegroup/htdocs/Research/psp_gga.html.

298. Perdew, J. P.; Burke, K.; Ernzerhof, M. *Phys. Rev. Lett.* **1996**, *77*, 3865–3868. doi:10.1103/physrevlett.77.3865.

299. Gallington, L. C.; Chapman, K. W.; Morelock, C. R.; Chupas, P. J.; Wilkinson, A. P. *J. Appl. Phys.* **2014**, *115*, 053512. doi:10.1063/1.4864258.

300. Ledbetter, H. M. *J. Appl. Phys.* **1973**, *44*, 1451–1454. doi:10.1063/1.1662392.

301. Ranganathan, S. I.; Ostoja-Starzewski, M. *Phys. Rev. Lett.* **2008**, 05504. doi:10.1103/PhysRevLett.101.055504.

302. Zunger, A.; Wei, S.-H.; Ferreira, L. G.; Bernard, J. E.; *Phys Rev Lett* **1990**, *65*, 353–356. doi:10.1103/physrevlett.65.353.

303. Schneider, T.; Srinivasan, G.; Enz, C. P. *Phys. Rev. A* **1972**, 1528–1536. doi:10.1103/physreva.5.1528.

304. Dove, M. T.; Gambhir, M.; Heine, V. *Phys. Chem. Minerals* **1999**, *26*, 344–353. doi:10.1007/s002690050194.

305. Cowley, R. A. *Phys. Rev. B* **1976**, *13*, 4877–4885. doi:10.1103/PhysRevB.13.4877.

306. Hamann, D. R. *Phys. Rev. B* **2013**, *88*, 085117. doi:10.1103/physrevb.88.085117.

307. Sumino, Y.; Anderson, O. L.; Suzuki, I. *Phys. Chem. Minerals* **1983**, *9*, 38–47. doi:10.1007/bf00309468.

308. Dickinson, J. M.; Armstrong, P. E. *J. Appl. Phys.* **1967**, *38*, 602–606. doi:10.1063/1.1709381.

309. Gates, S. D.; Lind, C. *J. Solid State Chem.* **2007**, *180*, 3510 (2007). doi:10.1016/j.jssc.2007.10.011.

310. Paraguassu, W.; Maczka, M.; Souza Filho, A. G.; Freire, P. T. C.; Mendes Filho, J.; Melo, F. E. A.; Hanuza, J. *Vib. Spectrosc.* **2007**, *44*, 66–77. doi:10.1016/j.vibspec.2006.08.006.

311. Arora, A. K.; Nithya, R.; Yagi, T.; Miyajima, N.; Mary, T. A. *Solid State Commun.* **2004**, *129*, 9–13. doi:10.1016/j.ssc.2003.08.032.

312. Greaves, G. N. *Notes Rec. R. Soc.* **2012**, *67*, 37–58. doi:10.1098/rsnr.2012.0021.

313. Qiu-Jie, L.; Bao-He, Y.; Wen-Bo, S.; Er-Jun, L.; Bin, Y. *Chin. Phys. B* **2012**, *21*, 046501. doi:/10.1088/1674-1056/21/4/046501.

314. Kreher, W. S. *Comp. Mater. Sci.* **1996**, *7*, 147–153. doi:10.1016/s0927-0256(96)00073-0.

315. Kreher, W. *J. Mech. Phys. Solids* **1990**, *38*, 115–128. doi:10.1016/0022-5096(90)90023-w.

316. Rice, R. W. *J. Mater. Sci.* **1997**, *32*, 1673–1692. doi:10.1023/a:1018511613779.

317. Griffith, A. A.; *Philos. Trans. R. Soc. London, Ser. A* **1921**, *221*, 169–198.

318. http://www.minitab.com.

319. Weibull, W. *J. Appl. Mech.* **1951**, *18*, 293–297.

320. Chen, X.; Papathanasiou, T. D. *Compos. Sci. Technol.* **2004**, *64*, 1101–1114. doi:10.1016/j.compscitech.2003.07.006.

321. Cousineau, D.; *IEEE Trans. Dielectr. Electr. Insul.* **2009**, *16*, 281–288. doi:10.1109/tdei.2009.4784578.

322. Anglin, B. S.: Lebensohn, R. A.; Rollett, A. D. *Comp. Mater. Sci.* **2014**, *87*, 209–217. doi:10.1016/j.commatsci.2014.02.027.

323. http://www.mathworks.com/products/matlab.

324. http://www.r-project.org.

325. Wojdyr, M. *J. Appl. Cryst.* **2010**, *43*, 1126–1128. doi:10.1107/s0021889810030499.

326. http://fityk.nieto.pl.

327. Siano, D. B.; Metzler, D. E. *J. Chem. Phys.* **1969**, *51*, 1856–1861. doi:10.1063/1.1672270.

328. Mouri, H. *Phys. Rev. E* **2013**, *88*, 042124. doi:10.1103/physreve.88.042124.

329. Ware, R.; Lad, F. Approximating the Distribution for Sums of Products of Normal Variables. University of Canterbury Research Reports, UCDMS2003/15. http://www.math.canterbury.ac.nz/research/ucdms2003n15.pdf.